UNIVERSITY OF SOUTHAMPTON

FACULTY OF ENGINEERING AND APPLIED SCIENCE

INSTITUTE OF SOUND AND VIBRATION RESEARCH

SMART PANEL WITH AN ARRAY OF DECENTRALISED CONTROL SYSTEMS FOR ACTIVE STRUCTURAL ACOUSTIC CONTROL

by

Emanuele Bianchi

A thesis submitted for the award of

Doctor of Philosophy

January 2003

My work is dedicated to Gigi, sincere and unforgettable friend: he always gave me precious advice and even now, from above, I know he's still doing it.

UNIVERSITY OF SOUTHAMPTON

ABSTRACT

FACULTY OF ENGINEERING AND APPLIED SCIENCE

INSTITUTE OF SOUND AND VIBRATION RESEARCH

Doctor of Philosophy

SMART PANEL WITH AN ARRAY OF DECENTRALISED CONTROL SYSTEMS FOR ACTIVE STRUCTURAL ACOUSTIC CONTROL

by Emanuele Bianchi

This thesis presents the results of a theoretical and experimental study of active sound transmission through a smart panel. The system studied consists of a thin aluminium panel with an embedded 4×4 array of square piezoceramic actuators. The sensing system consists of a 4×4 array of accelerometers positioned above the centres of the sixteen piezoceramic patches on the other side of the panel. Each of the sixteen sensor–actuator pairs is arranged to implement local (decentralised) velocity feedback control. The smart panel is mounted on the top of a rectangular cavity with rigid walls in order to measure the sound radiation from the panel when excited by either a primary acoustic source (a loudspeaker) within the cavity or a primary structural source (a shaker) acting directly on the panel.

This thesis can be divided into three parts. The first part contains a theoretical and numerical study of the smart panel with sixteen decentralised control units. A fully coupled model of the smart panel mounted on the cavity has been formulated, from which the total kinetic energy and sound radiation can be derived as a function of the feedback gain implemented in the sixteen decentralised control units. The stiffness and mass effects of the piezoelectric actuators, and the mass effects and local dynamics of the accelerometers have been taken into account in the model.

The second part describes the detailed design and implementation of the sixteen decentralised control units. The behaviour of the sensor-actuator pairs has been studied and their open loop frequency response functions are analysed, with particular regard to the effects of the sensor-actuator local dynamics and of the piezo patch dimensions. The implementation of velocity feedback on a single control unit is first described and its stability discussed. The implementation of the complete system with sixteen individual control loops has then been discussed and the stability of the multi-channel system has been analysed.

In the third part, the control effectiveness of the smart panel has been assessed experimentally. The reduction of the panel's total sound power radiation has been measured in an anechoic chamber when excited either by the acoustic field produced by a loudspeaker placed in the Perspex box or directly by a point force generated with a shaker. The variation of the vibratory field over the panel surface has also been measured with a laser vibrometer to describe the action of the smart panel and compare it with the predictions of the theoretical model.

LIST OF CONTENTS

LIST OF ILLUSTRATIONS

LIST OF TABLES

ACKNOWLEDGEMENTS

I would like to express my sincere gratitude to my supervisor, Dr. Paolo Gardonio for giving me the opportunity to work with him, and for his valuable and insightful guidance throughout this work. His support and encouragement during my studies at ISVR made the whole experience highly supportive and educational. Also, I wish to express my sincere thanks to Professor Steve Elliott for his valuable inputs, and critical suggestions at various points of this work, which made this thesis stronger.

I am indebted to my parents and my brother for supporting and encouraging me throughout my research. This work would not have been possible without their motivation and support.

1. INTRODUCTION

Active noise control (ANC) and active noise and vibration control (ANVC) systems have been successfully used for the control of tonal noise disturbances in relatively small enclosures such as the cabin of aircraft or cars, as described in reference [4]. These control systems operate with large numbers of error sensors and actuators distributed within the cavity via a fully-coupled multi input multi output (MIMO) adaptive feed-forward controller [4]. Therefore they are relatively bulky, heavy, invasive and costly systems that can control only tonal disturbances for which a causal reference signal unaffected by any control input is available. As a result they have been successfully implemented only in few applications as for example the control of tonal disturbances in propeller aircrafts (Section 10.15 of reference [4] and [5-8]) or engine noise in cars (Section 10.15 of reference [4] and [9,10]).

ANC systems using adaptive feed-forward controllers have also been developed for the control of stationary random disturbances. The success of these control systems depends on two issues: first, the possibility of modelling, within the controller, the feedback effects of the secondary sources on the reference sensors so that the control filters can be derived from the design of an optimal dummy controller and, second, the possibility of measuring the primary disturbance well in advance so that the optimal controller has a causal impulse response [4]. These two problems have made it very difficult and challenging to develop ANC or ANVC systems either for the control of random noise in aircraft [11,12] due to jet airflow noise, or the control of road and aerodynamic stationary random noise in cars [13,14]. Up to the present, the only really successful application has been for the control of fan random noise in ventilation ducts, where the reference signal can be taken sufficiently in advance to guarantee a causal optimal filter and the feedback effect of the control sources on the detection sensors can be clearly identified [4,15].

1.1 Feed-forward active structural acoustic control

During the past two decades scientists have begun to consider the possibility of reducing noise transmitted to enclosures by actively controlling the sound radiation/transmission through the side partitions. In this case structural actuators are integrated on the partitions in

such a way as to modify their vibration and thus reduce the sound radiation/transmission. A detailed introductory description of this method, also known as active structural acoustic control (ASAC), is given in reference [16]. This control approach was conceived and initially developed within the same scientific community that studied ANC systems. As a result the first ASAC systems were built using adaptive feed-forward controllers which a) require a set of error sensors scattered in the receiver room for the detection of the total sound power radiation as an error parameter to be minimised and b) enable only the control of tonal disturbances for which a causal reference signal could be feed trough to the controller [16,17]. Thus, although the actuators were integrated into the partition, these systems still had all the practical drawbacks listed for ANC and AVNC systems. It was also found that, in some frequency bands, the minimisation of the sound radiation was achieved by reconstructing the modal response of the partition so that the vibration field was slightly enhanced rather than reduced, with consequent potential problems related to mechanical failure [16-20] or an increase in nearfield pressure [35]. This phenomenon was found to be caused by the sound radiation mechanism. In general, above the critical frequency [21], the sound radiation of a partition is determined only by the self radiation efficiency of each structural mode, thus self radiation efficiencies are independent to the modal order [22]. In contrast, below the critical frequency the sound radiation of a partition is controlled both by the self radiation of each structural mode and by the mutual radiation of pairs of structural modes, also the self or mutual radiation efficiencies heavily depend on the mode orders (in general structural modes with both or one odd mode order have greater radiation efficiencies and the radiation efficiency tends to decrease as the mode order is increased) [21-23]. This detailed description of the sub-critical behaviour is generally necessary except for well separated resonance frequencies of the partition, i.e. for low modal overlap or modal density [24]. The overall vibration of the partition when it has well separated resonance frequency is primarily controlled by the resonant structural mode and thus the sound radiation is governed by the self radiation efficiency of the resonant structural mode itself [16,22]. However, either at off-resonance frequency bands or at higher frequencies, where the modal overlap of the partition is sufficiently high so that several resonant modes determines its vibration [24], the sound radiation contribution due to the mutual effects of pair of modes is not negligible [16,22,23]. Although the self radiation resistance of each structural mode is always positive, the mutual radiation resistance of pairs of structural modes could assume negative values which give rise to sound cancelling effects [22]. Thus, below the critical frequency, the control system can reduce the total sound power radiated/transmitted in narrow frequency

bands by rearranging the vibration contribution of each single structural mode in order to maximise this sound cancelling effect. This approach is termed modal restructuring [19] and can result into an enhancement of the vibration level of the partition [16,18-20]. Alternatively, at the resonance frequencies of well separated structural modes or at frequencies above the critical frequency, the control system can reduce the total sound power radiated only by reducing the vibration contribution of efficiently radiating structural modes. This approach is termed modal suppression [19]. Burdisso and Fuller [25] also considered the modal restructuring mechanism from a different point of view where the vibration of the structure after control is characterised by new eigenvalues and eigenfunctions which have lower radiation efficiencies.

An important step forward for this technology was achieved by integrating structural error sensors within the partition, which were able to estimate the far field sound radiation [26-33]. This allowed the construction of compact and light control systems with a relatively small number of input-output channels that were therefore more suitable for practical applications. Most of this research sprung up from the aerospace and naval sectors where there was a clear requirement of reducing the structure-borne noise transmission or radiation of the fuselage walls or marine hulls which are generally made of thin and lightly damped panels [34]. It was found that, at relatively low frequencies where the acoustic wavelength is larger than the dimensions of the panels that make up the fuselage walls or marine hull, the vibration of each panel can be considered to be the superposition of a number of frequency dependant self radiating radiation modes, of which by far the most efficient one corresponds closely to the net volume velocity of the panel over a relatively large frequency band [32,35] (for more details see references 1-7 in [32]). A lot of work has therefore been carried out to develop smart panels with integrated distributed strain sensors [31,35-51] or with arrays of sensors [49-60] that measure the vibration components of a panel that mostly contribute to the far field sound radiation, in particular the first radiation mode and the volumetric vibration of the panel [35]. Active control tends to be effective at relatively low frequencies where the first radiation mode, or its volume velocity approximation, produces most of the sound radiation. Thus, just one error sensor could be used to have a good estimate of the total sound radiation by a panel.

Work has also been carried out to build up input strain actuators made either with arrays of small piezoceramic patches or distributed piezoelectric films [36,39,41,49-52,61-70] to be

coupled with the sensor transducer. If the sensor-actuator transducers are collocated[1] and dual[2] [51,71-74] then the real part of their response function is constrained to be positive real so that a single input single output (SISO) adaptive feed-forward controller could be implemented with a very fast-acting controller [35,50,51]. Thus the technological progress in the construction of smart panels with collocated and dual sensor–actuator pairs has given the possibility of building very compact, light and non invasive control systems that could be very effective for the control of tonal disturbances [16,28-33].

Some attempts have also been made to develop adaptive feed-forward controllers for broadband random disturbances by placing detection sensors in the vicinity of the panel if not on the panel itself [75]. In this case the main problem is given by the fact that having closely placed detection sensor and control actuator transducers prevents the possibility of deriving a causal controller [76]. This type of control system has been developed with some level of success in double panel partitions, such as aircraft double wall constructions, by placing the detection transducers on the excited panel and the control and error transducers on the radiating panel [77].

1.2 Feedback active structural acoustic control

In parallel to the work carried out on feedforward systems, ASAC systems have also been developed using feedback controllers. The implementation of feedback control systems do not require a reference signal so that, when used for disturbance rejection applications, they could be used to control both tonal and random, wide-band, disturbances. Bauman et al, [26] and Bauman and Robertshaw [27] first proposed a methodology to design a feedback control system for the reduction of broad band sound radiation by a panel which uses structural error sensor and control actuator transducers acting on the panel. Their instructive work has led to several studies were MIMO feedback control systems using structural sensors and actuators have been used in smart panels for the control of sound radiation/transmission. The

[1] Collocation is a geometrical condition were point sensor-actuator transducers are placed in the same position of the structure and distributed sensor-actuator transducers are placed over the same area of the structure.

[2] Duality is a physical property were the sensor-actuator respectively excites and detects the vibrations of a structure in the same manner, i.e. they are characterised by the same detection and excitation function for each natural mode of the structure. Often dual sensor-actuator transducers pairs are also named to be "matched," "compatible" or "reciprocal."

background of most of the scientists that developed these control systems was modern feedback control theory, where the synthesis of the optimal feedback gains in the controller is made using a state-space formulation [50,51]. A series of papers have been published where optimal static- (fixed gains) or dynamic- (frequency dependent gains) controllers are designed with reference to H_2 or H_∞ cost functional that refer to either a set of states of the system (state-feedback) or a set of measured output parameters (output-feedback) [26,27,50,51,78-86]. Work has also been presented where the optimal controller has been derived from the standard linear quadratic regulator (LQR) or linear quadratic Gaussian (LQG) problems, which could be considered as a subset of the more general H_2 optimisation problem [50,51,87,88]. A consistent review of the various aspects that characterize the modern approach for the design of feedback controllers for vibration/sound-radiation rejection problems is given in references [50,51].

Although most of the initial studies have demonstrated the possibility of designing MIMO state-feedback control systems for ASAC purposes, the implementation stage has resulted into a series of practical problems. For example, in order to have compact smart panels, the parameter to be controlled, the radiated sound power, is not directly measured but derived from a set of structural sensors bonded on the panel. From the control point of view this means that the performance variables, i.e. the states, of the systems can not be directly measured and thus output-feedback controllers can not be implemented. As a consequence state-feedback control has to be implemented that requires a state estimator or observer system that models the essential physics of the system. In practice the state estimator consists in a set of analogue or digital filters which model the plate dynamics and the sound radiation mechanisms as suggested by Bauman et al, [26] and Bauman and Robertshaw [27].

1.3 Feedback SISO active structural acoustic control

Although the work carried out to develop distributed strain sensors and actuators for smart panels was initially aimed at the implementation of feed-forward control systems, scientists soon recognized that these types of transducers would also have great advantages in the design and implementation of feedback control systems. Indeed the possibility of building strain sensors which measure the radiation modes of panels has given the possibility of implementing output-feedback control systems where the state variables to be minimised could be directly derived from the measured radiation modes outputs without the need of a

state estimator. In particular, since the low frequency sound radiation is controlled by the first radiation mode, and knowing that, at relatively low frequencies, the first radiation mode could be approximated by the volume velocity vibration of the panel component which is frequency independent, the possibility of developing SISO feedback control systems based on the control of volume velocities was envisaged [32,35].

Scientists with a background in modern control theory designed optimal SISO feedback control systems using the state-space formulation for the minimisation of either an H_2 or H_∞ cost functional. In contrast scientists with a background in classic feedback control theory followed a different path, where the design of the sensor–actuator transducers is oriented to the implementation of SISO feedback control systems for disturbance rejection [89-92]. This control approach is characterised by the classic disturbance rejection feedback control loop in which the output of the system, for example the volumetric vibration or a specific radiation mode of the panel, is produced by the primary disturbance and control excitation that is itself proportional to the measured output via a feedback control function. In general the control function can be arranged in such a way to enhance the mass, stiffness and damping effects of the controlled structure. However for the specific case of disturbance rejection the most suitable strategy is active damping, which reduces the response of the structure at resonance frequencies and, as a result, the steady-state response to wide-band disturbances [51]. Active damping does not produce attenuation at off-resonance frequency bands, on the contrary it tends to fill in the response spectrum at anti-resonance frequencies. Therefore active damping is not particularly suitable for the control of tonal disturbances except in the particular case where the excitation frequency is close to a resonance frequency of the smart panel, which does not vary as the physical or operating conditions changes (variation of temperature or change of static loading etc.). The literature on classic feedback control is well established particularly for servo-mechanisms and a detailed summary of SISO classic feedback control theory of flexible structures is given in references [50,51].

The simplest way of achieving active damping is by implementing direct velocity, or rate, feedback. In this case the output of the sensor is directly feed back to the actuator via a fixed control gain. This control scheme is stable for any value of the control gain if the sensor–actuator frequency response is strictly positive real [35,50,51,70]. As highlighted in the previous section, this happens when the sensor–actuator transducers are collocated and dual. Most of the work carried out by scientists is therefore focussed on the design of collocated and dual sensor–actuator pairs so that a relatively simple feedback controller can be implemented, which is unconditionally stable [52]. If the sensor–actuator transducers are not

collocated and dual then only a limited range of control gains could be implemented in order to guarantee stability and this result in a reduced performance capability of the system. In this case the control performance could be enhanced by shaping the control function with standard compensator circuits as for example Lead, Lag, PI and PID compensators.

Building distributed sensor–actuator transducers, which are collocated and dual, is not an easy task. The most obvious way of building these sensor–actuator pairs is by placing the sensor on one side of the panel and the actuator on the opposite side of the panel. Gardonio et al. [70] have shown that in general this simple construction can not provide a strictly positive response function. The sensor output is determined by both the bending and in-plane vibration of the panel generated by the actuator. Although the in-plane vibration of the panel is relatively small compared with the bending one, the sensor output is severely affected by this component which produces an extra phase shift at the first in-plane resonant mode of the panel. As a result, at higher frequencies the sensor–actuator response function is not strictly positive real and is characterised by larger amplitude values than in the low frequency range of control. This precludes the implementation of direct velocity feedback control and even with an appropriate compensator circuit only relatively small control gains could be implemented and thus modest control effects are achieved [49,58,59]. Several alternative constructions have been studied to avoid this sensor–actuator feed-through effect. For example the distributed sensor has been substituted with a grid of accelerometers but even in this system, aliasing effects produce a non strictly positive real response function [57-60]. Alternatively Lee et al. [93] have proposed to use double-layer sensor-actuator transducers to be operated in such a way to avoid the detection of in-plane vibration and to excite the plate only in bending. In this case the implementation of the two transducers is corrupted by interlayer coupling effects [93]. Cole and Clark [94] have proposed a similar solution where only two transducers are used, which work simultaneously as actuators and sensors. This solution avoids the interlayer coupling effect described above. However, the implementation of these sensors-actuators is not trivial since relatively small charge outputs have to be derived from the large inputs to each transducer. This requires compensation techniques which are very sensitive to physical or operational changes of the system (static loads, temperature etc.). Finally the operation of relatively large distributed sensor or actuator transducers with shaped electrodes is relatively sensitive to shaping errors of the electrodes which could contribute to make the response function to be non strictly positive [95].

Because of their experience on the implementation of feed-forward digital controllers, some researchers developed a particular design approach for feedback systems, in which the

control system can be modelled with a feed-forward control scheme. This was done by building an internal model of the control path in the feedback loop and so the approach has become known as internal model control IMC [96]. With this approach, the implementation of a feedback control scheme is redirected to the derivation of a suitable model of the feedback path and the derivation of a classic adaptive feed-forward control filter. The implementation of ASAC with IMC feedback control schemes has been tested in a few cases [97-99].

1.4 Decentralised MIMO feedback active structural acoustic control

The problems encountered in the development of smart panels for SISO feedback ASAC control with distributed transducers that cover the entire surface of the panel have forced researchers to find alternative control solutions.

In Section 1.1 it was argued that below the critical frequency and for low frequencies such that the resonances of the panel are well separated, the sound radiation at resonance is controlled by the self radiation efficiency of the resonant mode. In contrast, the off-resonance frequency sound radiation is controlled by both the self- and mutual-radiation efficiencies of the structural modes. A new formulation of the sound radiation in terms of radiation modes was therefore proposed as a tool to design structural sensors that would have been able to estimate the sound radiation either at resonance or off-resonance frequencies. Such complicated sensors are not necessary to feedback controllers to actively damp the structural modes. Active damping feedback control tends to be effective only in the vicinity of resonance frequencies, where the sound radiation is controlled by the self radiation of the resonant mode, while it tends to enhance the vibration at anti-resonance frequencies, where the sound radiation is controlled by the self and mutual radiation effects of a set of modes. In order to implement active damping feedback control it is sufficient to have sensor–actuator transducers that are well coupled with the low order structural modes. Moving the sensor–actuator design problem from the control of radiation modes to that of structural modes is not a significant practical improvement, since distributed sensor and actuator transducers that cover the entire surface of the panel are still required. However Elliott et al [3] have shown that active damping of structural modes could be achieved with small localized control units that implement SISO velocity feedback control. They initially considered the ideal case of having a collocated and dual point-velocity and point-force sensor–actuator system which is

positioned away from the nodal lines of the modes to be controlled. These two transducers would enable the implementation of unconditionally stable direct velocity feedback control. Elliott et al. [3] noticed that as the control gain is gradually increased from zero, the active damping effect of the structural modes grows and consequently both the total kinetic energy and total sound radiation of the panel averaged in a certain frequency band decrease. However, they also found that this behaviour is only valid up to an optimal feedback control gain, above which the kinetic energy or sound radiation by the panel increases and can even become larger than before control. The analysis of this phenomenon showed that the velocity feedback control unit works as a sky-hook damper which absorbs energy from the structural modes. However, for relatively large control gains, the control actuator is actually driven to pin the panel at the error sensor position so that the vibration of the panel is moved back to that of a lightly damped structure with an extra pinning point. Therefore a set of new structural modes are created which could be excited at new lightly damped resonance frequencies and radiate sound even more effectively than the original modes (see section 2.5 of reference [21]).

Starting from these considerations Elliott et al. [3] proposed a new control configuration based on grids of decentralised velocity feedback control units using a piezoceramic patch actuator with on the centre a small accelerometer. Although it is non collocated and non dual, this sensor–actuator configuration enables relatively large feedback control gains at low frequency so that the equivalent of a grid of sky-hook dampers could be implemented provided the control gains do not exceed the optimal values. The large number of control units, which are uniformly distributed over the panel surface, allows the damping of a relatively large number of low frequency resonant modes and consequently the control of low frequency wide-band sound radiation. This type of decentralised vibration and sound radiation control effects was first observed by Petitjean and Legrain [100] in an experiment where a grid of 5×3 collocated piezoceramic patches mounted on either side of a panel were used to either implement a fully coupled MIMO LQG feedback controller or fifteen SISO rate feedback controllers. For this particular type of panel they found that the vibration reductions in the two control cases were very similar. This type of experiment was then repeated on a different smart panel [101] and it was again found that, despite its simplicity, decentralised feedback control was giving similar control effects to those of a MIMO optimal feedback controller. Indeed Petitjean et al. [101] noted that "Whatever the control algorithm, in this experiment of active noise control, it turns out that controlling panel vibrations through distributed actuators and sensors results in an attenuation of the pressure field. This

fact seems contradictory to some previously published studies on the topic, which point out that it is important to take the radiation efficiency of the plate modes whose frequencies lie within the frequency band of interest into account in the control law." The contradiction comes from the fact that radiation mode theory is important when feed-forward active control is implemented at off-resonance frequencies, where the mutual radiation effects can not be neglected. Alternatively, active damping of broadband disturbances using feedback control mainly regulates the vibration at resonance frequencies, where the sound radiation is determined only by the resonant modes.

1.5 Scope and objectives

This PhD dissertation presents a theoretical and experimental study of active sound transmission through a partition with a grid of decentralised velocity feedback control units. The system studied consists of a thin aluminium panel of dimensions $l_x \times l_y = 414 \times 314\,\text{mm}$, with a 4×4 array of small piezoceramic actuators bonded on one side of the panel and a collocated array of miniature accelerometers placed on the other side. Each control unit, composed of a square piezoelectric patch and a collocated accelerometer, is arranged to implement local (decentralised) velocity feedback control, by means of a simple analogue feedback controller that provides a constant gain. The smart panel is mounted on the top of a rectangular cavity with rigid walls in order to measure the sound transmission/radiation with reference to either a primary acoustic source (a loudspeaker) within the cavity or a primary structural source (a shaker) acting directly on the panel.

The three main objectives of this thesis are:

1. to investigate the physics of the smart panel with sixteen decentralised control units;
2. to assess the stability and robustness of the control system;
3. to design, build and implement a prototype smart panel.

A numerical model of the complete system (smart panel with sixteen decentralised velocity feedback control units and rigid cavity) has been formulated in order to assess the feasibility of such a control system and to pursue the first objective. Moreover, an exhaustive study of the sensor-actuator response functions has been carried out to meet the second objective. Finally, the practical issues involved in the experimental implementation of the decentralised control system (the third objective) have been addressed, including the construction of the

smart panel and cavity and the design of the sixteen analogue controllers.
The effectiveness of the decentralised velocity feedback control is demonstrated in a set of experimental tests that show the performances of the system in terms of reduction of the vibration level and reduction of the sound transmission for the two different types of excitations: loudspeaker in the cavity or shaker on the panel.

1.6 Structure and organization

This thesis can be divided into three parts. The first part, consisting of Chapters 2 and 3, contains the theoretical study and the numerical results concerned with the smart panel with sixteen decentralised control units. More precisely, in Chapter 2 the original idea of using a decentralised control system is investigated for the panel excited by an acoustic plane wave, while in Chapter 3, a further investigation of the prototype smart panel is carried out considering the testing configuration implemented in this study, i.e. smart panel mounted on the top of a rectangular cavity with rigid walls and excited by either a primary acoustic source (a loudspeaker) within the cavity or a primary structural source (a shaker) acting on the panel.

The second part of the thesis consists of Chapters 4, 5 and 6, and contains the design and implementation of the sixteen decentralised control units. In Chapter 4 the behaviour of the sensor-actuator pairs is studied and their open loop frequency response functions are analysed, with particular attention to the effects of the sensor-actuator local dynamics and of the piezo patch dimensions. In Chapter 5 the implementation of velocity feedback on a single control unit is discussed. An analysis of the stability of the single-channel control system is reported and the design of a phase-lag compensator, which increases the gain margin of the feedback controller, is also presented. The results of the on-line implementation of the single-channel control system are then discussed, in terms of attenuation of the vibration level of the plate and reduction of the sound transmission. Finally, in Chapter 6, the implementation of the complete system with sixteen individual control loops is described and the results obtained are discussed. Moreover the stability analysis of the multi-channel system is assessed using the Generalised Nyquist Criterion.

In the third part of the thesis, consisting of Chapters 7 and 8, the control effectiveness of the

smart panel has been assessed experimentally by measuring in a anechoic chamber the reduction of its total sound power radiation when it is mounted on a Perspex box with very thick and rigid side walls. The panel has been excited either by the acoustic field produced by a loudspeaker placed in the Perspex box or directly by a point force generated with a shaker (Chapter 7). Also, the variation of the vibratory field over the panel surface has been measured with a laser vibrometer in such a way as to describe the main operative features of the sixteen decentralised control units (Chapter 8). Conclusions and recommendations for future work are given in Chapter 9.

In this work most of the experimental results are plotted without specifying the reference parameter for the units expressed in decibels. This is due to fact that the plots presented are either used to highlight the main features of frequency response functions or to evaluate the relative attenuation of the vibration/sound radiation of the panel without and with control. The sensitivity parameters of the sensors used for the experimental acquisitions are given in Appendix A.

1.7 Contributions of the thesis

The main original contributions of this thesis are:

1. An analysis of the response of a smart panel that has embedded piezoelectric actuators and acceleration sensors, including a detailed investigation of the effects of these transducers on the overall dynamics.
2. The design of a feedback controller for a single piezoelectric actuator and acceleration sensor and an analysis of the effect on the performance of such a controller of the actuator and sensor dynamics.
3. The design, implementation and testing of a smart panel with a 4×4 array of piezoelectric actuators and acceleration sensors and its associated sixteen channels decentralised feedback controller.
4. The analysis of stability using the Generalised Nyquist criterion for the sixteen channels decentralised controller from experimental data.

2. SMART PANEL WITH A 4×4 ARRAY OF DECENTRALISED SENSORS/ACTUATORS

In this chapter the original idea of local velocity feedback using multiple actuators and sensors [1-3] is investigated considering a panel with an array 4×4 of miniature accelerometers and closely located piezoceramic actuators placed under each sensor. The performance of such a system is analysed in terms of the reduction of the vibration and sound transmission through the smart panel when it is excited by an acoustic plane wave. The theoretical model developed for this preliminary study is described in the next section, while the multi-channel feedback controller is analysed in the successive one. In the third section, the local dynamics of the sensor-actuator pairs is described and the effects they produce on the overall system are investigated. Finally, in the last section, the response of the panel and its sound radiation is discussed with reference to a range of feedback gains in the decentralised control systems.

2.1 Theoretical Model

As shown in Figure 2.1, the system studied consist of a clamped and baffled aluminium panel of dimensions 414 mm × 314 mm × 1 mm. The panel is excited on one side by a harmonic plane acoustic wave of unit amplitude. The azimuthal and lateral incidence angles of the acoustic wave are chosen to be of $\phi = 45^o$ and $\theta = 45^o$ so that all the structural modes of the panel are excited. The panel radiates sound on the other side of the panel into free field. A weakly coupled model is used to describe the sound transmission through the panel which assumes that the acoustic pressure of the radiated sound has no effect on the vibration of the panel, which is a reasonable assumption in air for this thickness of panel.

The panel is equipped with an array of 4 × 4 control systems that operate independently (see Figure 2.2). The sixteen control systems have been equally spaced along the x– and y–directions so that the distances between two actuators or between a lateral actuator and the edge of the plate are $d_x = l_x/5 = 82.8\,\text{mm}$ and $d_y = l_y/5 = 62.8\,\text{mm}$. Each control system consist of a piezoelectric actuator, of dimensions 25 mm × 25 mm × 0.5 mm, which is

bonded on the excited side of the panel and a small accelerometer which is placed on the other side of the panel in correspondence of the centre of the actuator. The actuator is driven by a small single–channel analogue controller that implement velocity feedback control and could be integrated within the accelerometer case. Tables 2.1 and 2.3 summarize the geometrical and physical properties of the system.

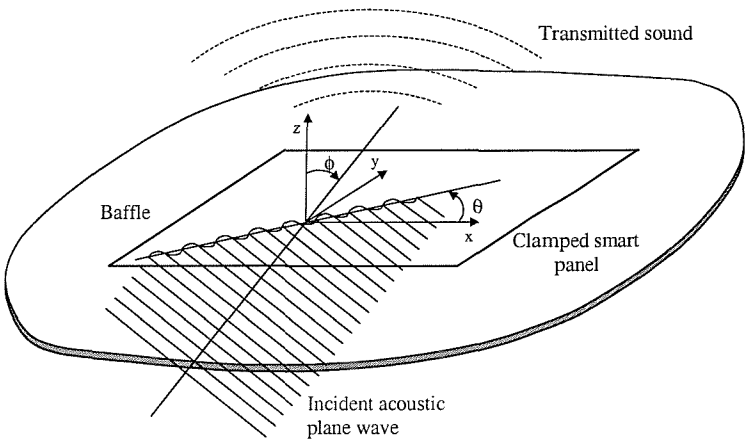

Figure 2.1: *Physical arrangement for the computer simulations, in which the vibration of a baffled clamped panel is excited by a plane acoustic wave on one side and radiates sound into an anechoic half space on the other side of the panel.*

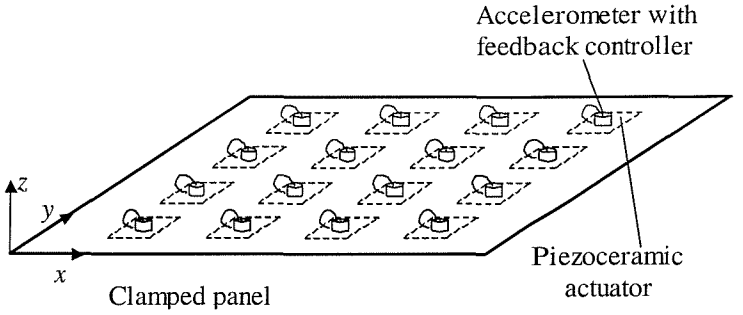

Figure 2.2: *Smart panel with a 4×4 array of decentralized control systems composed by an accelerometer sensor with a built in feedback control system and a piezoceramic actuator is mounted on the panel to implement vibro–acoustic control.*

The steady state response of the panel and sound radiation in a frequency range 0 to 1 kHz have been calculated assuming the primary disturbance to be harmonic with time dependence of the form $\exp(j\omega t)$. The velocity-type and force-type parameters used in the model have been taken to be the real part of counter clock wise rotating complex vectors, e.g. phasors. The velocity or force parameters are therefore given by $\dot{w}(t) = \mathrm{Re}\{\dot{w}(\omega)e^{j\omega t}\}$ or $f(t) = \mathrm{Re}\{f(\omega)e^{j\omega t}\}$ where $\dot{w}(\omega)$ and $f(\omega)$ are the velocity and force phasor at the instant $t = 0$ and $j = \sqrt{-1}$.

Table 2.1: *Geometry and physical constants for the panel.*

Parameter	Value
Dimensions	$l_x \times l_y = 414 \times 314$ mm
Thickness	$h_s = 1$ mm
Mass density	$\rho_s = 2700\ \mathrm{Kg/m^3}$
Young's modulus	$E_s = 7 \times 10^{10}\ \mathrm{N/m^2}$
Poisson ratio	$\nu_s = 0.33$
Loss factor	$\eta_s = 0.05$
Smeared mass density (including part of the mass effects of the piezo actuators)	$\overline{\rho}_s = 3000\ \mathrm{Kg/m^3}$
Smeared Young's modulus (including the stiffening effects of the piezo actuators)	$\overline{E}_s = 7.1 \times 10^{10}\ \mathrm{N/m^2}$

Table 2.2: Geometry and physical constants for the piezoceramic patches.

Parameter	Value
Dimensions of the PZT patches	$l_{xp} \times l_{yp} = 25 \times 25$ mm
Thickness of the PZT patches	$h_p = 0.5$ mm
Mass density	$\rho_s = 7500\ \mathrm{Kg/m^3}$
Young's modulus	$E_p = 50 \times 10^9\ \mathrm{N/m^2}$
Poisson ratio	$\nu_p = 0.29$
Stress constant	$e_{31} = 7.5\ \mathrm{N/Vm}$
Strain constant	$d_{31} = 150 \times 10^{-12}$ m/V
Distance between the centres of two adjacent patches	$d_x, d_y = 82.8, 62.8$ mm

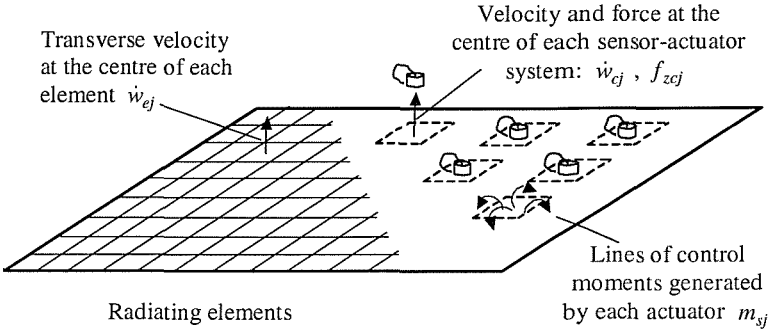

Figure 2.3: *Velocity and force-moment notation used in the mathematical model.*

The mathematical model built in for the simulations considers the panel divided into a grid of rectangular elements whose dimensions have been taken to be $l_{xe} = l_x/(4M)$ and $l_{ye} = l_y/(4N)$, where M and N are the higher modal orders used in the calculus.

The phasors of the transverse velocities, $\dot{w}_{ej}(\omega)$ at the centres of these elements have been grouped into the following vector:

$$\mathbf{v}_e(\omega) \equiv \begin{Bmatrix} \dot{w}_{e1}(\omega) \\ \dot{w}_{e2}(\omega) \\ \vdots \\ \dot{w}_{eP}(\omega) \end{Bmatrix}, \tag{2.1}$$

where $P = 8MN$ is the total number of elements. Similarly the phasors of the transverse velocities, $\dot{w}_{cj}(\omega)$, and forces, $f_{zcj}(\omega)$, at the centres of each control systems have been defined as follows:

$$\mathbf{v}_c(\omega) \equiv \begin{Bmatrix} \dot{w}_{c1}(\omega) \\ \dot{w}_{c2}(\omega) \\ \vdots \\ \dot{w}_{c16}(\omega) \end{Bmatrix} \qquad \mathbf{f}_c(\omega) \equiv \begin{Bmatrix} f_{zc1}(\omega) \\ f_{zc2}(\omega) \\ \vdots \\ f_{zc16}(\omega) \end{Bmatrix}. \tag{2.2a,b}$$

The primary excitation is given by the amplitude of the incident acoustic wave in which case:

$$\mathbf{f}_p(\omega) = p_i(\omega) \ . \tag{2.3}$$

The excitations of the sixteen piezoelectric control actuators can be approximated by four line moments, all with equal magnitude, acting along the edges of the piezoelectric patches so that the control excitations can be grouped into a vector of moments as follows:

$$\mathbf{f}_s(\omega) = \begin{Bmatrix} m_{s1}(\omega) \\ m_{s2}(\omega) \\ \vdots \\ m_{s16}(\omega) \end{Bmatrix}. \tag{2.4}$$

The vibration of the panel at the centres of the elements and at the centres of the control systems can be expressed in matrix form using mobility functions so that:

$$\mathbf{v}_e(\omega) = \mathbf{Y}_{ep}(\omega)\mathbf{f}_p(\omega) + \mathbf{Y}_{es}(\omega)\mathbf{f}_s(\omega) \ , \tag{2.5}$$

$$\mathbf{v}_c(\omega) = \mathbf{Y}_{cp}(\omega)\mathbf{f}_p(\omega) + \mathbf{Y}_{cs}(\omega)\mathbf{f}_s(\omega) \ , \tag{2.6}$$

where the elements of the four mobility matrices are defined as follows [102]:

$$Y_{ep}^{p,1}(\omega) = \frac{\dot{w}_{e,p}(\omega)}{p_i(\omega)} = j\omega \sum_{m=1}^{M}\sum_{n=1}^{N} \frac{\phi(x_{ep}, y_{ep}) \int_0^{l_y}\int_0^{l_x} \phi(x,y)dxdy}{\Lambda_{mn}\left[\omega_{mn}^2(1+j\eta_s) - \omega^2\right]} \ , \tag{2.7}$$

$$Y_{es}^{p,q}(\omega) = \frac{\dot{w}_{e,p}(\omega)}{m_{s,q}(\omega)} = \\ = j\omega \sum_{m=1}^{M}\sum_{n=1}^{N} \frac{\phi(x_{ep}, y_{ep})\left\{\int_0^{a_x} \psi^{(y)}(x_{sq}, y_{sq1}) - \psi^{(y)}(x_{sq}, y_{sq2})dx + \int_0^{a_y} -\psi^{(x)}(x_{sq1}, y_{sq}) + \psi^{(x)}(x_{sq2}, y_{sq})dy\right\}}{\Lambda_{mn}\left[\omega_{mn}^2(1+j\eta_s) - \omega^2\right]} \ , \tag{2.8}$$

$$Y_{cp}^{p,1}(\omega) = \frac{\dot{w}_{c,p}(\omega)}{p_i(\omega)} = j\omega \sum_{m=1}^{M}\sum_{n=1}^{N} \frac{\phi(x_{cp}, y_{cp}) \int_0^{l_y}\int_0^{l_x} \phi(x,y)dxdy}{\Lambda_{mn}\left[\omega_{mn}^2(1+j\eta_s) - \omega^2\right]} \ , \tag{2.9}$$

$$Y_{cs}^{p,q}(\omega) = \frac{\dot{w}_{c,p}(\omega)}{m_{s,q}(\omega)} = \\ = j\omega \sum_{m=1}^{M}\sum_{n=1}^{N} \frac{\phi(x_{cp}, y_{cp})\left\{\int_0^{a_x} \psi^{(y)}(x_{sq}, y_{sq1}) - \psi^{(y)}(x_{sq}, y_{sq2})dx + \int_0^{a_y} -\psi^{(y)}(x_{sq1}, y_{sq}) + \psi^{(y)}(x_{sq2}, y_{sq})dy\right\}}{\Lambda_{mn}\left[\omega_{mn}^2(1+j\eta_s) - \omega^2\right]} \ , \tag{2.10}$$

where:

$\dot{w}(\omega)$	is the phasor of the panel velocity in z–direction,
$p_i(\omega)$	is the sound pressure phasor of the incident acoustic wave,
ω	is the circular frequency ,
$j = \sqrt{-1}$	is the complex operator ,
m, n	are modal indices ,

ω_{mn} is the natural frequency of the *m,n*-th mode,

$\phi_{mn}(x,y)$ is the *m,n*-th bending natural mode at position (x,y) ,

E_s is the Young's modulus of elasticity ,

ρ_s is the density of the material of the panel ,

ν_s is the Poisson ratio ,

η_s is the hysteresis loss factor ,

$\Lambda_{mn} = \rho_s h_s l_x l_y / 4$ is a modal normalisation parameter ,

$\psi_{mn}^{(x)}(x,y) = \dfrac{\partial \phi_{mn}(x,y)}{\partial x}$, is the first derivative in *x* direction of the *m,n*-th bending natural mode at position (x,y) ,

$\psi_{mn}^{(y)}(x,y) = -\dfrac{\partial \phi_{mn}(x,y)}{\partial y}$, is the first derivative in *y* direction of the *m,n*-th bending natural mode at position (x,y) ,

For a clamped rectangular thin panel the natural frequencies are given by [102]:

$$\omega_{fmn} = \sqrt{\frac{E_s h_s^2}{12\rho_s(1-\nu_s^2)}} \cdot \left(\frac{\pi}{l_x}\right)^2 q_{mn} \quad , \tag{2.11}$$

where ω_{fmn} is in rad/s and

$$q_{mn} = \sqrt{G_x^4(m) + G_y^4(n)\left(\frac{l_x}{l_y}\right)^4 + 2\left(\frac{l_x}{l_y}\right)^2 \left[\nu H_x(m) H_y(n) + (1-\nu) J_x(m) J_y(n)\right]} \quad , \tag{2.12}$$

and the constants G_x, G_y, H_x, H_y, J_x, J_y are summarised in Table 2.3 below.

The plate natural modes $\phi_{mn}(x,y)$ are given by the product of the $\varphi_m(x)$ and $\varphi_n(y)$ beam functions

$$\phi_{mn}(x,y) = \varphi_m(x)\varphi_n(y). \tag{2.13}$$

Table 2.3: *Values for the constants G_x, G_y, H_x, H_y, J_x, J_y when a rectangular plate has all four edges are clamped.*

m or n	G_x or G_y	H_x or H_y	J_x or J_y
1	1.506	1.248	1.248
2,3,4,....	$m+\frac{1}{2}$	$\left(m+\frac{1}{2}\right)^2\left(1-\frac{4}{(2m+1)\pi}\right)$	$\left(m+\frac{1}{2}\right)^2\left(1-\frac{4}{(2m+1)\pi}\right)$

The function $\varphi_m(x)$ represents the natural modes of a beam having the same boundary conditions of the plate under consideration at $y=0$ and $y=l_y$ and, in the same way, the function $\varphi_n(y)$ represents the natural modes of a beam having the same boundary conditions of the plate under consideration at $x=0$ and $x=l_x$.

The boundary conditions for a plate with all edges clamped are given by [103]:

$$\begin{array}{lll} x=0 \text{ and } x=l_x & w=0 & \dfrac{\partial w}{\partial x}=0 \\ y=0 \text{ and } y=l_y & w=0 & \dfrac{\partial w}{\partial y}=0 \end{array}, \tag{2.14}$$

and the beam functions in the x-direction for a clamped-clamped beam, also given in references [102,103], are:

$$\begin{aligned} \varphi_{1,3,5,\ldots}(x) &= \cos\gamma_m\left(\frac{x}{l_x}-\frac{1}{2}\right)+k_m\cosh\gamma_m\left(\frac{x}{l_x}-\frac{1}{2}\right) \\ \varphi_{2,4,8,\ldots}(x) &= \sin\gamma'_m\left(\frac{x}{l_x}-\frac{1}{2}\right)+k'_m\sinh\gamma'_m\left(\frac{x}{l_x}-\frac{1}{2}\right) \end{aligned}, \tag{2.15a,b}$$

where in this case

$$k_m=\frac{\sin(\gamma_m/2)}{\sinh(\gamma_m/2)} \qquad k'_m=-\frac{\sin(\gamma'_m/2)}{\sinh(\gamma'_m/2)}, \tag{2.16a,b}$$

and the constants γ_m and γ'_m are the m-th zeros of the two following implicit equations

$$\tan(\gamma_m/2)+\tanh(\gamma_m/2)=0 \qquad \tan(\gamma'_m/2)-\tanh(\gamma'_m/2)=0, \tag{2.17a,b}$$

whose roots are summarised in Table 2.4. The beam functions in the y-direction are the same as those in the x-direction given by equations (2.15a) and (2.15b) and are all normalised so that the norm Λ_{mn} for a plate with all edges clamped is given by $\Lambda_{mn} = \rho_s h_s l_x l_y / 4$.

Table 2.4: Roots for the 2 equations (2.17a) and (2.17b). r=6,7,8,9,....

$\gamma_1 = 4{,}7300$	$\gamma'_2 = 7{,}8532$
$\gamma_3 = 10{,}9956$	$\gamma'_4 = 14{,}1372$
$\gamma_5 = 17{,}2788$	$\gamma'_6 = 20{,}4204$
$\gamma_7 = 23{,}5620$	$\gamma'_8 = 26{,}7036$
$\gamma_9 = 29{,}8452$	$\gamma'_{10} = 32{,}9868$
$\gamma_{11,13,\ldots} = (4r-1)\pi/2$	$\gamma'_{12,14,\ldots} = (4r+1)\pi/2$

Using beam functions, the first derivative modes function are given by the following relations:

$$\psi^{(x)}_{mn}(x,y) = \varphi_m(x)\frac{\partial \varphi_n(y)}{\partial y} \qquad \psi^{(y)}_{mn}(x,y) = -\varphi_m(y)\frac{\partial \varphi_n(x)}{\partial x} \quad , \tag{2.18a,b}$$

so that

$$\begin{aligned} \frac{\partial \varphi_{1,3,5,\ldots}(x)}{\partial x} &= \frac{\gamma_m}{l_x}\left\{-\sin\gamma_m\left(\frac{x}{l_x}-\frac{1}{2}\right)+k_m\sinh\gamma_m\left(\frac{x}{l_x}-\frac{1}{2}\right)\right\} \\ \frac{\partial \varphi_{2,4,6,\ldots}(x)}{\partial x} &= \frac{\gamma'_m}{l_x}\left\{\cos\gamma'_m\left(\frac{x}{l_x}-\frac{1}{2}\right)+k'_m\cosh\gamma'_m\left(\frac{x}{l_x}-\frac{1}{2}\right)\right\} \end{aligned} \quad . \tag{2.19a,b}$$

2.2 Multi-channel Feedback controller

If there is no control action, i.e. $\mathbf{f}_s(\omega) \equiv \mathbf{0}$, then the transverse velocities at the centre positions of the panels can be calculated directly from equation (2.5) to be:

$$\mathbf{v}_e(\omega) = \mathbf{Y}_{ep}(\omega)\mathbf{f}_p(\omega) \quad . \tag{2.20}$$

If, as shown in Figure 2.4, for each sensor–actuator pair a decentralized feedback control loop is implemented with constant feedback gain, h, such that:

$$\mathbf{f}_s(\omega) = -\mathbf{H}(\omega)\mathbf{v}_c(\omega) \ , \tag{2.21}$$

then

$$\mathbf{H}(\omega) = \begin{bmatrix} h_1 & & & \\ & h_2 & & \\ & & \ddots & \\ & & & h_{16} \end{bmatrix} , \tag{2.22}$$

Assuming for the time being that the closed loop system is stable, then the velocities at the centre positions of the control system can be deduced by the block diagram in Figure 2.4 and are given by:

$$\mathbf{v}_c(\omega) = \left(\mathbf{I} + \mathbf{Y}_{cs}(\omega)\mathbf{H}(\omega)\right)^{-1}\mathbf{Y}_{cp}(\omega)\mathbf{f}_p(\omega) \ . \tag{2.23}$$

Also, from equations (2.5), (2.21) and (2.23), the transverse velocities at the centre positions of the panels can be calculated as a function of the primary excitation vector and the gains in the matrix $\mathbf{H}(\omega)$:

$$\mathbf{v}_e(\omega) = \left[\mathbf{Y}_{ep}(\omega) - \mathbf{Y}_{es}(\omega)\mathbf{H}(\omega)\left(\mathbf{I} + \mathbf{Y}_{cs}(\omega)\mathbf{H}(\omega)\right)^{-1}\mathbf{Y}_{cp}(\omega)\right]\mathbf{f}_p(\omega) \ . \tag{2.24}$$

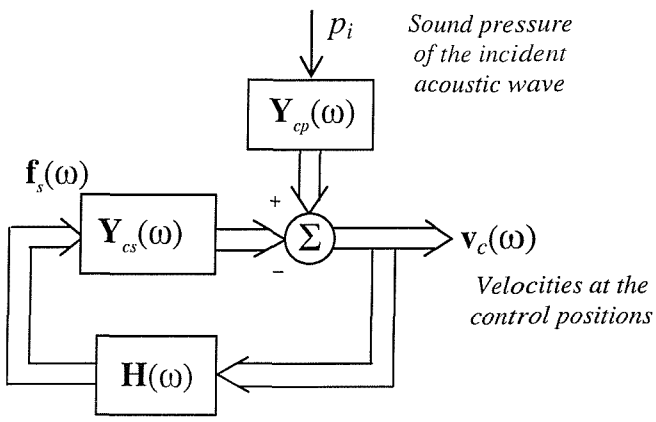

Figure 2.4: *Multichannel feedback control system, which for a passive plant response, $\mathbf{Y}_{cs}(\omega)$, and a passive controller $\mathbf{H}(\omega)$, is unconditionally stable.*

It should be underlined that these results are valid provided the sixteen decentralized feedback control units are all stable. Elliott et all. [3] have shown that this is true when collocated and compatible transducers are used. Elliott et all. [3] have also shown that for a collocated piezoceramic actuator patch and accelerometer sensor, where the actuator is modelled as a set of four line-moment excitation and the sensor is modelled such that it precisely measures the transverse velocity in correspondence to the centre of the actuator patch, the system is also stable. In the second part of this dissertation the true behaviour of these two transducers is analysed in more details both experimentally and numerically. It is here anticipated that when the true transducers are analysed, then each control unit is not guaranteed to be stable above few kilo Hertz. A limited feedback gain is therefore required in equations (2.21) and (2.22) otherwise they can not assumed to be valid since the control units are unstable.

The total kinetic energy of the panel or the total sound power radiated per unit primary excitation can be derived from the velocities of the radiating elements given in equation (2.24). The total kinetic energy of the panel is given by

$$E(\omega) = \frac{\rho_s h_s}{2} \int_{S_s} |\dot{w}(x, y, \omega)|^2 \, dx \, dy \quad , \tag{2.25}$$

where S_S is the surface area of the panel. This expression can be approximated to the summation of the kinetic energies of each element into which the panel has been subdivided so that:

$$E(\omega) = \frac{m_s}{2} \mathbf{v}_e^H(\omega) \mathbf{v}_e(\omega) \quad , \tag{2.26}$$

where $m_s = \rho_s h_s$ is the mass per unit area of the panel. The total sound power radiation by a baffled panel can be derived by integrating the product of the nearfield sound pressure on the radiating side and the transverse velocity of the panel so that

$$W(\omega) = \frac{1}{2} \int_0^{l_x} \int_0^{l_y} p_o(x, y, \omega)^* \dot{w}(x, y, \omega) \; dx \; dy \quad . \tag{2.27}$$

The sound pressures in front of the panel $p_o(x, y, \omega)$ is related to the transverse velocity of the panel at the same position $\dot{w}(x, y, \omega)$ by the specific acoustic impedance in air Z_o so that:

$$p_o(x, y, \omega) = Z_o(x, y, \omega)\, \dot{w}(x, y, \omega). \tag{2.28}$$

Similarly to the case of kinetic energy, the integral in equation (2.27) can be approximated to the radiated sound power by all the elements into which the panel has been subdivided so that the total sound power radiation can be expressed as:

$$W(\omega) = \frac{\Delta S_s}{2} \mathrm{Re}\left[\mathbf{v}_e^H(\omega)\mathbf{p}(\omega)\right], \tag{2.29}$$

where ΔS_s is the area of each element and $\mathbf{p}(\omega)$ is the vector with the sound pressure terms in front of the panel at the centre positions of the grid of elements:

$$\mathbf{p}(\omega) = \begin{Bmatrix} p_1(\omega) \\ p_2(\omega) \\ \vdots \\ p_{16}(\omega) \end{Bmatrix}. \tag{2.30}$$

Equation (2.29) can also be written as

$$W(\omega) = \frac{\Delta S_s}{2} \mathrm{Re}\left[\mathbf{v}_e^H(\omega)\mathbf{Z}(\omega)\mathbf{v}(\omega)_e\right] = \mathbf{v}_e^H(\omega)\mathbf{R}(\omega)\mathbf{v}_e(\omega), \tag{2.31}$$

where $\mathbf{Z}$ is the matrix with the point and transfer acoustic impedance terms over the grid of point into which the panel has subdivided [32],

$$\mathbf{Z}(\omega) = \frac{\omega^2 \rho_o \Delta S_s}{2\pi c_o} \begin{bmatrix} 1 & \frac{\sin(k_o r_{12})}{k_o r_{12}} & \cdots & \frac{\sin(k_o r_{1I})}{k_o r_{1I}} \\ \frac{\sin(k_o r_{21})}{k_o r_{21}} & 1 & & \\ \cdots & \cdots & \cdots & \cdots \\ \frac{\sin(k_o r_{I1})}{k_o r_{I1}} & & & 1 \end{bmatrix}, \tag{2.32}$$

where $k_o = \omega/c_o$ is the acoustic wavenumber in air and r_{ij} is the distance between i-th and j-th elements. The radiation matrix $\mathbf{R}$ is therefore given by [32]:

$$\mathbf{R}(\omega) = \left(\frac{\Delta S_s}{2}\right) \mathrm{Re}[\mathbf{Z}(\omega)] = \frac{\omega^2 \rho_o \Delta S_s^2}{4\pi c_o} \begin{bmatrix} 1 & \frac{\sin(k_o r_{12})}{k_o r_{12}} & \cdots & \frac{\sin(k_o r_{1I})}{k_o r_{1I}} \\ \frac{\sin(k_o r_{21})}{k_o r_{21}} & 1 & & \\ \cdots & \cdots & \cdots & \cdots \\ \frac{\sin(k_o r_{I1})}{k_o r_{I1}} & & & 1 \end{bmatrix} \quad (2.33)$$

Although the sound power radiated by the panel usefully quantifies the far-field pressure it generates, high vibration levels in weakly radiated modes can give rise to significant pressure levels in the near-field of the panel. It has been shown that the total kinetic energy of a panel provides a better measure of near-field pressure than radiated sound power [35], and so if there is any possibility that listeners may be in close proximity to the panel, as well as being further away, then both of these criteria are important for active structural acoustic control.

For practical computations only a finite number of modes can be used in the expansion for the mobility functions given by equations (2.7) to (2.10). The convergence of the modal series can be investigated by calculating the ratio of the velocity computed at a point on the panel with a modal summation using N modes, to that computed with a large number of modes, such as 500, with natural frequencies up to 25 kHz. This result can be misleading for the active control simulations presented here, however, since very high levels of attenuation are predicted at some frequencies and so the residual components of the vibration may be more sensitive to modal truncation. The results presented here were obtained by taking in equation (2.7) to (2.10) the natural modes and natural frequencies up to 25 kHz. This was chosen since none of the results presented here was significantly altered if the upper limit of the modal summation was higher. A large number of modes is required to accurately model the velocity with a collocated actuator because the velocity is influenced by the nearfield of the actuator, which is more intense for the piezoelectric actuator than it is for the point force. It should be noted that only the line moment excitation of the piezoelectric actuator [20] has been taken into account in the model, not the local stiffening effect.

2.3 Sensor-actuator Effects

The matrix model introduced above neglects two features of the system:

(a) the dynamic effects of the piezoelectric actuators and accelerometer sensors, and

(b) the frequency response function of the accelerometer sensor.

The small dimensions of one sensor–actuator pair compared to that of the panel justify this choice. However, because the panel is equipped with sixteen of these control systems, their dynamic effects are certainly important even at low frequencies. Also, the accelerometer sensor operates as a single degree resonant system with natural frequency at relatively high frequency, in general about 30–50 kHz, and thus the high frequency response of the panel with the sixteen accelerometer sensors could be quite different to that of the panel on itself. Since the piezoelectric patches are uniformly distributed over the panel surface and, up to 15 kHz, their surface dimensions are not negligible if compared to the wave length of the bending vibration in the panel (see Section 4.4), then their stiffness and part of the mass effects could be modelled as a smeared effect over the entire surface of the panel so that low order mode shapes remains unaltered and the variation of the natural frequencies can be easily derived assuming a higher bending stiffness and density of the panel. The local dynamics of sensor–accelerometer plus part of the mass effect of the piezo actuator have instead been modelled with a lumped parameter system that accounts for the inertial mass, stiffness and damping of the accelerometer and the mass of accelerometer case plus part of the mass of the piezoelectric actuator arranged as shown in Figure 2.5.

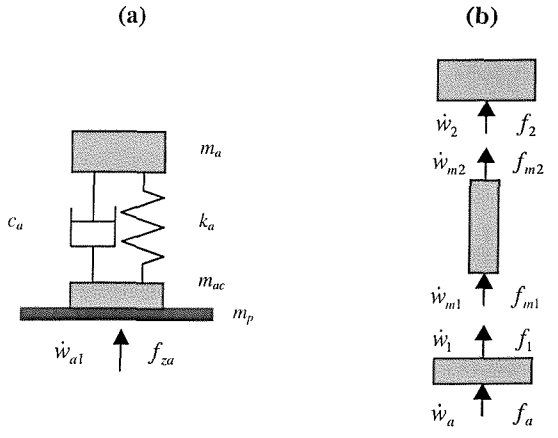

Figure 2.5: *Mobility diagram of one sensor–actuator system, which has been modelled with three lumped elements: the accelerometer inertial mass, equivalent stiffness and damping of the sensing piezo element and the mass of the accelerometer case. The dynamic effects of the piezoelectric actuator have been smeared over the panel surface by modifying the Young's modulus and density parameters of the panel.*

The driving point impedance of each accelerometer sensor $Z(\omega) = f_{cz}(\omega)/\dot{w}_c(\omega)$ can easily derived by considering the diagram in Figure 2.5 above [104]. For the top and bottom masses the following two relations can be written:

$$\dot{w}_2(\omega) = Y_2(\omega) f_2(\omega) \ , \tag{2.34}$$

$$\dot{w}_1(\omega) = Y_1(\omega) f_1(\omega) + Y_1(\omega) f_a(\omega) \ , \tag{2.35}$$

where $Y_2(\omega)$ and $Y_1(\omega)$ are the mobility terms for the two masses:

$$Y_2(\omega) = \frac{1}{j\omega m_a} \ , \qquad Y_1(\omega) = \frac{1}{j\omega m_{ac}} \ . \tag{2.36,2.37}$$

Also, for the four poles mounting system described by a spring element and damping element in parallel, the following two equations can be written:

$$\begin{aligned} f_{m1}(\omega) &= Z_{m11}(\omega)\dot{w}_{m1}(\omega) + Z_{m12}(\omega)\dot{w}_{m2}(\omega) \\ f_{m2}(\omega) &= Z_{m21}(\omega)\dot{w}_{m2}(\omega) + Z_{m22}(\omega)\dot{w}_{m2}(\omega) \end{aligned} \ , \tag{2.38a,b}$$

where the four impedance terms are given by

$$\begin{aligned} Z_{m11}(\omega) &= \left(c_a + \frac{k_a}{j\omega} \right) \quad Z_{m12}(\omega) = -\left(c_a + \frac{k_a}{j\omega} \right) \\ Z_{m21}(\omega) &= -\left(c_a + \frac{k_a}{j\omega} \right) \quad Z_{m22}(\omega) = \left(c_a + \frac{k_a}{j\omega} \right) \end{aligned} \ . \tag{2.39a-c}$$

Using (a) the dynamic equilibrium and (b) compatibility conditions at the top and bottom junctions, so that

(a) dynamic equilibrium $\quad f_1 = -f_{m1}$ and $f_2 = -f_{m2}$, (2.40a,b)

(b) compatibility $\quad \dot{w}_1 = \dot{w}_{m1}$ and $\dot{w}_2 = \dot{w}_{m2}$, (2.41a,b)

the following equation is obtained

$$\dot{w}_1(\omega) = \frac{Y_1(\omega)}{1-T(\omega)} f_a(\omega) \quad , \tag{2.42}$$

where

$$T(\omega) = -Y_1(\omega)Z_{m11}(\omega) + \frac{Y_1(\omega)Z_{m12}(\omega)Y_2(\omega)Z_{m21}(\omega)}{1+Y_2(\omega)Z_{m22}(\omega)} \quad . \tag{2.43}$$

Thus, since $\dot{w}_a(\omega) = \dot{w}_1(\omega)$, the equivalent impedance of the mechanical system shown in Figure 2.5 can be calculated to be:

$$Z_{eq}(\omega) = \frac{f_a(\omega)}{\dot{w}_a(\omega)} = \frac{1-T(\omega)}{Y_1(\omega)} \quad . \tag{2.44}$$

As well known, the output signal of accelerometers is proportional to the differential acceleration of the accelerometer–mass and accelerometer–case:

$$\text{measured acceleration} \propto \ddot{w}_2 - \ddot{w}_a \quad . \tag{2.45}$$

Thus, for a given velocity at the mounting point of the accelerometer $\dot{w}_c = \dot{w}_a$, the measured value is given by:

$$\dot{w}_{mes}(\omega) = A(\omega)\dot{w}_c(\omega) \quad , \tag{2.46}$$

where $A(\omega)$ is the accelerometer frequency response function [105]:

$$A(\omega) = \frac{m_a}{k_a - m_a\omega^2 + jc_a\omega} = \frac{1}{\omega_n^2 - \omega^2 + j\xi_a 2\omega\omega_n} \quad , \tag{2.47}$$

with $\omega_n = \sqrt{k_a/m_a}$ the accelerometer natural frequency and $\xi_a = c_a/2\sqrt{k_a m_a}$ the damping ratio of the accelerometer.

Table 2.5: Physical properties of the sensor-actuator transducers.

Parameter	Value
Mass of the piezo actuator	$m_p = 0.2\times10^{-3}$ Kg
Mass of the accelerometer case	$m_{ac} = 0.2\times10^{-3}$ Kg
Inertia mass of the accelerometer	$m_a = 0.22\times10^{-3}$ Kg
Stiffness of the accelerometer	$k_a = 1.1\times10^{7}$ N/m
Mounted frequency resonance of accelerometer	$f_a = \omega_n/2\pi = 33.6\times10^{3}$ Hz
Damping coefficient of the accelerometer	$c_a = 2.5$ N/ms^{-1}

In the next section, for the simulations in which the sensor-actuator local dynamic effects have been taken into account, the physical parameters given in Table 2.5 above have been used. As discussed above the mass effect of the piezo actuators have been taken into account partially as a localized effect and partially as a smeared effect over the panel surface. As a result, the lumped mass of each piezo actuator has been taken to be $m_p = 0.2\times10^{-3}$ Kg, although the true mass is 1×10^{-3} Kg. In order to account for the smeared inertia effect of the sixteen piezo actuators, the density of the material of the panel has been taken to be: $\overline{\rho}_s = 3000\,\mathrm{Kg/m^3}$. The stiffening effect of the piezo actuators has also been smeared over the panel and thus the Young's modulus of elasticity used in the simulations has been assumed to be $\overline{E}_s = 7.1\times10^{10}$ N/m^2.

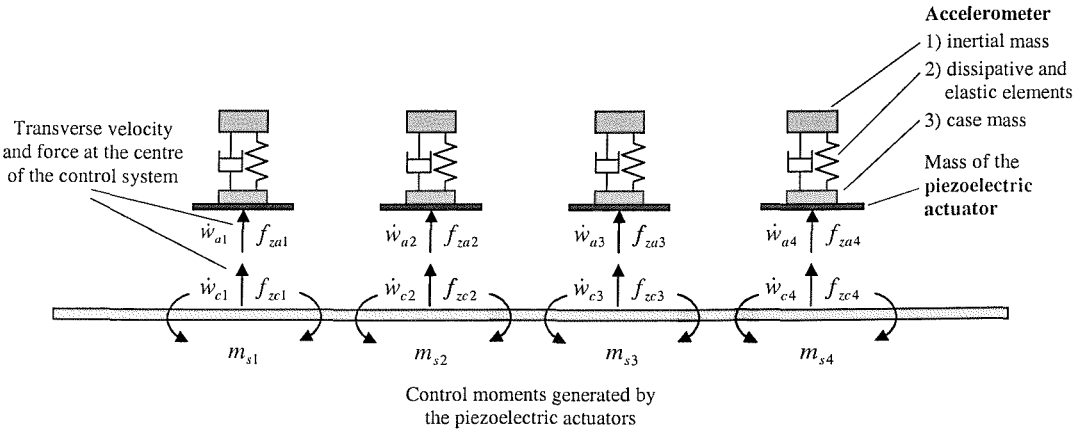

Figure 2.6: *Schematic representation of the sensor–actuator elements, which are represented by four lumped elements: the mass of the piezoelectric actuator, the mass of the case of the accelerometer and the spring and inertial mass in the accelerometer.*

When the dynamic effects of the sixteen sensor–actuator systems are taken into account then, according to the notation shown in Figure 2.6 above, equations (2.5) and (2.6) should be reformulated as follows:

$$\mathbf{v}_e(\omega) = \mathbf{Y}_{ec}(\omega)\mathbf{f}_c(\omega) + \mathbf{Y}_{ep}(\omega)\mathbf{f}_p(\omega) + \mathbf{Y}_{es}(\omega)\mathbf{f}_s(\omega) \ , \tag{2.48}$$

$$\mathbf{v}_c(\omega) = \mathbf{Y}_{cc}(\omega)\mathbf{f}_c(\omega) + \mathbf{Y}_{cp}(\omega)\mathbf{f}_p(\omega) + \mathbf{Y}_{cs}(\omega)\mathbf{f}_s(\omega) \ , \tag{2.49}$$

where the elements of the $\mathbf{Y}_{ec}(\omega)$ and $\mathbf{Y}_{cc}(\omega)$ matrices are given by:

$$Y_{ec}^{p,q}(\omega) = \frac{\dot{w}_{e,p}(\omega)}{f_{zc,q}(\omega)} = j\omega \sum_{m=1}^{M}\sum_{n=1}^{N} \frac{\phi(x_{ep}, y_{ep})\phi(x_{eq}, y_{eq})}{\Lambda_{mn}\left[\omega_{mn}^2(1+j\eta_s) - \omega^2\right]} \ , \tag{2.50}$$

$$Y_{cc}^{p,q}(\omega) = \frac{\dot{w}_{c,p}(\omega)}{f_{zc,q}(\omega)} = j\omega \sum_{m=1}^{M}\sum_{n=1}^{N} \frac{\phi(x_{cp}, y_{cp})\phi(x_{cq}, y_{cq})}{\Lambda_{mn}\left[\omega_{mn}^2(1+j\eta_s) - \omega^2\right]} \ . \tag{2.51}$$

According to equation (2.44), the phasors of the transverse velocities , $\dot{w}_{aj}(\omega)$, and forces, $f_{zaj}(\omega)$, at the centres of each control systems can be related by the following impedance expression:

$$f_{zaj}(\omega) = Z_{eq}(\omega)\dot{w}_{aj}(\omega) \ . \tag{2.52}$$

Thus, defining the vectors $\mathbf{v}_a(\omega)$ and $\mathbf{f}_a(\omega)$ to be given by the velocities and forces at the bottom of the accelerometer sensors respectively:

$$\mathbf{v}_a(\omega) \equiv \begin{Bmatrix} \dot{w}_{a1}(\omega) \\ \dot{w}_{a2}(\omega) \\ \vdots \\ \dot{w}_{a16}(\omega) \end{Bmatrix} \qquad \mathbf{f}_a(\omega) \equiv \begin{Bmatrix} f_{za1}(\omega) \\ f_{za2}(\omega) \\ \vdots \\ f_{za16}(\omega) \end{Bmatrix} \ , \tag{2.53a,b}$$

then

$$\mathbf{f}_a(\omega) = \mathbf{Z}_{aa}(\omega)\mathbf{v}_a(\omega) \ , \tag{2.54}$$

where the impedance matrix $\mathbf{Z}_{aa}(\omega)$ is diagonal

$$\mathbf{Z}_{aa}(\omega) = \begin{bmatrix} Z_{eq1} & & & \\ & Z_{eq2} & & \\ & & \ddots & \\ & & & Z_{eq16} \end{bmatrix}, \tag{2.55}$$

since the sixteen sensor – actuator systems are coupled only via the plate structure as shown in Figure 2.6.

If there is no control action, i.e. $\mathbf{f}_s(\omega) = \mathbf{0}$, then the transverse velocities at the centre positions of the panels can be calculated using (a) the dynamic equilibrium and (b) compatibility conditions at the junctions between the control units and the plate:

(a) dynamic equilibrium $\mathbf{f}_c = -\mathbf{f}_a$, (2.56)

(b) compatibility $\mathbf{v}_c = \mathbf{v}_a$. (2.57)

Therefore the velocities of the panel at the centre of the sensor-actuator units is found to be:

$$\mathbf{v}_c(\omega) = [\mathbf{I} + \mathbf{Y}_{cc}(\omega)\mathbf{Z}_{aa}(\omega)]^{-1}\mathbf{Y}_{cp}(\omega)\mathbf{f}_p(\omega) , \tag{2.58}$$

and the transverse velocities at the centre positions of the panels are given by

$$\mathbf{v}_e(\omega) = \mathbf{Y}_{ep}(\omega)\mathbf{f}_p(\omega) - \mathbf{Y}_{ec}(\omega)\mathbf{Z}_{aa}(\omega)[\mathbf{I} + \mathbf{Y}_{cc}(\omega)\mathbf{Z}_{aa}(\omega)]^{-1}\mathbf{Y}_{cp}(\omega)\mathbf{f}_p(\omega) . \tag{2.59}$$

As discussed in the previous case, when the system is stable, if for each sensor–actuator pair a decentralized feedback control loop using the measured velocity $\dot{w}_{mes}(\omega) = T(\omega)\dot{w}_c(\omega)$ given by equation (2.46) is implemented with constant feedback gain, h, such that:

$$\mathbf{f}_s(\omega) = -\mathbf{H}(\omega)\mathbf{v}_m(\omega) , \tag{2.60}$$

and

$$\mathbf{v}_m(\omega) = \mathbf{A}(\omega)\mathbf{v}_c(\omega) , \tag{2.61}$$

where $\mathbf{H}(\omega)$ is given by equation (2.22) and

$$\mathbf{A}(\omega) = \begin{bmatrix} A_1 & & & \\ & A_2 & & \\ & & \ddots & \\ & & & A_{16} \end{bmatrix}, \tag{2.62}$$

with

$$\mathbf{v}_m(\omega) \equiv \begin{Bmatrix} \dot{w}_{m1}(\omega) \\ \dot{w}_{m2}(\omega) \\ \vdots \\ \dot{w}_{m16}(\omega) \end{Bmatrix}, \tag{2.63}$$

then, the velocities of the panel at the accelerometer positions is found to be:

$$\mathbf{v}_c(\omega) = \left[\mathbf{I} + \mathbf{Y}_{cs}(\omega)\mathbf{H}(\omega)\mathbf{A}(\omega) + \mathbf{Y}_{cc}(\omega)\mathbf{Z}_{aa}(\omega)\right]^{-1}\mathbf{Y}_{cp}(\omega)\mathbf{f}_p(\omega) , \tag{2.64}$$

and the transverse velocities at the centre positions of the panels are given by

$$\mathbf{v}_e(\omega) = \mathbf{Y}_{ep}(\omega)\mathbf{f}_p(\omega) - \left[\mathbf{Y}_{es}(\omega)\mathbf{H}(\omega)\mathbf{A}(\omega) + \mathbf{Y}_{ec}(\omega)\mathbf{Z}_{aa}(\omega)\right]\mathbf{G}^{-1}(\omega)\mathbf{Y}_{cp}(\omega)\mathbf{f}_p(\omega) , \tag{2.65}$$

where:

$$\mathbf{G}(\omega) = \mathbf{I} + \mathbf{Y}_{cs}(\omega)\mathbf{H}(\omega)\mathbf{A}(\omega) + \mathbf{Y}_{cc}(\omega)\mathbf{Z}_{aa}(\omega) . \tag{2.66}$$

In the following two sections the kinetic energy of the panel and the total sound radiated per unit incident acoustic plane wave are plotted in a frequency range 0 to 1 kHz.

2.4 Simulation results with piezoelectric actuators

In this section, the response of the panel and its sound radiation is discussed with reference to a range of feedback gains in the decentralised control loops. First, the analysis is carried out without considering the stiffness and mass effects of the piezoceramic patches and the dynamic and mass effects of the velocity transducers. Therefore the kinetic energy and sound

power radiation, given by equations (2.26) and (2.31) have been calculated using equations (2.20) and (2.24) for the velocities of the radiating elements in the two cases of no control or active control.

Figure 2.7 shows the total kinetic energy of the panel excited by the plane wave before control and when subject to control with sixteen individual single channel control system with various feedback gains, h. The modal response of the panel is clearly seen in the plot of the kinetic energy against frequency before control, with the resonances associated with the first four natural modes, (1,1), (1,2), (2,1) and (1,3) occurring respectively at about 70, 118, 163 and 197 Hz. As the gains of the feedback loops are increased, the resonances in the response become more heavily damped, as one would expect with velocity feedback control.

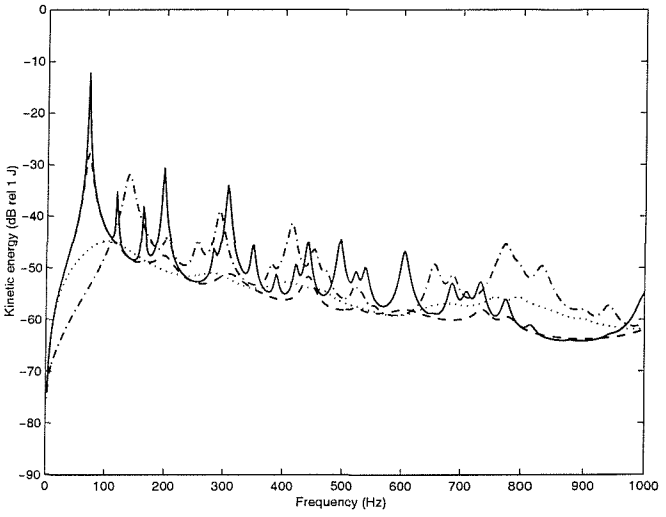

Figure 2.7: *Kinetic energy of the plane wave-excited panel when the dynamics of the sensor-actuator transducers are not taken into account with no control, solid line, and with the 16 decentralised feedback control systems having a feedback gain of 10, dashed, 100, dotted, and 1000, dot-dashed lines.*

If the gains of the feedback loops are increased beyond a certain value, however, the closed loop response displays new peaks, such as that at about 140 Hz for example, which become more pronounced as the feedback gain is increased. As discussed by Elliott et al [3] these extra peaks are due to the resonances of the controlled dynamic system, which is effectively pinned at the sensor positions with high feedback gain. If feedback controllers having very high gain were used, the velocities at each sensor could be driven to zero and the physical result would be equivalent to that of perfect control of the sensor outputs with a feedforward

control system, which could have been implemented if a suitable reference signal were available.

Figure 2.8 shows the ratio of the sound power radiated on one side of the panel to the incident sound power due to the plane wave excitation on the other side, which is termed the sound transmission ratio, T. Before control only the modes whose modal integers are odd radiate sound significantly at low frequencies and also anti-resonances appear, due to destructive interference between the sound pressures radiated by adjacent odd modes. As the feedback gains are increased, similar trends are observed in the reduction of the sound transmission ratio as in the reduction of the kinetic energy of the panel, except that the new resonance at about 140 Hz has the greatest prominence, since its velocity distribution has the greatest net volume velocity.

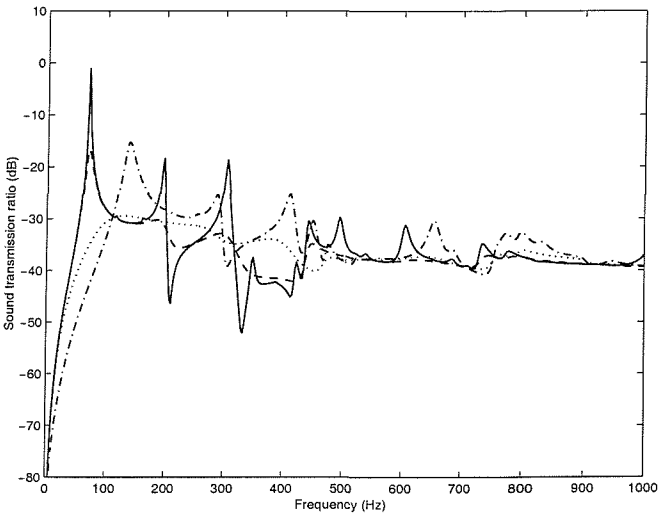

Figure 2.8: *Sound transmission ratio of the plane wave-excited panel when the dynamics of the sensor-actuator transducers are not taken into account with no control, solid line, and with the 16 decentralised feedback control systems having a feedback gain of 10, dashed, 100, dotted, and 1000, dot-dashed lines.*

When the panel's kinetic energy is integrated across the bandwidth shown in Figure 2.7 (up to 1 kHz) and this is plotted against feedback gain, a clear minimum of 15.8 dB is observed, for a gain of about 100, as shown in Figure 2.9 (solid line). These velocities give rise to a poor estimate of the panel's global response when the feedback gains are high enough for the new resonances to become significant. Figure 2.10 shows the variation with feedback gain for the sound transmission ratio integrated across this bandwidth, which corresponds to the total

radiated sound power if the plate is subject to broadband excitation by a plane wave up to a frequency of 1 kHz, and this also has a minimum value of 10 dB for a feedback gain of about 100. At high feedback gains the overall sound power radiated after control is some 3.4 dB higher than it was with no control, because of the effect of the new resonance at about 140 Hz.

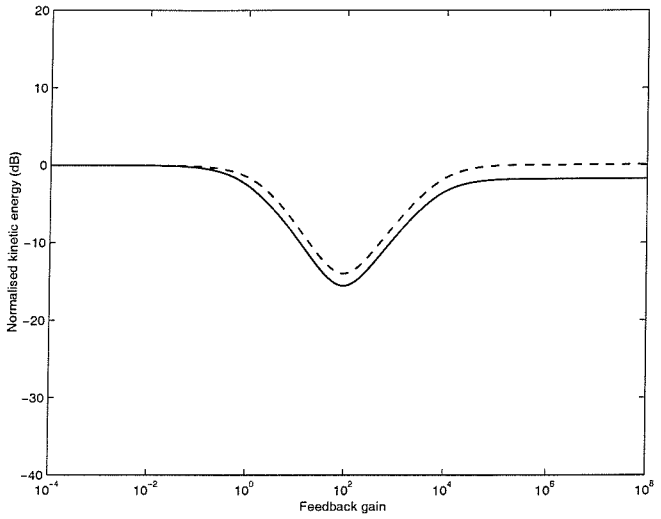

Figure 2.9: *Normalised kinetic energy level of the panel, integrated from 0 Hz to 1 kHz, plotted against the gain in the decentralised feedback controller, h, when the dynamics of the sensor-actuator transducers are not taken into account, solid line, or are taken into account, dashed line.*

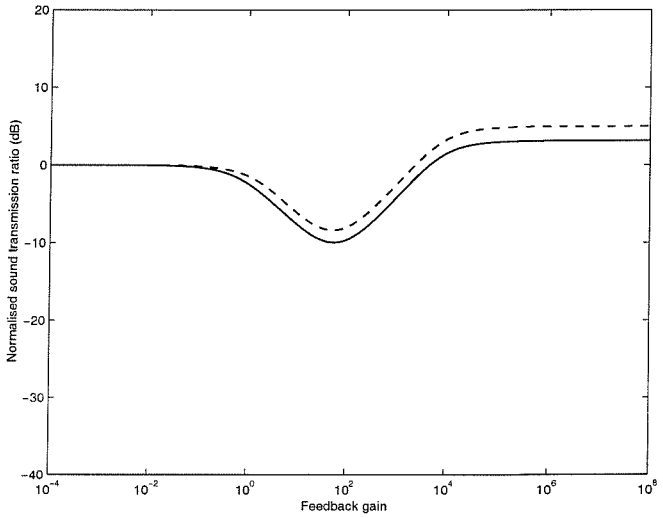

Figure 2.10: *Normalised sound transmission ratio level, integrated from 0 Hz to 1 kHz, plotted against the gain in the decentralised feedback controller, h, when the dynamics of the sensor-actuator transducers are not taken into account, solid line, or are taken into account, dashed line.*

In the second case studied, the stiffness and mass effects of the piezoceramic patches and the dynamic and mass effects of the velocity transducers have both been taken into account. Thus the kinetic energy and sound power radiation, given by equations (2.26) and (2.31) have been calculated using equations (2.59) and (2.65) for the velocities of the radiating elements in the two cases of no control or active control.

Figure 2.11 shows the total kinetic energy of the panel excited by the plane wave before control and when subject to control with sixteen individual single channel control system with various feedback gains, h. The modal response of the panel is slightly different to that shown in Figure 2.7 for the previous case. Indeed the resonances associated with the first four modes, (1,1), (1,2), (2,1) and (1,3) occur at slightly lower frequencies: 67, 115, 160 and 193 Hz instead of 70, 118, 163 and 197 Hz. This is due to the added mass effects of the sensors and actuators transducers. The resonance due to the accelerometer occurs at too high frequency to be evident in this figure. As the gains of the feedback loops are increased, the resonances in the response also become more heavily damped as one would expect and when the gains of the feedback loops are increased beyond a certain value, the closed loop response displays new peaks due to the additional constraints at the sensors positions.

Figure 2.12 shows for this second case the sound transmission ratio, T before control and when subject to control with sixteen individual single channel control system with various feedback gains, h. As the feedback gains are increased, similar trends are observed in the reduction of the sound transmission ratio and of the kinetic energy of the panel.

The frequency averaged kinetic energy and sound transmission ratio across the 0 to 1 kHz bandwidth are given by the dashed lines in Figures 2.9 and 2.10. Both curves have a similar trend to those found for the previous case. In this case, the sixteen decentralised control units seems to be slightly less effective since the maximum reduction of the kinetic energy and sound transmission ratio of the smart panel are of about 14 dB and 9 dB respectively instead of 16 dB and 10 dB when no actuator and sensor dynamics were taken into account. This is due to the fact that the control effectiveness in terms of reduction of the kinetic energy or sound transmission of the panel is limited to the same lower limit as in the previous case. However the added mass of the sensors and actuators transducers have reduced the kinetic energy and sound transmission of the panel before control by 2–3 dB. As a result the reductions of these two parameters generated by the control system are less pronounced than in the previous case. Apart from this minor effect on the dynamics of the smart panel without control, the mechanical influence of the actuator and sensor does not appear to have a significant effect on the attenuations achievable in principle.

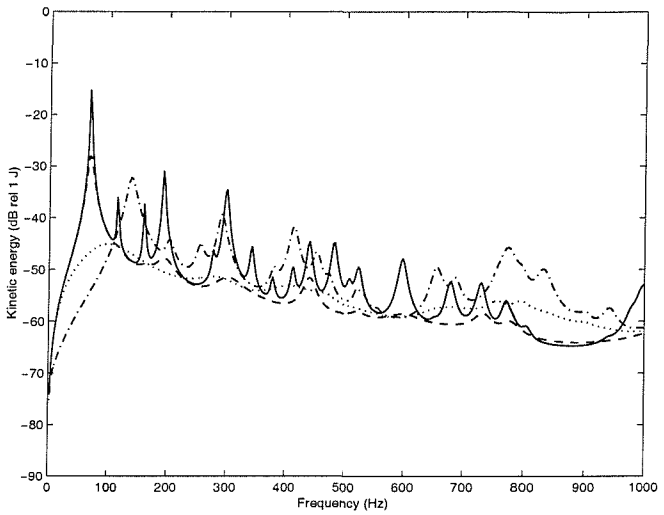

Figure 2.11: *Kinetic energy of the plane wave-excited panel when the dynamics of the sensor-actuator transducers are taken into account with no control, solid line, and with the 16 decentralised feedback control systems having a feedback gain of 10, dashed, 100, dotted, and 1000, dot-dashed lines.*

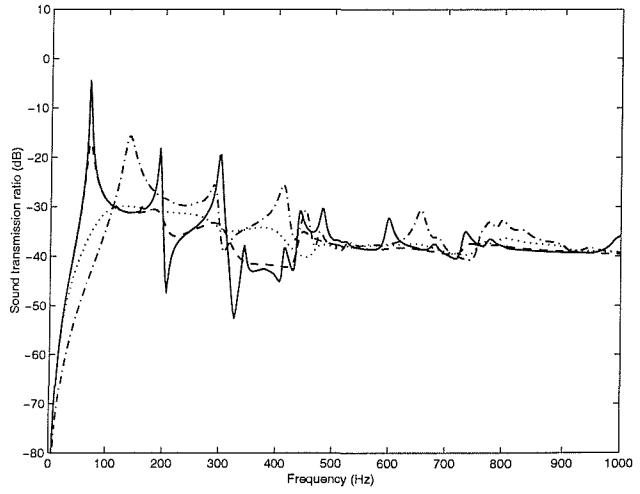

Figure 2.12: *Sound transmission ratio of the plane wave-excited panel when the dynamics of the sensor-actuator transducers are taken into account with no control, solid line, and with the 16 decentralised feedback control systems having a feedback gain of 10, dashed, 100, dotted, and 1000, dot-dashed lines.*

3. ANALYSIS OF THE SMART PANEL MOUNTED ON A CAVITY

In the previous chapter, the idea of using decentralized vibration control units to reduce the vibration and sound radiation/transmission of panels has been presented and the response of the panel and its sound radiation has been discussed with reference to a range of feedback gains in the decentralised velocity feedback control loops. When the system is excited by a harmonic plane acoustic wave, it has been found that the kinetic energy or sound radiation integrated between 0 and 1 kHz are reduced respectively by 14 dB and 9 dB in correspondence of the optimal gain of 100. Starting from this promising study, a further investigation of a prototype smart panel has been carried out considering the testing configuration where the smart panel is mounted on the top of a rectangular cavity with rigid walls. This particular configuration has been chosen to simplify the experimental work of measuring the sound transmission/radiation for either a primary acoustic source (a loudspeaker) within the cavity or a primary structural source (a shaker) acting on the panel (see Figure 3.1).

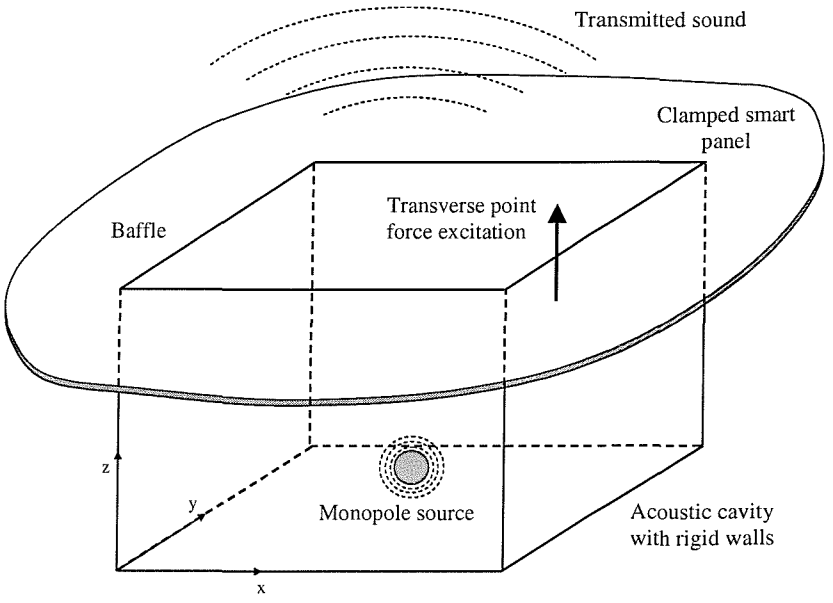

Figure 3.1: *Physical arrangement for the computer simulations, in which the vibration of a baffled clamped panel is excited either by the sound field in the cavity or by a transverse point force and radiates sound into an anechoic half space on the other side of the panel.*

In this chapter the smart panel and testing cavity are designed. The dimensions of the panel have been chosen in such a way as they are similar to those of a section of aircraft fuselage skin confined between two frames and two stringers. Also the dimensions of the piezoceramic patch actuators have been chosen in such a way as to provide enough control authority and cover only small parts of the panel itself. The acceleration sensors have been chosen in such a way to guarantee the necessary sensitivity provided the weight is reasonably low. Finally the rectangular section has been designed with reference to practical issues as for example space and weight.

The control effectiveness of the designed smart panel when is mounted on the cavity has then been assessed and the main differences with the control performances found in the previous chapter for the panel excited by a plane wave have been highlighted.

In the first two sections the design of the smart panel and the test rig are described, while in the following one, the fully coupled model developed to describe the effects of the acoustic cavity on the dynamics of the panel is illustrated. Following, the response of the panel and its sound radiation is discussed with reference to a range of feedback gains in the decentralised control loops, taking into account the acoustic coupling with the cavity and considering both the primary excitation types (acoustic source or structural source). Finally, the construction of the smart panel and test rig is described and the resulting experimental setup is illustrated.

3.1 Design of the smart panel

The testing smart panel built for this study consists of an aluminium panel of thickness $t = 1\,\text{mm}$, which has been clamped on a rigid frame so that the "vibrating area" is $l_x \times l_y = 414 \times 314\,\text{mm}$. The natural frequencies of the panel calculated without taking into account the stiffening and mass effects of the control transducers are given in Table 3.1.

As shown in Figure 3.2, the panel is equipped with an array of 4×4 control systems that operate independently. The sixteen control systems have been equally spaced along the x– and y– directions so that the distances between two actuators or between a lateral actuator and the edge of the plate are $d_x = l_x/5 = 82.8\,\text{mm}$ and $d_y = l_y/5 = 62.8\,\text{mm}$.

Table 3.1: *Calculated natural frequencies of the clamped panel up to 1 kHz (the stiffening and mass effects of the control transducers are not taken into account).*

m	n	Frequency (Hz)	m	n	Frequency (Hz)	m	n	Frequency (Hz)
1	1	69.7	5	1	441.3	2	5	776.2
2	1	118	1	4	495.6	7	1	795.8
1	2	163.4	5	2	522.4	6	3	814.7
3	1	197.3	4	3	522.9	5	4	837.7
2	2	208	2	4	538.8	3	5	846.1
3	2	283.0	6	1	604.8	7	2	875.1
4	1	305.3	3	4	609.3	4	5	944.3
1	3	305.7	5	3	654.3	6	4	995.7
2	3	349.1	6	2	684.8	7	3	1003.5
4	2	388.2	4	4	708.8	8	1	1014.0
3	3	421.1	1	5	732.9	1	6	1017.6

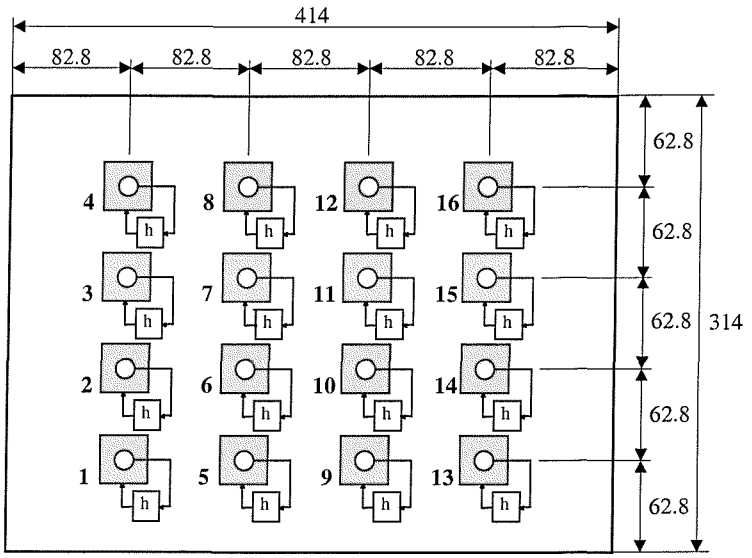

Figure 3.2: *Arrangement of sixteen piezoelectric actuators, as shown by the squares, driven locally by the output of sixteen velocity sensors, as shown by the circles, via individual control loops with a gain of h (dimensions are in mm).*

3.2 Design of the test rig facility

In order to assess the performance of the control system in terms of attenuation of the sound power radiation, the panel has been mounted on a Perspex box, which has inside a loudspeaker that generates the primary disturbance. The internal dimensions of the Perspex

box are: $p_x \times p_y \times p_z = 414 \times 314 \times 360\,\text{mm}$ and the natural frequencies of the acoustic modes up to 1.5 kHz were calculated using the formulas given in [106] and are reported in Table 3.2.

Table 3.2: *Calculated natural frequencies of the acoustic cavity up to 1.56 kHz*

i	j	k	Frequency (Hz)	i	j	k	Frequency (Hz)	i	j	k	Frequency (Hz)
1	0	0	414.25	1	0	2	1038.9	3	1	0	1357.5
0	0	1	476.39	0	2	0	1092.4	2	2	0	1371
0	1	0	546.18	0	1	2	1098.2	2	1	2	1375.7
1	0	1	631.31	2	1	1	1100.8	0	0	3	1429.2
1	1	0	685.5	1	2	0	1168.3	3	1	1	1438.6
0	1	1	724.75	1	1	2	1173.8	0	2	2	1449.5
2	0	0	828.5	0	2	1	1191.7	2	2	1	1451.4
1	1	1	834.78	3	0	0	1242.8	1	0	3	1488
0	0	2	952.78	1	2	1	1261.7	1	2	2	1507.5
2	0	1	955.7	2	0	2	1262.6	0	1	3	1530
2	1	0	992.33	3	0	1	1330.9	3	0	2	1566

As shown in Figure 3.3, a pair of rigid aluminium frames has been used to clamp the smart panel on the top open side of the box. Both frames have a width of $w=30$ mm, but they have different thickness: 25 mm for the bottom frame and 10 mm for the top one. The dimensions of the plate used to build the smart panel have been chosen to match the width and length of the clamping frame so that $l_{px} \times l_{py} \times t = 444 \times 344 \times 1\,\text{mm}$.

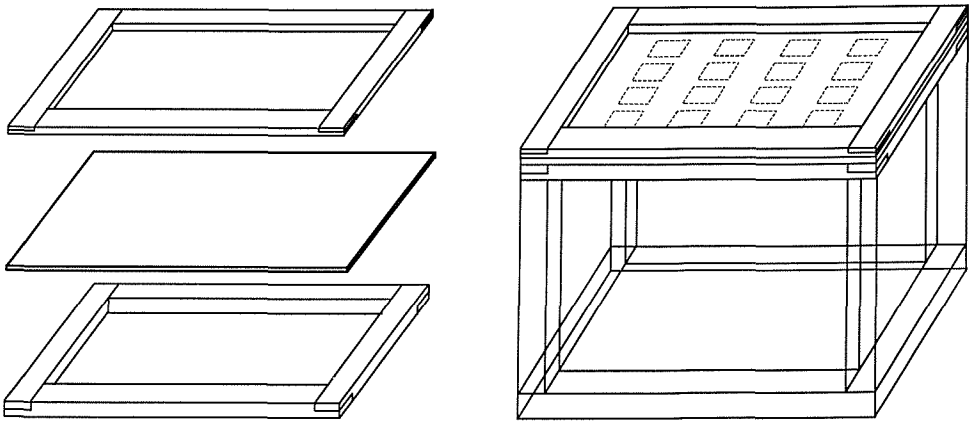

Figure 3.3: *Design of the rigid frames using for mounting the smart panel on the open side of the Perspex box.*

3.3 Mathematical model of the sound transmission

In this section the sound transmission through the smart panel under study is evaluated numerically. As previously mentioned, the system studied consists of a clamped and baffled aluminium panel of dimensions $l_x \times l_y = 414 \times 314$ mm and thickness 1 mm which is mounted on a rectangular cavity of dimensions $l_{xb} \times l_{yb} \times l_{zb} = 414 \times 314 \times 385$ mm. The panel is either excited by a transverse point force acting at position $(x_f , y_f) = (120 , 86)$ mm or by the acoustic field generated in the cavity by a monopole source which is positioned at position $(x_p , y_p , z_p) = (200 , 120 , 5)$ mm.

A fully coupled model is used to describe the effects of the acoustic cavity on the dynamics of the panel. In contrast, it is assumed that the acoustic pressure of the radiated sound has no effect on the vibration of the panel, which is a reasonable assumption in air for this thickness of panel.

The steady state response of the panel and sound radiation in a frequency range 0 to 2 kHz has been calculated assuming the primary disturbance acting on the panel or in the cavity to be harmonic with time dependence of the form $\exp(j\omega t)$. Similarly to what has been done in the theoretical formulation of Section 2.1, the velocity-type and force-type parameters used in the model have been taken to be the real part of counter clock wise rotating complex vectors, so that: $\dot{w}(t) = \mathrm{Re}\{\dot{w}(\omega)e^{j\omega t}\}$ or $f(t) = \mathrm{Re}\{f(\omega)e^{j\omega t}\}$ where $\dot{w}(\omega)$ and $f(\omega)$ are the velocity and force phasors at $t = 0$, ω is the circular frequency and $j = \sqrt{-1}$.

As shown in Figure 3.4, the mathematical model for the simulations considers the panel divided into a grid of rectangular elements whose dimensions have been taken to be $l_{xe} = l_x/(4M)$ and $l_{ye} = l_y/(4N)$, where M and N are the higher plate modal orders used in the modal summations. The top side of the cavity is also divided into a grid of rectangular elements of equal dimensions than those defined for the panel.

The phasors of the transverse velocities and forces, $\dot{w}_j(\omega)$ and $f_{zj}(\omega)$, at the centres of the panel and cavity elements have been grouped into the following vectors:

$$\mathbf{v}_e(\omega) \equiv \begin{Bmatrix} \dot{w}_{e1}(\omega) \\ \dot{w}_{e2}(\omega) \\ \vdots \\ \dot{w}_{eP}(\omega) \end{Bmatrix}, \mathbf{f}_e(\omega) \equiv \begin{Bmatrix} f_{ze1}(\omega) \\ f_{ze2}(\omega) \\ \vdots \\ f_{zeP}(\omega) \end{Bmatrix} \text{ and } \mathbf{v}_b(\omega) \equiv \begin{Bmatrix} \dot{w}_{b1}(\omega) \\ \dot{w}_{b2}(\omega) \\ \vdots \\ \dot{w}_{bP}(\omega) \end{Bmatrix}, \mathbf{f}_b(\omega) \equiv \begin{Bmatrix} f_{zb1}(\omega) \\ f_{zb2}(\omega) \\ \vdots \\ f_{zbP}(\omega) \end{Bmatrix}, \quad (3.1\text{-}3.4)$$

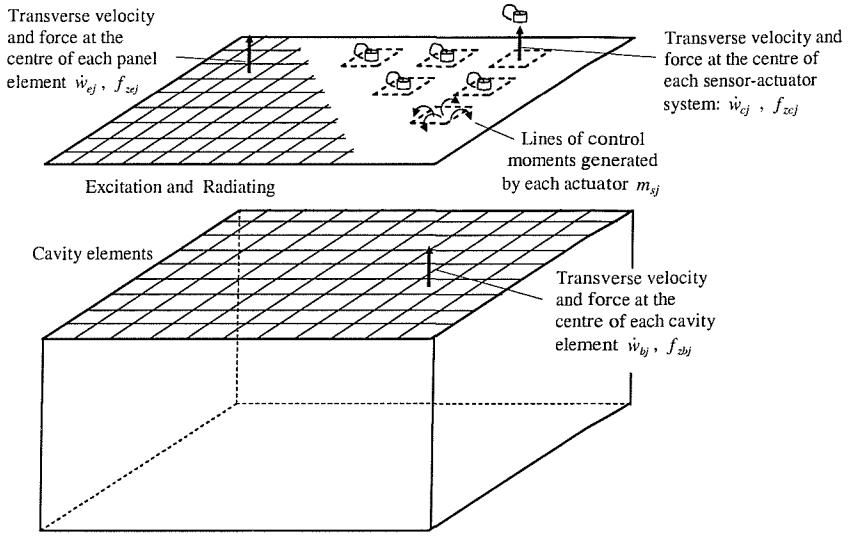

Figure 3.4: *Velocity and force-moment notation used in the mathematical model.*

where $P = 8MN$ is the total number of elements. Similarly the phasors of the transverse velocities, $\dot{w}_{ci}(\omega)$, and forces, $f_{zci}(\omega)$, at the centres of each control systems have been defined as follows:

$$\mathbf{v}_c(\omega) \equiv \begin{Bmatrix} \dot{w}_{c1}(\omega) \\ \dot{w}_{c2}(\omega) \\ \vdots \\ \dot{w}_{c16}(\omega) \end{Bmatrix} \qquad \mathbf{f}_c(\omega) \equiv \begin{Bmatrix} f_{zc1}(\omega) \\ f_{zc2}(\omega) \\ \vdots \\ f_{zc16}(\omega) \end{Bmatrix} . \tag{3.5,3.6}$$

The primary excitations are given either by the amplitude of the transverse force acting on the panel or by the strength of the monopole acoustic source placed in the cavity which have been groped in the two excitation vectors below:

$$\mathbf{f}_p(\omega) = f_p(\omega)e^{j\omega t} \qquad \mathbf{q}_p(\omega) = q_p(\omega)e^{j\omega t} . \tag{3.7,3.8}$$

The excitations of the sixteen piezoelectric control actuators can be approximated by four line moments, all with equal magnitude, acting along the edges of the piezoelectric patches so that the control excitations can be grouped into a vector of moments as follows:

$$\mathbf{f}_s(\omega) = \begin{Bmatrix} m_{s1}(\omega) \\ m_{s2}(\omega) \\ \vdots \\ m_{s16}(\omega) \end{Bmatrix} . \tag{3.9}$$

The vibration of the panel at the centres of the elements and at the centres of the control systems can be expressed in matrix form using mobility functions so that:

$$\mathbf{v}_e(\omega) = \mathbf{Y}_{ec}(\omega)\mathbf{f}_c(\omega) + \mathbf{Y}_{ee}(\omega)\mathbf{f}_e(\omega) + \mathbf{Y}_{ep}(\omega)\mathbf{f}_p(\omega) + \mathbf{Y}_{es}(\omega)\mathbf{f}_s(\omega) \ , \tag{3.10}$$

$$\mathbf{v}_c(\omega) = \mathbf{Y}_{cc}(\omega)\mathbf{f}_c(\omega) + \mathbf{Y}_{ce}(\omega)\mathbf{f}_e(\omega) + \mathbf{Y}_{cp}(\omega)\mathbf{f}_p(\omega) + \mathbf{Y}_{cs}(\omega)\mathbf{f}_s(\omega) \ , \tag{3.11}$$

where the components of the velocity/force mobility matrices, $\mathbf{Y}_{ec}(\omega), \mathbf{Y}_{ee}(\omega), \mathbf{Y}_{ep}(\omega)$ and $\mathbf{Y}_{cc}(\omega), \mathbf{Y}_{ce}(\omega), \mathbf{Y}_{cp}(\omega)$, between the elements i and k, are given by [102]:

$$Y^{i,k}(\omega) = \frac{\dot{w}_i(\omega)}{f_{z,k}(\omega)} = j\omega \sum_{m=1}^{M}\sum_{n=1}^{N} \frac{\phi(x_i, y_i)\,\phi(x_k, y_k)}{\Lambda_{mn}\left[\omega_{mn}^2(1+j\eta_s) - \omega^2\right]} \ , \tag{3.12}$$

and the components of the velocity/piezo-excitation matrices, $\mathbf{Y}_{es}(\omega)$ and $\mathbf{Y}_{cs}(\omega)$, between the element i and the piezo-actuator k, are given by:

$$Y^{i,k}(\omega) = \frac{\dot{w}_i(\omega)}{m_k(\omega)} = \\ = j\omega \sum_{m=1}^{M}\sum_{n=1}^{N} \frac{\phi(x_i, y_i)\left\{\int_0^{a_x} \psi^{(y)}(x_k, y_{k1}) - \psi^{(y)}(x_k, y_{k2})dx + \int_0^{a_y} -\psi^{(x)}(x_{k1}, y_k) + \psi^{(x)}(x_{k2}, y_k)dy\right\}}{\Lambda_{mn}\left[\omega_{mn}^2(1+j\eta_s) - \omega^2\right]} \ , \tag{3.13}$$

where:

m,n are the modal indices ,

ω_{mn} is the natural frequency of the m,n-th mode ,

$\phi_{mn}(x,y)$ is the m,n-th bending natural mode at position (x,y) ,

E_s is the Young's modulus of elasticity ,

ρ_s is the density of the material of the panel ,

ν_s is the Poisson ratio ,

η_s is the hysteresis loss factor ,

$\Lambda_{mn} = \rho_s h_s l_x l_y / 4$ is the modal normalisation parameter ,

$\psi_{mn}^{(x)}(x,y) = \partial\phi_{mn}(x,y)/\partial x$, is the first derivative in x direction of $\phi_{mn}(x,y)$,

$\psi_{mn}^{(y)}(x,y) = -\partial\phi_{mn}(x,y)/\partial y$, is the first derivative in y direction of $\phi_{mn}(x,y)$,

a_x , a_y are the dimensions of the PZT patch ,

x_{k1} , x_{k2} are the x-positions of the two a_y edges of the k-th PZT patch,

y_{k1} , y_{k2} are the y-positions of the two a_x edges of the k-th PZT patch.

The natural frequencies and natural modes of the clamped panel have been calculated, as in the previous section, using the formulation presented in references [102,103].

The transverse forces, f_{zbi}, acting at the centres of the elements of the top side of the rectangular box are given by:

$$\mathbf{f}_b(\omega) = \mathbf{Z}_{bb}(\omega)\mathbf{v}_b(\omega) + \mathbf{Z}_{bq}(\omega)\mathbf{q}_p(\omega) \ , \tag{3.14}$$

where, assuming the area of the elements to be small compared to the bending and acoustic wavelengths in the frequency range considered in the simulations presented in this section, the elements of the force/velocity impedance matrices between the elements i and k are given by:

$$Z_{bb}^{i,k}(\omega) = \frac{f_{z,i}(\omega)}{\dot{w}_k(\omega)} = \sum_{r=1}^{R}\sum_{s=1}^{S}\sum_{t=1}^{T} \frac{\omega\rho_o c_o^2 \Delta S_s^2 \, \chi(x_i,y_i)\,\chi(x_k,y_k)}{\Lambda_{rst}\left[2\zeta_{rst}\omega_{rst}\omega + j(\omega^2 - \omega_{rst}^2)\right]} \ , \tag{3.15}$$

and the elements of the force/primary excitation-strength impedance matrix between the element i and the monopole source are given by:

$$Z_{bp}^{i,p}(\omega) = \frac{f_{z,i}(\omega)}{q_p(\omega)} = \sum_{r=1}^{R}\sum_{s=1}^{S}\sum_{t=1}^{T} \frac{\omega\rho_o c_o^2 \Delta S_s \, \chi(x_i,y_i)\,\chi(x_p,y_p)}{\Lambda_{rst}\left[2\zeta_{rst}\omega_{rst}\omega + j(\omega^2 - \omega_{rst}^2)\right]} \ , \tag{3.16}$$

where:

r,s,t are the modal indices ,

ω_{rst} is the natural frequency of the r,s,t-th mode of the cavity ,

$\chi_{rst}(x,y,z)$ is the r,s,t-th natural mode of the cavity at position (x,y,z) ,

c_o is the speed of sound ,

ρ_o is the density of air ,

ζ_{rst} is the damping ratio or the r,s,t-th natural mode of the cavity ,

ΔS_s is the area of the elements ,

$\Lambda_{rst} = l_{xb}\, l_{yb}\, l_{zb}$ is the modal normalisation parameter .

The natural frequencies and natural modes of the rectangular cavity have been calculated using the formulation presented in reference [106].

The panel is equipped with sixteen control units, thus their dynamic effects should be taken into account even at low frequencies. According to what has been done in the theoretical formulation reported in Section 2.3, the stiffness and part of the mass of the piezoceramic actuators have been modelled as a smeared effect over the entire surface of the panel. Moreover, the local dynamics of a sensor–accelerometer plus part of the mass effect of the collocated piezo actuator have been considered with a lumped parameter model that accounts for the inertial mass, stiffness and damping of the accelerometer and the mass of accelerometer case plus part of the mass of the piezoelectric actuator arranged as shown in Figure 2.5 of Section 2.3.

The phasors of the transverse velocities, $\dot{w}_{aj}(\omega)$, and forces, $f_{zaj}(\omega)$, at the centres of each control systems can be related by the following impedance expression:

$$f_{zaj}(\omega) = Z_{eq}(\omega)\dot{w}_{aj}(\omega) \ , \tag{3.17}$$

where the driving point impedance of each accelerometer sensor $Z_{eq}(\omega)$ has been expressed by equation (2.44) of Section 2.3.

Defining the vectors of the velocities $\mathbf{v}_a(\omega)$ and of the forces $\mathbf{f}_a(\omega)$ at the bottom of the accelerometer sensors as in equations (2.53a) and (2.53b), then

$$\mathbf{f}_a(\omega) = \mathbf{Z}_{aa}(\omega)\mathbf{v}_a(\omega) \ , \tag{3.18}$$

where the impedance matrix $\mathbf{Z}_{aa}(\omega)$ is the diagonal matrix of the driving point impedances of each accelerometer sensor (see equation (2.55)).

The response of the panel taking into account the coupled response with the acoustic cavity and with the dynamics of the sixteen control units can now be derived using the dynamic equilibrium and compatibility principles at the connecting points between the centres of the elements of the panel and those of the acoustic cavity and at the connecting points between the sixteen control positions in the panel and the centres of sixteen control units so that:

	Elements centres	*Control points*	
(a) dynamic equilibrium	$\mathbf{f}_e = -\mathbf{f}_b$	$\mathbf{f}_c = -\mathbf{f}_a$	(3.19)
(b) compatibility	$\mathbf{v}_e = \mathbf{v}_b$	$\mathbf{v}_c = \mathbf{v}_a$	(3.20)

Using equations (3.10), (3.11), (3.14) and (3.18) the following two relations can be derived for the velocities of the panel at the element centres and at the control points:

$$\mathbf{v}_e(\omega) = -\mathbf{Q}_{ec}(\omega)\mathbf{v}_c(\omega) - \mathbf{Q}_{eq}(\omega)\mathbf{q}_p(\omega) + \mathbf{Q}_{ep}(\omega)\mathbf{f}_p(\omega) + \mathbf{Q}_{es}(\omega)\mathbf{f}_s(\omega), \tag{3.21}$$

$$\mathbf{v}_c(\omega) = -\mathbf{Q}_{ce}(\omega)\mathbf{v}_e(\omega) - \mathbf{Q}_{cq}(\omega)\mathbf{q}_p(\omega) + \mathbf{Q}_{cp}(\omega)\mathbf{f}_p + \mathbf{Q}_{cs}(\omega)\mathbf{f}_s(\omega), \tag{3.22}$$

where

$$\mathbf{Q}_{ec}(\omega) = \left(\mathbf{I} + \mathbf{Y}_{ee}\mathbf{Z}_{bb}\right)^{-1}\mathbf{Y}_{ec}\mathbf{Z}_{aa} \qquad \mathbf{Q}_{ce}(\omega) = \left(\mathbf{I} + \mathbf{Y}_{cc}\mathbf{Z}_{aa}\right)^{-1}\mathbf{Y}_{ce}\mathbf{Z}_{bb}$$

$$\mathbf{Q}_{eq}(\omega) = \left(\mathbf{I} + \mathbf{Y}_{ee}\mathbf{Z}_{bb}\right)^{-1}\mathbf{Y}_{ee}\mathbf{Z}_{bq} \qquad \mathbf{Q}_{cq}(\omega) = \left(\mathbf{I} + \mathbf{Y}_{cc}\mathbf{Z}_{aa}\right)^{-1}\mathbf{Y}_{ce}\mathbf{Z}_{bq}$$

$$\mathbf{Q}_{ep}(\omega) = \left(\mathbf{I} + \mathbf{Y}_{ee}\mathbf{Z}_{bb}\right)^{-1}\mathbf{Y}_{ep} \qquad \mathbf{Q}_{cp}(\omega) = \left(\mathbf{I} + \mathbf{Y}_{cc}\mathbf{Z}_{aa}\right)^{-1}\mathbf{Y}_{cp}$$

$$\mathbf{Q}_{es}(\omega) = \left(\mathbf{I} + \mathbf{Y}_{ee}\mathbf{Z}_{bb}\right)^{-1}\mathbf{Y}_{es} \qquad \mathbf{Q}_{cs}(\omega) = \left(\mathbf{I} + \mathbf{Y}_{cc}\mathbf{Z}_{aa}\right)^{-1}\mathbf{Y}_{cs}\,. \tag{3.23.a-h}$$

Equations (3.21) and (3.22) can further be manipulated to get:

$$\mathbf{v}_e(\omega) = \mathbf{T}_{eq}(\omega)\mathbf{q}_p(\omega) - \mathbf{T}_{ep}(\omega)\mathbf{f}_p(\omega) - \mathbf{T}_{es}(\omega)\mathbf{f}_s(\omega)\,, \tag{3.24}$$

$$\mathbf{v}_c(\omega) = \mathbf{T}_{cq}(\omega)\mathbf{q}_p(\omega) - \mathbf{T}_{cp}(\omega)\mathbf{f}_p(\omega) - \mathbf{T}_{cs}(\omega)\mathbf{f}_s(\omega)\,, \tag{3.25}$$

where

$$\mathbf{T}_{eq}(\omega) = \left(\mathbf{I} - \mathbf{Q}_{ec}\mathbf{Q}_{ce}\right)^{-1}\left(\mathbf{Q}_{ec}\mathbf{Q}_{cq} - \mathbf{Q}_{eq}\right) \qquad \mathbf{T}_{cq}(\omega) = \left(\mathbf{I} - \mathbf{Q}_{ce}\mathbf{Q}_{ec}\right)^{-1}\left(\mathbf{Q}_{ce}\mathbf{Q}_{eq} - \mathbf{Q}_{cq}\right)$$

$$\mathbf{T}_{ep}(\omega) = \left(\mathbf{I} - \mathbf{Q}_{ec}\mathbf{Q}_{ce}\right)^{-1}\left(\mathbf{Q}_{ec}\mathbf{Q}_{cp} - \mathbf{Q}_{ep}\right) \qquad \mathbf{T}_{cp}(\omega) = \left(\mathbf{I} - \mathbf{Q}_{ce}\mathbf{Q}_{ec}\right)^{-1}\left(\mathbf{Q}_{ce}\mathbf{Q}_{ep} - \mathbf{Q}_{cp}\right)$$

$$\mathbf{T}_{es}(\omega) = \left(\mathbf{I} - \mathbf{Q}_{ec}\mathbf{Q}_{ce}\right)^{-1}\left(\mathbf{Q}_{ec}\mathbf{Q}_{cs} - \mathbf{Q}_{es}\right) \qquad \mathbf{T}_{cs}(\omega) = \left(\mathbf{I} - \mathbf{Q}_{ce}\mathbf{Q}_{ec}\right)^{-1}\left(\mathbf{Q}_{ce}\mathbf{Q}_{es} - \mathbf{Q}_{cs}\right) \text{ .(3.26.a-f)}$$

As previously discussed in Section 2.3, the accelerometer sensor operates as a single degree resonant system with relatively high natural frequency, in general about 30–50 kHz, and thus the high frequency response of the panel with the sixteen accelerometer sensors could be quite different to that of the panel on itself. The output signal of accelerometers is proportional to the differential acceleration of the accelerometer–mass and accelerometer–case so that, for a given velocity at the mounting point of the accelerometer $\dot{w}_c = \dot{w}_a$, the measured value is given by equation (2.46).

The measured velocities by the sixteen accelerometers can be grouped in the following vector:

$$\mathbf{v}_m(\omega) \equiv \begin{Bmatrix} \dot{w}_{m1}(\omega) \\ \dot{w}_{m2}(\omega) \\ \vdots \\ \dot{w}_{m16}(\omega) \end{Bmatrix}, \tag{3.27}$$

which can be related to the panel velocities at the control points by the following matrix relation:

$$\mathbf{v}_m(\omega) = \mathbf{A}(\omega)\mathbf{v}_c(\omega) \ , \tag{3.28}$$

where $\mathbf{A}(\omega)$ is the diagonal matrix of the accelerometer frequency response functions (see equation (2.62)).

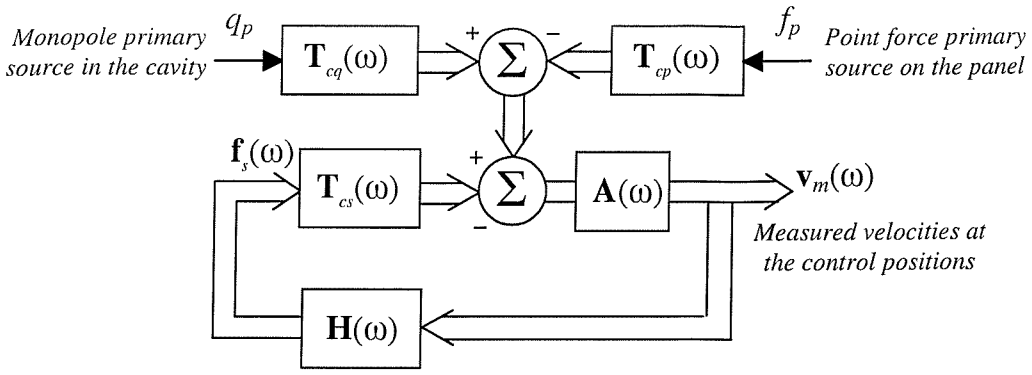

Figure 3.5: *Block diagram of the decentralised feedback control system implemented in the smart panel.*

When there is no control action, i.e. $\mathbf{f}_s(\omega) \equiv \mathbf{0}$, then the transverse velocities at the centre positions of the panels can be calculated directly from equation (3.24) to be:

$$\mathbf{v}_e(\omega) = \mathbf{T}_{eq}(\omega)\mathbf{q}_p(\omega) - \mathbf{T}_{ep}(\omega)\mathbf{f}_p(\omega) \ . \tag{3.29}$$

Provided the control system is stable, if, as shown in Figure 3.5, for each sensor–actuator pair a decentralized feedback control loop is implemented with constant feedback gain, h, such that:

$$\mathbf{f}_s(\omega) = -\mathbf{H}(\omega)\mathbf{v}_m(\omega) \ , \tag{3.30}$$

where

$$\mathbf{H}(\omega) = \begin{bmatrix} h_1 & & & \\ & h_2 & & \\ & & \ddots & \\ & & & h_{16} \end{bmatrix}, \tag{3.31}$$

then, as can be deduced by the block diagram in Figure 3.5, the velocities at the accelerometer positions is found to be:

$$\mathbf{v}_c(\omega) = \left[\mathbf{I} - \mathbf{T}_{cs}(\omega)\,\mathbf{H}\,\mathbf{A}(\omega)\right]^{-1}\left[\mathbf{T}_{cq}(\omega)\mathbf{q}_p(\omega) - \mathbf{T}_{cp}(\omega)\mathbf{f}_p(\omega)\right], \tag{3.32}$$

and the transverse velocities at the centre positions of the panels are given by

$$\mathbf{v}_e(\omega) = \mathbf{T}_{eq}(\omega)\mathbf{q}_p(\omega) - \mathbf{T}_{ep}(\omega)\mathbf{f}_p(\omega) + \\ + \mathbf{T}_{es}(\omega)\,\mathbf{H}\,\mathbf{A}(\omega)\left[\mathbf{I} - \mathbf{T}_{cs}(\omega)\,\mathbf{H}\,\mathbf{A}(\omega)\right]^{-1}\left[\mathbf{T}_{cq}(\omega)\mathbf{q}_p(\omega) - \mathbf{T}_{cp}(\omega)\mathbf{f}_p(\omega)\right]. \quad (3.33)$$

The total kinetic energy of the panel or the total sound power radiated per unit primary excitation can be derived from the velocities of the radiating elements given in equation (3.29) and (3.33), as explained in Section 2.2. Therefore the total kinetic energy of the panel (equation (2.25)) can be approximated to the summation of the kinetic energies of each element into which the panel has been subdivided, as expressed in equation (2.26).
The total sound power radiation by a baffled panel can be derived by integrating the product of the nearfield sound pressure on the radiating side, $p_o(x, y, \omega)$, and the transverse velocity of the panel, $\dot{w}(x, y, \omega)$ (see equations (2.27) and (2.29)). Similarly to the case of kinetic energy, the integral in equation (2.27) can be approximated to the radiated sound power by all the elements into which the panel has been subdivided so that the total sound power radiation can be expressed as in equations (2.29) and (2.31).

3.4 Simulation results with primary loudspeaker

In this section the response of the panel and its sound radiation is discussed with reference to a range of feedback gains in the sixteen decentralised control units. First, the analysis is carried out considering the system to be excited only by the monopole acoustic source placed within the cavity. The kinetic energy and sound power radiation, given by equations (2.26) and (2.31), have been calculated using equations (3.29) and (3.33) for the velocities of the radiating elements in the two cases of no control or active control.
Figure 3.6 shows the total kinetic energy of the panel excited by the monopole acoustic source in the cavity when the sixteen decentralised control units are implemented with various feedback gains, h. Since the primary excitation acts on the acoustic cavity, the low frequency response of the panel before control is characterised by a selected number of panel or cavity resonant modes. For example the first three resonances are close to the natural frequencies of the panel relative to the modes (1,1), (1,3), and (3,1) which occur at 70, 197 and 305 Hz and are well coupled to the low frequency volumetric response of the cavity. The

fourth resonance peak is due to the first two natural modes of the cavity, the (0,1,0) and the (0,0,1), which occurs respectively at 414 and 445 Hz. These two cavity modes are well coupled to the panel modes (3,3) and (1,5) whose natural frequencies are at 421 and 441 Hz. At higher frequencies the same type of behaviour is seen where well defined resonance peaks are found to correspond to either panel or cavity natural frequencies of strongly coupled panel-cavity modes.

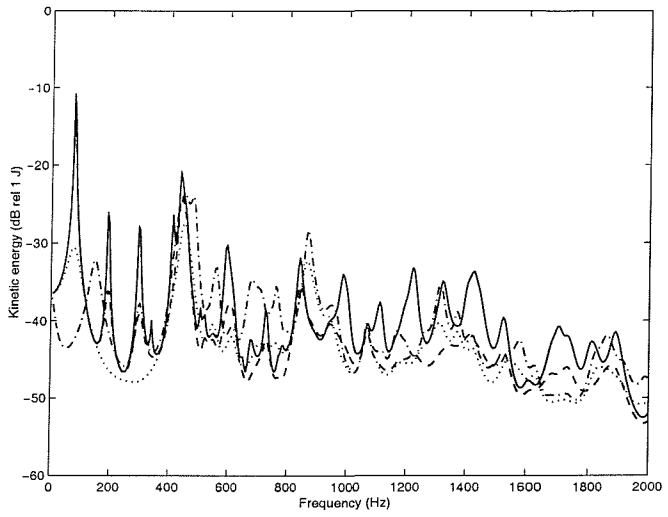

Figure 3.6: *Calculated kinetic energy of the panel when it is excited by an acoustic monopole source in the cavity. With no control, solid line, and with the 16 decentralised feedback control systems having a feedback gain of 10, dashed, 100, dotted, and 1000, dot-dashed lines*

When the feedback control system is turned on, it can be noticed that as the gains of the feedback loops are increased, the resonances which are controlled mainly by the panel natural modes become more heavily damped, as one would expect with velocity feedback control. In contrast, however, the resonances due to the cavity natural modes are not controlled. This behaviour could be explained by considering the particular case where only one control unit is acting on the panel. In this case, as shown in Figure 3.7, the error signal, i.e. the measured velocity at the control position $v_m(\omega)$, is generated both by the primary source via the transfer function $T_{cq}(\omega)$ and the secondary source via the transfer function $T_{cs}(\omega)$ pre multiplied by the control gain h. When the response of the panel is controlled by a resonance of the panel then, presumably, the two transfer functions $T_{cq}(\omega)$ and $T_{cs}(\omega)$ have similar amplitudes and relatively small control gains are required to bring down the error signal. In contrast when the response of the panel is controlled by a resonance of the cavity then the transfer function $T_{cq}(\omega)$ has much greater amplitude than $T_{cs}(\omega)$ and thus higher control gains would be

required to bring down the error signal. Also, it should be noted that the first resonance at 70 Hz, which is controlled by the (1,1) mode of the panel, requires much higher control gains to achieve the same control results obtained for higher order panel modes. This is probably due to the coupling of the (1,1) mode of the panel with the volumetric response of the cavity that produces a stiffening effect. If the gains of the feedback loops are increased beyond a certain value the closed loop response display new peaks, such as that at about 145 Hz for example, which become more pronounced as the feedback gain is increased. As discussed by Elliott et al [3] and seen in the previous section, these extra peaks are due to the resonances of the controlled panel, which is effectively pinned at the sensor positions with high feedback gains. If feedback controllers having very high gain were used, the velocities at each sensor could be driven to zero and thus the response of the panel would be characterised by a new set of natural modes defined by the clamping conditions at the four edges and by the pinning conditions at the sixteen control points. It is important to underline that these new modes are lightly damped since the sixteen control units are not introducing any active damping effect at high gains but are acting to pin the panel at the control positions.

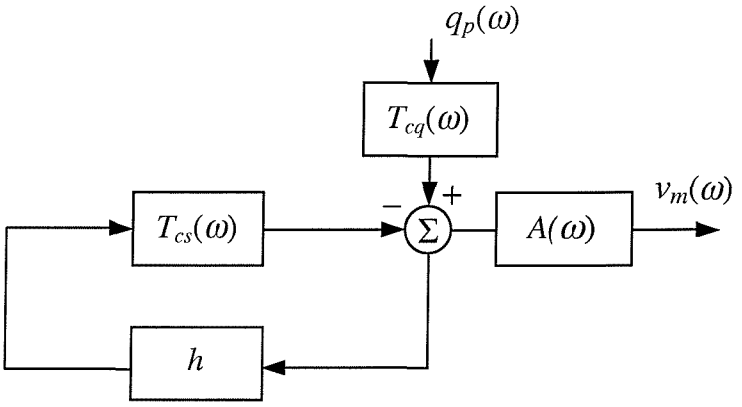

Figure 3.7: *Block diagram of one closed loop control system: direct velocity feedback.*

Figure 3.8 shows the ratio of the sound power radiated on one side of the panel to the strength of the primary monopole source in the cavity which is here called sound transmission. As discussed above, before control, the response of the panel is controlled by the coupling of the panel-cavity modes. However, at low frequencies, only the panel modes whose modal integers are odd radiate sound significantly [21]. Also anti-resonances appear, due to destructive interference between the sound pressures radiated by adjacent odd-odd modes [21]. As the feedback gains are increased, similar trends are observed in the reduction of the sound transmission coefficient as in the reduction of the kinetic energy of the panel,

except that the new resonance at about 145 Hz has the greatest prominence, since its velocity distribution has the largest net volume velocity and therefore sound radiation. Also, it can be noticed that for those peaks controlled by cavity modes, for example those with natural frequencies 414 and 445 Hz, there is almost no reduction of the sound radiation for any value of the control gain. Indeed between 400 and 1200 Hz there is no control, on the contrary the sound radiation is enhanced for relatively high gains. Between 1200 and 1500 Hz good control levels are achieved despite the relatively higher frequencies.

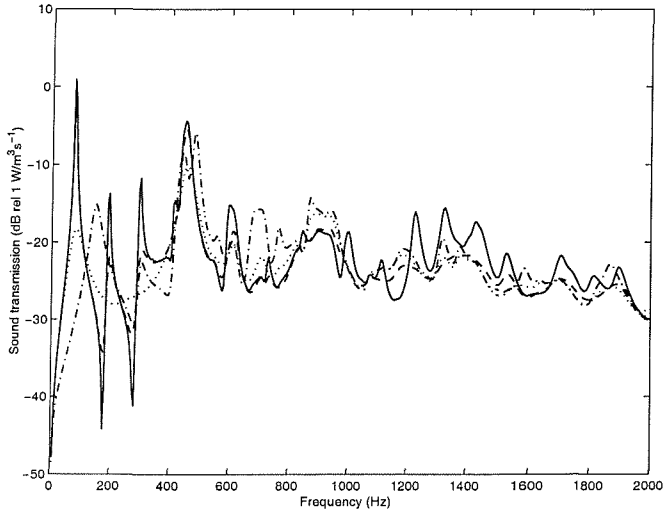

Figure 3.8: *Calculated sound transmission of the panel when it is excited by an acoustic monopole source in the cavity. With no control, solid line, and with the 16 channel decentralised feedback control systems having a feedback gain of 10, dashed, 100, dotted, and 1000, dot-dashed lines*

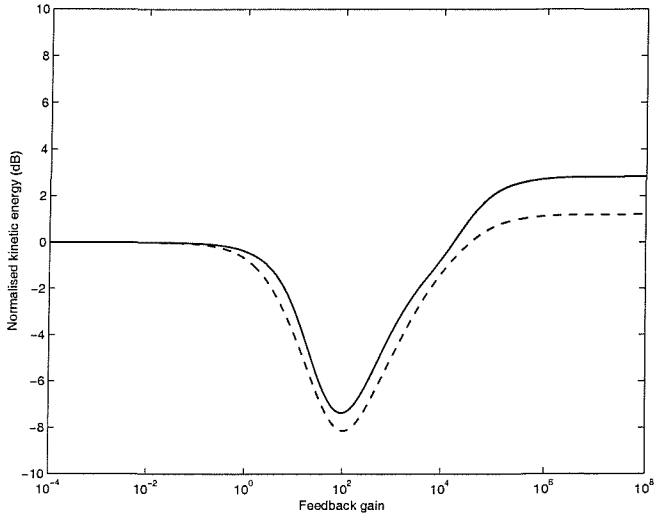

Figure 3.9: *Normalised kinetic energy level of the panel, integrated from 0 Hz to 2 kHz, plotted against the gain in the decentralised feedback controller, h, when the panel is excited by an acoustic monopole source in the cavity (solid line) or by a point force (dashed line)*

When the kinetic energy of the panel is integrated across the bandwidth shown in Figure 3.6 (up to 2 kHz) and this is plotted against feedback gain, a clear minimum of 7.4 dB is observed, for a gain of about 100, as shown in Figure 3.9 (solid line). For higher gains the total kinetic energy after control is actually enhanced by about 2.8 dB because of the lightly damped new modal response of the panel as described above.

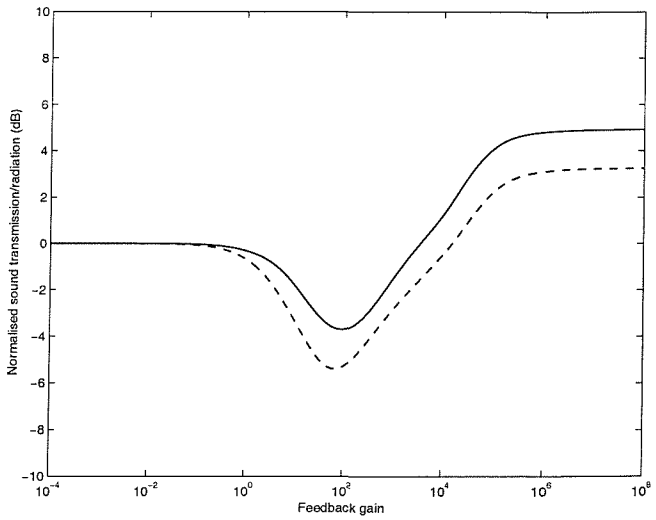

Figure 3.10: *Normalised sound transmission of the panel, integrated from 0 Hz to 2 kHz, plotted against the gain in the decentralised feedback controller, h, when the panel is excited by an acoustic monopole source in the cavity (solid line) or by a point force (dashed line)*

The solid line in Figure 3.10 shows the variation with feedback gain of the sound transmission ratio integrated across this bandwidth, which corresponds to the total radiated sound power if the plate is subject to broadband cavity excitation up to a frequency of 2 kHz, and this also has a minimum value of 3.7 dB for a feedback gain of about 100. At higher feedback gains the overall sound power radiated after control is some 4.8 dB higher than it was with no control, because of the lightly damped new modal response of the panel as described above.

3.5 Simulation results with primary force

The second analysis has been carried out considering the system to be excited only by the transverse point force acting on the panel. Figure 3.11 shows the total kinetic energy of the panel before control and when subject to control with sixteen decentralised control systems

with various feedback gains, *h*. The modal response of the panel is quite different to that shown in Figure 3.6 since the point force excites most, if not all, the modes of the panel. Also, because the cavity exerts only a passive effect on the panel, then the cavity controlled peaky resonances seen in the previous analysis are not so marked in this case. Indeed at low frequencies the first four resonances are close to the first four natural frequencies of the panel modes (1,1), (1,2), (2,1) and (1,3) which occur at frequencies: 70, 118, 163 and 197 Hz. Also, there are not the dominant resonance peaks at about 414 and 445 Hz due to the cavity natural modes as found when the primary excitation is given by the monopole source in the cavity.

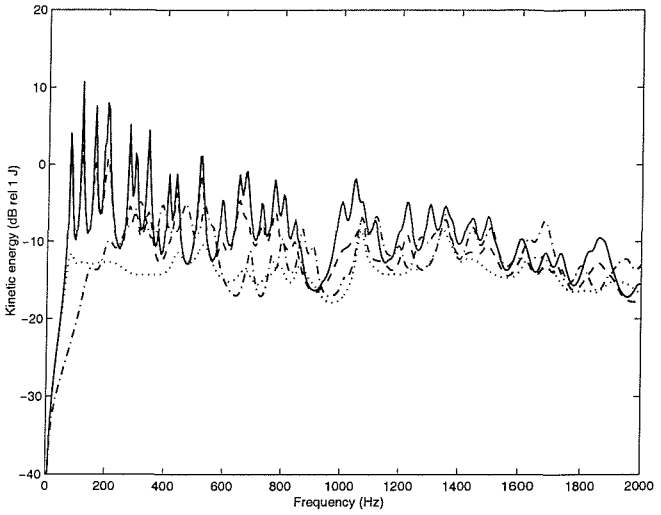

Figure 3.11: *Calculated kinetic energy of the panel when it is excited by a point force. With no control, solid line, and with the 16 channel decentralised feedback control systems having a feedback gain of 10, dashed, 100, dotted, and 1000, dot-dashed lines.*

In this case, when the control system is turned on, as the gains of the feedback loops are increased, most of the low frequency resonances are progressively damped so that for an optimal gain of 100 an overall reduction of the kinetic energy of the panel of about 8.1 dB is achieved as shown by the dashed line in Figure 3.9. For higher values of gains the response of the panel is characterised by a new set of resonance frequencies which, as seen above, are due to the new, lightly damped, modes of the panel generated by the control units which, for higher gains, are pinning the panel at the sixteen control positions. As a result, for higher gains the overall kinetic energy in the frequency range 0 to 2 kHz is increased by about 1.2 dB as shown by the dashed line in Figure 3.9. It is quite interesting to note that also in this case larger control gains are required to achieve the same level of control for the first few resonances of the panel as for the resonances at higher frequencies. As discussed above this is due to the coupling between the low frequency natural modes and the volumetric response of

the cavity which contrasts the damping mechanism of the sixteen control units.

Figure 3.12 shows the ratio of the sound power radiated on one side of the panel to the amplitude of the primary force acting on the panel. This spectrum is also characterised by a larger number of resonances when compared to that derived for the case in which the primary excitation is the monopole source in the cavity. Most of the resonances in the frequency range 0 to 2 kHz are damped when the optimal gain of about 100 is used so that an overall reduction of the sound radiation of about 5.5 dB is produced as shown by the dashed line in Figure 3.10.

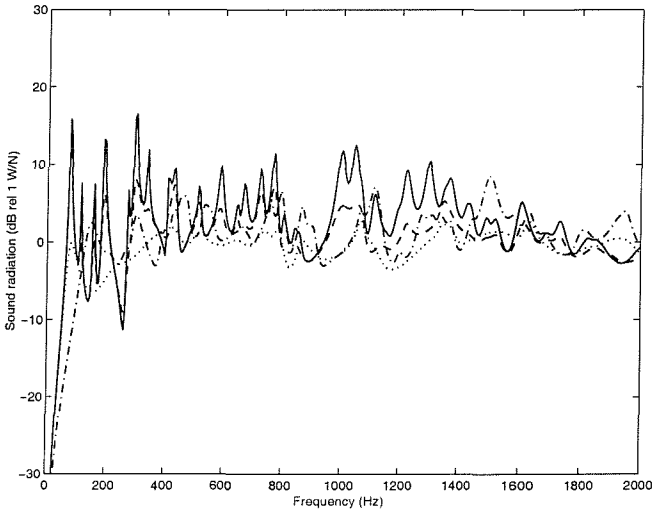

Figure 3.12: *Calculated sound transmission of the panel when it is excited by a point force. With no control, solid line, and with the 16 channel decentralised feedback control systems having a feedback gain of 10, dashed, 100, dotted, and 1000, dot-dashed lines.*

Considering the optimal gain, some of the low frequency modes of the panel are less damped because of the loading effect of the acoustic cavity. Also, as shown by the dashed line in Figure 3.10, when higher values of gain are implemented, because of the pinning effect of the sixteen control units, then the sound radiation is actually enhanced to about 3.2 dB.

3.6 Construction of the smart panel

The smart panel built for this study is illustrated in Figure 3.13a and b. An equally spaced 4×4 array of piezo patch actuators has been bonded on the bottom side of the panel. Each actuator has dimensions of 25 mm $\times$ 25 mm $\times$ 0.5 mm and it is made of lead zirconate

titanate (PZT) piezoelectric material, whose geometric and physics characteristics are reported in Table 2.2. On the upper side of the panel, an identical 4×4 array of accelerometers (PCB Piezotronics, model 352C67) has been placed in such a way to match the centre of each actuator, obtaining a set of sixteen closely located control units. The sensors employed in this application are high sensitivity, miniature (2 grams), ceramic shear ICP accelerometers, which are particularly suitable for shock and vibration studies. Some of the characteristics of these accelerometers are reported in Table 2.5.

As previously mentioned, a couple of aluminium frames has been designed to clamp the smart panel at the top of the rigid cavity, as illustrated in Figure 3.13b.

Therefore, the complete testing configuration consists of the smart panel mounted on a rectangular cavity with rigid walls, which sound properties are discussed in the next section. This configuration facilitates the measure of the sound transmission/radiation through the plate with reference to either a primary acoustic source in the cavity (loudspeaker) or a primary structural source acting on the panel (shaker).

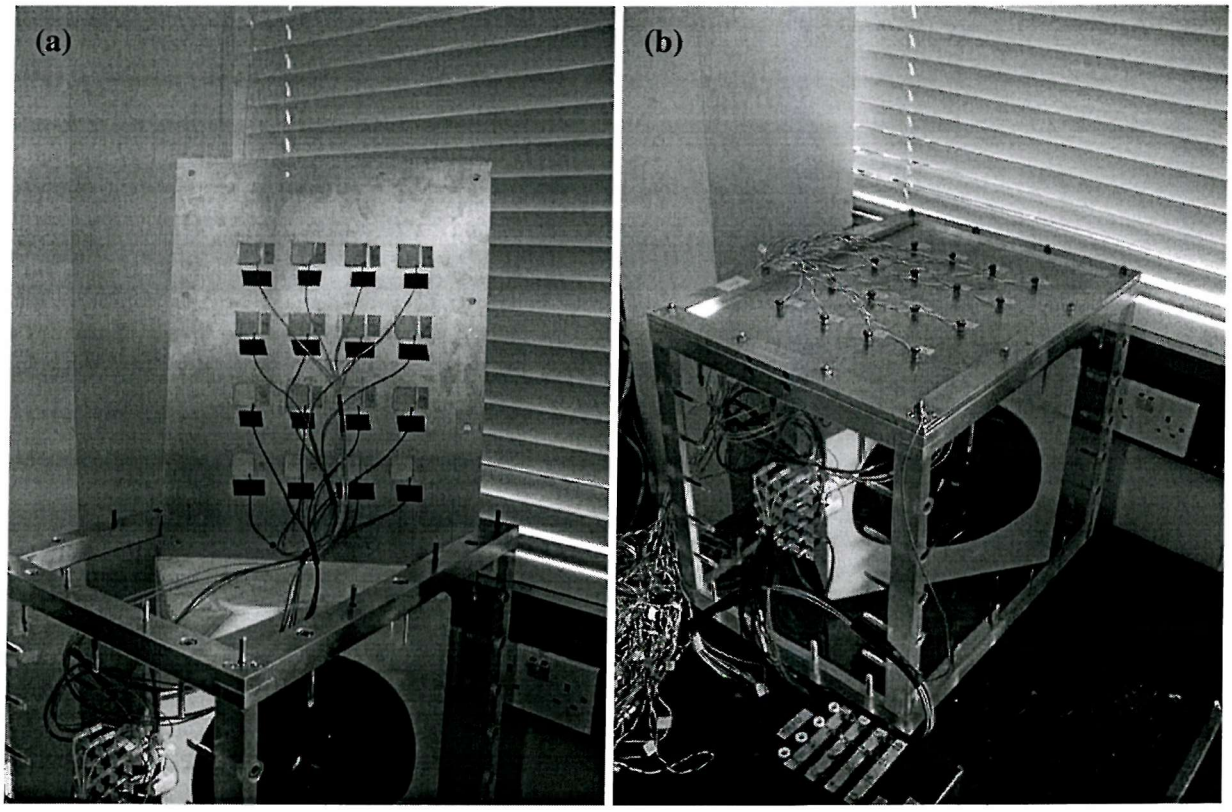

Figure 3.13: *Panel with 16 piezoceramic actuators (a) and 16 collocated accelerometers (b). Each sensor actuator pair is driven by a decentralized analogue feedback controller. The panel is mounted on a Perspex box with inside a loudspeaker, which generates the primary disturbance (b)*

3.7 Construction and testing of the experimental rig for sound radiation property

The cavity box is made with relatively thick plates of Perspex (30 mm) so that the acoustic field generated by the loudspeaker inside it is essentially transmitted through the smart panel. In order to assess the real sound radiation property of this test rig, an experimental validation has been performed in the anechoic chamber. The total transmitted sound power through the panel in presence of a primary acoustic source in the cavity has been calculated by a space integration of the sound intensity over a hypothetical surface that surrounds the structure. A rectangular array of microphone positions has been used to measure the space average of the mean-square sound pressure over the measurement surface, in a frequency range of 0-2 kHz. Subsequently, the smart panel has been removed from the testing facility; a thick wood panel has been sealed on the top side of the box and then covered by a heavy metal plate, as shown in Figure 3.14. In this way the sound transmission through the top of the box has been significantly reduced and it has been possible to measure the sound transmission via the lateral sides of the Perspex box in presence of the primary acoustic source in the cavity.
Moreover, the frequency response functions of the velocity at different points of the lateral Perspex sides of the box and at the central point of the metal plate for unit excitation of the loudspeaker have been monitored during the sound pressure measurement.

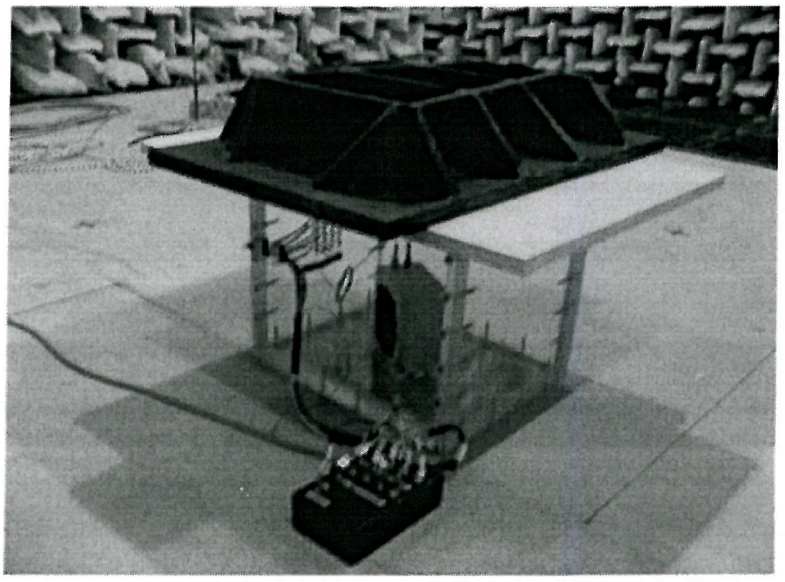

Figure 3.14: *The test rig during the sound radiation property investigation: a wood panel has been sealed on the top side of the box and then covered by a heavy metal plate. In this way the sound transmission through the top of the box has been significantly reduced, in such a way as to measure the sound transmission via the lateral sides of the Perspex box.*

The average frequency response functions of the nine microphone signals per unit excitation of the loudspeaker are reported in Figure 3.15 for both configurations (test rig with the smart panel, represented by the solid line and test rig covered by the heavy metal plate, represented by the dashed line), for two frequency ranges: 0-1 kHz and 0-2 kHz. It can be noted that at the low frequencies, up to 300 Hz, the sound transmission through the smart panel is about 20-30 dB higher than the flanking component radiated by the Perspex walls. Then, between 300 Hz and 1.5 kHz, some flanking components radiated by the walls affect the overall sound transmission of the system, particularly in correspondence of the cavity modes (390 Hz, 490 Hz, 700 Hz and 950 Hz). Finally, above 1.5 kHz, the sound transmission through the smart panel is about 10 dB higher than the flanking component.

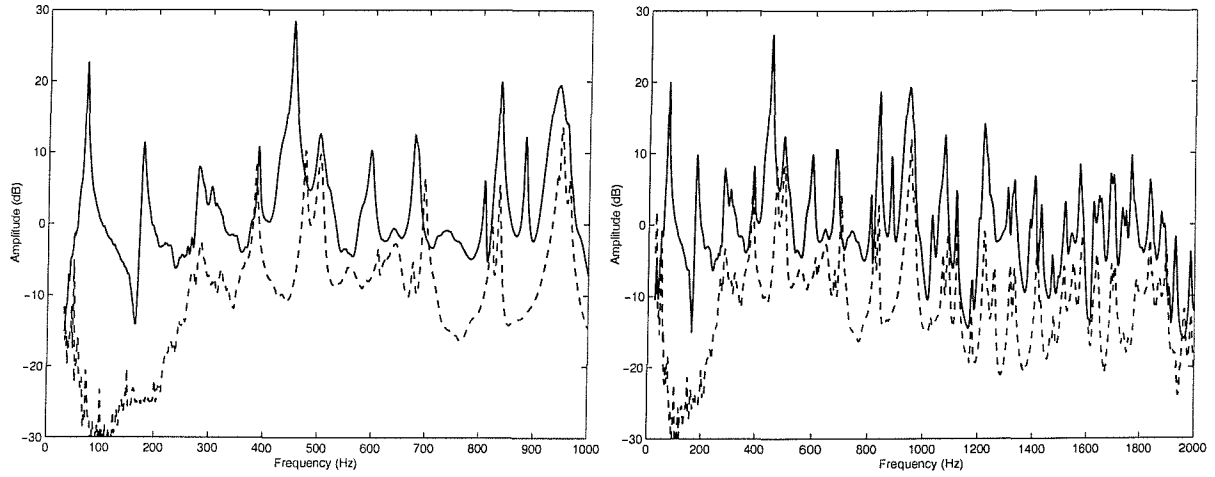

Figure 3.15: *Investigation of the sound radiation property of the test rig (0-1 kHz, left figure and 0-2 kHz, right figure): frequency response function between the averaged sound pressure measured by the nine microphones and the excitation of the primary loudspeaker source, under normal condition (solid line) and averaged sound pressure due to the flanking sound radiation through the side walls of the Perspex box, measured with the panel blocked (dashed line).*

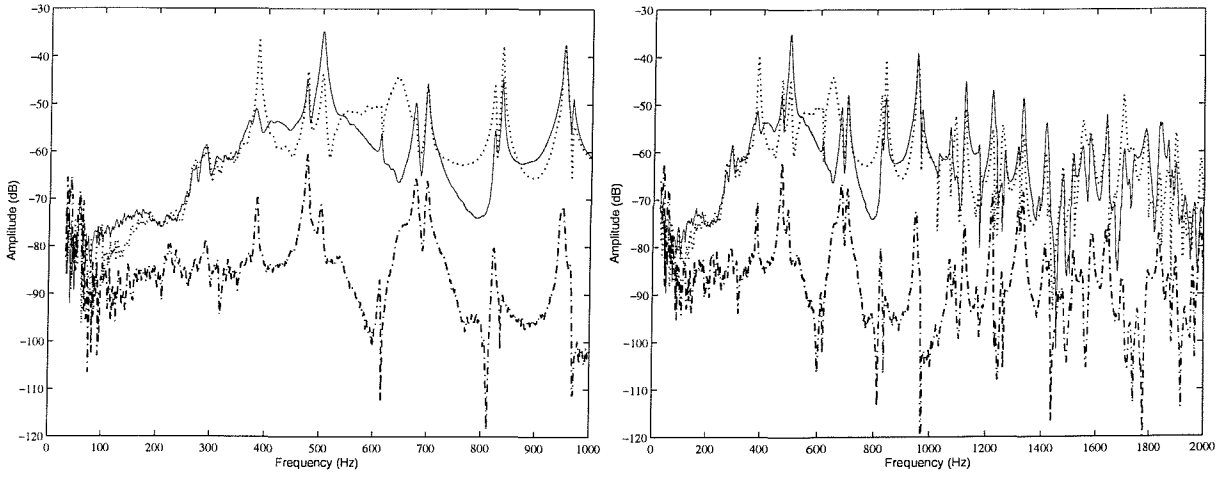

Figure 3.16: *Investigation of the sound radiation property of the test rig (0-1 kHz, left figure and 0-2 kHz, right figure): frequency response functions of the velocity of two point of the lateral walls, chosen at one corner respectively of the largest side (faint line) and of the smallest side (dotted line), and frequency response function of the velocity at the central point of the heavy metal plate (dash-dotted line).*

In the plots of Figure 3.16 are reported the frequency response functions, for unit excitation of the loudspeaker, of the velocity measured at two points on the Perspex side walls chosen at one corner respectively of the largest and of the smallest sides (represented with the faint and the dotted lines) and of the velocity at the central point of the heavy metal plate (represented with the dash-dotted line). From these plots, it clearly appears that the velocity of the top metal plate is 20-40 dB lower than the velocity of the lateral side of the box, i.e. its sound radiation can be considered negligible. Moreover, it can be seen a significant correspondence between the resonance peaks in the frequency response function of the velocity of the side walls and those in the frequency response function of the average sound pressure due to the flanking sound transmission through the lateral sides of the box. Indeed the two plots in Figure 3.15 indicate that the flanking sound transmission produces only small effects on the sound transmission via the smart panel in correspondence to the resonances of the cavity.

These experimental tests of the sound property of the test rig have shown that this arrangement is characterised by a flanking sound transmission of about 20-30 dB lower than the main sound transmission via the smart panel. However, in correspondence to the cavity resonances, the flanking sound transmission could be comparable to that of the smart panel. The evaluation of the reduction of sound transmission through the smart panel is thus possible, except in correspondence of the cavity resonance frequencies that produce relatively high flanking sound transmission effects.

4. THE FREQUENCY RESPONSE BETWEEN THE ACTUATORS AND SENSORS

This chapter is concerned with the theoretical and experimental study of the open loop sensors-actuator frequency response functions in a frequency range up to 50 kHz. In the first section, the measured frequency response functions of a sensor-actuator pair are analysed and contrasted with those provided by the mobility-impedance model presented in Section 3.3. The dynamic effects of the sixteen sensors and actuators due to the size and stiffness/mass of each piezoelectric patch as well as the effects due to the mass and mounted fundamental resonance of each accelerometer sensor are also investigated, as explained in the two successive sections.

Finally, in the last section a further experimental analysis of the vibration level around a single control unit carried out using a laser vibrometer is reported.

4.1 Measured and Simulated sensors/actuator frequency response functions

In this section a comparison between the measured sensor-actuator frequency response functions and the simulated responses are presented. An Advantest spectral analyser, model R9211B/C, has been used to measure the frequency response functions of the sensor/actuator pair n. 7 in Figure 3.2. For these measurements the panel has been mounted on a rectangular cavity with rigid walls which is described in more details in Section 3.7.

The measured frequency response functions have been compared with simulated ones, which have been derived using the mathematical model presented in Section 3.3. When the dynamic effects of the sixteen sensor–actuator systems are taken into account and no primary excitation is present in the cavity or applied to the panel, i.e. $\mathbf{q}_p(\omega) \equiv 0$ and $\mathbf{f}_p(\omega) \equiv 0$, then, according to equations (3.28) and (3.25) the relation between the sixteen measured velocities at the error sensor positions, $\mathbf{v}_m(\omega)$, and the control excitations of the sixteen piezoelectric patches, $\mathbf{f}_s(\omega)$ is given by:

$$\mathbf{v}_m(\omega) = \mathbf{T}_{ms}(\omega)\mathbf{f}_s(\omega) \ , \tag{4.1}$$

where $\mathbf{T}_{ms}(\omega) = \mathbf{A}(\omega)\mathbf{T}_{cs}(\omega)$ and the $\mathbf{A}(\omega)$ and $\mathbf{T}_{cs}(\omega)$ matrices are given by equations (2.62) and (3.26) respectively in Sections 2.3 and 3.3. The transfer matrix $\mathbf{T}_{cs}(\omega)$ accounts for both the passive effect of the acoustic cavity on which the panel is mounted and the dynamic effects of piezo and accelerometer transducers. As shown in Figure 4.4 the dynamics of each sensor-actuator unit has been modelled with three lumped elements: a) a bottom mass that includes part of the piezoelectric actuator mass and the mass of the accelerometer case; b) a lumped spring and damper for the piezoelectric element in the accelerometer and c), the inertial mass of the accelerometer. The dynamic effects of the piezo actuator have been smeared over the panel surface by modifying the Young modulus and density parameters of the material of the panel.

The sixteen sensor actuator frequency response functions can be extracted from equation (4.1) by taking the sixteen diagonal terms of the matrix $\mathbf{T}_{ms}(\omega)$. For example the frequency response function giving the measured velocity at the accelerometer sensor n. 7 due to the unit excitation of the collocated piezo actuator n. 7 is given by the frequency response function $T_{ms\,7,7}(\omega)$.

In practice the physical properties of the sixteen accelerometer sensors and piezo actuators differs from each other, in particular each accelerometer has a different resonance frequency which, for the sixteen transducers used in the smart panel, have been found to go from a minimum of 35 kHz to a maximum of about 42 kHz. This variability of the resonance frequency is rather important and therefore the simulations shown below have been obtained by using the physical parameters summarised in Table 2.5 with the inertia masses of the sixteen accelerometers, m_a, spread in a range of values such that the natural frequencies of the sixteen accelerometers are uniformly distributed between 35 kHz and 42 kHz. Also, in order to account for the inertia and stiffening effects of the piezo actuators the smeared density $\overline{\rho}_s = 3000\,\mathrm{Kg/m^3}$ and smeared Young's modulus of elasticity $\overline{E}_s = 7.1\times10^{10}\ \mathrm{N/m^2}$ have been used in the simulations of the panel response.

In the following three Figures, 4.1 to 4.3, the measured sensor-actuator frequency response functions are contrasted with those obtained from the numerical model respectively for three frequency ranges of 0-1 kHz, 0-10 kHz and 0-50 kHz. In these plots, together with the measured frequency response function (faint line) two other curves are plotted: the first is the simulated sensor-actuator frequency response function when the sensor-actuator mass and dynamics effects are not accounted for (dashed line), and the second is the simulated sensor-

actuator frequency response function when the sensor-actuator mass and dynamics effects are instead taken into account (solid line).

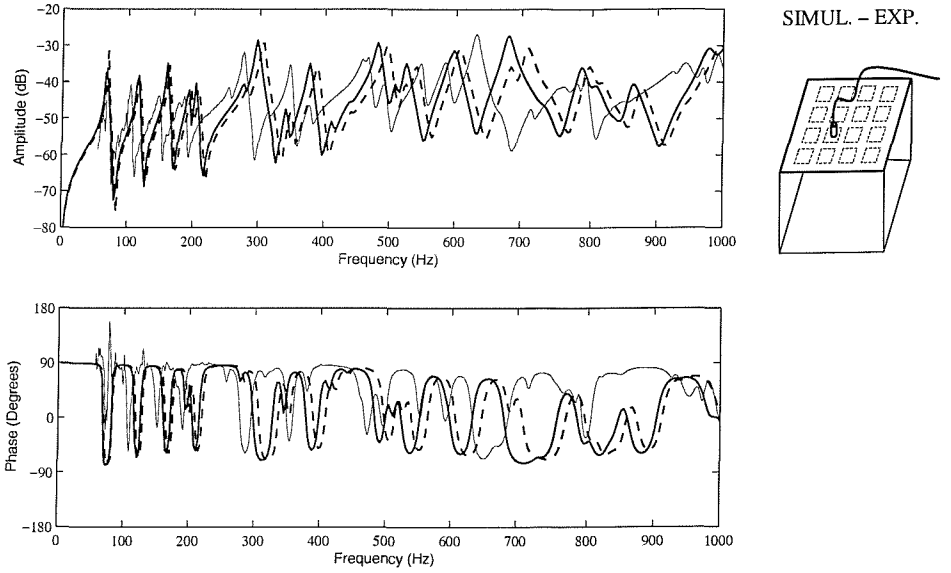

Figure 4.1: *Open loop frequency response function (0-1 kHz) of the sensor/actuator pair n. 7: simulated FRF with no sensor-actuator dynamic effects (dashed line), with sensor-actuator mass and dynamics effects (solid line), and measured FRF (faint line)*

Figure 4.1 shows that, for frequencies up to the sixth resonance frequency of the plate (283 Hz), the solid line, which represent the simulated frequency response function with the sensor-actuator dynamic effects, overlaps the dashed line, which represent the simulated frequency response function without effects. However, for frequencies above the sixth resonance, the sensor-actuator dynamic effect produces a small downward shifting of the resonance frequencies of the plate as one would expect with an increment of the mass. Comparing the measured frequency response function with the numerical simulation when the dynamic effects of the sensor-actuator transducers are taken into account, it can be seen that the agreement between the experimental and numerical results is relatively good up to 200 Hz and can be considered satisfactory at higher frequencies. The measured frequency response function is well reproduced by the simulation except for a shift in frequency that is probably due to the uncertainty for some parameters used to model the dynamic effects of the actuator and sensor transducers.

Figure 4.2 shows the two simulated frequency response functions compared with the measured frequency response function in a frequency range of 0-10 kHz. Above 4 kHz, the amplitude of the simulated frequency response function with sensor-actuator dynamics effects (solid line) has a flatter modulus than that which does not account for these effects

(dashed line). In terms of amplitudes, both simulated curves present small differences respect to the measured one (faint line) and in terms of phase values a good agreement can be seen, particularly between the measured and simulated frequency response functions which include the sensor-actuator effects.

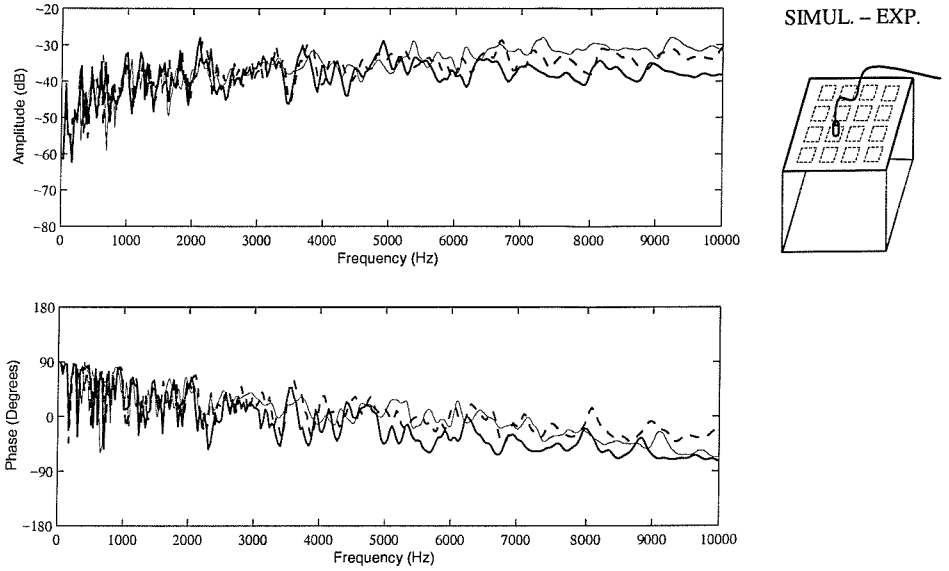

Figure 4.2: *Open loop frequency response function (0-10 kHz) of the sensor/actuator pair n. 7: simulated FRF with no sensor-actuator dynamic effects (dashed line), with sensor-actuator mass and dynamics effects (solid line) and measured FRF (faint line)*

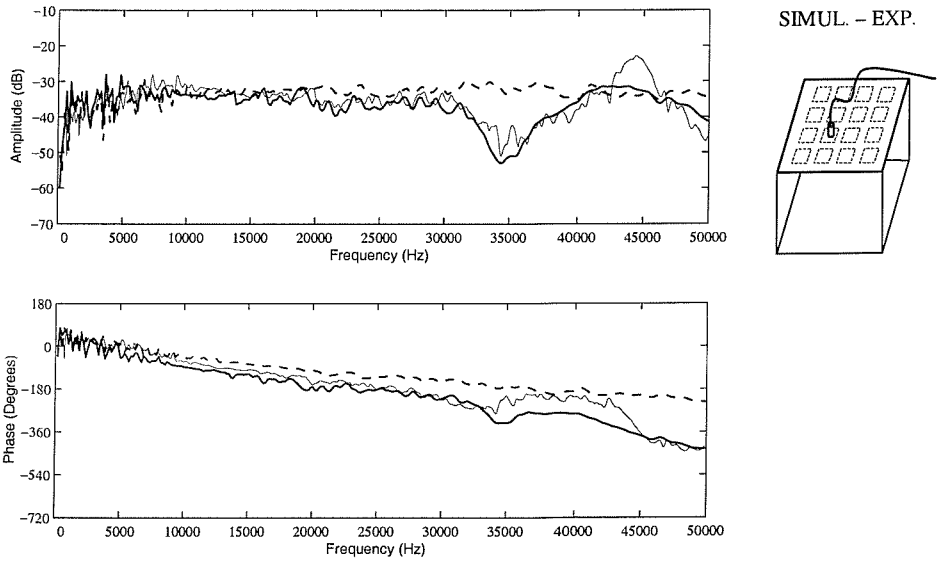

Figure 4.3: *Open loop frequency response function (0-50 kHz) of the sensor/actuator pair n. 7: simulated FRF with no sensor-actuator dynamic effects (dashed line), with sensor-actuator mass and dynamics effects (solid line) and measured FRF (faint line)*

Figure 4.3 shows the two simulated frequency response functions compared with the measured frequency response function in a frequency range of 0-50 kHz. The simulated frequency response function that does not account for sensor-actuator dynamics effects (dashed line) presents an almost flat amplitude trend in the whole frequency range. In contrast, the frequency response function which takes into account both the piezo actuator mass effect and the accelerometer dynamics (solid line) has a relatively wide frequency band trough between 30 kHz and 40 kHz and a broad peak between 43 kHz and 46 kHz, which better agrees with the measured response.

4.2 Sensor-actuator dynamic effects

As shown in Figure 4.4, the accelerometer can be considered as a single degree of freedom neutralizer that reduces the vibration level at the measurement point in correspondence to its natural frequency. In fact each input impedance frequency function of the accelerometers has a peak in correspondence to the resonance frequency of the accelerometers and then a trough at higher frequencies. Figure 4.5 shows the simulated input impedances of the sixteen accelerometers with the physical parameters given in Table 2.5 with variable inertia mass so that their resonance frequencies are uniformly spread between 35 kHz and 42 kHz. From this plot it is evident that there is a relatively high impedance effect at the frequency band of the resonances that tends to reduce the vibration of the panel as found in Figure 4.3.

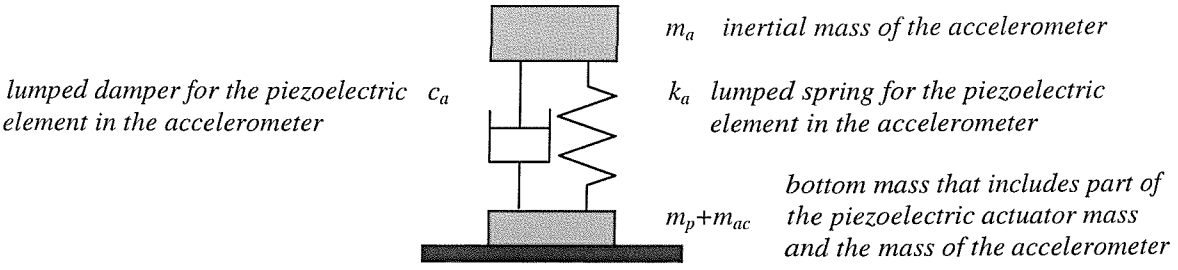

Figure 4.4: *Schematic representation of one sensor–actuator system.*

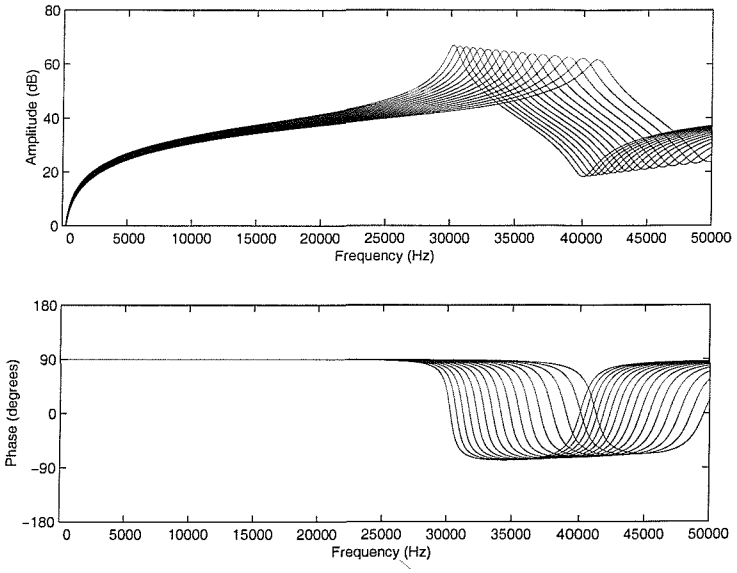

Figure 4.5: *Input impedance frequency functions of the sixteen accelerometer sensors used in the numerical model for the response of the smart panel.*

The sensitivity functions that give the ratio between the measured velocity signals by the accelerometers and the true velocities underneath the accelerometers are characterised by a peak in correspondence to the resonance frequencies of the accelerometers. However, for each accelerometer, this effect is limited to a relatively narrow frequency band as shown in Figure 4.6 below for the accelerometer n. 7. Therefore, the measured sensor–actuator frequency response function remains characterized by the trough at 30 kHz to 40 kHz and the crest between 43 kHz and 46 kHz generated by the sixteen accelerometers that works as neutralizers.

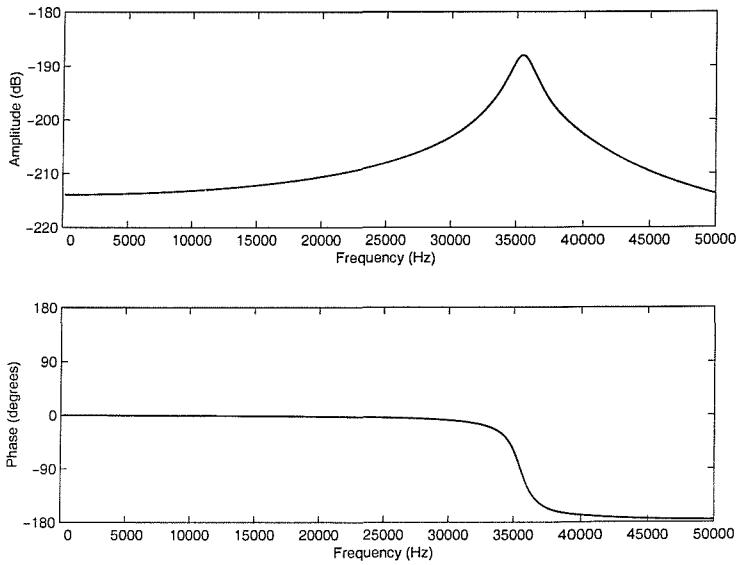

Figure 4.6: *Sensitivity function of one accelerometer used in the numerical model for the response of the smart panel.*

The analysis of the measured and simulated sensor-actuator frequency response functions shows that the frequency responses are affected by an evident phase shift above 10 kHz as shown for example in Figure 4.3. This phase lag is due to the fact that the accelerometer and the piezoelectric patch are not a truly collocated and dual sensor–actuator pair. The actuation mechanism of the piezoceramic actuator can be modelled as four lines of moments acting along the edges of the piezoelectric patch [36]. The sensor is instead measuring the transverse velocity at the centre position of the actuator patch. There are thus two types of problems: the actuation and sensing are not collocated and also the moment actuation is not compatible to the linear transverse velocity sensing. Both effects contribute to determine a non–positive definite real part frequency response function at higher frequencies [53, 72-74].

4.3 Effect due to piezo actuators dimensions

Intuitively, the non–collocated positioning effect found above 10 kHz for the accelerometer sensor piezo actuator frequency response function depends on the size of the actuator patch with reference to the bending wavelength vibration of the plate. The collocated positioning effect can therefore be extended to a wider frequency range by using a smaller piezoceramic patch actuator. Figure 4.7 shows the predicted sensor–actuator frequency response functions with two different piezoelectric patch actuators, of dimensions 25×25 mm (faint line) and 12×12 mm (solid line). The bottom plot confirms that with a smaller patch the phase roll off is much lower than with the larger patch. Indeed by halving the size of the actuator the frequency response function is then found to be positive definite up to about 35 kHz. The draw back is that by reducing the size of the piezoceramic patch the control authority is also decreased. Therefore a compromise has to be found between the possibility of extending the minimum phase property of the sensor actuator frequency response function to higher frequencies and the required control authority to produce the desired control effect.

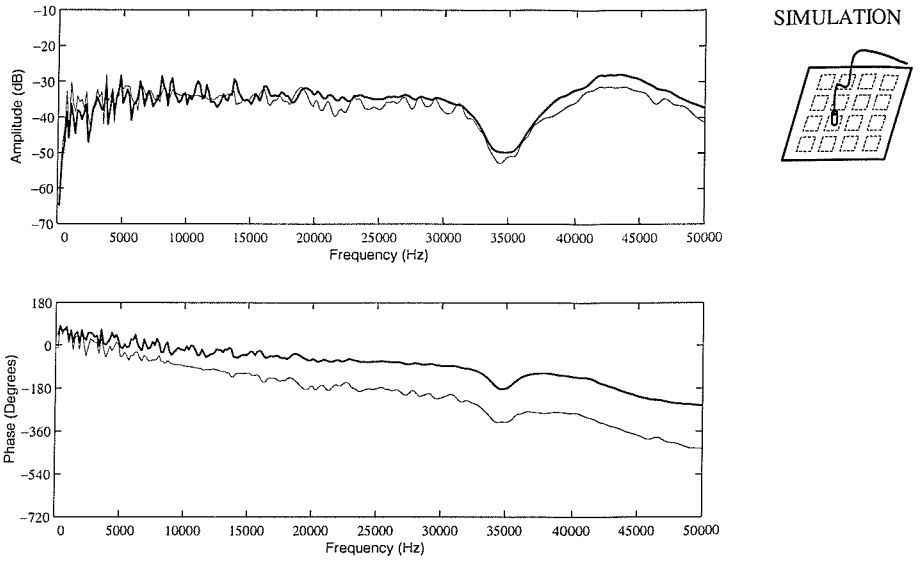

Figure 4.7: *Open loop frequency response function (0-50 kHz) of the sensor/actuator pair n. 7: simulated FRF with standard size piezoelectric patch (faint line) and with smaller size patch (solid line)*

4.4 Investigation of the sensor-actuator dynamic with the laser vibrometer

In order to investigate the behaviour of the piezoelectric actuator at the high frequencies, a further analysis of the vibration level around a sensor-actuator pair has been carried out using Laser Doppler Vibrometer (LDV)[1]. The system has been excited with a random signal up to 50 kHz directly applied to the piezo actuator n. 7. A grid of 480 points to be scanned has been defined on a square surface of double side of the piezo patch (see Figure 4.8), centred respect to the sensor n. 7 and a set of frequency response functions between the velocity at each grid point and the primary disturbance has been measured by means of the laser vibrometer. This set of data has been processed by the laser software system in order to obtain two dimensional (2D) colour coded images of the velocity distribution around the sensor-actuator pair at different frequencies, as shown in the plots below.

[1] A briefly description of the laser vibrometer functioning is reported in Appendix C, while a further application of this device is reported in Chapter 8 with reference to the experimental assessment of the decentralised control system.

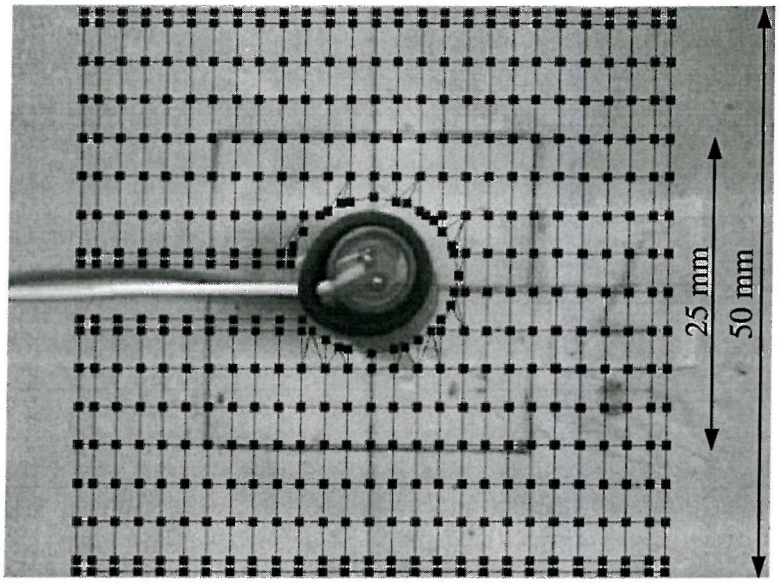

Figure 4.8: *Grid of desired measurement points (480) on the surface of the plate around the sensor actuator pair n. 7 to be scanned with the vibrometer when the system is excited by a structural primary source on the panel (piezo actuator)*

Figure 4.9 show the distribution of the vibration velocity of the scanned area around the sensor-actuator pair n.7 at 343 Hz (left side picture) and 2.116 kHz (right side picture). It can clearly be seen that at these relatively low frequencies the vibration level is uniformly distributed on the scanned area since the wavelength of the bending wave is bigger than the actual size of the piezo patches. In fact, as shown in Figure 4.10, the wavelength of the bending wave is inversely proportional to the square of the frequency and, for this specific case, the wavelength becomes smaller than the piezo patch dimension above 15 kHz. For frequencies higher than this critical value, the distribution of velocity becomes less uniform, as shown if Figure 4.11 for the frequencies of 16 kHz (left side picture) and 44 kHz (right side picture). At such higher frequencies the bending wavelength are shorter then the piezo dimensions. Also, the various components of the sensor-actuator transducers behave less and less as "lumped parameter" elements and therefore directly affect the overall vibration of the panel in the vicinity of the control unit. As explained in the previous section, at these frequencies the sensor-actuator pair cannot be considered truly collocated with the consequence of a non–positive definite real part frequency response function.

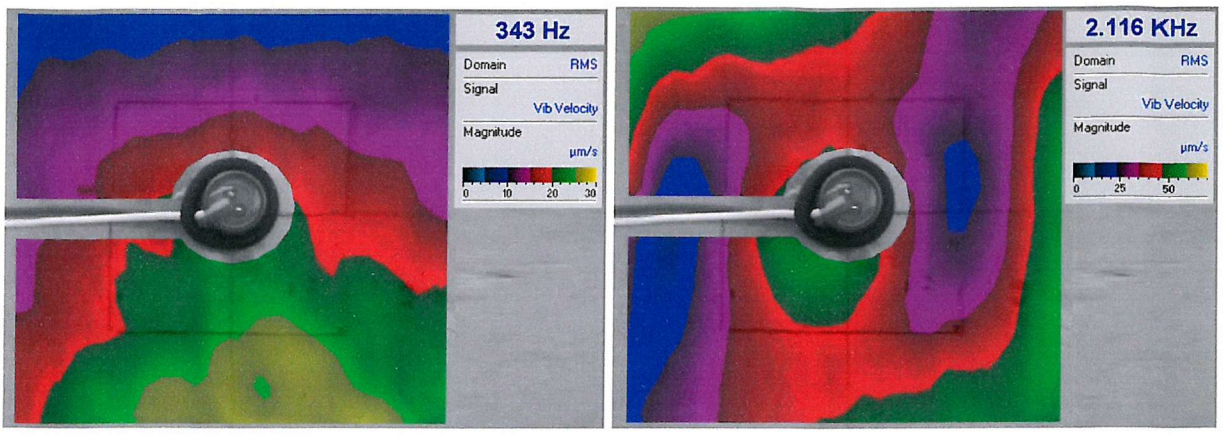

Figure 4.9: *Vibration velocity of the plate in correspondence of a sensor actuator pair, assessed with the laser vibrometer and using the piezo actuator as primary excitation: 343 Hz (left picture) and 2.116 kHz (right picture).*

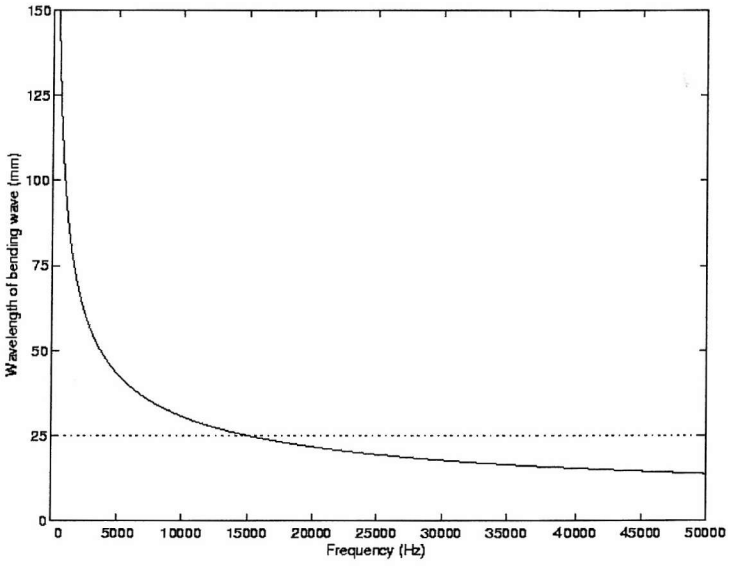

Figure 4.10: *Wavelength of the bending wave of the panel (solid line) as function of frequency. The dashed line represents the actual size of the piezo patch (25x25 mm)*

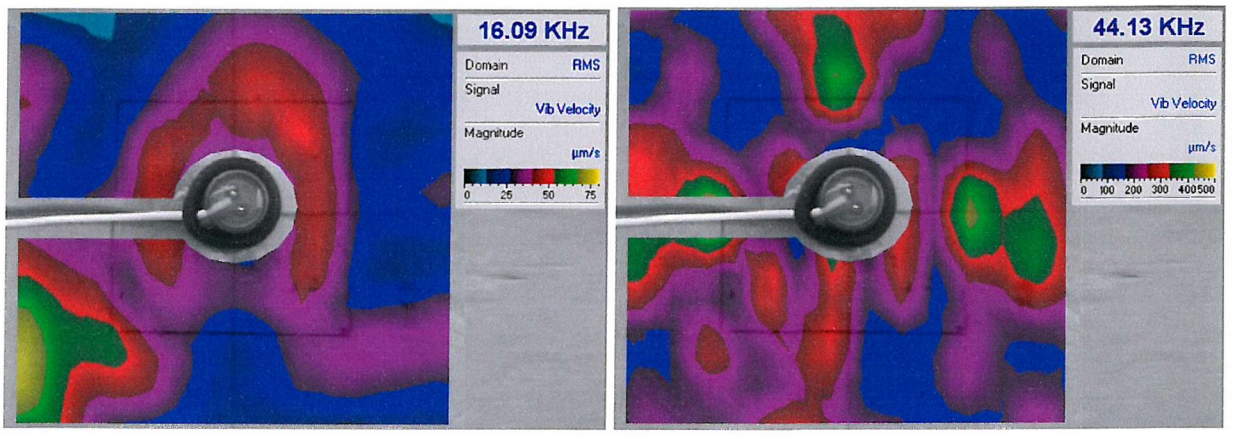

Figure 4.11: *Vibration velocity of the plate in correspondence of a sensor actuator pair, assessed with the laser vibrometer and using the piezo actuator as primary excitation: 16.09 kHz (left picture) and 44.13 kHz (right picture).*

5. IMPLEMENTATION OF VELOCITY FEEDBACK USING A SINGLE SENSOR/ACTUATOR PAIR

In this chapter the design of a single channel velocity feedback controller is described and its experimental implementation is discussed. This investigation has been carried out for the control unit (accelerometer-feedback controller-piezo actuator) n.7 in Figure 3.2, considering the smart panel mounted on the rectangular cavity and excited by the acoustic primary source (loudspeaker) or by the structural primary source (shaker).

The main features of the velocity feedback are described in the next section, while, in the following one, the stability analysis of the system is investigated. Subsequently, the design of a phase lag compensator for the implementation of the velocity feedback is discussed considering its effects on the closed loop frequency response function of the system. Finally, the on-line implementation of the single channel velocity feedback is described in the last two sections, with reference to the two types of primary excitations (loudspeaker and shaker); the results in terms of attenuation of the vibration level and of reduction of the sound transmission are reported.

5.1 Design of a single feedback control system

The design of the single channel velocity feedback control systems has been tested on the sensor–actuator pair n. 7 when the panel is mounted on the rectangular cavity which is described in more details in Section 3. Figure 5.1 shows the block diagram of the single–input single–output feedback control system that has been implemented. The total output velocity measured by the accelerometer sensor, $y(j\omega)$, is given by the vibration generated by the primary disturbance, $d(j\omega)$, which can be either an acoustic source in the cavity underneath the panel (loudspeaker) or a primary force acting on the panel (shaker), and by the vibration generated by the control actuator which is set to be proportional, but with opposite phase, to the velocity measured by the accelerometer sensor itself. Therefore, for this feedback control scheme, the ratio between the error signal, $y(j\omega)$, and that of the primary disturbance, $d(j\omega)$, is given by [51]:

$$\frac{y(j\omega)}{d(j\omega)} = \frac{D(j\omega)}{1+G(j\omega)H(j\omega)} \quad , \tag{5.1}$$

where $G(j\omega)$ is the frequency response function between the sensor and actuator pair, $D(j\omega)$ is the frequency response function between the sensor and the excitation source (loudspeaker or shaker) and $H(j\omega)$ is the control function.

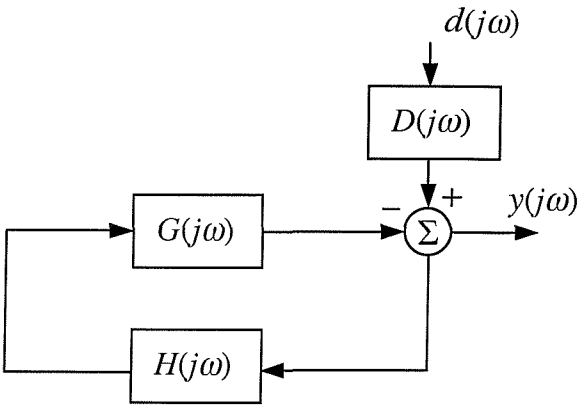

Figure 5.1: *Block diagram of the closed loop control system: direct velocity feedback.*

5.2 Stability analysis

As shown in Figure 5.1, in order to implement direct velocity feedback control, the control function is set to be a constant gain $H(j\omega)=h$ so that, provided the sensor actuator frequency response function is positive real, by increasing the gain h the ratio $y(j\omega)/d(j\omega)$ is always brought down. In order to guarantee an unconditionally stable control operability that gives reductions of vibration at all frequencies, the Nyquist plot of the open loop frequency response function $G(j\omega)H(j\omega)$ should stay in the right–hand half of the complex plane for any frequency [51]. The analysis presented in the previous section has shown that the frequency response function of the sensor–actuator is not minimum phase. Indeed above about 10 kHz the phase exceed –90° and constantly rises up to –360° in correspondence to 48 kHz. Also, the amplitude gradually rises up to 2 kHz and then remains constant around the maximum amplitude values at higher frequencies. There is also a trough between 30 kHz and 40 kHz, which is followed by a crest with relatively high amplitudes between 43 kHz and 46 kHz. Therefore it is likely that at higher frequencies the sensor–actuator frequency response function enters the left hand side of the Nyquist plot and, for relatively low values

of gains, goes into the circle of radius 1 and centre $(0,-1)$ or even encircles the Nyquist point $(0,-1)$ since the amplitude of the sensor–actuator response was found to be relatively large even at high frequencies. Thus, it is possible that even for small values of gain the control system is affected by control spillover at the higher frequencies or even goes unstable [51].

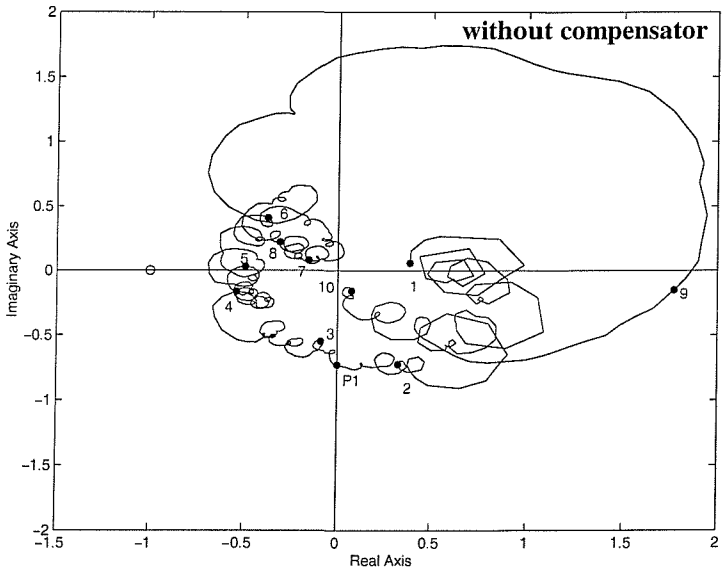

Figure 5.2: *Nyquist plot (0-50 kHz) of the measured frequency response function of the sensor-actuator pair n. 7 without compensator (gain of 30, P1=12.5 kHz): 1=5 kHz, 2=10 kHz, 3=15 kHz, 4=20 kHz, 5=25 kHz, 6=30 kHz, 7=35 kHz, 8=40 kHz, 9=45 kHz, 10=50 kHz, 12=50 kHz.*

The Nyquist plot of the open frequency response function $G(j\omega)H(j\omega)$ is shown in Figure 5.2 for a constant control gain $h = 30$, in a frequency range 5-50 kHz. This plot is focussed of higher frequency response in order to assess the stability of the controller. The low frequency part of the transfer function has been omitted to avoid overcomplicating the graph. Considering this plot it can be noticed that the trough of the amplitude of the sensor–actuator frequency response function between 30 kHz and 40 kHz, which is due the neutralizing effects of the sixteen accelerometers, occupies exactly the negative, left hand side, of the Nyquist plot. Therefore, as expected the Nyquist plot is characterised by a left hand side part which however is quite squeezed towards the imaginary axis. This is a very important result, since, even if the sensor–actuator frequency response function is not minimum phase, still relatively large control gains could be implemented without entering in instability and without having too large control spillover phenomena at relatively higher frequencies. Also, the resonance effect due to the accelerometer sensor at around 44 kHz is, in this case, not compromising the stability of the control system since the sensor–actuator frequency response function between 40 kHz and about 50 kHz is positive definite. It must be

said that this type of sensor-actuator response function was not designed in advance and has come out from a happy choice of the accelerometer and the mass of the piezoceramic patch. Since it is very difficult to construct a collocated and dual sensor-actuator pair at all frequencies, it is then very important to design the two transducers in such a way as the Nyquist plot of the sensor-actuator response function has very little negative real part.

5.3 Design of phase lag compensator

As discussed above, the test panel studied for one control unit is prone to generate instabilities in a frequency range between 12.5 kHz and 40 kHz. Therefore, in order to give the possibility of implementing the high gains required to obtain the wanted reductions of the vibration and sound radiation of the panel, a phase–lag compensator with frequency response function $C(j\omega)$ has been designed and implemented in the controller that is shown in Figure 5.3.

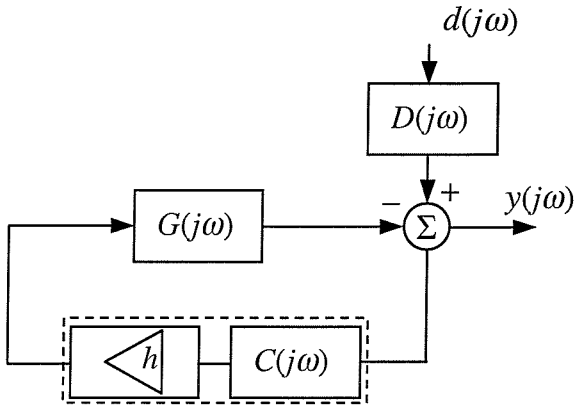

Figure 5.3: *Block diagram of the closed loop control system: velocity feedback with compensator.*

The first order compensator represented in Figure 5.4 is commonly used to improve the performance of the analogue feedback systems and increase their relative stability. The optimal values for the resistors and capacitor of the compensator circuit have been derived iteratively by simulating the open loop frequency response function $T(j\omega) = H(j\omega)G(j\omega)$, where

$$H(j\omega) = hC(j\omega) \tag{5.2}$$

and $C(j\omega)$ is the phase–lag compensator frequency response function which, according to the notation given in Figure 5.4, is given by:

$$C(j\omega) = \frac{V_o(j\omega)}{V_i(j\omega)} = \frac{1 + j\omega R_2 C}{1 + j\omega(R_1 + R_2)C} \quad . \tag{5.3}$$

The iterative procedure has brought to the design of a phase-lag compensator with the following electric characteristics: R_1=18 kΩ, R_2=1 kΩ and C=15 nF. Therefore the resulting pole frequency of the compensator is $\omega = 1/(R_1 + R_2)C = 3703.7\ rad/s$, and the zero frequency is $\omega = 1/R_2 C = 66666.67\ rad/s$.

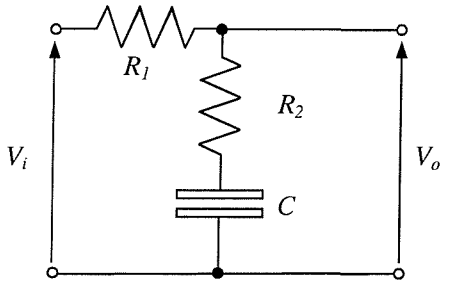

$$C(j\omega) = \frac{V_o(j\omega)}{V_i(j\omega)} = \frac{1 + j\omega R_2 C}{1 + j\omega(R_1 + R_2)C}$$

$R_1 = 18\ \text{k}\Omega$
$R_2 = 1\ \text{k}\Omega$
$C = 15\ \text{nF}$

Figure 5.4: *Phase lag compensator built in the feedback controller*

The frequency response function of the compensator is shown in the Figure 5.5. It can be seen that, at low frequencies, the gain of this circuit is unity and the phase shift is small, while at high frequencies the phase shift is again small but the gain is now $R_2/(R_1 + R_2)$; therefore, the loop gain can be considerable attenuated at frequencies for example around the Nyquist point, with little phase shift. In the frequency region from the pole to the zero frequencies, the phase lag is negative (up to –65° at 3 kHz), but it occurs quite far from the Nyquist point without affecting the stability of the feedback system [107].

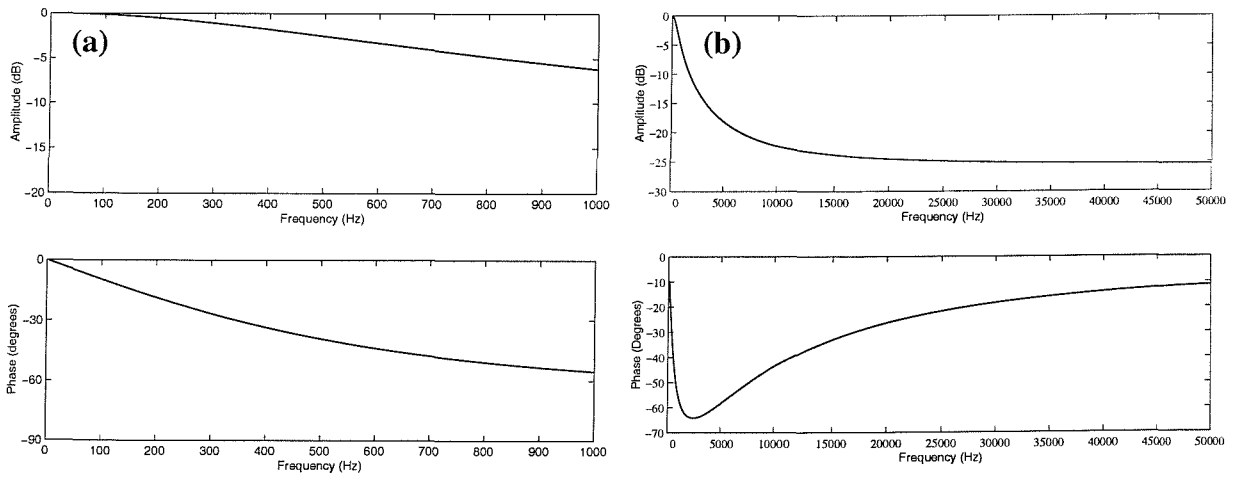

Figure 5.5: *Transfer function of the compensator in the range 0-1 kHz (a) and 0-50 kHz (b)*

Figure 5.6 shows the Nyquist plot of the open loop frequency response function $T(j\omega)$ with the phase lag compensator and a control gain $h = 450$, in a frequency range 5-50 kHz. The response below 5 kHz has again been omitted from this figure to avoid overcomplicating the graph, but this has a considerably larger amplitude with the compensator that has the case in Figure 5.2. Figure 5.6 shows how the compensator has rotated the Nyquist plot in clock wise direction such that the real part of the transfer function $T(j\omega)$ enters the negative side of the plot at 9.5 kHz to leave it at about 40 kHz. However, comparing this plot with that relative to the implementation of direct velocity feedback in Figure 5.2, it can be noticed that the same stability margin is achieved with the compensator than in the case of direct velocity feedback but with a fifteen times higher control gain.

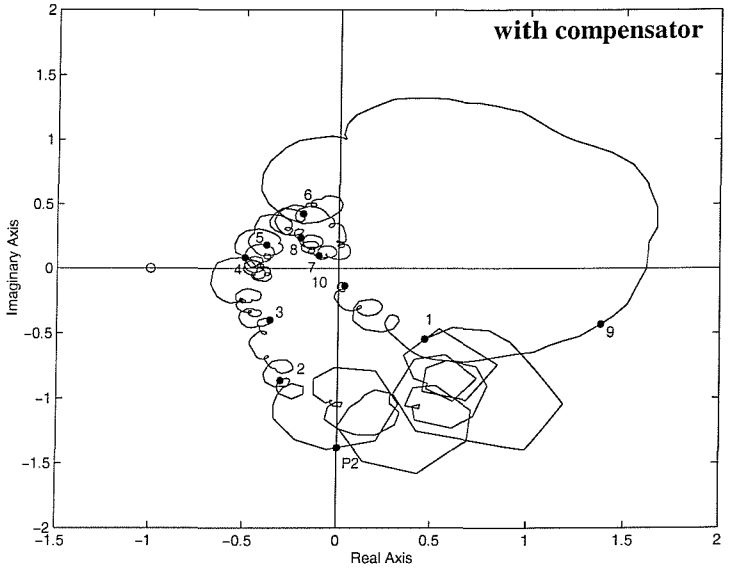

Figure 5.6: *Nyquist plot (0-50 kHz) of the measured frequency response function of the sensor-actuator pair n. 7 with compensator (gain of 450, P2=9.25 kHz): 1=5 kHz, 2=10 kHz, 3=15 kHz, 4=20 kHz, 5=25 kHz, 6=30 kHz, 7=35 kHz, 8=40 kHz, 9=45 kHz, 10=50 kHz, 12=50 kHz.*

5.4 On-line implementation with an acoustic primary source in the cavity

The practical implementation of the feedback control number 7 in Figure 3.2 is now discussed. This experimental work has been carried out with the panel mounted on the rectangular cavity with rigid walls. The control effectiveness of the system has been first assessed with reference to the acoustic source in the cavity (loudspeaker).

The two plots in Figure 5.7 and 5.8 show the measured velocity at error sensor n. 7 per unit excitation of the loudspeaker in the cavity between 0-1 and 0-2 kHz without control

(solid line) and when the feedback control system with compensator n. 7 is implemented using a relatively high gain that nevertheless guarantees stability (faint line). These two plots indicate that relatively good reductions of the vibration level are achieved up to 2 kHz.

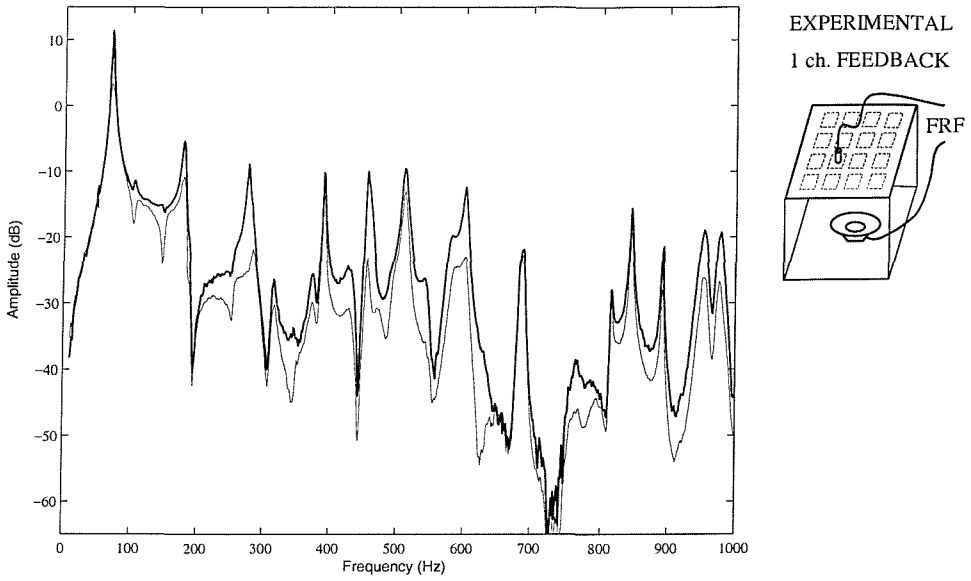

Figure 5.7: *Measured velocity at error sensor n. 7 per unit excitation of the loudspeaker in the cavity between 0-1 kHz without control (solid line) and when the feedback control system with compensator n. 7 is implemented (faint line).*

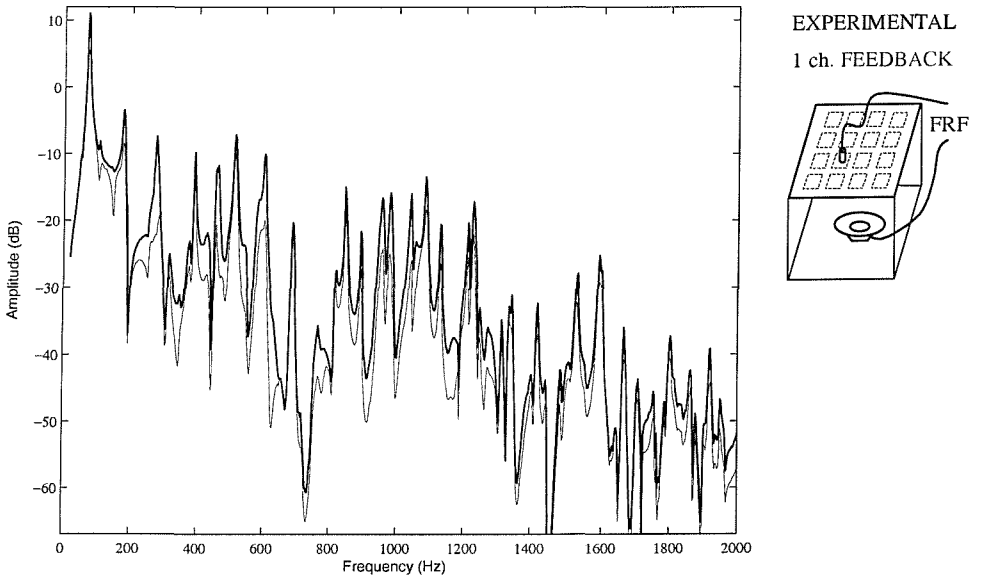

Figure 5.8: *Measured velocity at error sensor n. 7 per unit excitation of the loudspeaker in the cavity between 0-2 kHz without control (solid line) and when the feedback control system with compensator n. 7 is implemented (faint line).*

Considering in more details Figure 5.7 it can be noticed that the control system find rather difficult to damp down the resonance frequencies at 70, 178, 391, 519, 675, 814, 843 and 871 Hz. This is due to two possible factors: the low control authority of the sensor–actuator n. 7 for some of the resonant modes and the loading effect on the plate generated by the low frequency volumetric acoustic response of the cavity. However, except for these modes, reductions from 5 up to 15 dB are measured up to 1 kHz. Also, considering Figure 5.8, at higher frequencies still reductions of about 6 dB are measured within narrow frequency bands.

In Figure 5.9 the frequency response function of the velocity at the error sensor n. 7 per unit excitation of the loudspeaker in the cavity between 0-5 kHz is reported. It can be seen that the single channel velocity feedback is not able to contrast the vibration of the plate above 2 kHz, but also that it is not affected by any control spillover effects.

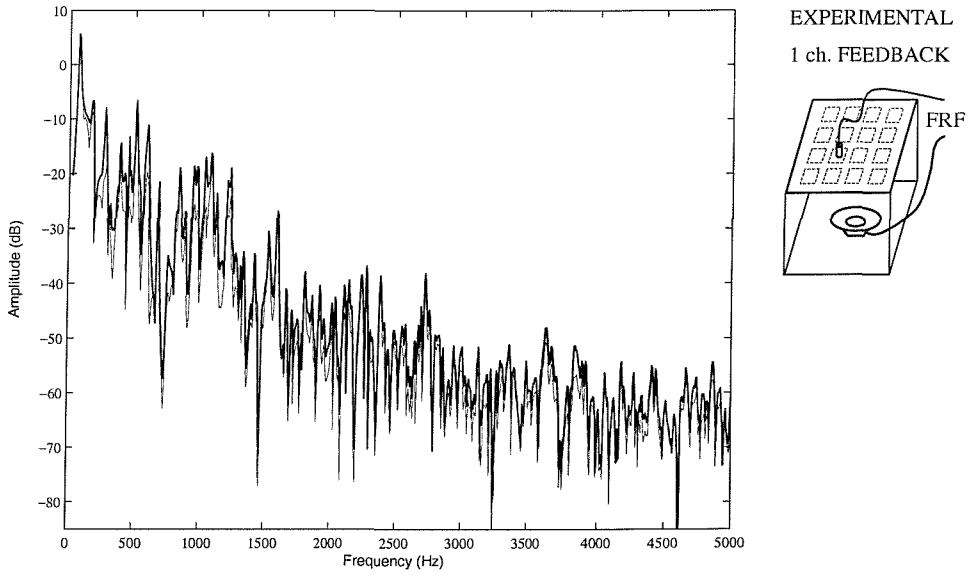

Figure 5.9: *Measured velocity at error sensor n. 7 per unit excitation of the loudspeaker in the cavity between 0-5 kHz without control (solid line) and when the feedback control system with compensator n. 7 is implemented (faint line).*

An estimate of the panel sound transmission is shown in Figure 5.10, 5.11 and 5.12 with reference to a frequency band 0-1, 0-2 and 0-5 kHz. The solid line represents the measured sound pressure at about 0.5 m above the panel in correspondence to the centre of the panel itself without control while the faint line represents the measured sound pressure when all sixteen control units are working with the same feedback control gain used in the previous measurements.

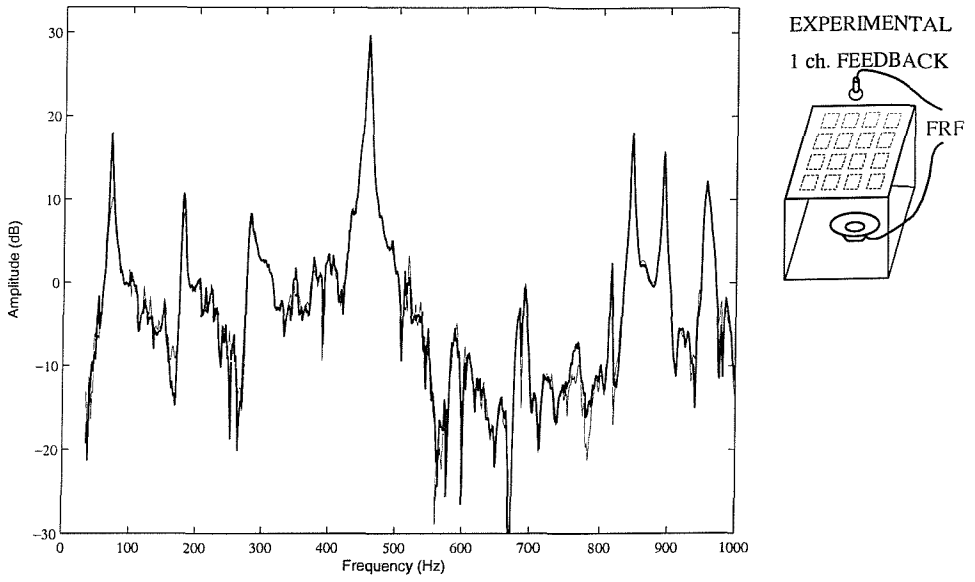

Figure 5.10: *Measured signal of the microphone per unit excitation of the loudspeaker in the cavity between 0-1 kHz without control (solid line) and when the feedback control system with compensator n. 7 is implemented (faint line).*

From the analysis of these plots, it can clearly be seen that the single channel feedback loop is effective only on the first resonance, with an attenuation of about 7 dB. As previously mentioned, the use of the only sensor-actuator pair number 7 is not sufficient to contrast the loading effect on the plate generated by the low frequency volumetric acoustic response of the cavity and therefore the performance of the single channel control system in terms of attenuation of the sound transmission are relatively modest.

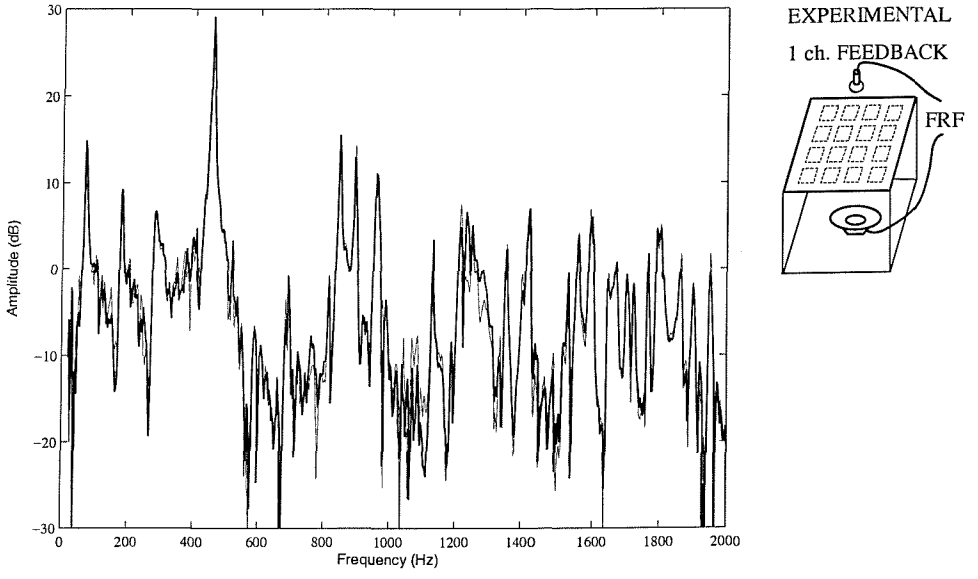

Figure 5.11: *Measured signal of the microphone per unit excitation of the loudspeaker in the cavity between 0-2 kHz without control (solid line) and when the feedback control system with compensator n. 7 is implemented (faint line).*

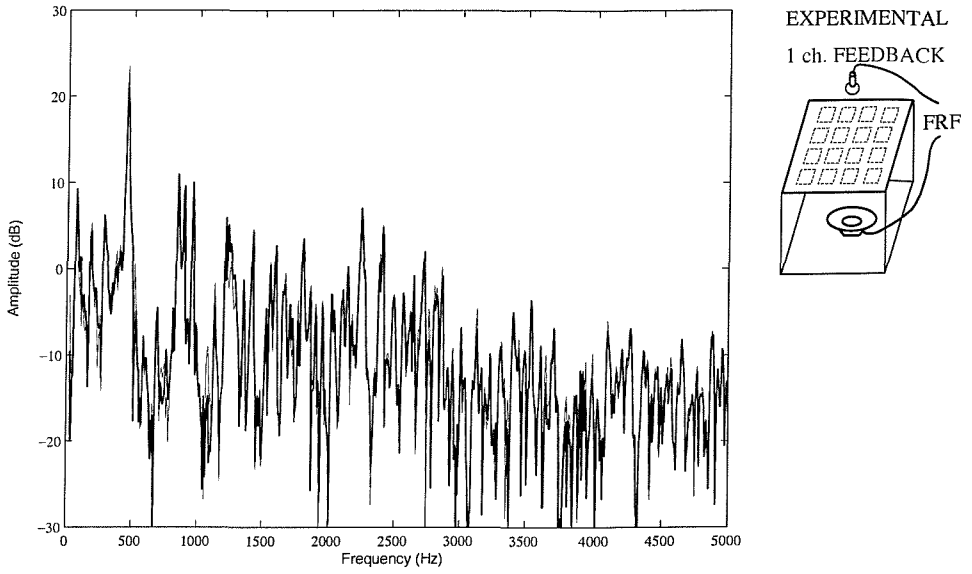

Figure 5.12: *Measured signal of the microphone per unit excitation of the loudspeaker in the cavity between 0-5 kHz without control (solid line) and when the feedback control system with compensator n. 7 is implemented (faint line).*

5.5 On-line implementation with a structural primary source on the panel

The control effectiveness of the single channel control system has been also assessed with reference to the structural source on the panel (shaker). The two plots in Figure 5.13 and 5.14 show the measured velocity at error sensor n. 7 per unit excitation of the shaker on the panel between 0-1 and 0-2 kHz without control (solid line) and when the feedback control system with compensator n. 7 is implemented using a relatively high gain (faint line). These two plots indicate similar results to those found for the loudspeaker primary excitation with relatively large reductions of the vibration level up to 2 kHz. Figure 5.13 shows that also in this case the control system find rather difficult to damp down some low frequency resonances particularly those at 70, 102, 183, 508, 643, 712 and 744 Hz mainly because of the low spatial control authority given by the single acting control unit. Except for these modes, reductions from 5 up to 15 dB are measured up to 1 kHz and relatively better reductions of about 5 dB than those found in the previous case are measured at higher frequencies.

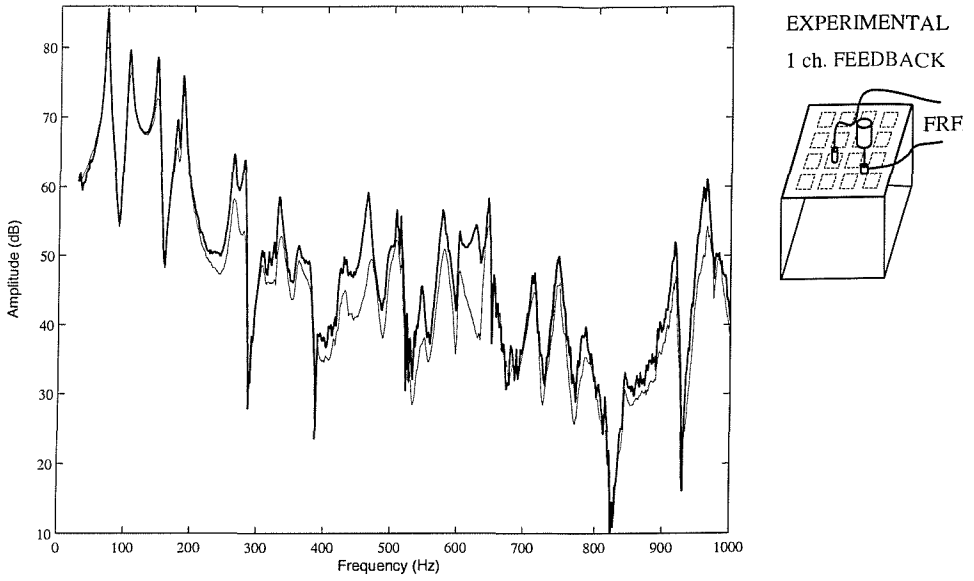

Figure 5.13: *Measured velocity at error sensor n. 7 per unit excitation of the shaker on the panel between 0-1 kHz without control (solid line) and when the feedback control system with compensator n. 7 is implemented (faint line).*

In Figure 5.15 the frequency response function of the velocity at the error sensor n. 7 per unit excitation of the shaker between 0-5 kHz is also reported. In this case it can be seen that the single channel velocity feedback at the high frequency it is not affected by any control spillover effects, and also it provides an attenuation of 2-3 dB up to 3.5 kHz.

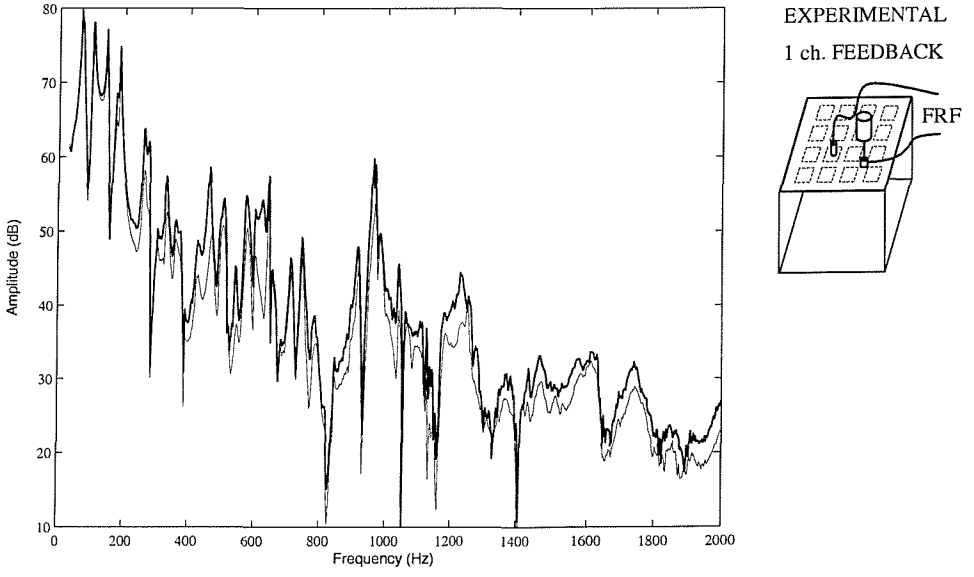

Figure 5.14: *Measured velocity at error sensor n. 7 per unit excitation of the shaker on the panel between 0-2 kHz without control (solid line) and when the feedback control system with compensator n. 7 is implemented (faint line).*

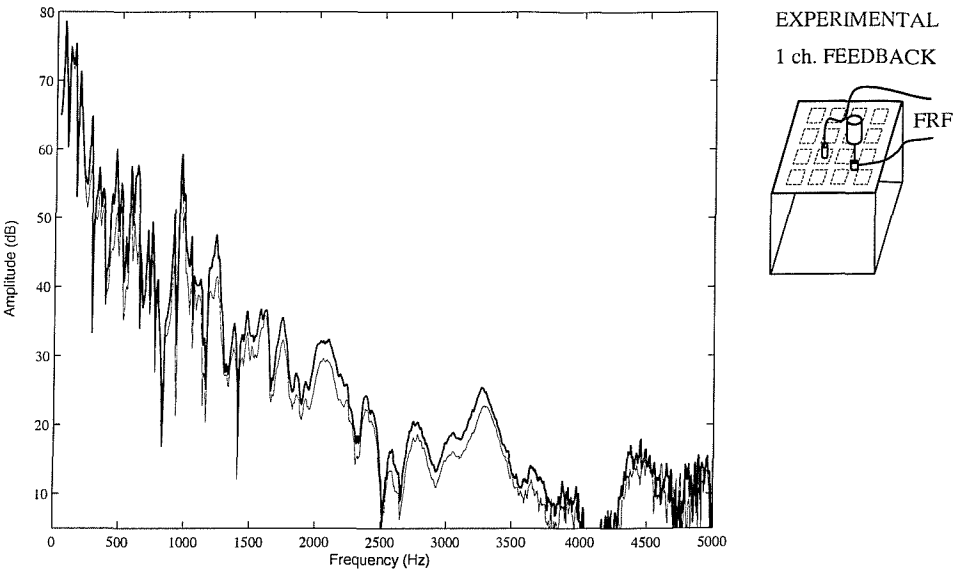

Figure 5.15: *Measured velocity at error sensor n. 7 per unit excitation of the shaker on the panel between 0-5 kHz without control (solid line) and when the feedback control system with compensator n. 7 is implemented (faint line).*

Similarly to the case with acoustic primary disturbance, an estimate of the panel sound radiation from the panel has been reported in Figures 5.16, 5.17 and 5.18 with reference to a frequency band 0-1, 0-2 and 0-5 kHz. Again, the control effectiveness in terms of reduction of the sound radiation is moderately low if it is compared with the correspondent attenuation of the vibration level. Nevertheless, it can be seen that, with respect to the case of acoustic primary excitation, the single feedback is able to attenuate not only the first resonance (6 dB), but also the second one (3 dB), the resonance at about 650 Hz (4 dB) and a little narrow band frequency around 950 Hz (7 dB).

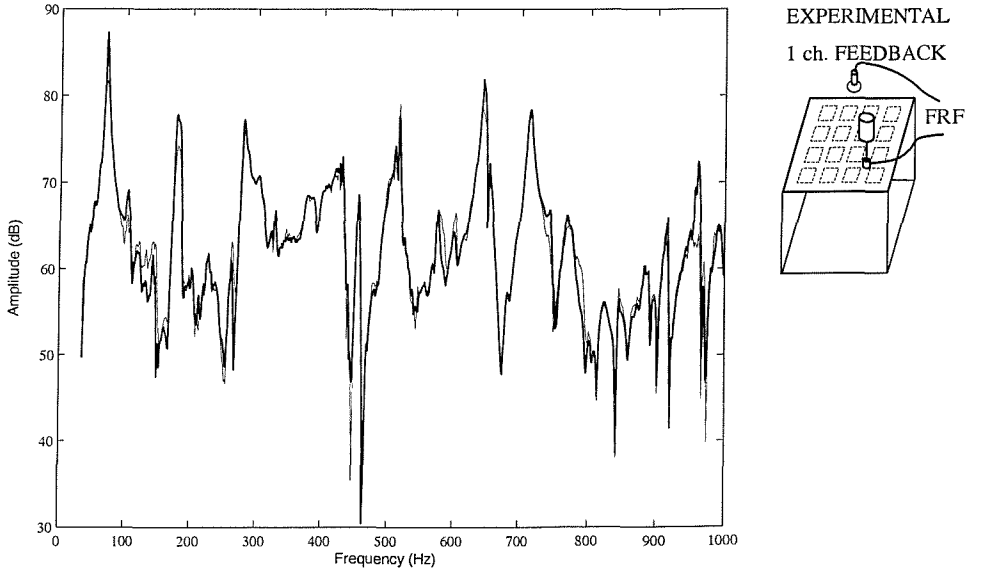

Figure 5.16: *Measured signal of the microphone per unit excitation of the shaker on the panel between 0-1 kHz without control (solid line) and when the feedback control system with compensator n. 7 is implemented (faint line).*

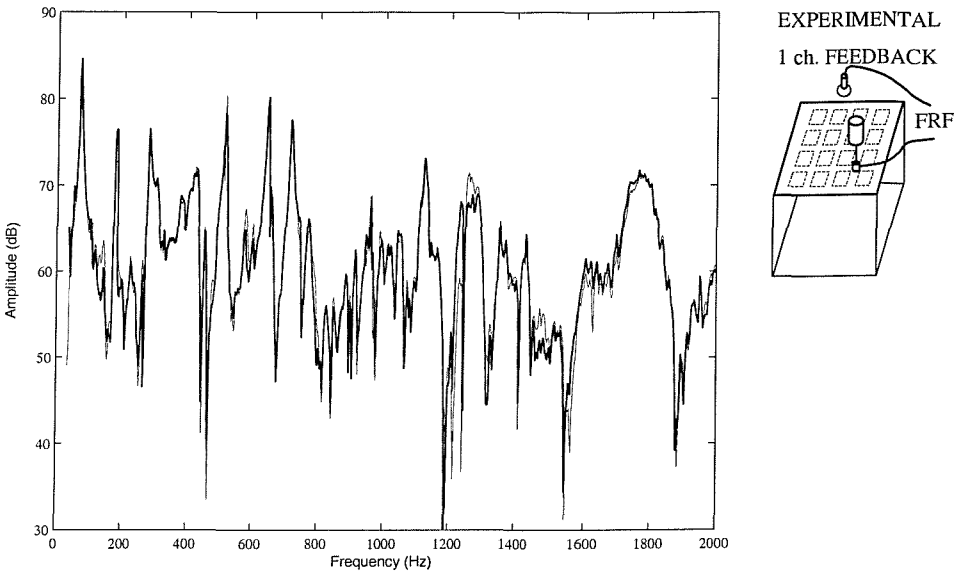

Figure 5.17: *Measured signal of the microphone per unit excitation of the shaker on the panel between 0-2 kHz without control (solid line) and when the feedback control system with compensator n. 7 is implemented (faint line).*

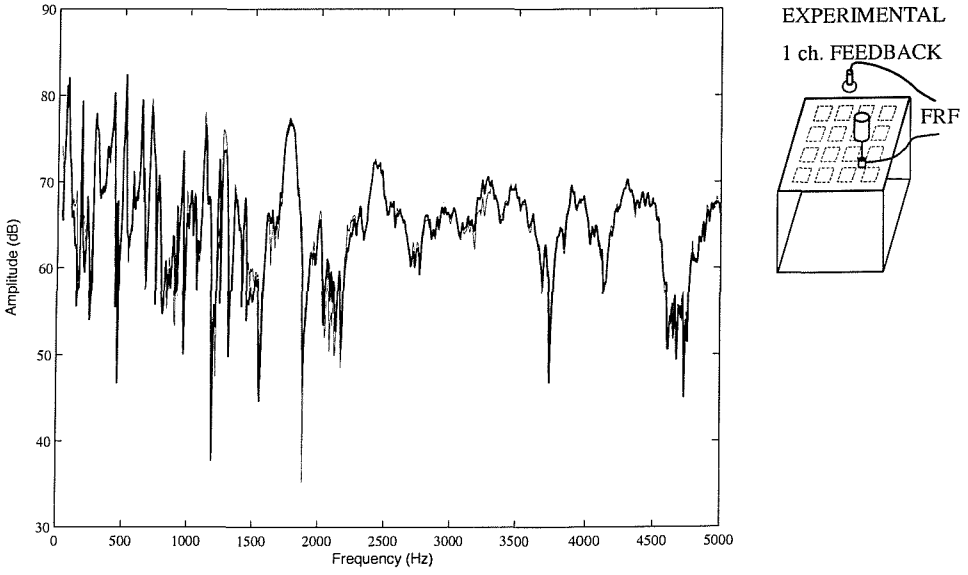

Figure 5.18: *Measured signal of the microphone per unit excitation of the shaker on the panel between 0-5 kHz without control (solid line) and when the feedback control system with compensator n. 7 is implemented (faint line).*

6. IMPLEMENTATION OF THE DECENTRALISED CONTROL SYSTEM

This chapter is concerned with the design of the multi-channel controller for the implementation of the decentralised velocity feedback control system. The development of the multi-channel analogue controller is based on the work done to implement the single channel control system. Therefore this chapter can be considered as the complement of the previous one and it is structured according to the same scheme. In the first section, the main features of the sixteen channels controller and its design are discussed and, in the following two, the frequency response functions between each sensor and actuator are analysed with reference to the stability of the multi-channel control system. Finally, the on-line implementation of the control system is described and a set of results obtained in a preliminary testing of its performances is reported.

6.1 Design of the controller

The analogue control systems built for each decentralized control unit consists of four main elements: an integrator circuit to transform the output of the accelerometer sensor to velocity, a phase lag compensator circuit, a low-power unit with adjustable gain and a power amplifier, as shown in Figure 6.1.

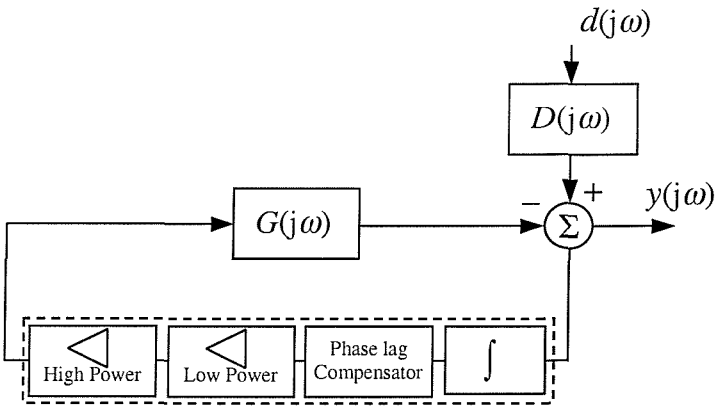

Figure 6.1: *Block diagram of the closed loop control system: velocity feedback with compensator and power units.*

The phase lag compensator implemented in each control unit is the same as that described in Section 5.3. The high power units are sixteen ILP HY2001 power amplifier, which provide a maximum voltage signal of 30 Volts peak to peak for an output power of 40 Watts RMS into an 8 Ω loud. Figure 6.2 shows the complete circuit diagram used for each channel of the analogue control system. Besides the four main components previously mentioned, further electric devices are also present in each board, such as the switching circuit driven by a manual switch to select the output (inverted, non-inverted, no output) and the operational amplifier driven by another switch to enable/disable all the control signals at the same time.

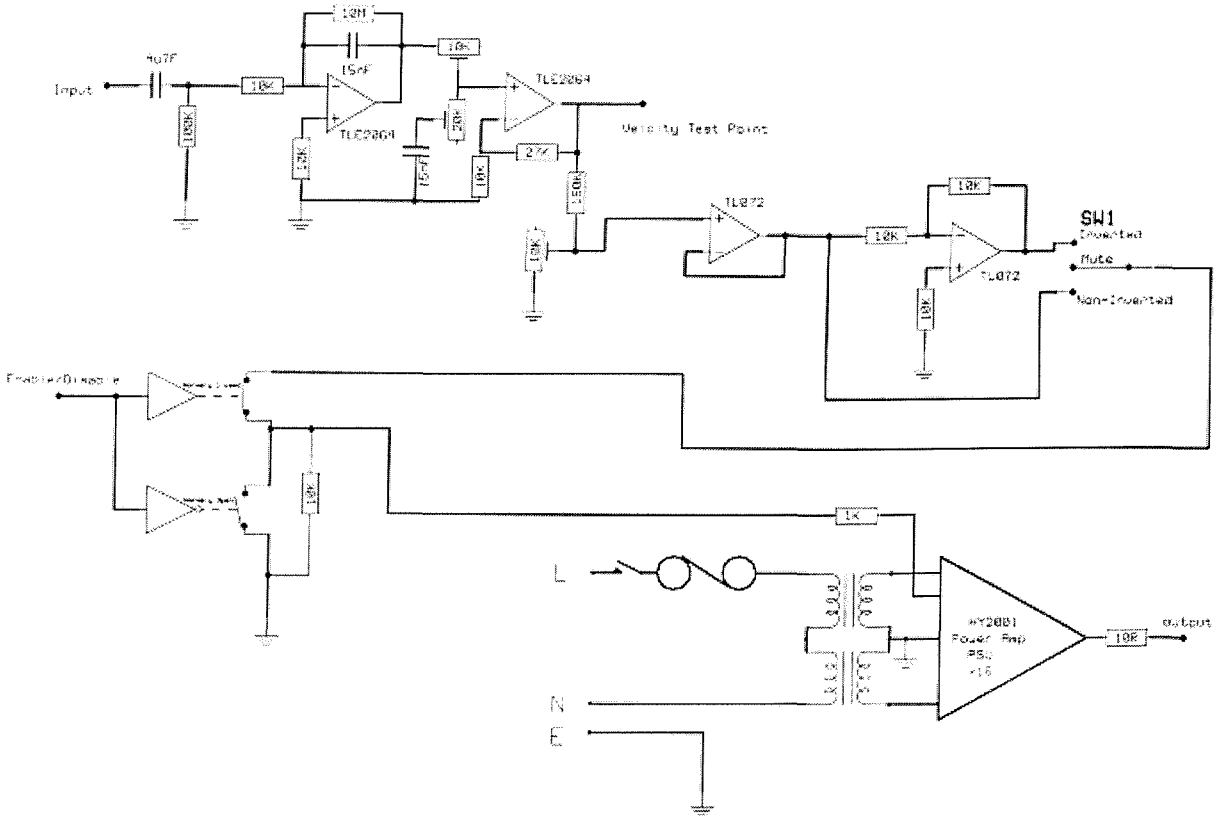

Figure 6.2: *Circuit diagram of each of the 16 channels decentralised feedback control system*

All the sixteen channels have been assembled in the single enclosure shown in Figure 6.3 below. The complete test system is shown in Figure 6.4, where in the centre can be noticed the Perspex box with the loudspeaker primary source inside and on top the smart panel with the sixteen piezo actuators and accelerometer sensors. On the left side is visible the sixteen channel PCB signal conditioner while on the right hand side the analogue sixteen channels decentralised feedback control units system is shown.

Sixteen independent velocity feedback loops are implemented between each collocated sensor and actuator: the signal measured from each accelerometer passes through the PCB

signal conditioner that has been set to pre-amplify the signal by a gain of five, and then is applied to the control board which drives the piezo actuator.

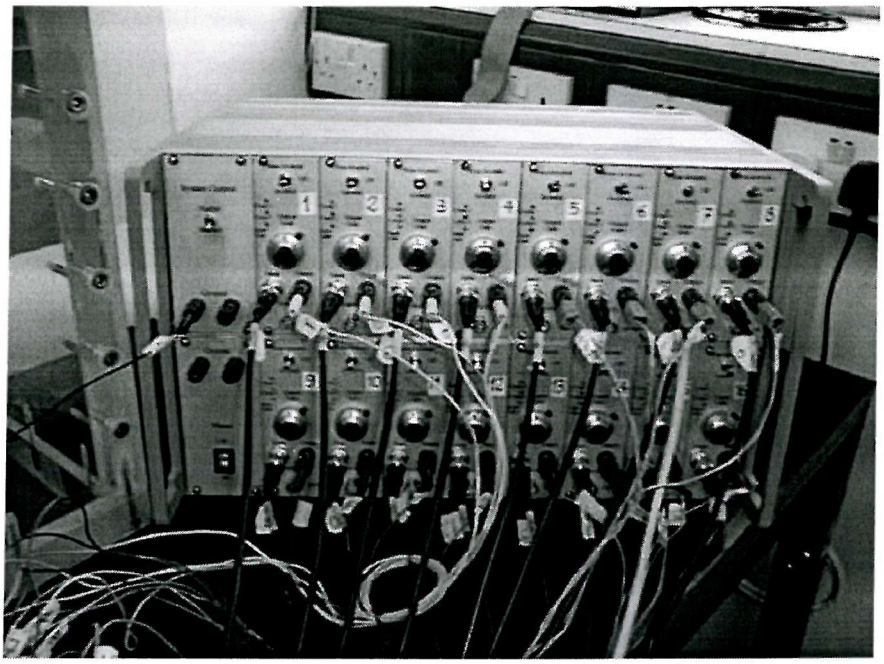

Figure 6.3: *The sixteen channels decentralised feedback control system*

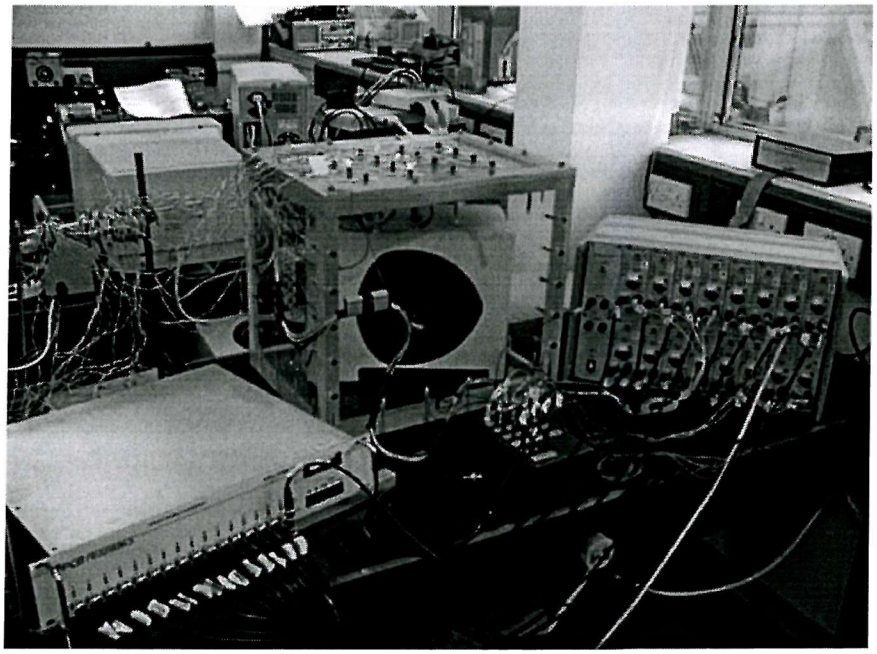

Figure 6.4: *The complete experimental setup with the Perspex box with on top the smart panel and the control equipment: signal conditioner (left), controller (right).*

6.2 Measure of the frequency response functions between the sixteen sensors and the sixteen actuators

In this section the multi-channel decentralised control system with equal numbers of collocated actuators and sensors is analysed. In this specific case, the plant response, $\mathbf{G}(j\omega)$, is the fully populated matrix of input and transfer responses between the actuators and sensors on the panel and the controller response $\mathbf{H}(j\omega)$ is a diagonal matrix that contains the frequency responses of the decentralised controller (fixed control gain multiplied by the phase lag compensator). The same control gain, h, used in the experiments presented in Chapter 5 and the phase lag compensator previously designed (see equation 5.3) has been implemented in the sixteen feedback controllers.

Provided the control system is stable, the vector of spectra for the residual signals at the sensor outputs, $\mathbf{y}(j\omega)$, is related to that of the sensor outputs before control, $\mathbf{D}(j\omega)\mathrm{d}(j\omega)$, by the expression:

$$\mathbf{y}(j\omega) = [\mathbf{I} + \mathbf{G}(j\omega)\mathbf{H}(j\omega)]^{-1}\mathbf{D}(j\omega)d(j\omega) \ , \tag{6.1}$$

where $\mathbf{D}(j\omega)$ is the vector of frequency response functions between the sensors and the excitation source $\mathrm{d}(j\omega)$ (loudspeaker or shaker).

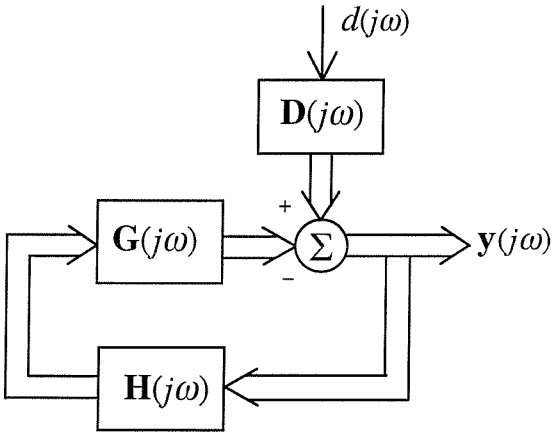

Figure 6.5: *Block diagram of the multichannel decentralised velocity feedback control system*

If collocated and compatible transducer are used, then the real part of $\mathbf{G}(j\omega)$ must be positive definite, since the total power supplied to the uncontrolled system by all the actuator must be positive [3]. Moreover, if the controller is designed so that it has a positive real part at all

frequencies (e.g. in the case of constant gain for which $\mathbf{H}(j\omega)=h\mathbf{I}$ with $h>0$), both the plant and the controller are passive and the feedback controller illustrated above must be unconditionally stable. Thus if multiple local feedback loops are implemented with fixed gains then the system is stable provided each of the individual feedback gains is positive. Under this condition the feedback gains can, in principle, be increased without limit and the signals from the control sensors can be driven to zero [3]. However, this property cannot be guaranteed with piezoelectric actuators and velocity sensors since, as emphasised in Section 4.2, the actuation and sensing are not truly collocated and the moment actuation is not compatible to the linear transverse velocity sensing. Both effects contribute to determine a non–positive definite real part frequency response function at higher frequencies.

Thus it is necessary to determine the stability of the system according to general criteria for multivariable feedback controller, for example the Generalised Nyquist criterion, which states that the system is stable provided the locus of none of the eigenvalues of $\mathbf{G}(j\omega)\mathbf{H}(j\omega)$ encloses the Nyquist point (-1,0) as ω varies from $-\infty$ to $+\infty$ [108,109].

In order to examine the eigenvalues loci of $\mathbf{G}(j\omega)\mathbf{H}(j\omega)$, a set of experimental measures of the open loop frequency response functions of the system has been carried out[1]: a random input signal in a frequency range of 0-50 kHz has been used to drive each piezo patch and the frequency response functions of the controller outputs have been obtained with references to the gains adopted for the implementation of the decentralised control system.

Figures 6.6a and 6.6b show respectively the amplitude and the phase of the set of frequency response functions measured by exciting the actuator number 7 and measuring the signal at each of the sixteen sensors. For each function, denoted *GH* in the *y* label, the two numbers between brackets indicates respectively the reference number of the input used (piezo patch) and the reference number of the output (controller output), with respect to the numbering used in Figure 3.2. Inspection of the measured frequency response functions of Figure 6.6a and of those obtained driving the others piezo actuators (see Appendix B) reveals that the

[1] In order to measure the $\mathbf{G}(j\omega)\mathbf{H}(j\omega)$ matrix it would have been necessary to measure the frequency response functions between an input signal to each controller and the velocity output at each sensors. This measurement configuration however can not be easily done in this specific test rig because the integrator (that can be considered part of the sensing) is included in the electric scheme of the controller and can not be separated or disconnected. Therefore, in the practical testing, the frequency response functions between an input signal to each actuator and the output of each controller have been measured, obtaining the matrix $\mathbf{H}(j\omega)\mathbf{G}(j\omega)$ instead of the desired $\mathbf{G}(j\omega)\mathbf{H}(j\omega)$. However, with respect to the stability analysis, the two matrixes $\mathbf{H}(j\omega)\mathbf{G}(j\omega)$ and $\mathbf{G}(j\omega)\mathbf{H}(j\omega)$ have the same eigenvalues.

diagonal terms of the matrix $\mathbf{G}(j\omega)\mathbf{H}(j\omega)$, i.e. the elements that represent the response of each collocated control unit, tend to be larger than the off-diagonal elements. Assuming that all the controllers have the same response[2], it can be deduced that the matrix $\mathbf{G}(j\omega)$ is close to being

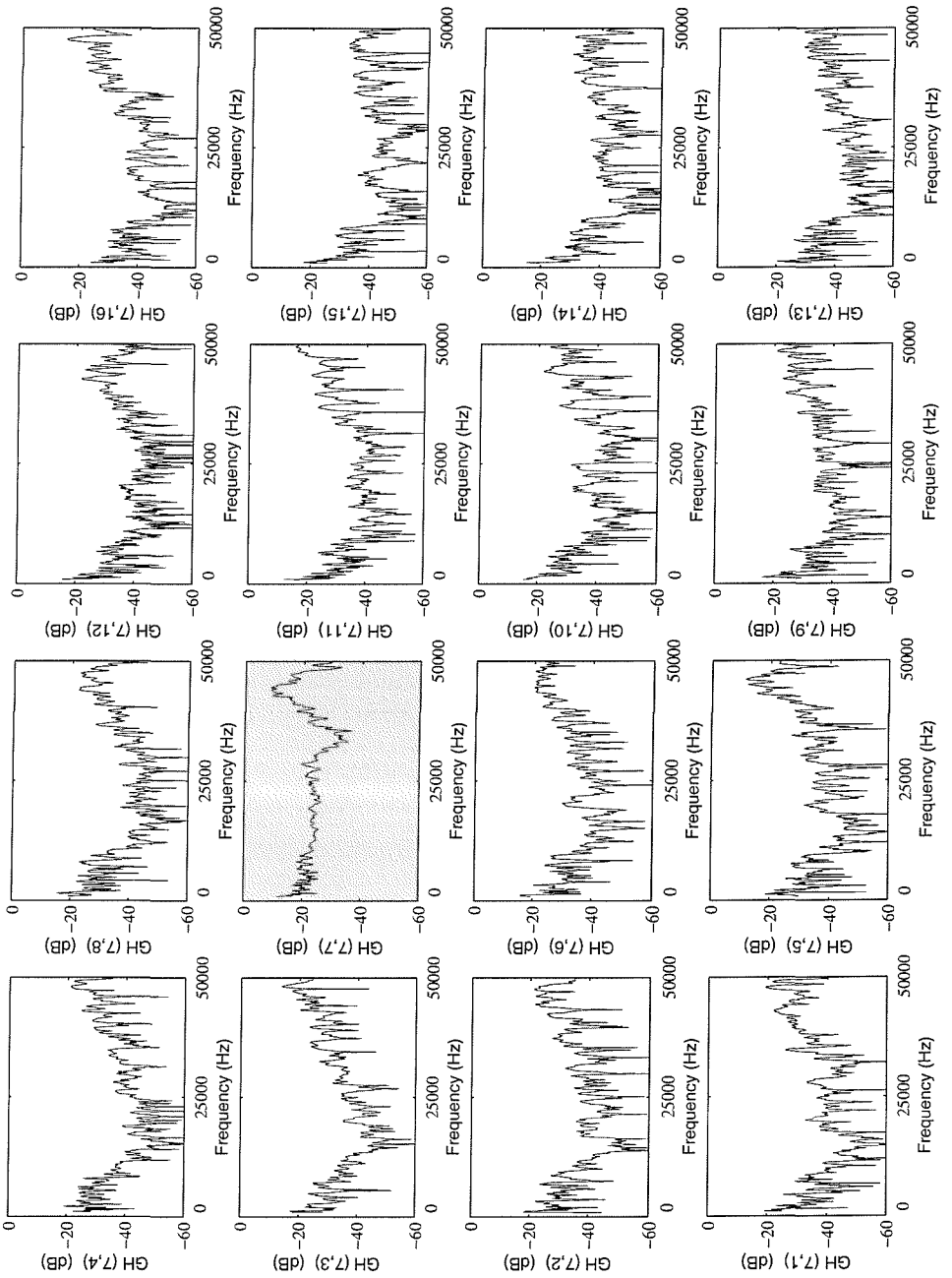

Figure 6.6a: *Amplitude of the sixteen measured frequency response functions between the sixteen control outputs and the piezo actuator n. 7, exciting the plate in a frequency range of 50 kHz*

[2] In the real implementation this supposition can not be considered to be strictly true, however, since the same design and implementation has been used for each controller, it can be assumed valid at least for some qualitative comments of the results.

diagonal. This characteristic is important for the implementation of a decentralised control system, because it suggests that the plant to be controlled can be consider as a collection of independent sub-plants and each control term may be designed independently [108]. A more formal analysis of stability, using the eigenvalues of $\mathbf{G}(j\omega)\mathbf{H}(j\omega)$, is considered below.

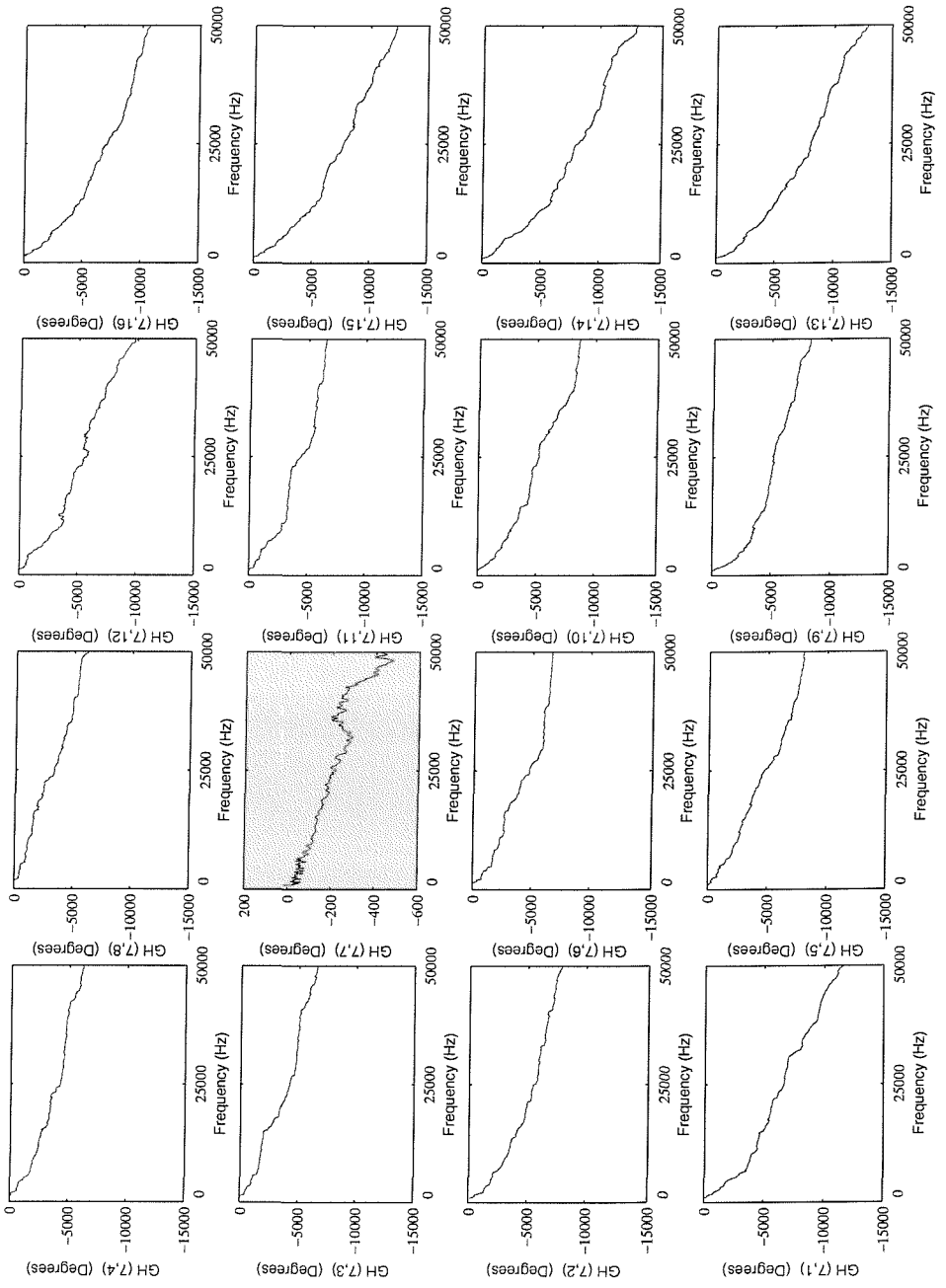

Figure 6.6b: *Phase of the sixteen measured frequency response functions between the sixteen control outputs and the piezo actuator n. 7, exciting the plate in a frequency range of 50 kHz*

6.3 Stability analysis

The eigenvalues of the measured matrix $\mathbf{G}(j\omega)\mathbf{H}(j\omega)$ have been calculated and are shown as series of plots of amplitude versus frequency in Figure 6.7.

In order to determine the stability of the multi-channel feedback system, according to the generalised Nyquist criterion, a polar representation of the eigenvalues has been used, as shown in Figure 6.8, in a frequency range 5-50 kHz. The low frequency part of the plots has been omitted to avoid overcomplicating the graph. It can be noted that none of the

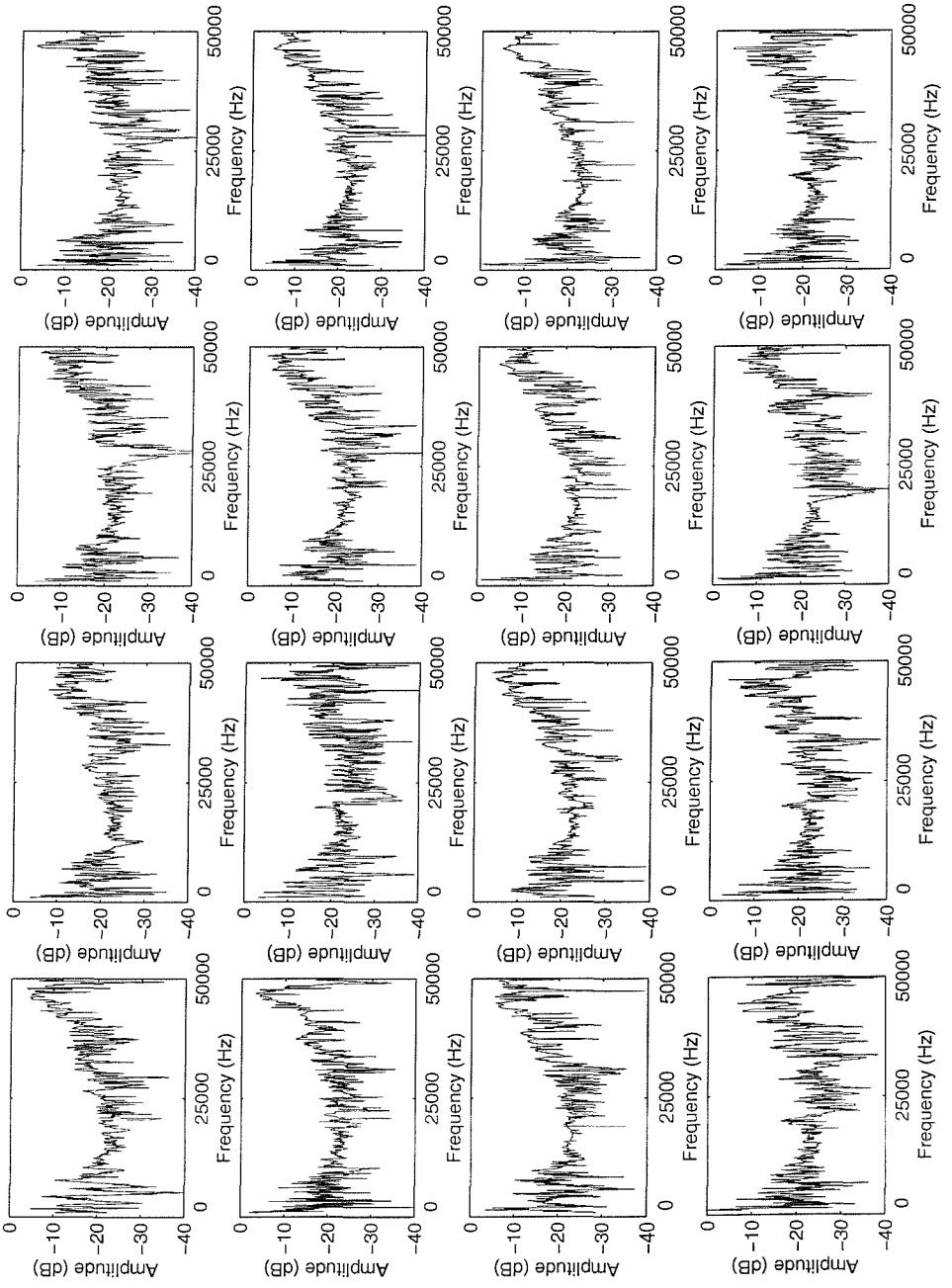

Figure 6.7: *Modulus of eigenvalues of the matrix* $\mathbf{G}(j\omega)\mathbf{H}(j\omega)$ *as functions of frequency (0-50 kHz)*

eigenvalues loci of $\mathbf{G}(j\omega)\mathbf{H}(j\omega)$ encircle the (-1,0) point, and thus the closed-loop system is stable for the set of gain implemented in the decentralised feedback. However, all the eigenvalues cross the negative real axis and therefore the system is not unconditionally stable, as one would expect. From the diagrams it is also possible to evaluate the gain margin (GM) of the system, which in this specific case is GM=5. However, it must be underlined that this gain margin can only indicate stability with respect to a simultaneous parameter change in all the control loops [108].

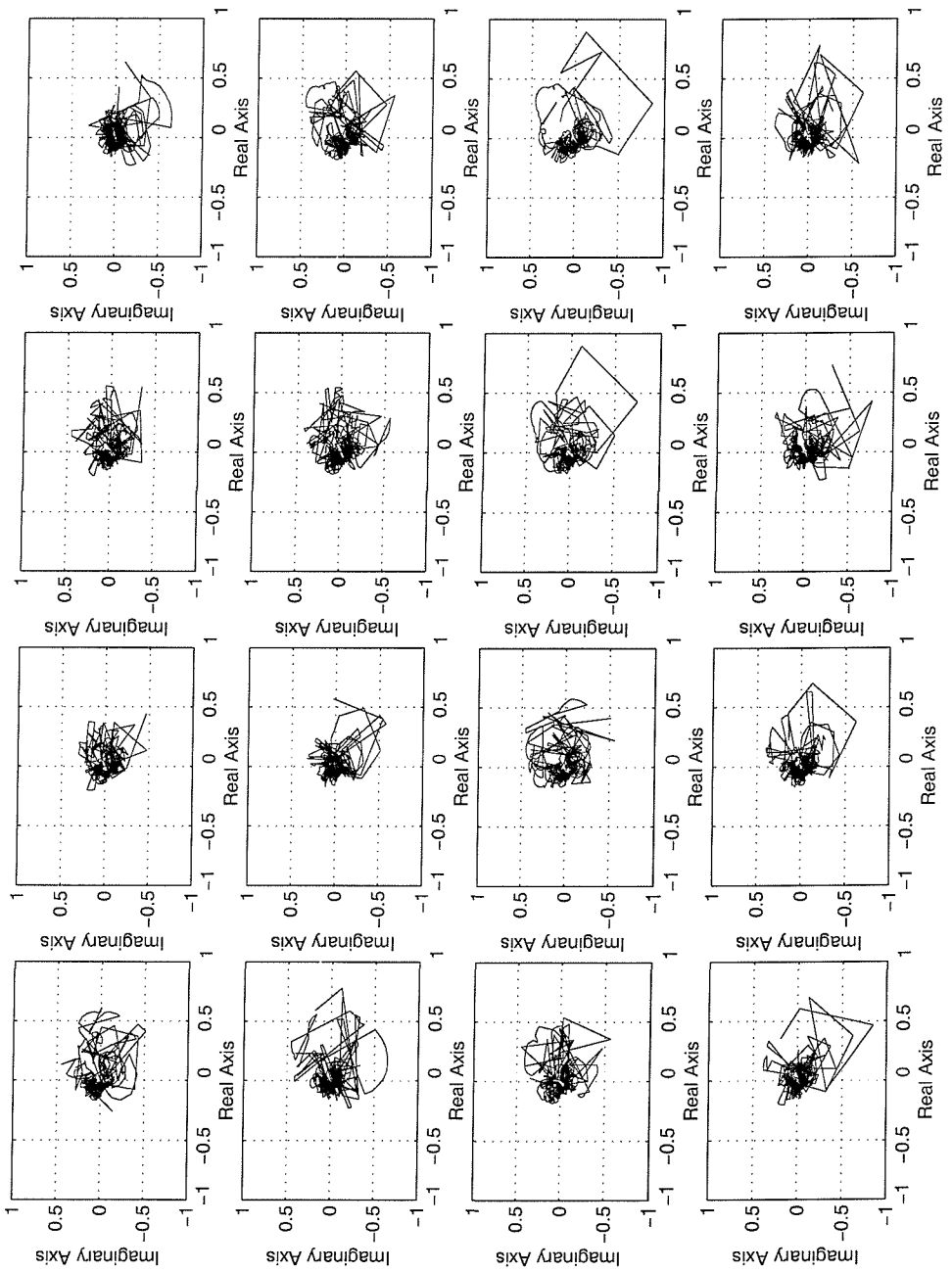

Figure 6.8: *Loci of the eigenvalues of the measured sensor–controller–actuator transfer matrix* $\mathbf{G}(j\omega)\mathbf{H}(j\omega)$.

6.4 On-line implementation with an acoustic primary source in the cavity

This section presents the results of the active control when the system is excited by the primary loudspeaker placed in the cavity. The vibration of the panel at the error sensor n. 7 is shown in Figures 6.9, 6.10 and 6.11 with reference to a frequency band 0 - 1, 0 - 2 and 0 - 5 kHz. The solid line shows the measured response of the plate without control while the faint line represents the response when all sixteen control units are working with a fixed feedback control gain chosen to guarantee stability and low spillover effects at higher frequencies.

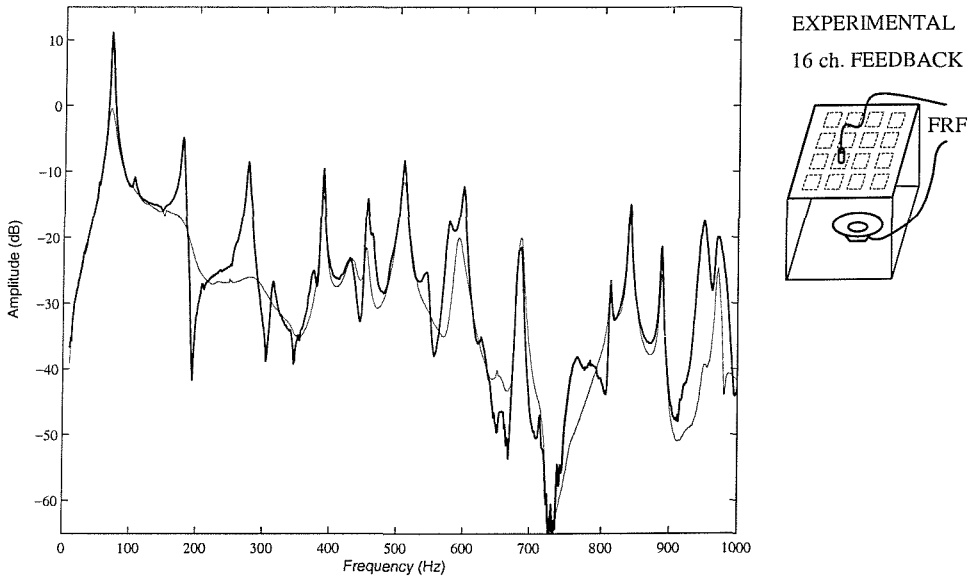

Figure 6.9: *Measured velocity at error sensor n. 7 per unit excitation of the loudspeaker in the cavity between 0-1 kHz without control (solid line) and when the sixteen decentralised feedback control systems with compensator are implemented (faint line).*

Compared to the experiment with only a single control unit, larger reductions of the vibration level are achieved up to 2 kHz. In particular, as shown in Figure 6.9, the two uncontrolled resonance frequencies at 70 and 178 Hz are now much more heavily damped, since the sixteen control units have provided the larger control strength necessary to damp the low frequency natural modes that are well coupled with the volumetric response of the acoustic cavity underneath the panel. However, even the sixteen decentralised control units still find it difficult to control the other resonance frequency, at 391, 519, 675, 814, 843 and 871 Hz. These are resonances generated by the strong coupling between a natural mode of the panel and a natural mode of the acoustic cavity that in order to be damped require even larger control authority than that provided by the sixteen units. However, except for these modes,

reductions from 5 to 20 dB are measured up to 1 kHz and reductions of about 6 dB are measured within a relatively larger number of narrow frequency bands at higher frequencies than in the case of a single active control unit.

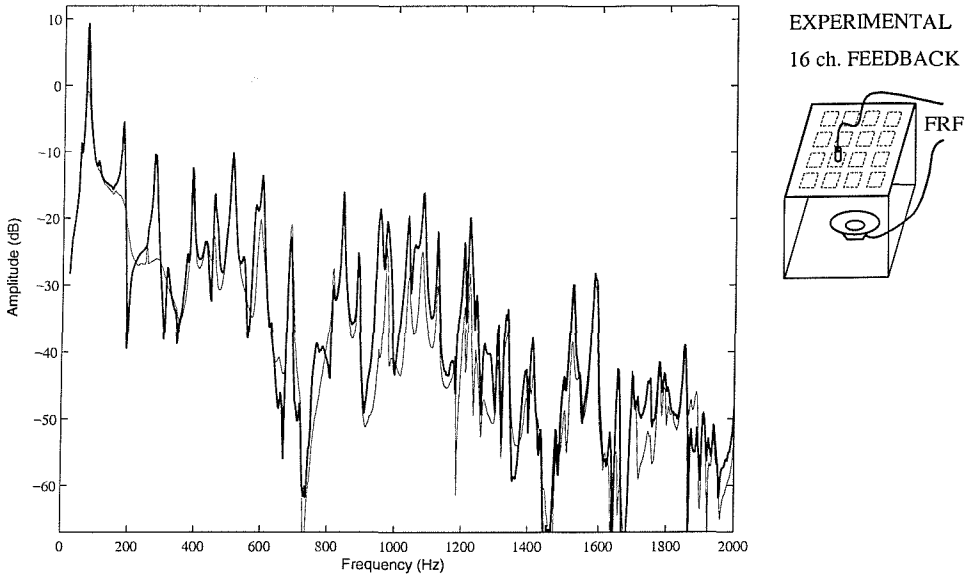

Figure 6.10: *Measured velocity at error sensor n. 7 per unit excitation of the loudspeaker in the cavity between 0-2 kHz without control (solid line) and when the sixteen decentralised feedback control systems with compensator are implemented (faint line).*

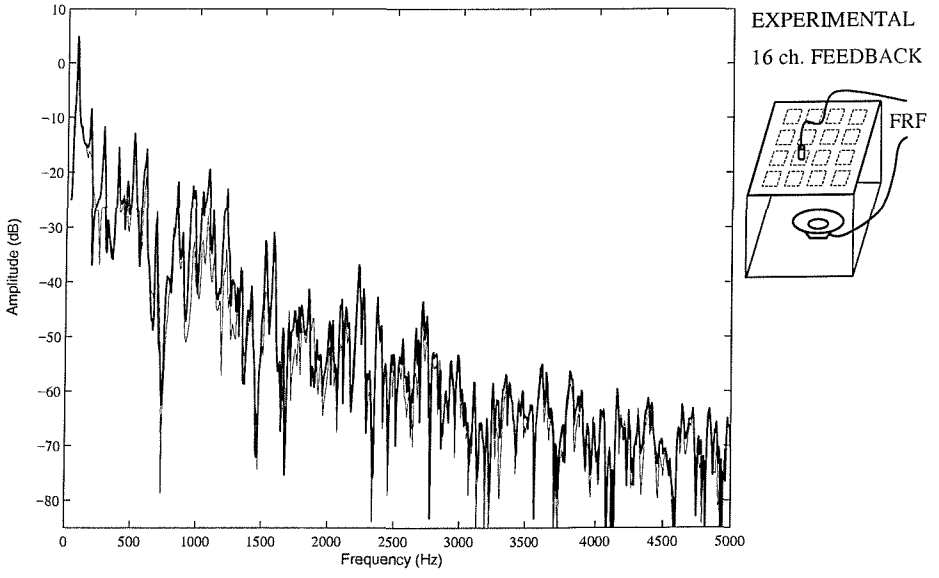

Figure 6.11: *Measured velocity at error sensor n. 7 per unit excitation of the loudspeaker in the cavity between 0-5 kHz without control (solid line) and when the sixteen decentralised feedback control systems with compensator are implemented (faint line).*

The plot in Figure 6.11, for measurements up to 5 kHz, highlights that, for the chosen control gains, there is very little control spillover effects. There is, however, a little enhancement of the response at the low frequency anti-resonance frequencies, as can be noticed in Figure 6.10.

An estimate of the panel sound transmission is shown in Figures 6.12, 6.13 and 6.14 for the frequency bands 0 - 1, 0 - 2 and 0 - 5 kHz. The solid line represents the measured sound pressure at about 0.5 m above the centre of the panel without control, while the faint line represents the measured sound pressure when all sixteen control units are working with the same feedback control gain used in the measurements shown in Figures 6.9-6.11.

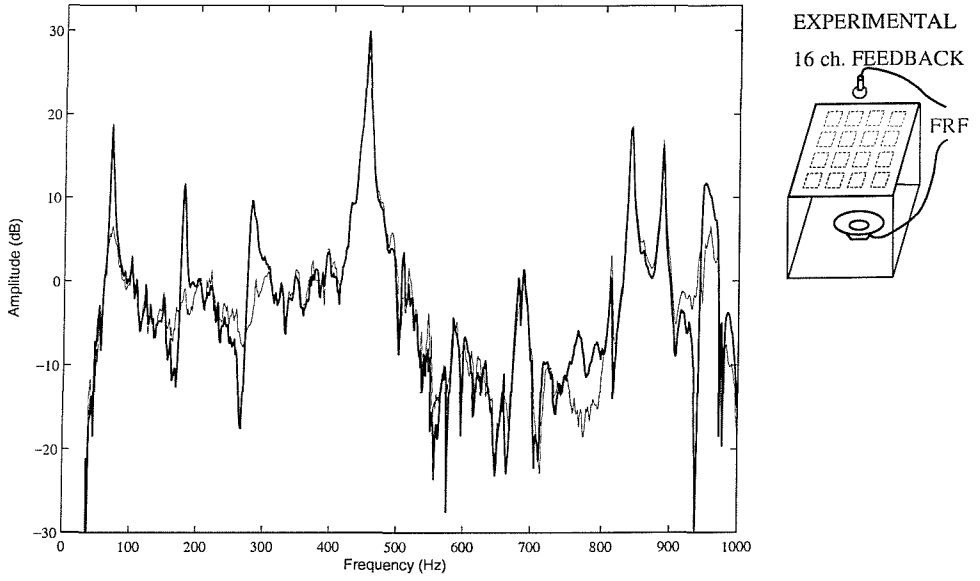

Figure 6.12: *Measured signal of the microphone per unit excitation of the loudspeaker in the cavity between 0-1 kHz without control (solid line) and when the sixteen decentralised feedback control systems with compensator are implemented (faint line).*

The plot in Figure 6.12 shows that the first three resonance frequencies are well controlled with reductions of the sound level that goes from a minimum of about 10 dB for the first mode, which is difficult to control because of the volumetric acoustic load of the cavity, to a maximum of about 15 dB for the other two modes. Between 400 and 1200 Hz there is little control effect. In particular, as anticipated with the theoretical study, the resonance frequency controlled by the first few cavity modes with natural frequencies at 387, 448, 595, 676 Hz can not be attenuated. However, again in agreement with the theoretical predictions, between 1200 and 1400 Hz reductions of about 20 dB are seen in the measured sound level at the microphone. The plot in Figure 6.14 does not show further reductions of the radiated sound at higher frequencies. Also, no problems of control spillover are found up to 5 kHz except at

relatively low frequencies in correspondence of anti-resonances. It is important to underline that these conclusions must only be considered to be indicative, since they refers to an estimate of the sound radiated taken with a single monitor microphone 0.5 m away from the panel, measured in the laboratory.

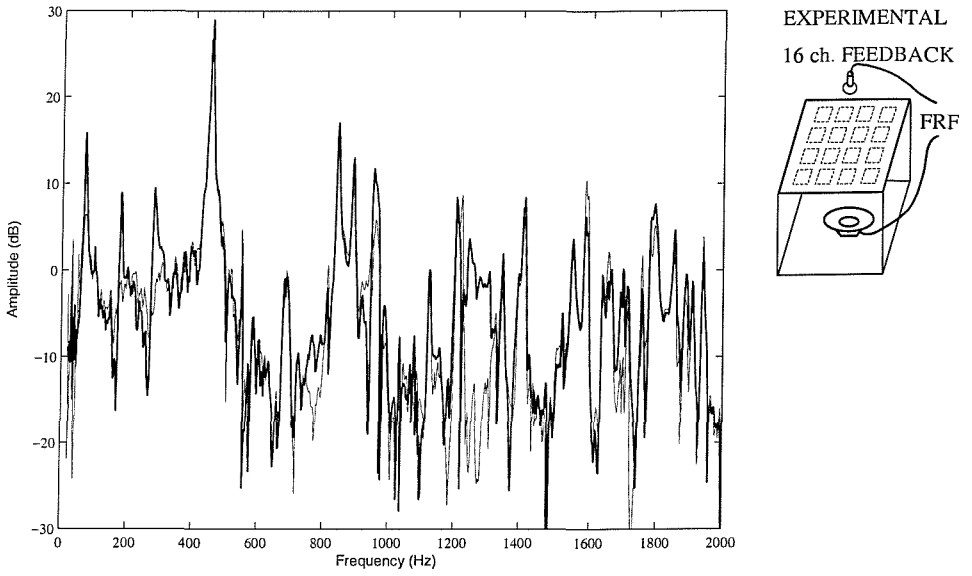

Figure 6.13: *Measured signal of the microphone per unit excitation of the loudspeaker in the cavity between 0-2 kHz without control (solid line) and when the sixteen decentralised feedback control systems with compensator are implemented (faint line).*

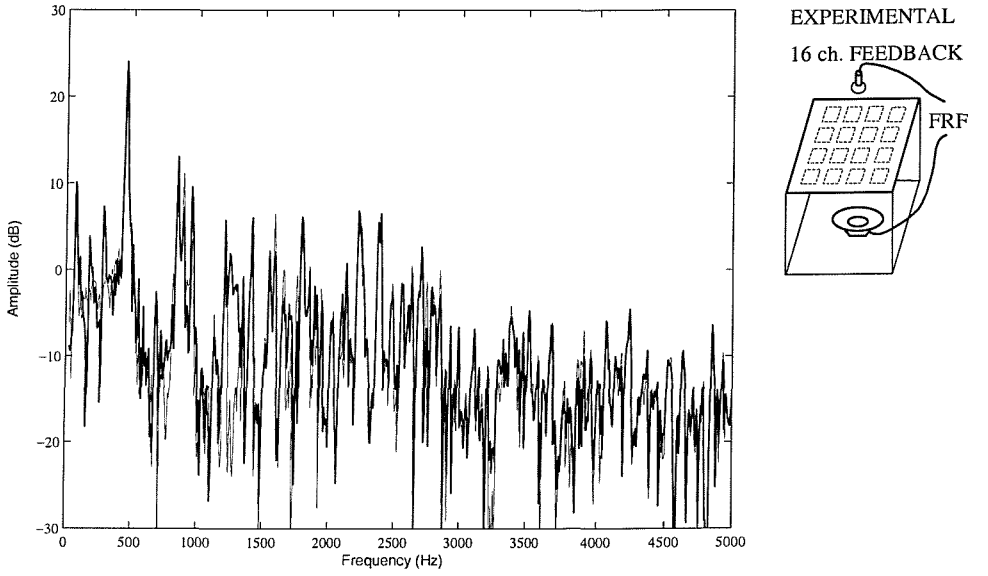

Figure 6.14: *Measured signal of the microphone per unit excitation of the loudspeaker in the cavity between 0-5 kHz without control (solid line) and when the sixteen decentralised feedback control systems with compensator are implemented (faint line).*

6.5 On-line implementation with a structural primary source on the panel

The active control tests when the system is excited by the primary shaker acting on the panel are now presented. The vibration of the panel at the error sensor n. 7 is shown in Figures 6.15, 6.16 and 6.17 with reference to a frequency band 0 - 1, 0 - 2 and 0 - 5 kHz. The solid line represents the measured response of the plate without control while the faint line represents the response when all sixteen control units are working with a fixed feedback control gain chosen to guarantee stability and low spillover effects at higher frequencies.

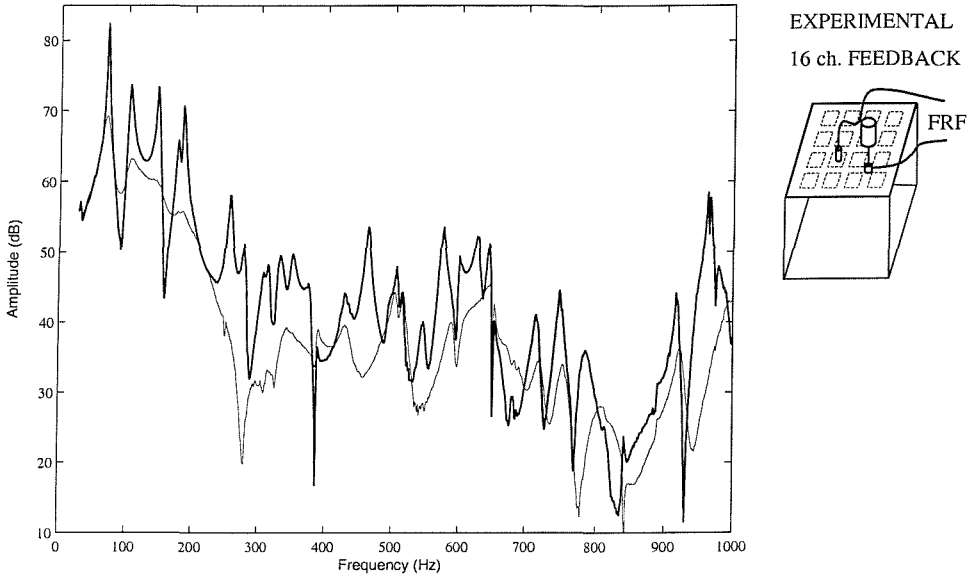

Figure 6.15: *Measured velocity at error sensor n. 7 per unit excitation of the shaker between 0-1 kHz without control (solid line) and when the sixteen decentralised feedback control systems with compensator are implemented (faint line).*

Comparing the measured vibration level at the error sensor n. 7 when either the primary loudspeaker or primary shaker excite the system, solid lines in Figures 6.9 and 6.15 respectively, it is clear that the shaker primary source excites many more low frequency modes of the panel. Indeed the frequency response function in Figure 6.15 is characterised by a relatively larger number of low frequency resonances than that in Figure 6.9. In this case the sixteen channel control system produces a larger damping effects than the single control unit, particularly for the resonances frequency at 70, 102, 183, 508 and 712 Hz where reductions from 10 to 20 dB are achieved. This is probably due to the fact that having sixteen decentralised control units distributed over the panel produces a relatively larger control strength for many low frequency modes.

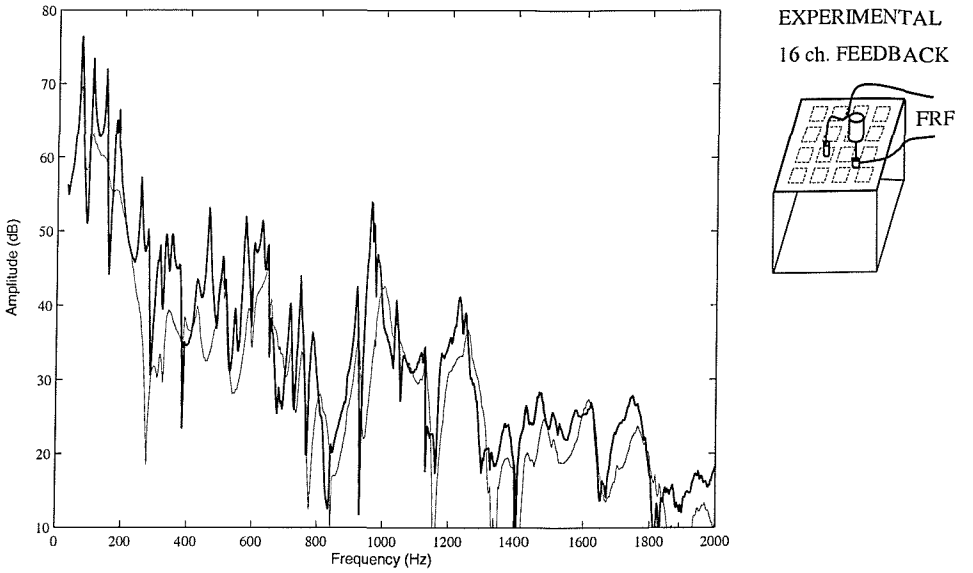

Figure 6.16: *Measured velocity at error sensor n. 7 per unit excitation of the shaker between 0-2 kHz without control (solid line) and when the sixteen decentralised feedback control systems with compensator are implemented (faint line).*

In general, reductions from 5 to 25 dB are measured between 0 and 1 kHz and reductions of about 8 dB are found for a wide frequency band between 1200 and 2000 Hz. Little control spillover effects are found at anti-resonance frequencies or at narrow frequency bands such as those around 680, 1010 and 1300 Hz. The plot in Figure 6.17 shows that the control system produces relatively good reductions of the vibration at the error sensor up to 3.8 kHz. Even at higher frequencies, for example around 4.8 kHz reductions of about 4 dB are still measured.

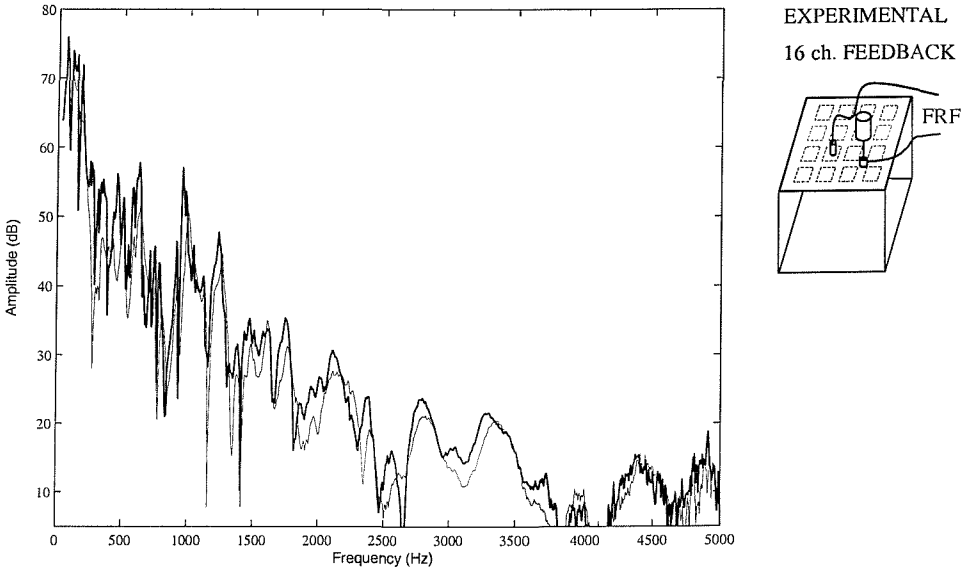

Figure 6.17: *Measured velocity at error sensor n. 7 per unit excitation of the shaker between 0-5 kHz without control (solid line) and when the sixteen decentralised feedback control systems with compensator are implemented (faint line).*

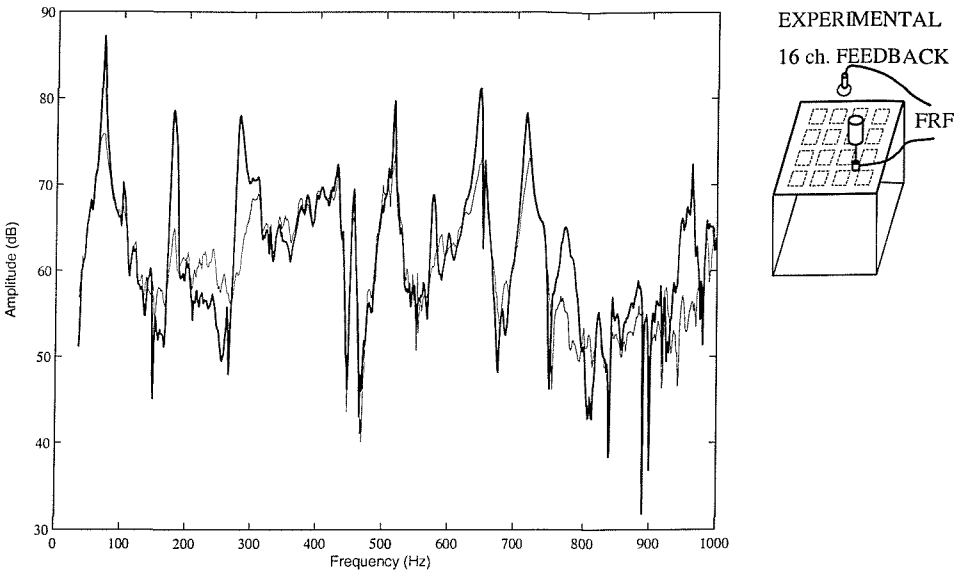

Figure 6.18: *Measured signal of the microphone per unit excitation of the shaker between 0-1 kHz without control (solid line) and when the sixteen decentralised feedback control systems with compensator are implemented (faint line).*

Similarly to what has been done for the acoustic primary disturbance, an estimate of the panel sound radiation due to the shaker excitation is shown in Figures 6.18, 6.19 and 6.20 with reference to a frequency band 0 - 1, 0 - 2 and 0 - 5 kHz. The solid line represents the measured sound pressure at about 0.5 m above the panel in correspondence to the centre of the panel itself without control while the faint line represents the measured sound pressure when all sixteen control units are working.

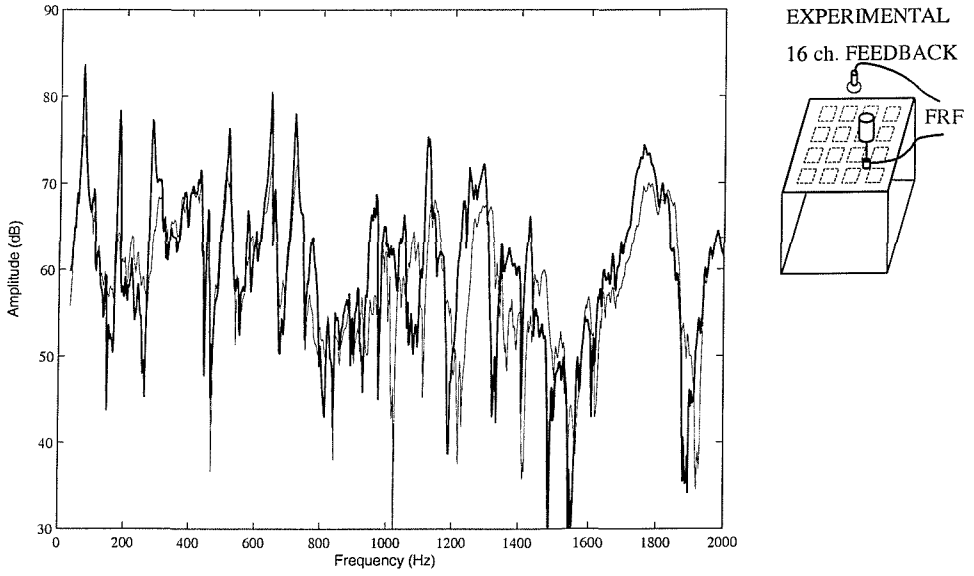

Figure 6.19: *Measured signal of the microphone per unit excitation of the shaker between 0-2 kHz without control (solid line) and when the sixteen decentralised feedback control systems with compensator are implemented (faint line).*

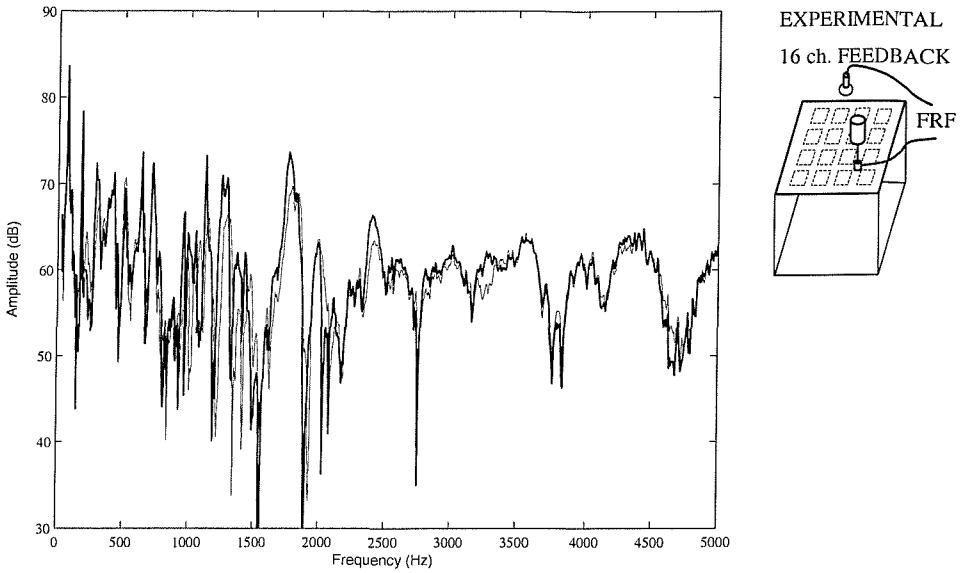

Figure 6.20: *Measured signal of the microphone per unit excitation of the shaker between 0-5 kHz without control (solid line) and when the sixteen decentralised feedback control systems with compensator are implemented (faint line).*

The plot in Figure 6.18 shows that the first three resonance frequencies are well controlled with reductions of the sound level that, in this case, goes from a minimum of about 10 dB for the first mode to a maximum of about 18 dB for the other two modes. Poor control effects are found in the frequency band between 350 and 550 Hz where there are three resonance frequencies which are dominated in the overall dynamics by the coupled panel-cavity modes. Even if the primary excitation is acting directly on the panel, the passive effect of the cavity underneath the panel plays an important role and limits the control of the sound radiation of the panel. Between 550 and 1400 Hz the control system reduces the sound radiation fairly well at the resonance frequencies, with reductions from 7 dB up to 15 dB. Beyond 1.4 kHz the measured frequency responses in Figures 6.19 and 6.20 do not show clear resonance frequencies. This is due to various phenomena, among whom the principal two are the raised panel and cavity modal density and the higher frequencies sound radiation mechanisms of the panel [21]. However, the control system still produces control effects of about 3 to 5 dB up to 3.5 kHz. Also, in these tests relatively little control spillover effects have been found. As commented for the previous case, however, the conclusions drawn in this section refers to an estimate of the sound radiated taken with a single monitor microphone 0.5 m away from the panel and further measurements are required to fully characterised the sound radiation, as reported in the next section.

7. EXPERIMENTAL ASSESSMENT OF THE DECENTRALISED CONTROL SYSTEM IN THE ANECHOIC CHAMBER

This chapter is concerned with the experimental assessment of the decentralised control system in the anechoic chamber. The total radiated/transmitted sound power has been calculated by a space integration of the sound intensity over a hypothetical surface that surrounds the noise source (vibrating panel) when no control system was applied and in presence of the decentralised feedback controller. A rectangular array of microphone positions has been used to measure the space average of the mean-square sound pressure over the measurement surface. The analysis has been performed using two different primary disturbances in a frequency range up to 5 kHz: first an acoustic source in the cavity (loudspeaker) and second, a structural point force on the panel (shaker).
In the first section, a description of the anechoic room and of the experimental measures has been reported. In the following two sections, the results of the experimental assessment of the decentralised control system have been reported respectively for the loudspeaker and point force primary excitation, for three frequency ranges: 0-1, 0-2 and 0-5 kHz. Moreover, a third octave analysis in a frequency range of 0-5 kHz of the sound radiated/transmitted from the plate is reported additionally to the narrow bands study.

7.1 Description of the experimental measures

An anechoic chamber is a room in which the walls, floor and ceiling are lined with sound absorbing material, usually foam or glass-fibre wedges. The lining prevents the reflection of sound from the room boundaries so that *free-field* conditions exist. A hemi-anechoic room has a reflective floor, but all other boundaries are highly absorbent. Both the anechoic and hemianechoic environments can be used to determine the sound power level of a source from sound pressure level measurements made in a free field or in a free field over a reflecting plane. In this specific application, the measure of the sound power level has been performed in the large anechoic chamber of the Institute of Sound and Vibration Research (ISVR), according to ISO 3744 for engineering-grade accuracy. Without wedges, the bare chamber is 9.15 × 9.15 × 7.32 m, volume 611 cubic metres. There are over 8000 non-flammable glass-

fibre cored wedges, extending 910 mm from the walls, floor and ceiling; the usable space between the wedges is 7.33 × 7.33 × 5.50 m, giving a usable volume of 295 cubic metres. A grid of removable floor panels can support a spread load of several tons with a minimum of interference with the anechoic nature of the chamber. An optional floor of varnished chipboard has been used for this measurement in order to obtain a hemianechoic environment (free field above a reflecting plane); free-field conditions exist in the chamber at frequencies above about 80 Hz.

The determination of the sound power level radiated in the hemianechoic room is based on the assumption that the reverberant field is negligible at the measurement positions, so that the acoustic intensity can be deduced from the free field pressure, and that the total radiated sound power is obtained by a space integration of the sound intensity over an hypothetical surface that surrounds the noise source. The measurement surface must be in the far field of the source. The space average of the mean square sound pressure over the measurement surface is determined by choosing an array of microphone positions over the surface. The number of microphone positions that are required depends on the accuracy required and the directivity of the source. According to the standard procedure, a parallelepiped measurement surface of about 20 m^2 of area has been selected in such a way to envelope the source (i.e. the vibrating panel clamped to the Perspex box) and the key microphone positions lie on that surface, as shown in Figure 7.1. All the geometric details of the microphone positions and of the geometric dimension of the surface are reported in Table 7.1.

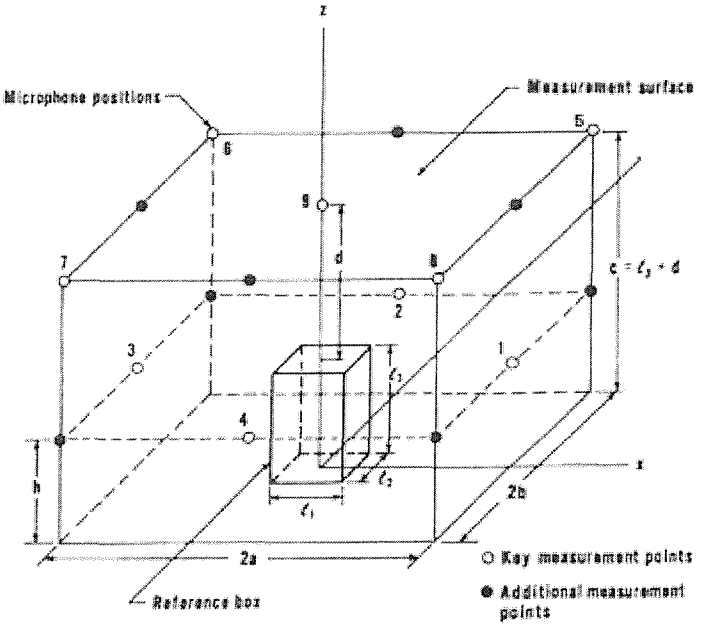

Figure 7.1: *Scheme of the microphone positions used in the anechoic chamber measurements of the sound pressure level according to ISO 3744.*

Table 7.1: *Co-ordinates of key measurement points and dimensions of the geometric parameters of the parallelepiped used in the anechoic chamber measurements.*

No.	*x*	*y*	*z*
1	a	0	h
2	0	b	h
3	-a	0	h
4	0	-b	h
5	a	b	c
6	-a	b	c
7	-a	-b	c
8	a	-b	c
9	0	0	c

parameter	**length** (m)
l_1	0.475
l_2	0.375
l_3	0.428
a	1.2375
b	1.1875
c	1.428
h	0.714
d	1

The sound power level radiated/transmitted by the plate has been measured using two different primary disturbances: the acoustic primary source in the cavity (loudspeaker) and the structural point force on the panel (shaker). In both the cases, a white noise signal has been used to drive the primary actuator for three frequency ranges: 0 - 1 kHz, 0 - 2 kHz and 0 - 5 kHz. The sound pressure level at the nine positions of the parallelepiped surface has been measured employing a single condenser microphone, positioned, in succession, at each measurement point. This approach has benefit in terms of efficiency, since the measurement system becomes more compact and the calibration procedure can be executed only once.

The experimental setup is represented in Figure 7.2. The test rig, consisting of the smart panel clamped on the Perspex box and equipped with the 16 sensor/actuator pairs and the two primary actuators (loudspeaker inside the cavity and shaker on the plate), has been placed in the middle of the anechoic chamber, on the reflecting floor. The microphone has been moved in each measurement position of the hypothetical surface using a boom. All the electronic devices (spectrum analyser, signal conditioner and filters, microphone amplifier and control system) have been arranged outside the test environment, in a control room adjacent to the anechoic chamber; a special wiring has been designed to connect the electronic system with the test rig through a small hole in the wall between the two rooms. In this way, the test environment is preserved from any additional noise sources that might affect the determination of the sound power level.

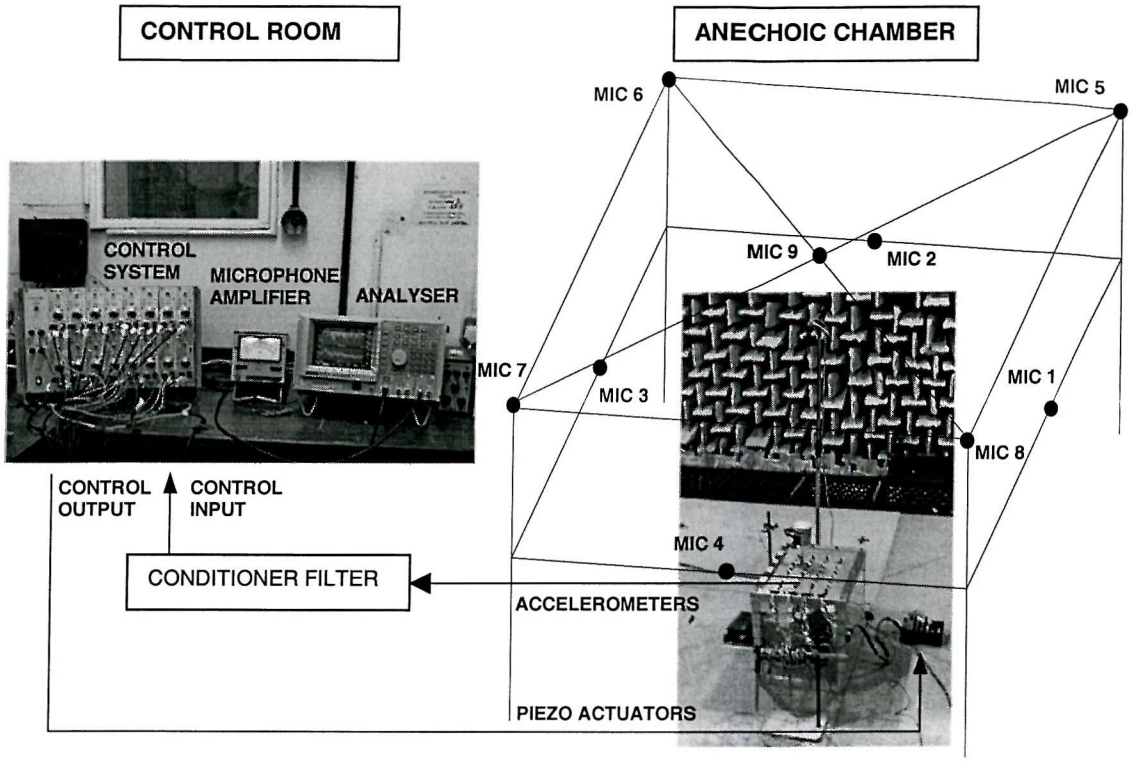

Figure 7.2: *Testing set up in the anechoic chamber for the measurement of the sound pressure radiated by the smart panel when excited either by the loudspeaker in the Plexiglas box or by the shaker mounted on the panel.*

An average sound pressure level over the measurement surface, $\overline{L}_{pm}$, can be calculated from the measured sound pressure levels L_{pi} resulting from the ith measurement, in decibels, by using the following equation:

$$\overline{L}_{pm} = 10\log_{10}\left(\frac{1}{n}\sum_{i=1}^{n}10^{L_{pi}/10}\right), \tag{7.1}$$

where N is the total number of measurement (in this specific case N=9).

In order to obtain the surface sound pressure level, the value of $\overline{L}_{pm}$ should be corrected by the environmental correction factor K, which however has been neglected considering the high quality of the anechoic room test environment.

Therefore, the sound power level, L_W, characterizing the noise emitted by the source can be calculated from this equation:

$$L_W = \overline{L}_{pm} + 10\log_{10} S\ , \tag{7.2}$$

where S=19.37 m^2 is the total area of parallelepiped measurement surface.

The approach used in this experimental activity was to measure a set of frequency response functions between the microphone signal at each position and the primary disturbance (loudspeaker or shaker) without control and in presence of the decentralised feedback controller for the three different frequency ranges: 0 - 1 kHz, 0 - 2 kHz and 0 - 5 kHz. Thus, for both the case of acoustic excitation and force excitation of the system, it has been possible to calculate the overall sound pressure level and the sound power level radiated/transmitted by the panel using Equations 7.1 and 7.2 respectively, before and after the control action.

In the next two sections, the main results obtained in the experimental testing of the control system in the anechoic chamber are discussed with respect to the two type of primary excitation. In addition to this narrow band frequency response study, a third octave analysis of the sound power radiation has been carried out for a frequency range of 0 – 5 kHz (2 decades with centre band frequency from 63 Hz to 4000 Hz).

7.2 On-line implementation with an acoustic primary source in the cavity

In Figures 7.3 and 7.4 the results of the narrow band analysis in the frequency range of 0–1 kHz are reported. The frequency response functions between each sound pressure measured by the nine microphones and the excitation of the primary loudspeaker source are plotted in Figure 7.3 for both the cases of no control system applied (solid line) and decentralised controller turned on (faint line). The sound power level calculated from the previous measurements is then reported in Figure 7.4, using the same notation for the solid and the faint lines. This plot also shows the sound power level due to the flanking sound radiation through the side walls of the Perspex box (dashed line). This result has been obtained by replacing the smart panel with a very rigid block of metal, about 4 cm thick, whose low frequency sound radiation is negligible, as explained in Section 3.7.

From these figures it can be seen that the first three resonance frequencies are well controlled with reductions of the sound level that goes from a minimum of about 8 dB for the third mode, to a maximum of about 13 dB for the other two modes. The sixteen control units provides the control strength to damp the first three resonant modes of the panel which, as highlighted in the theoretical study, are strongly coupled to the volumetric excitation of the cavity underneath the panel. Between 350 and 1000 Hz there is little control effect except for the resonance at about 600 Hz. In particular, the resonance frequency controlled by the first

few cavity modes with natural frequencies at 448, 499, 595, 676 Hz can not be controlled, as anticipated in the theoretical study. Moreover, the flanking radiation of sound through the walls of the box affects the performance of the control system at three resonance frequencies,

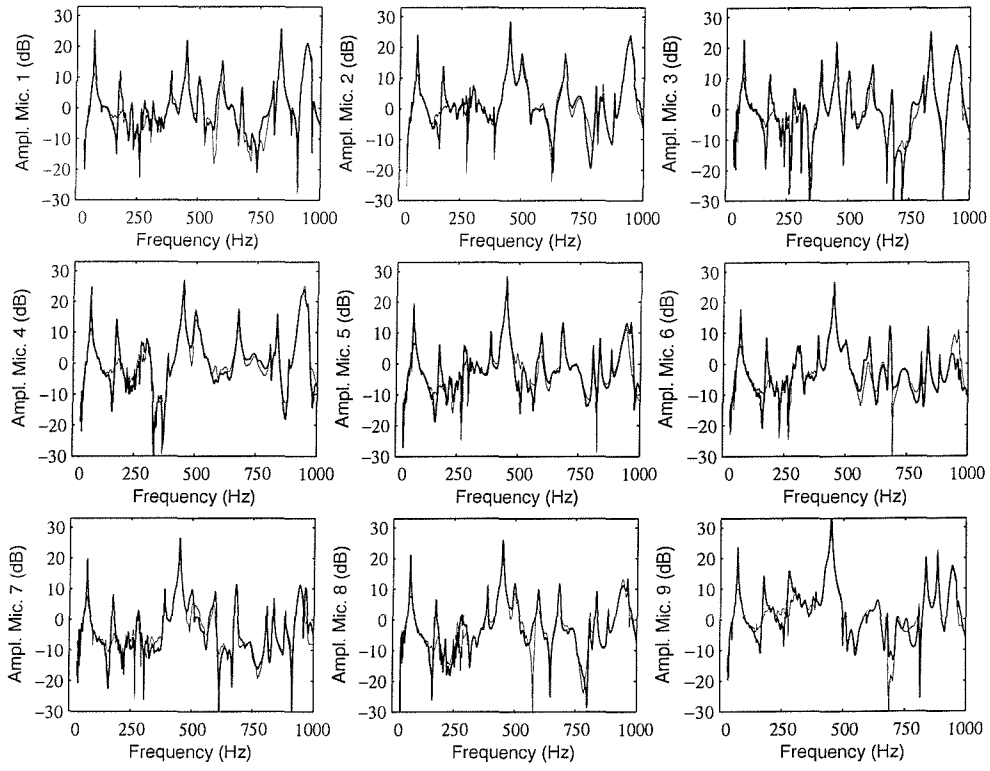

Figure 7.3: *Frequency response functions between each of the nine microphones and the excitation of the primary loudspeaker source (0–1 kHz). Sound pressure without (solid line) and with decentralised control (faint line).*

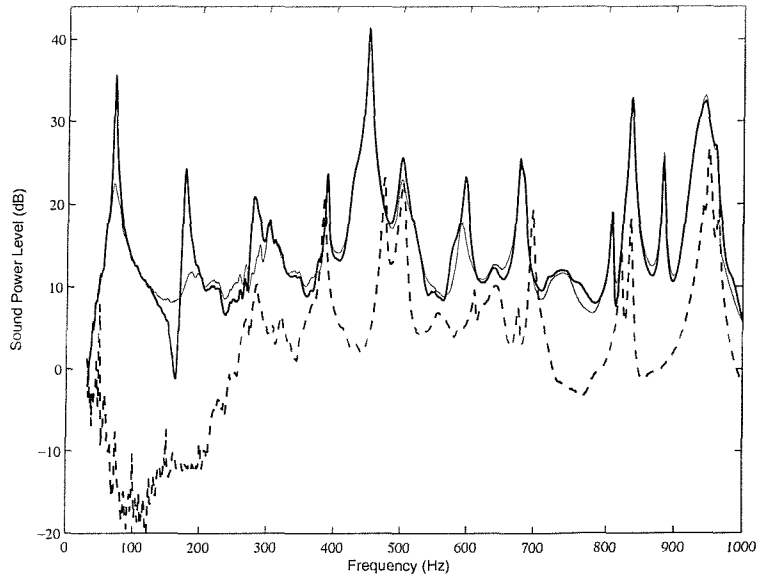

Figure 7.4: *Sound power level per unit excitation of the primary loudspeaker source (0–1 kHz), without (solid line) and with decentralised control system (faint line). The sound power level due to the flanking sound radiation through the side walls of the Perspex box is also shown (dashed line).*

at 387, 470 and 499 Hz. Due to these unfavourable factors, and in particular the failure to control the dominant resonance at about 450 Hz, the overall reduction of the sound transmission through the panel in the frequency range of 0-1 kHz is only 1 dB.

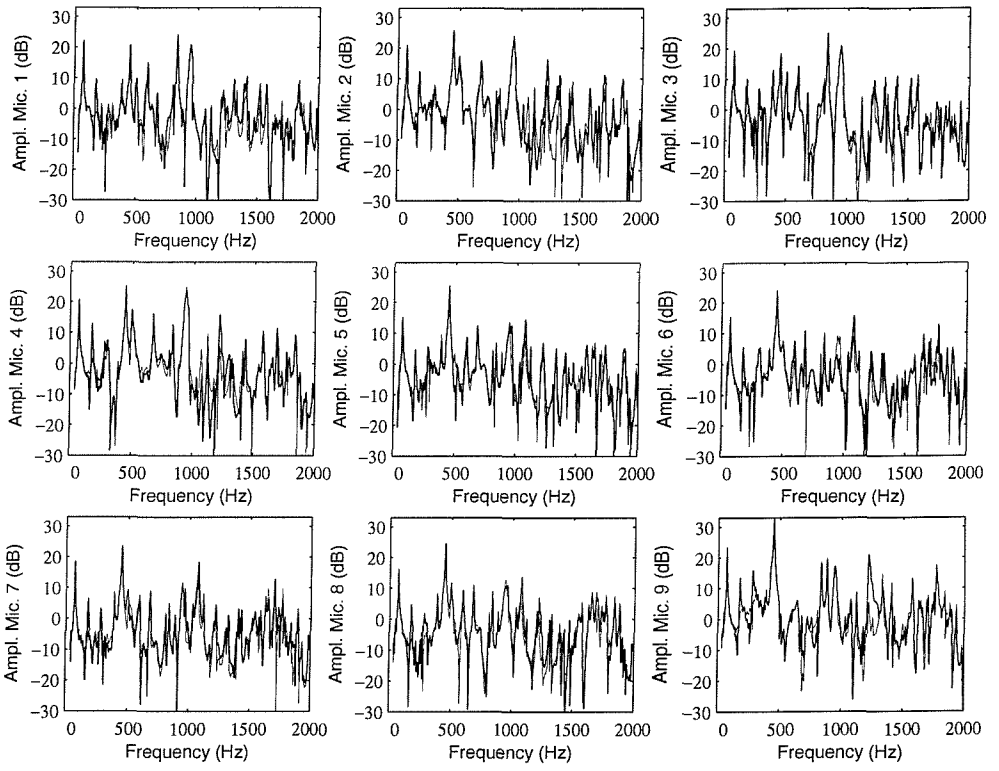

Figure 7.5: *Frequency response functions between each of the nine microphones and the excitation of the primary loudspeaker source (0–2 kHz). Sound pressure without (solid line) and with decentralised control (faint line).*

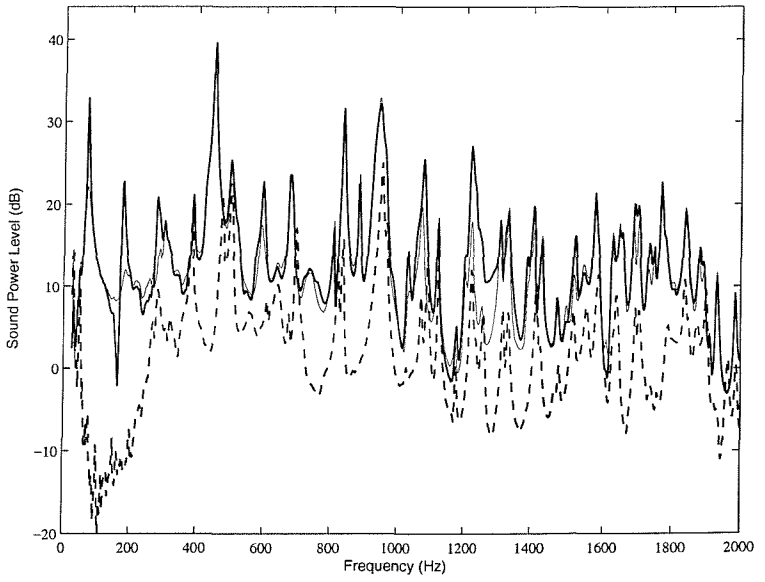

Figure 7.6: *Sound power level per unit excitation of the primary loudspeaker source (0–2 kHz), without (solid line) and with decentralised control system (faint line). The sound power level due to the flanking sound radiation through the side walls of the Perspex box is also shown (dashed line).*

The results concerned with the frequency ranges of 0-2 and 0-5 kHz are reported in Figures 7.5, 7.6, 7.7 and 7.8, according to the same scheme used for the previous analysis. As shown in the Figure 7.6, once more in agreement with the theoretical predictions, between 1200 and

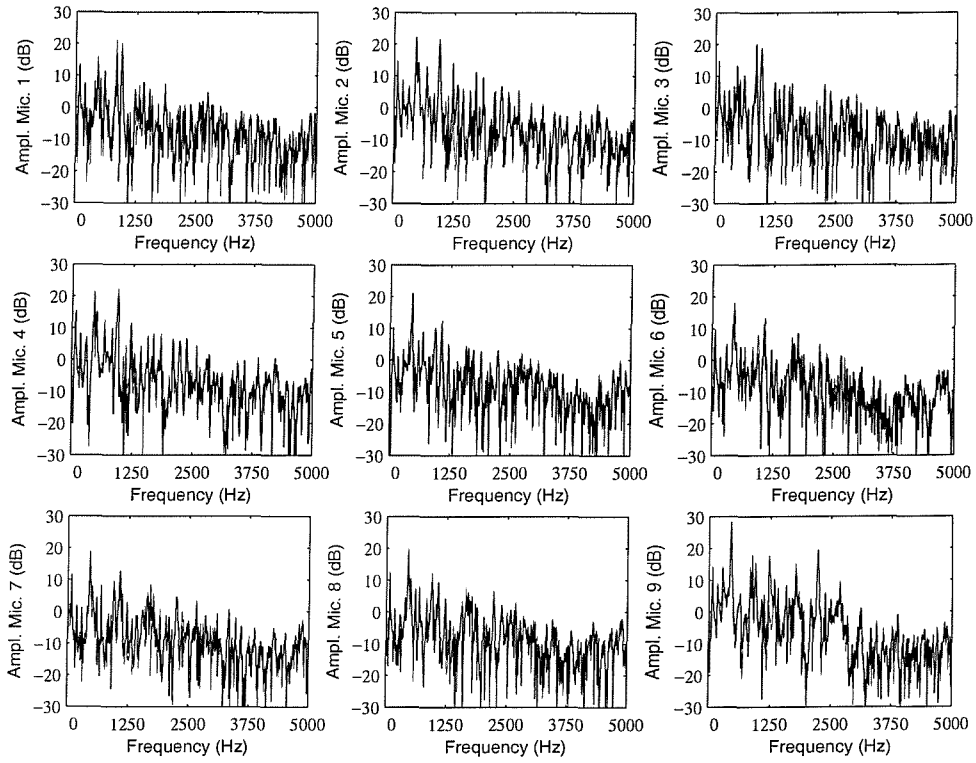

Figure 7.7: *Frequency response functions between each of the nine microphones and the excitation of the primary loudspeaker source (0–5 kHz). Sound pressure without (solid line) and with decentralised control (faint line).*

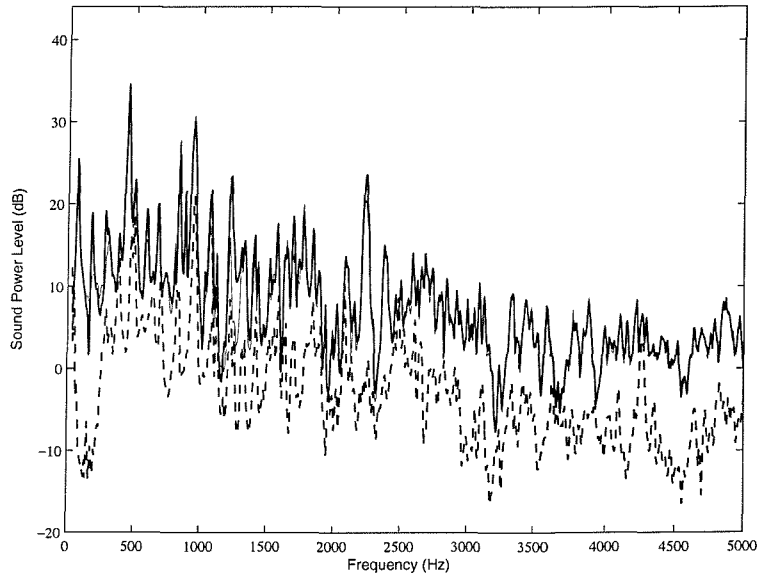

Figure 7.8: *Sound power level per unit excitation of the primary loudspeaker source (0–5 kHz), without (solid line) and with decentralised control system (faint line). The sound power level due to the flanking sound radiation through the side walls of the Perspex box is also shown (dashed line).*

1400 Hz reductions of about 10 dB of the measured sound power level are registered. No further reductions of the radiated sound at higher frequencies are shown. Very little control spillover effects have been found and in most cases they correspond to anti-resonance frequencies as one would expect with active damping.

A further analysis of the sound power level radiated by the plate in presence of the acoustic primary source in the cavity has been carried out in terms of third octave bands, for a frequency range of 0-5 kHz. The same approach used for the narrow band analysis has been adopted except for the primary disturbance signal that in this case was a pink noise filtered at 5 kHz. Figure 7.9 shows the bar chart of the total radiated sound power in third octave bands between 0 and 5 kHz. The white and grey columns represent respectively the sound power radiated without and with control system turned on per unit loudspeaker excitation in the cavity. The black column represents the total radiated sound power through the side walls of the Perspex box per unit loudspeaker excitation in the cavity. Frequency averaged reductions of about 6 dB are found in correspondence to the third octave bands at 63, 80 and 1250 Hz. Smaller reductions are measured for the other third octave bands. The overall reduction of the sound transmission through the panel in the frequency range of 0-5 kHz is 2.5 dB.

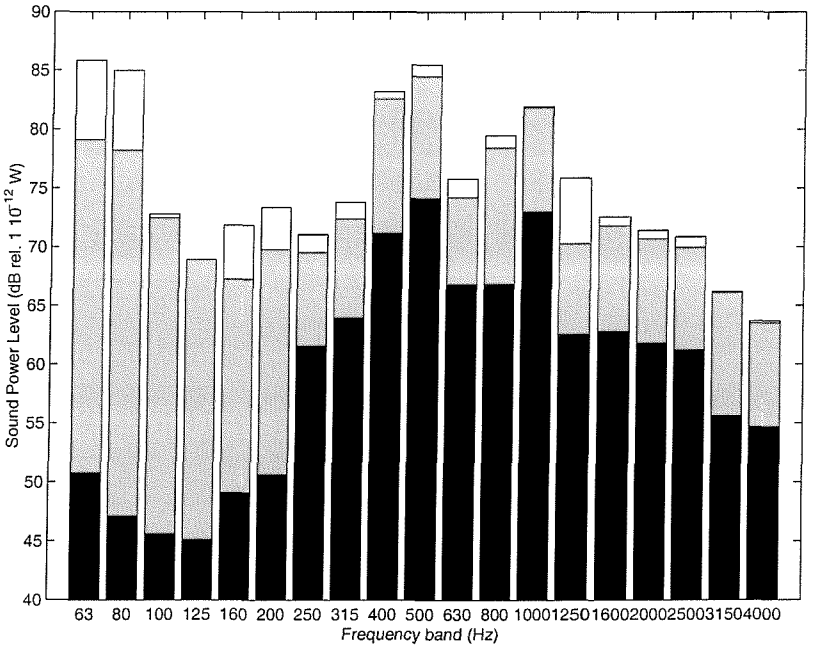

Figure 7.9: *Total radiated sound power in third octave bands between 0 and 5 kHz for pink noise loudspeaker excitation without control (white columns) and with decentralised feedback control (grey columns). Total sound power radiated through the side walls of the Perspex box (black columns).*

7.3 On-line implementation with a structural primary source on the panel

Similarly to what has been done for the acoustic primary source in the cavity, an analysis of the sound radiated by the plate in presence of a structural point force disturbance has been carried out either in terms of narrow band frequency response functions between the sound pressure measured by the nine microphones and the excitation of the primary source (shaker) in the frequency ranges 0–1, 0–2 and 0-5 kHz or in terms of the estimated sound power level plotted in third octave bands for a frequency range of 0–5 kHz (2 decades with centre band frequency from 63 Hz to 4000 Hz).

In Figure 7.10 and 7.11 the results of the narrow band analysis in the frequency range of 0–1 kHz are reported. The frequency response functions between each sound pressure measured by the nine microphones and the excitation of the primary shaker source are plotted in Figure 7.10 for both the cases of no control system applied (solid line) and decentralised controller turned on (faint line). The sound power level calculated from these measurements is then reported in Figure 7.11, using the same notation for the solid and the faint lines.

Comparing the plots in Figures 7.4 and 7.11 it can be noticed that the latter ones are characterised by a larger number of resonances at relatively low frequencies. This is because the shaker excites nearly all the structural modes of the panel while only the structural modes of the panel that are well coupled to the acoustic cavity underneath it are excited by the loudspeaker. As a result for example the sound radiation of the panel below 300 Hz is characterised either by three or five resonances depending whether the testing system is excited by the loudspeaker or by the shaker respectively. In contrast at higher frequencies above 1 kHz it is the plot in Figure 7.6 that is characterised by a relatively larger number of resonances with respect to that in Figure 7.13. This is because above 400 Hz the response of the cavity is characterised by cavity modes whose number grows rapidly with frequency. Thus, when the panel is excited by the acoustic field in the cavity a large number of modes are found in the sound radiation which are due to the cavity modes. In contrast, when the panel is exited directly by a point force very little effects of the cavity modes are seen in the radiated sound power.

The plot in Figure 7.11 shows that the first five resonance frequencies are well controlled with reductions of the radiated sound power that, in this case, goes from a minimum of about 12 dB for the first and fifth modes to a maximum of about 18 dB for the other three modes. The overall reduction of sound radiated in the frequency range of 0-1 kHz is 3.9 dB.

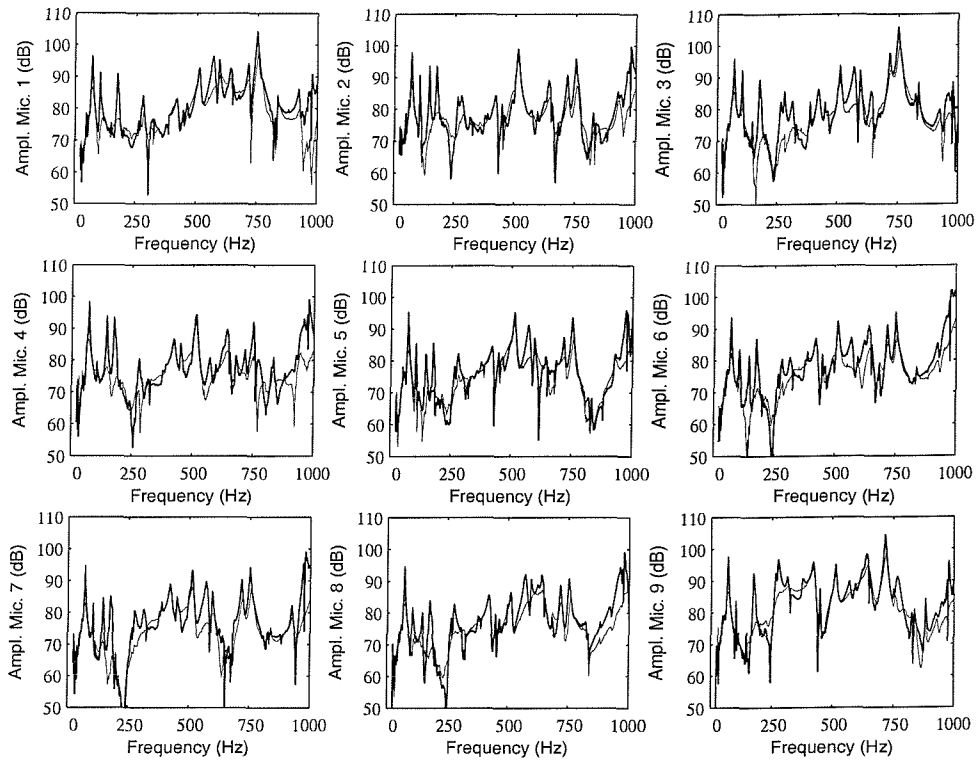

Figure 7.10: *Frequency response functions between each of the nine microphones and the excitation of the primary shaker source (0–1 kHz). Sound pressure without (solid line) and with decentralised control (faint line).*

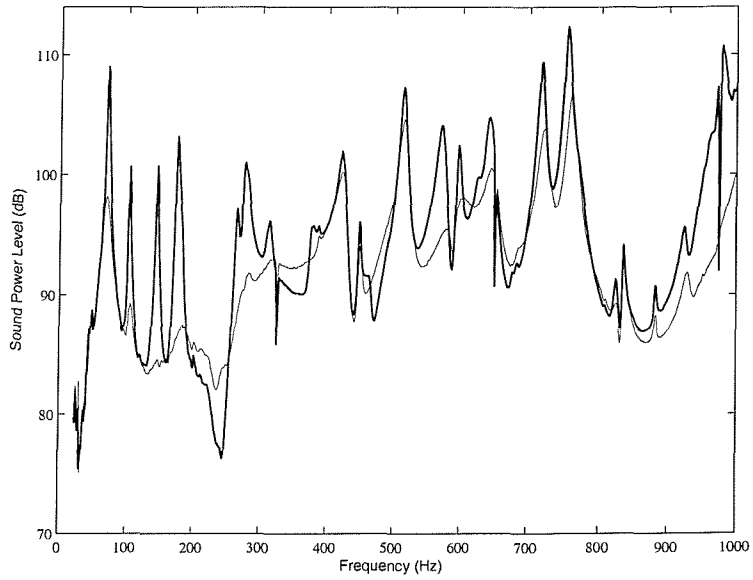

Figure 7.11: *Sound power level per unit excitation of the primary shaker source (0–1 kHz), without (solid line) and with decentralised control system (faint line).*

Significant control effects are also found in the frequency bands between 350 and 1300 Hz and between 1600 and 1800 Hz with reductions of the sound power level of the order of 3 to 8 dB (Figures 7.12 and 7.13). In this case the acoustic cavity underneath the panel produces only a passive loading effect which is not characterized by strong coupling effects between

the cavity and panel natural modes and thus smaller control strength is necessary to produce the wanted active damping on the panel.

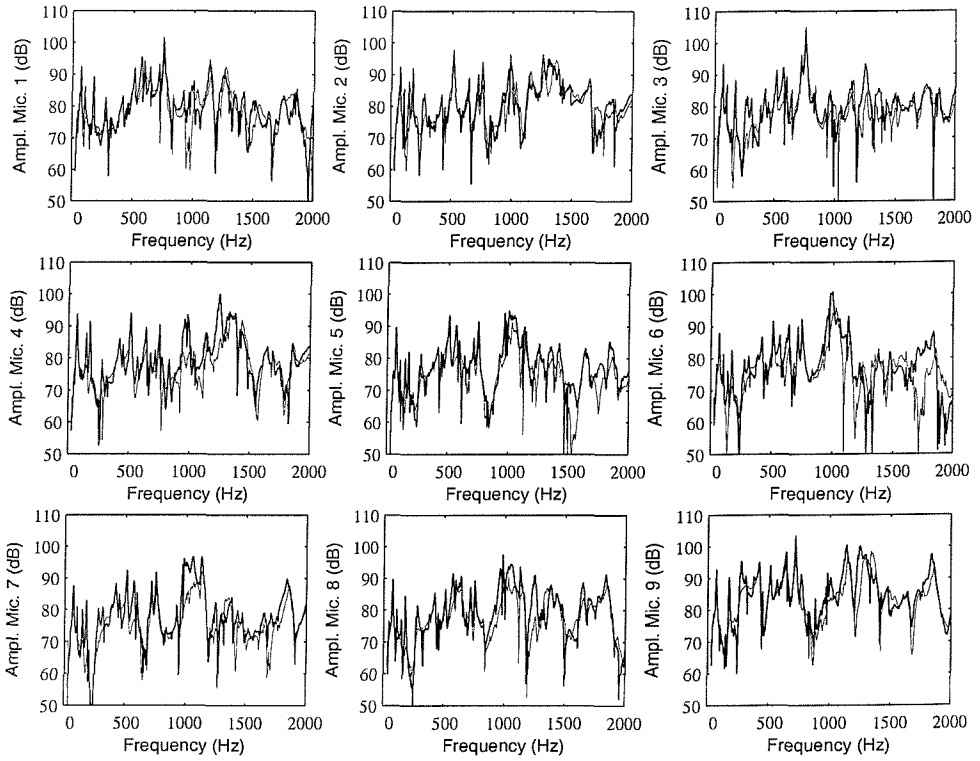

Figure 7.12: *Frequency response functions between each of the nine microphones and the excitation of the primary shaker source (0–2 kHz). Sound pressure without (solid line) and with decentralised control (faint line).*

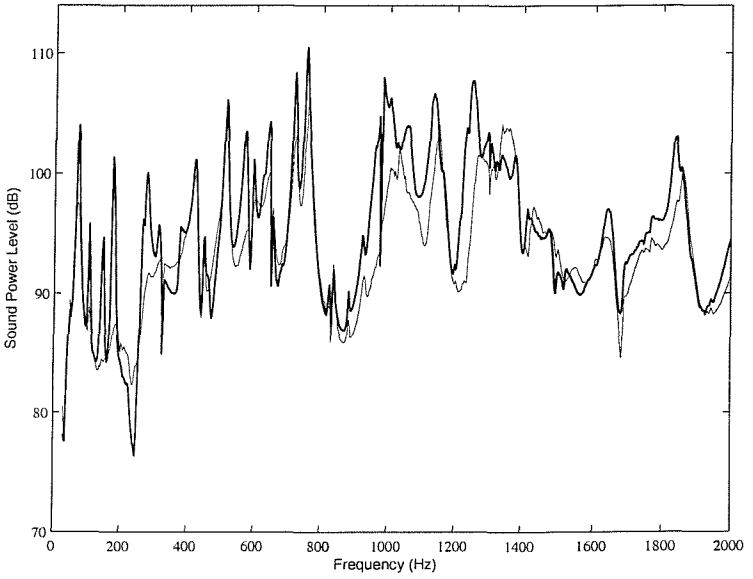

Figure 7.13: *Sound power level per unit excitation of the primary shaker source (0–2 kHz), without (solid line) and with decentralised control system (faint line).*

Also in these tests relatively little control spillover effects have been found (see Figure 7.15). In most cases they occur at antiresonance frequencies except in the frequency band between 1300 and 1350 Hz where a relatively high enhancement of the sound power level, about 3 dB, has been measured.

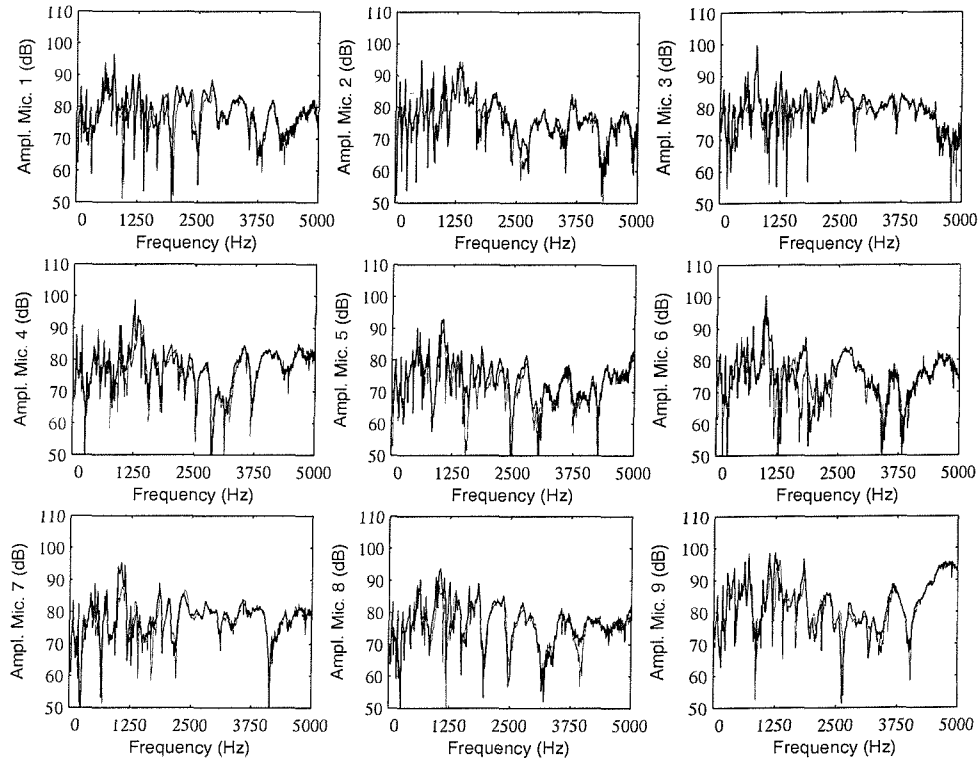

Figure 7.14: *Frequency response functions between each of the nine microphones and the excitation of the primary shaker source (0–5 kHz). Sound pressure without (solid line) and with decentralised control (faint line).*

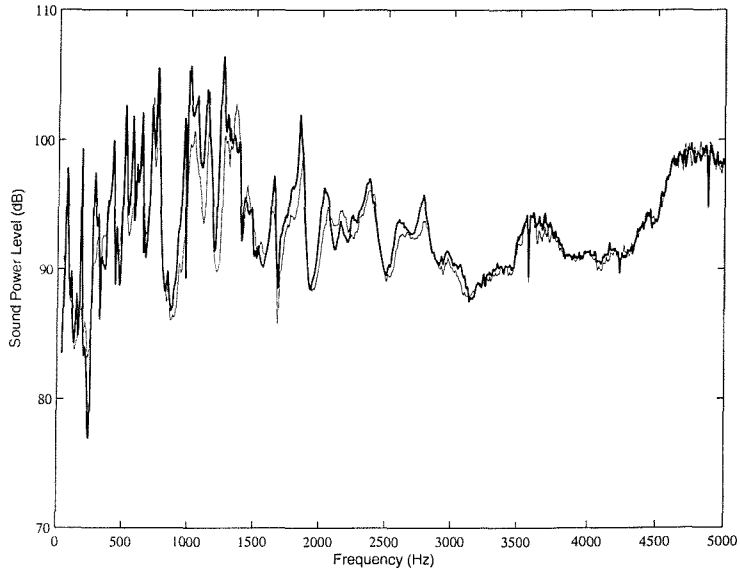

Figure 7.15: *Sound power level per unit excitation of the primary shaker source (0–5 kHz), without (solid line) and with decentralised control system (faint line).*

Figure 7.16 shows the bar chart of the total radiated sound power in third octave bands between 0 and 5 kHz. The white and grey columns represent the sound power radiated without and with control system turned on per unit loudspeaker excitation in the cavity. Comparing this plot with that in Figure 7.9 it is evident that much larger reductions of the radiated sound power are measured for all frequency bands. In this case reductions of the sound radiation are measured in correspondence of all third octave bands and there are at least seven bands, at 63, 80, 125, 160, 250, 315, 400, 1000 Hz, with reductions of about 5 to 8 dB. The overall reduction of the sound transmission through the panel in the frequency range of 0-5 kHz is 4.4 dB.

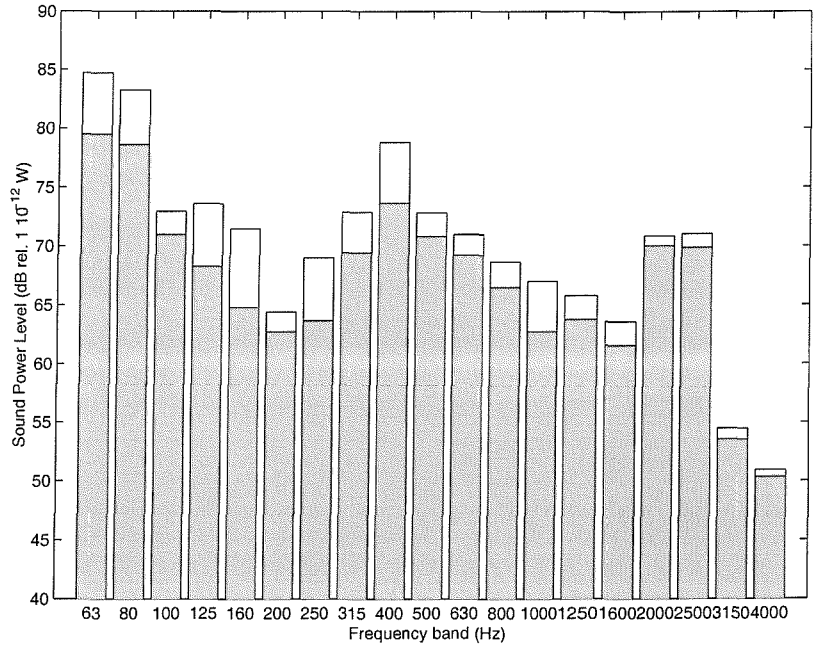

Figure 7.16: *Total radiated sound power in third octave bands between 0 and 5 kHz for pink noise shaker excitation without control (white columns) and with decentralised feedback control (grey columns).*

8. EXPERIMENTAL ASSESSMENT OF THE DECENTRALISED CONTROL SYSTEM USING A LASER VIBROMETER

This chapter is concerned with the experimental assessment of the decentralised control system using laser vibrometer. The panel surface of the rig under study has been scanned with a Laser Doppler Vibrometer (LDV) in order to measure the normal velocity of the plate due to the primary excitation (loudspeaker in the cavity or point force on the panel) before and after applying the decentralised control system.

In the first section, a description of the laser Doppler principles and of the experimental measures has been reported. In the following two sections, the results of the experimental assessment of the decentralised control system have been reported respectively for the loudspeaker and point force primary excitation, in a frequency range of 0-1 kHz.

8.1 Description of the experimental measures

A Laser Doppler Vibrometer (LDV) is based on the principle of the detection of the Doppler shift of coherent laser light that is scattered from a small area of the test object. The object scatters or reflects light from the laser beam and the Doppler frequency shift is used to measure the component of velocity, which lies along the axis of the laser beam. More details of the LDV and its functioning are reported in Appendix C.

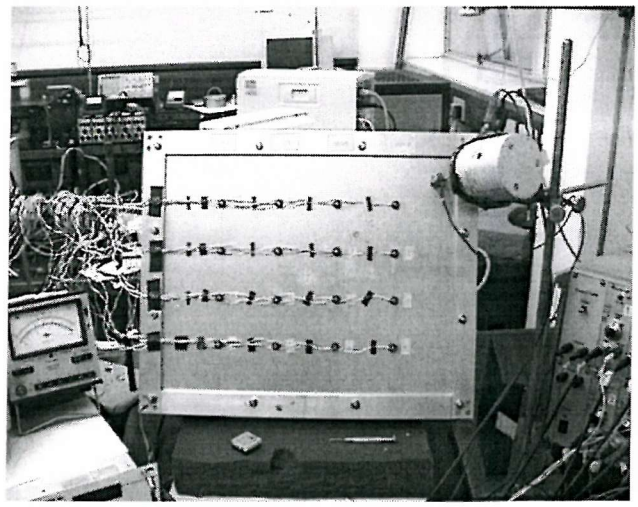

Figure 8.1: *View of the test rig (smart panel & Perspex box) from the laser camera.*

In this specific application, the control system performance has been verified experimentally by scanning the panel in correspondence of a grid of points with the laser vibrometer, both before and after control, for two different primary disturbances: acoustic primary source in the cavity (loudspeaker) and structural primary force on the panel (shaker). Figure 8.1 represents the view of the test rig (smart panel and Perspex box) from the laser camera: the panel surface has been vertically positioned in such a way to facilitate the scanning of the laser within the 40^{o}x40^{o} field of view. The distance between the laser and the panel surface was about 1.5 m.

The system has been excited by the loudspeaker or by the shaker with a white noise primary signal, provided by the LDV processing system, in a frequency range of 0-1 kHz. A set of frequency response functions between the velocity at each grid point and the primary disturbance has been automatically measured by means of the Data Management System (DMS) of the vibrometer in absence or in presence of the decentralised controller. This set of data has been processed by the laser software system in order to obtain plots of the frequency response functions in specific points of the plate, plots of the overall vibration level of the plate, 2D images of the velocity distribution on the panel before and after control, as reported in the following two sections for the different types of excitations.

8.2 On-line implementation with an acoustic primary source in the cavity

In order to measure the vibration level of the plate excited by the acoustic primary source in the cavity (loudspeaker), a grid of 133 points to be scanned has been defined on the plate

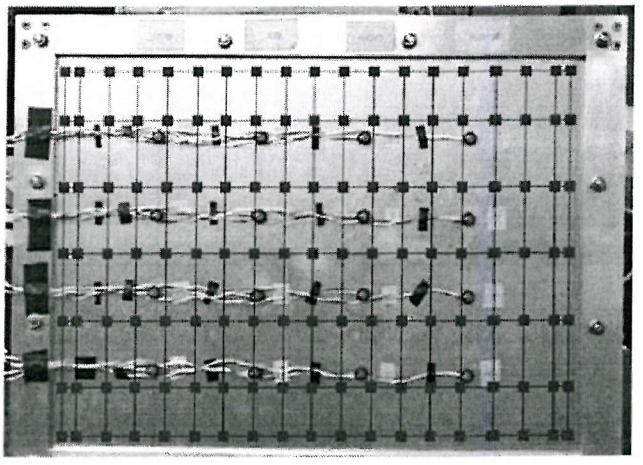

Figure 8.2: *Illustration of the panel surface overlapped with the grid of desired measurement points (133) to be scanned with the laser vibrometer. The system is excited by the loudspeaker primary source in presence or not of the decentralised feedback controller.*

surface, covering the whole vibration area of the structure (see Figure 8.2). As previously explained, a random signal in a frequency range of 0-1 kHz has been used to drive the loudspeaker and the frequency response functions between the velocity at each point of the grid per unit of excitation of the loudspeaker have been measured by means of the laser vibrometer in absence and in presence of the decentralised control system.

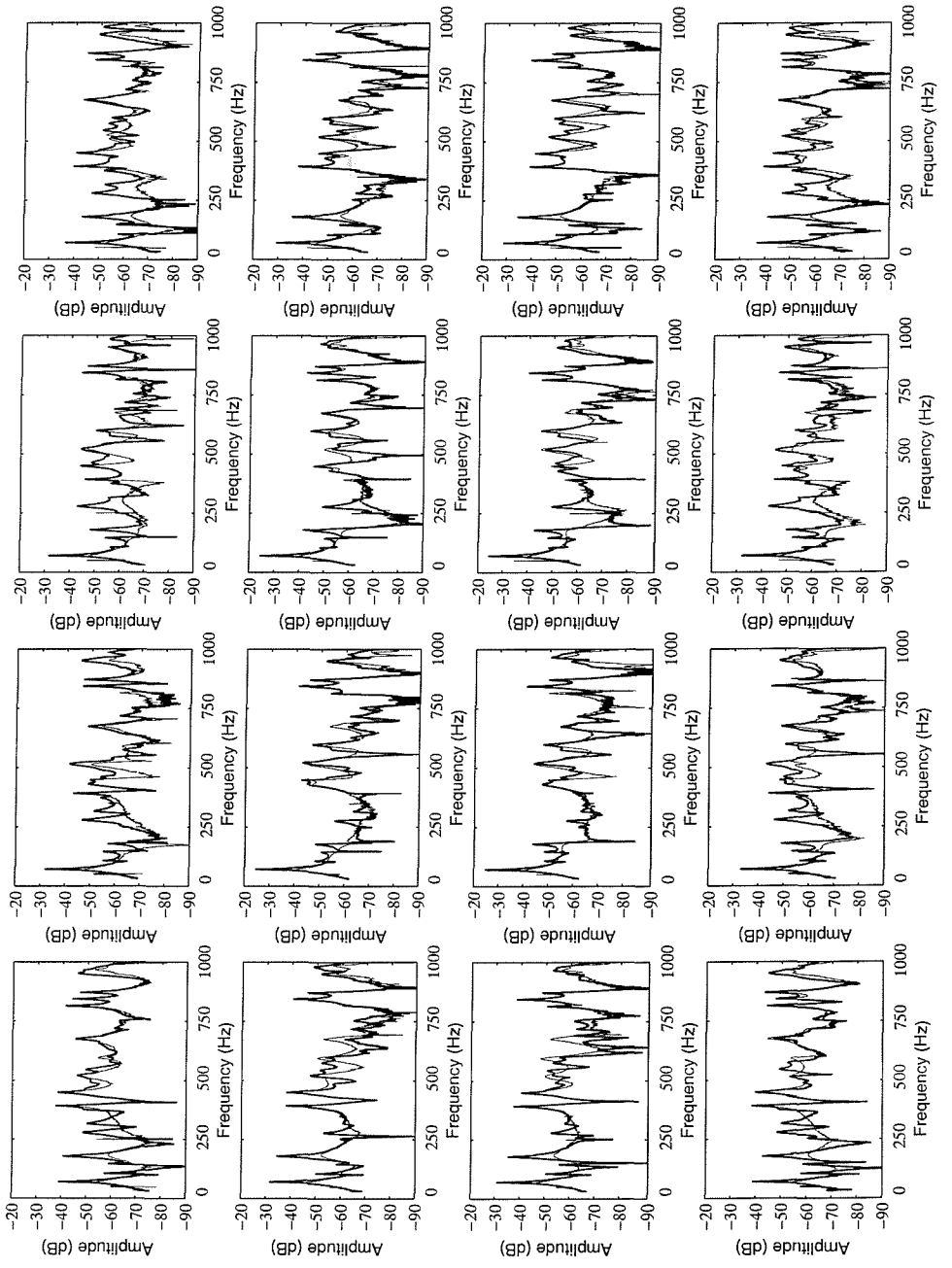

Figure 8.3: *Frequency response functions measured by the vibrometer at sixteen points of the grid located in the vicinity of each control units: FRF of the velocity signal per unit excitation of the loudspeaker (0-1 kHz) with no control system (solid line) and with decentralised feedback control (faint line).*

In Figure 8.3 the sixteen frequency response functions measured by the vibrometer at sixteen points of the grid which are located in the vicinity of each control units are reported. The solid line represents the measured response of the plate without control while the faint line represents the response when all sixteen control units are working with a fixed feedback control gain chosen to guarantee stability and low spillover effects at higher frequencies. The analysis of these results confirms the indications provided by the preliminary testing of the decentralised control system (see Section 6.4): with an acoustic primary source in the cavity, the control system is able to damp down the first five resonances with attenuation factor up to 18 dB, but it founds very difficult to contrast higher resonance frequencies.

The average spectrum of the vibration level of the plate in the frequency range 0-1 kHz is reported in Figure 8.4. The two curves in that plot have been calculated as the average of all the 133 frequency response functions measured by the laser vibrometer in correspondence of the points of the grid, considering again the response of the system before (solid line) and after (faint line) the control effort. It can be seen that the average attenuation factors of the first five resonances are respectively 16 dB (at 70 Hz), 4 dB (at 102 Hz), 18 dB (at 178 Hz), 15 dB (at 280 Hz) and 10 dB (at 326 Hz). Moreover there are further attenuations of about 5 dB in the narrow bands around 600 Hz and 950 Hz. The overall attenuation factor in the frequency range of 0-1 kHz is 3.6 dB.

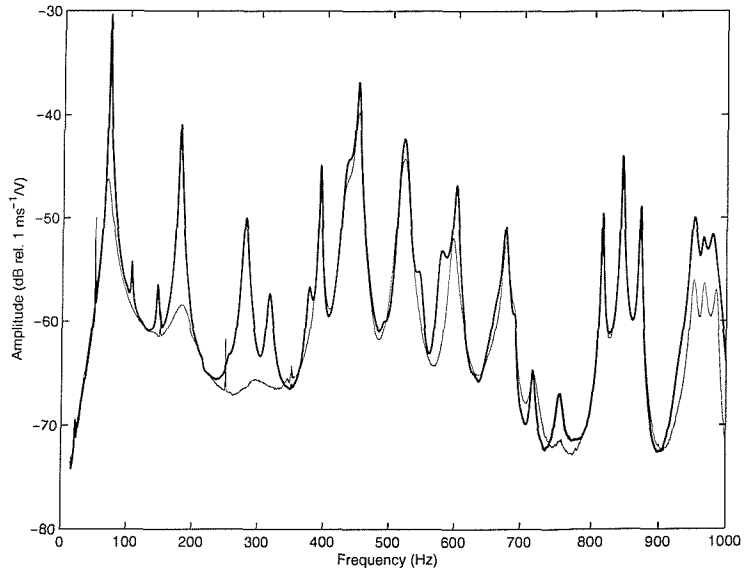

Figure 8.4: *Average frequency response function of the panel velocity (0-1 kHz) per unit excitation of the loudspeaker calculated as the average of all the 133 frequency response functions measured at the grid points: no control system (solid line) and with decentralised feedback control (faint line).*

A further representation of the results obtained with the laser vibrometer consists of a set of two dimensional (2D) images of the velocity distribution on the panel before control (left hand side image) and after control (right hand side image) in correspondence of specific resonances of the velocity average spectrum. The value of the frequency response function calculated along the plate surface is plotted in a colour coded image to facilitate the identification of the mode shape and the visualization of the control system efficiency.

Figures 8.5 and 8.6 report the images related to the first (70 Hz) and the third (178 Hz) resonances of the plate associated to the (1,1) and (1,3) modes of the smart panel respectively. It can be seen that, as the sixteen control gains are turned up, the amplitude of the vibratory fields at the resonance frequencies of 70 and 178 Hz still are characterised by the (1,1) and (1,3) natural modes of the panel but their amplitudes are much lower (attenuation factor of 15 dB). In general the near field sound radiation of a panel is directly associated to the panel vibration itself since there are no cancelling effects as can be seen in the far field radiated sound [21]. Therefore it is expected that, at resonance, the sixteen control units produce both a reduction of the near field and far field sound radiation as was highlighted in Figure 7.4.

Figure 8.7 and 8.8 report the images related to higher frequency resonances, respectively at 279 Hz and 316 Hz. The same considerations reported above can be extended to these results except for the attenuation ratio that, in this case, is about 10 dB.

Figure 8.9 shows the vibration of the panel in correspondence to the resonance frequency of 448 Hz associated to the (1,4) mode of the smart panel. In this case as the control gain is turned up there is just a very little variation of the vibratory field with nearly no reduction of the vibration amplitude. As a consequence at this resonance frequency there is no reduction of the near field sound radiation and, as shown in Figure 7.4, also the far field sound radiation is not reduced. Figure 8.9 suggest that the sixteen control units are not producing any control effect primarily because they are lying along the nodal lines of the (1,4) natural mode of the smart panel. Therefore in order to control the vibration associated to this mode, the sixteen control units should be arranged with a different geometry over the panel surface. Probably a less regular arrangement of the sixteen control units would allow the control of a larger number of modes provided larger control gains could be generated by each control unit in order to make up for the lower number of effective control units for each mode of the panel.

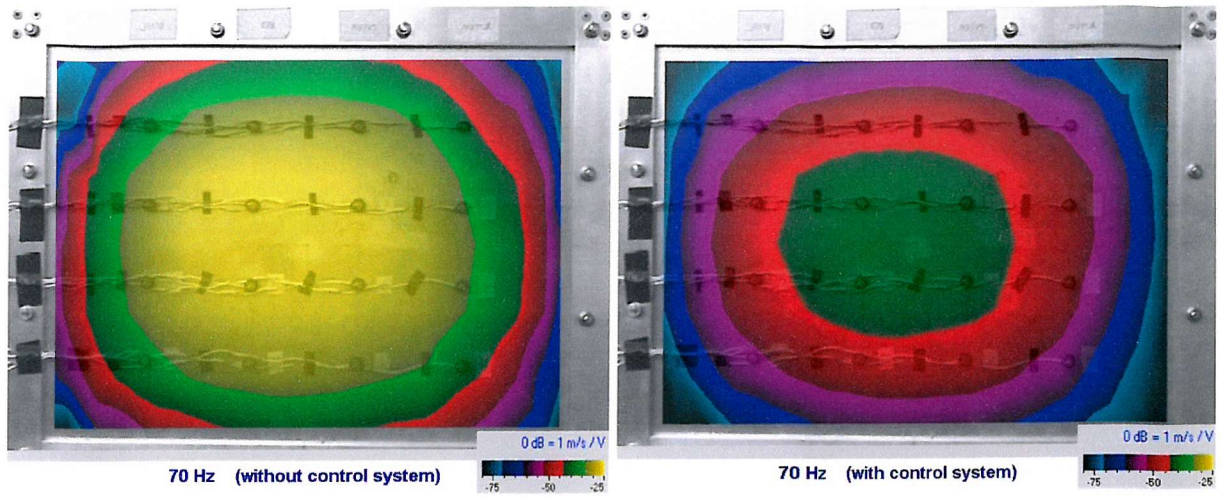

Figure 8.5: *Vibration level of the panel per unit excitation of the loudspeaker measured with the laser vibrometer at 70 Hz without control (left pictures) and with sixteen decentralised feedback control systems (right pictures).*

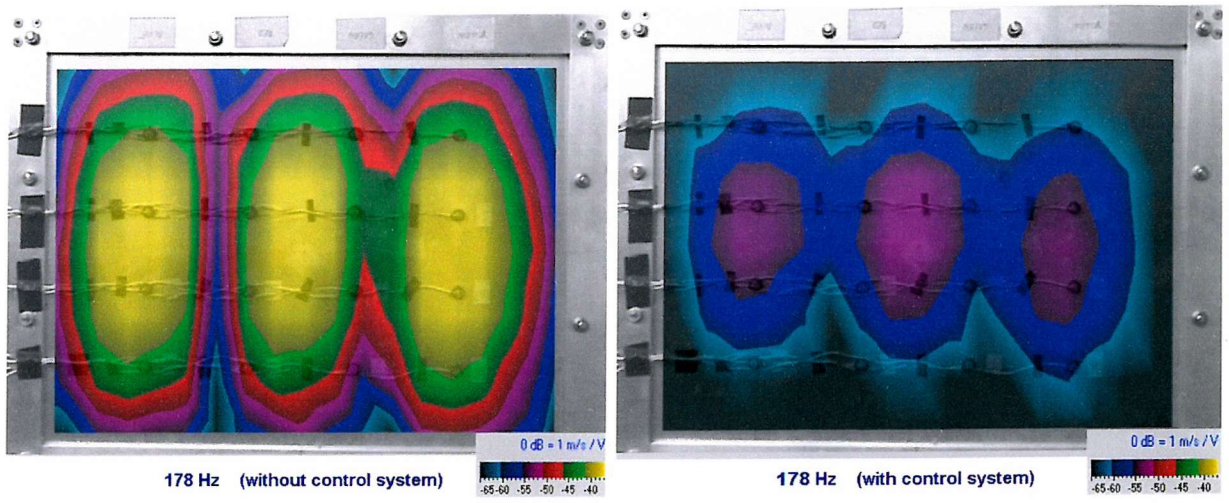

Figure 8.6: *Vibration level of the panel per unit excitation of the loudspeaker measured with the laser vibrometer at 178 Hz without control (left pictures) and with sixteen decentralised feedback control systems (right pictures).*

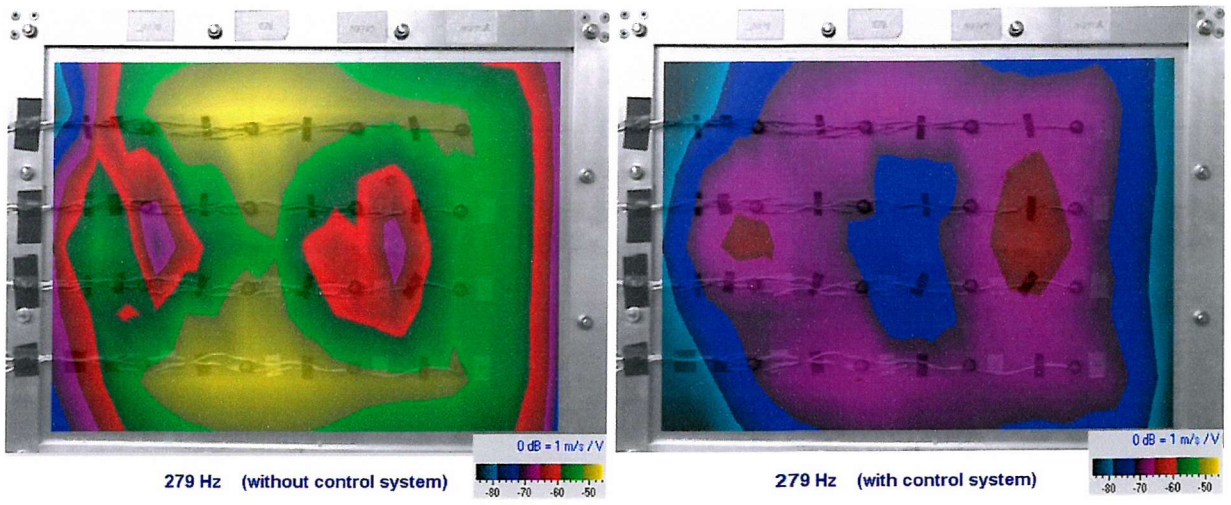

Figure 8.7: *Vibration level of the panel per unit excitation of the loudspeaker measured with the laser vibrometer at 279 Hz without control (left pictures) and with sixteen decentralised feedback control systems (right pictures).*

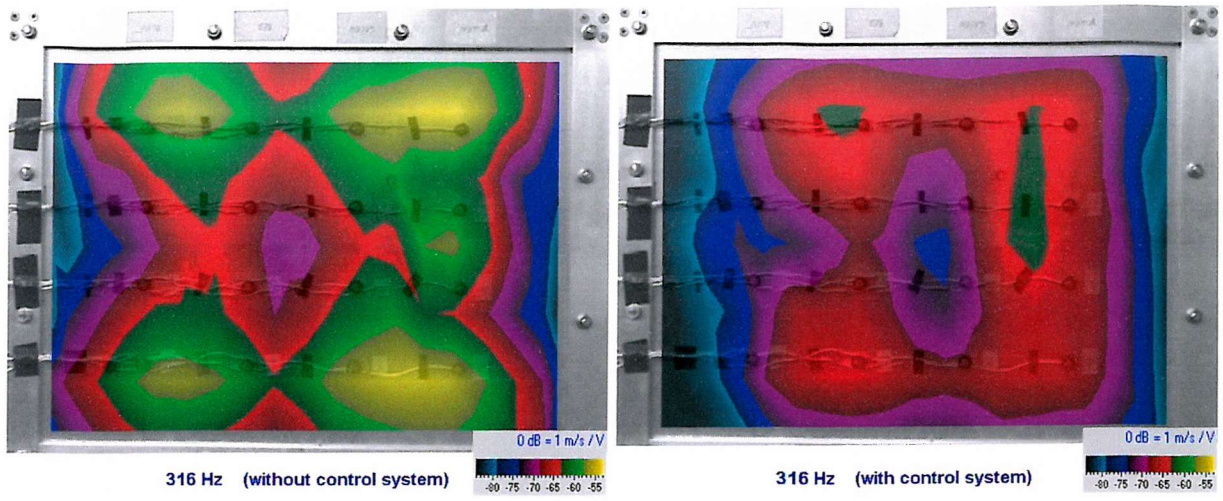

Figure 8.8: *Vibration level of the panel per unit excitation of the loudspeaker measured with the laser vibrometer at 316 Hz without control (left pictures) and with sixteen decentralised feedback control systems (right pictures).*

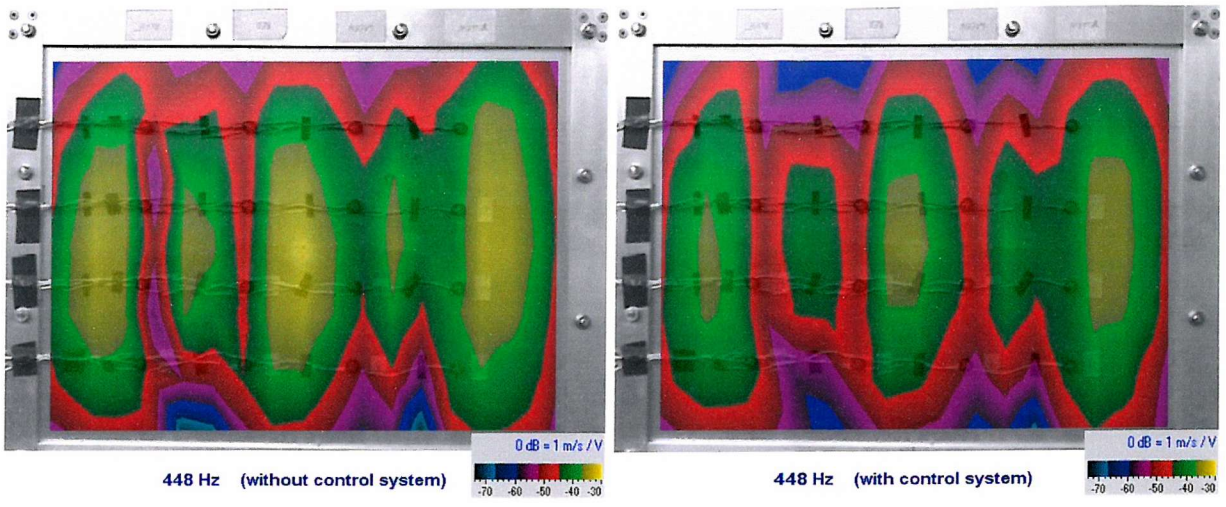

Figure 8.9: *Vibration level of the panel per unit excitation of the loudspeaker measured with the laser vibrometer at 448 Hz without control (left pictures) and with sixteen decentralised feedback control systems (right pictures).*

8.3 On-line implementation with a structural primary source on the panel

Similarly to what has been done for the acoustic primary disturbance test, a grid of 133 points has been used for the scanning of the plate surface in presence of a structural point force disturbance (see Figure 8.10). In this case the excitation point of the shaker has been moved quite close to one corner of the panel and the shaker has been oriented at an angle with respect to the normal to the panel in order to enable the vibration measurement over the whole surface with the vibrometer. A random signal in a frequency range of 0-1 kHz has been used to drive the shaker and the frequency response functions between the velocity at each point of the grid per unit excitation of the loudspeaker have been measured in absence and in presence of the decentralised control system.

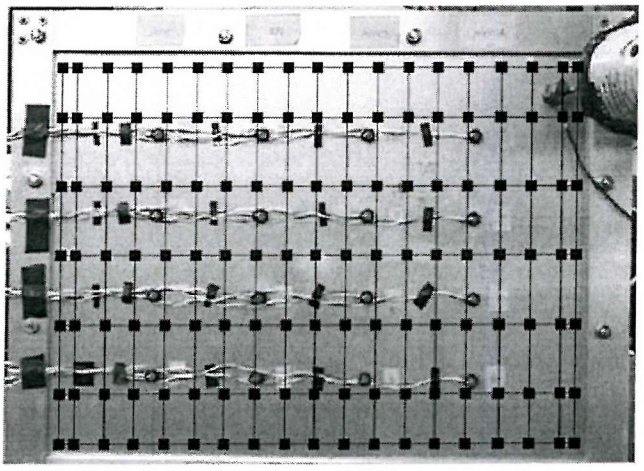

Figure 8.10: *Illustration of the panel surface overlapped with the grid of desired measurement points (133) to be scanned with the laser vibrometer. The system is excited by the shaker primary source in presence or not of the decentralised feedback controller.*

In Figure 8.11 the sixteen frequency response functions measured by the vibrometer at sixteen points of the grid which are located in the vicinity of each control units are reported. The solid line represents the measured response of the plate without control while the faint line represents the response when all sixteen control units are working with a fixed feedback control gain chosen to guarantee stability and low spillover effects at higher frequencies. It can be noted that the decentralised control system is able to damp down all the resonances up to 750 Hz with attenuation factor of 5-20 dB and little control spillover effects appear at anti-resonance frequencies or at narrow frequency bands such as those around 800 and 950 Hz.

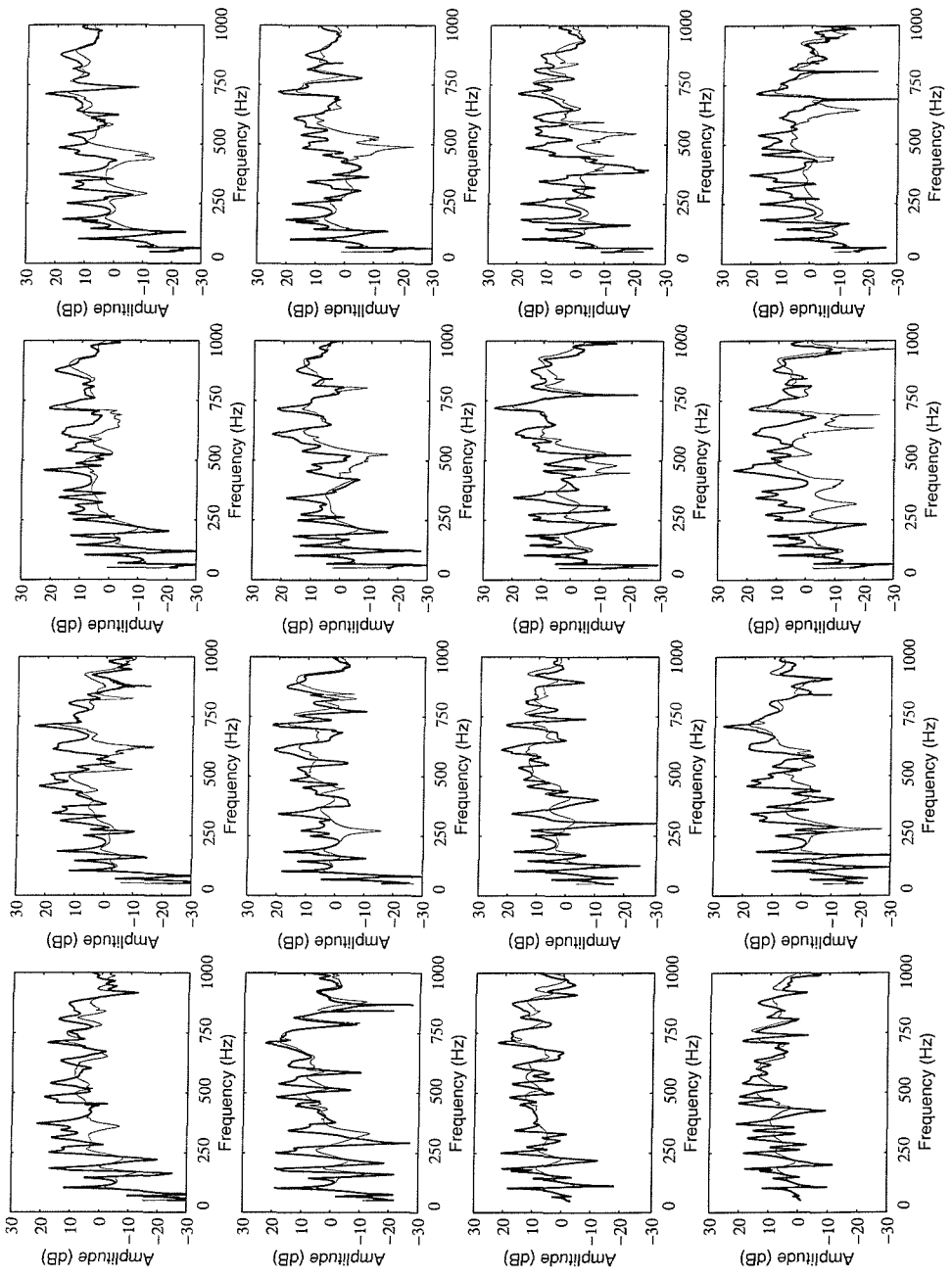

Figure 8.11: *Frequency response functions measured by the vibrometer at sixteen points of the grid located in the vicinity of each control units: FRF of the velocity signal per unit excitation of the shaker (0-1 kHz) with no control system (solid line) and with decentralised feedback control (faint line).*

The average spectrum of the vibration level of the plate excited by the shaker in the frequency range 0-1 kHz is reported in Figure 8.12 for both the case of uncontrolled (solid line) or controlled (faint line) system. It can be seen that the average attenuation factors of the first five resonances are respectively 6 dB (at 70 Hz), 13 dB (at 102 Hz), 10 dB (at 144 Hz), 13 dB (at 185 Hz) and 12 dB (at 250 Hz). Moreover there are further attenuations of about 5-10 dB in correspondence of the higher frequency resonances. The overall attenuation factor in the frequency range of 0-1 kHz is 3.3 dB.

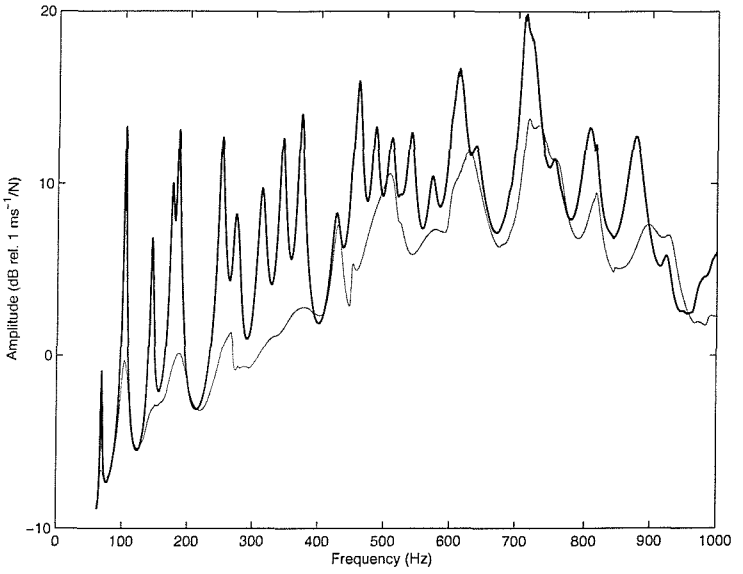

Figure 8.12: *Average frequency response function of the panel velocity (0-1 kHz) per unit excitation of the shaker calculated as the average of all the 133 frequency response functions measured at the grid points: no control system (solid line) and with decentralised feedback control (faint line).*

Figure 8.13 shows the vibratory field of the panel without control (left hand side pictures) and with control (right hand side pictures) when it is excited directly by the shaker at the frequencies of 70 Hz. As for the loudspeaker primary excitation case, the pictures show the vibration of the panel in correspondence to the resonance frequency associated to the (1,1) mode of the smart panel. In this case, the shaker produces a point force at the right hand top corner of the panel and therefore the vibratory field is characterised by the superposition of the (1,1) mode and the local response to the point excitation. Considering Figure 8.5, it can be noticed that the acoustic excitation by the cavity underneath the panel does not produce any localized effect and therefore the response of the panel at 70 Hz is exactly characterized by the vibration field of the (1,1) mode of the panel. The left hand side picture in Figure 8.13 shows that as the sixteen control gains are turned up the amplitude of the vibratory field is reduced over most of the smart panel surface except in correspondence to the excitation point. Probably a much larger control gain should be implemented on the top left control unit in order to damp the local response of the panel to the concentrated force excitation exerted by the shaker. The overall result is that the near field sound radiation is not reduced so much as in the previous case with the loudspeaker primary excitation. In contrast the far field sound radiation is still controlled by the overall vibration of the panel and thus, as shown in Figure 7.11 there is good reduction of sound radiation at the first resonance at 70 Hz.

Similar behaviour is noticed for pictures in Figures 8.14-8.18 which shows the vibration of the panel in correspondence to the resonance frequencies respectively associated to the (1,2),

(2,1), (2,2), (2,3) and (3,2) modes of the smart panel. These modes are not visible when the panel is excited by the acoustic field in the cavity underneath it. Indeed, at such low frequency range, the cavity produce a volumetric excitation on the panel that can not excite the mode numbers of the panel without a net volumetric displacement, as for example the above mentioned modes. The point force can instead excite this type of modes and therefore the resonance frequencies at 102, 144, 184, 250 and 312 Hz are measured as shown in the Figures below. Also in this case the controller produces good reductions of the vibration over the panel surface except in the vicinity of the point excitation exerted by the shaker.

The pictures in Figure 8.19 show the vibration of the panel in correspondence to the resonance frequency of 343 Hz where the response is characterised by the (2,4) mode. Also in this case, when the sixteen control gains are turned up, good reductions of the overall vibration are achieved. Moreover, after control, the vibratory field is more irregular since the response of the panel is characterised by a set of modes rather than the (2,4) mode only.

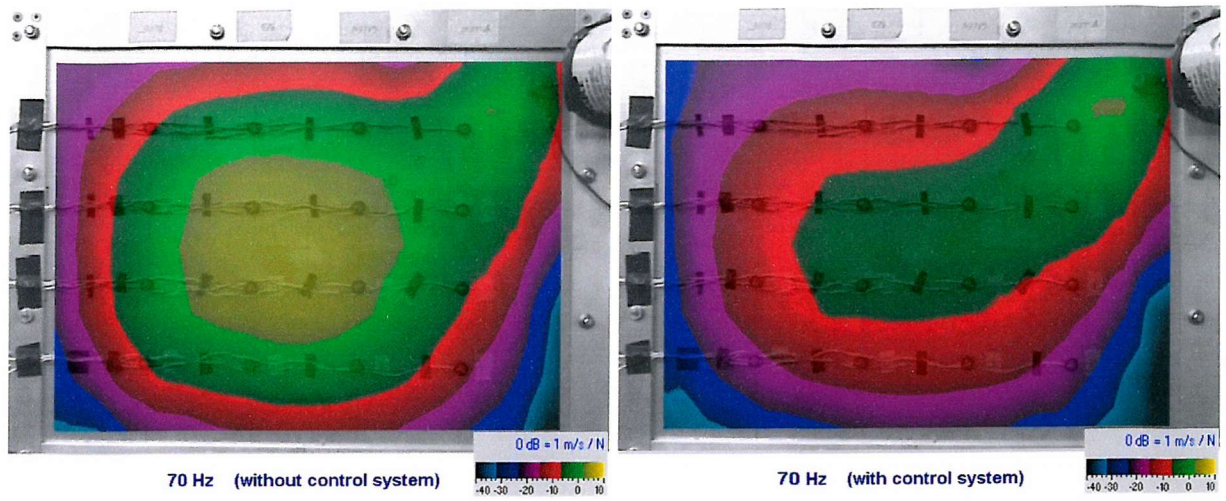

Figure 8.13: *Vibration level of the panel per unit excitation of the shaker measured with the laser vibrometer at 70 Hz without control (left pictures) and with sixteen decentralised feedback control systems (right pictures).*

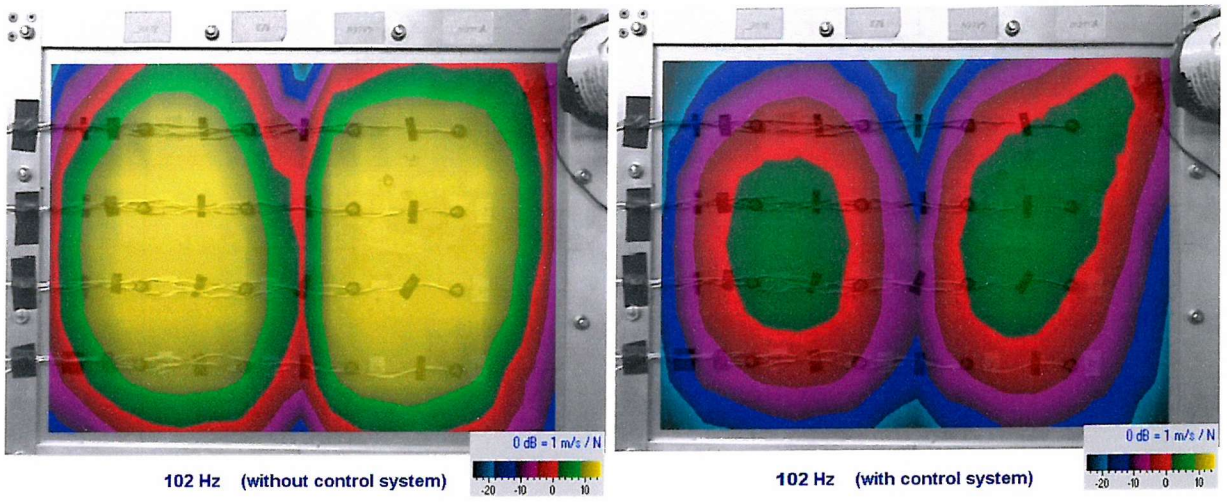

Figure 8.14: *Vibration level of the panel per unit excitation of the shaker measured with the laser vibrometer at 102 Hz without control (left pictures) and with sixteen decentralised feedback control systems (right pictures).*

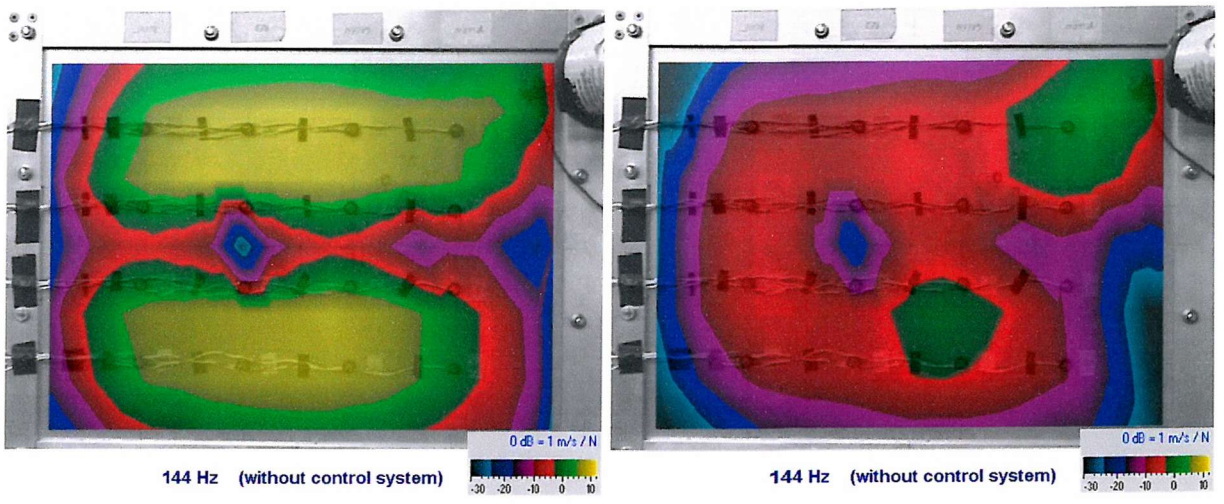

Figure 8.15: *Vibration level of the panel per unit excitation of the shaker measured with the laser vibrometer at 144 Hz without control (left pictures) and with sixteen decentralised feedback control systems (right pictures).*

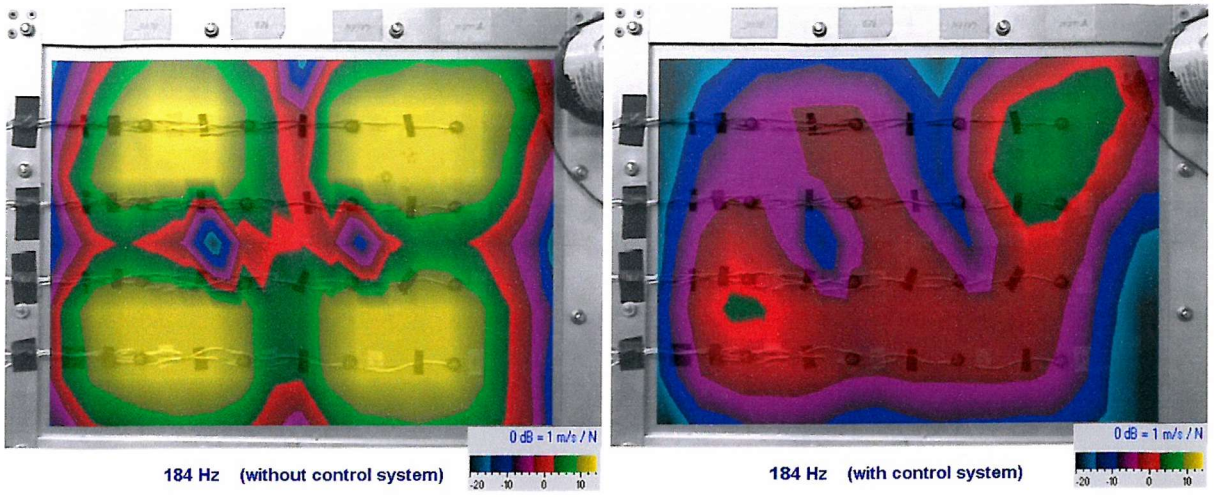

Figure 8.16: *Vibration level of the panel per unit excitation of the shaker measured with the laser vibrometer at 184 Hz without control (left pictures) and with sixteen decentralised feedback control systems (right pictures).*

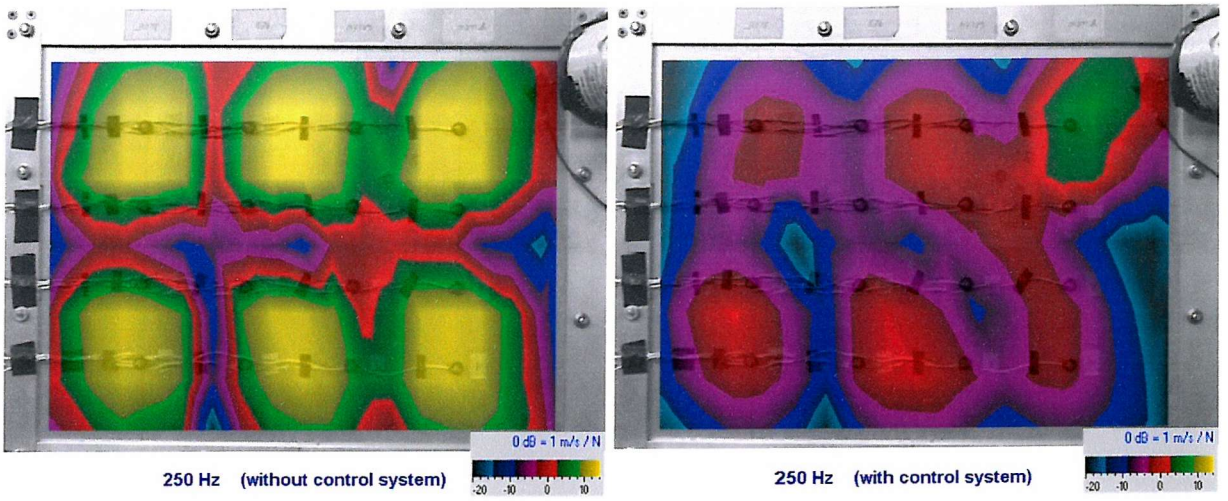

Figure 8.17: *Vibration level of the panel per unit excitation of the shaker measured with the laser vibrometer at 250 Hz without control (left pictures) and with sixteen decentralised feedback control systems (right pictures).*

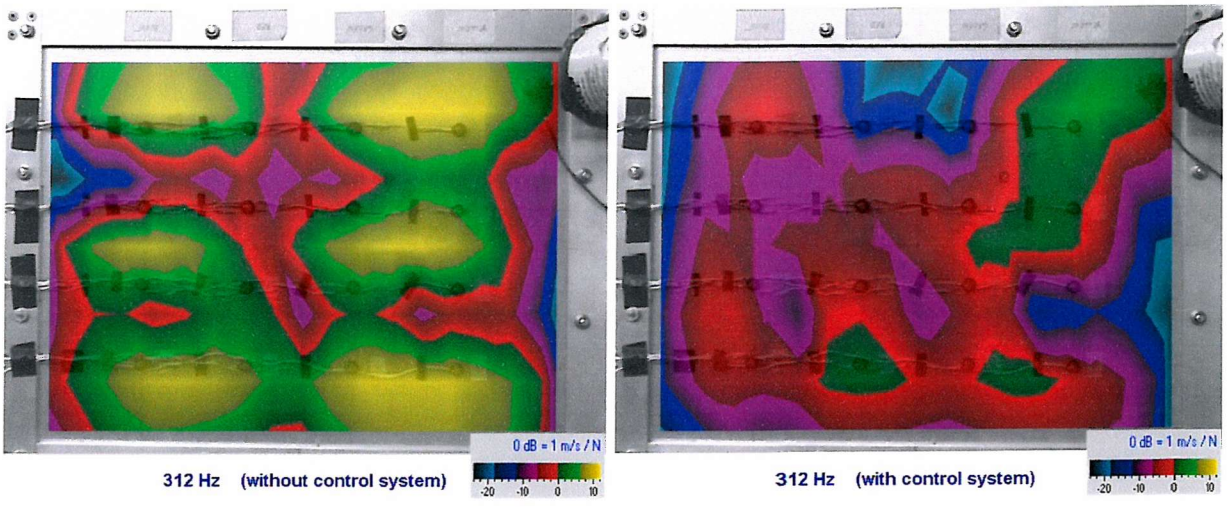

Figure 8.18: *Vibration level of the panel per unit excitation of the shaker measured with the laser vibrometer at 312 Hz without control (left pictures) and with sixteen decentralised feedback control systems (right pictures).*

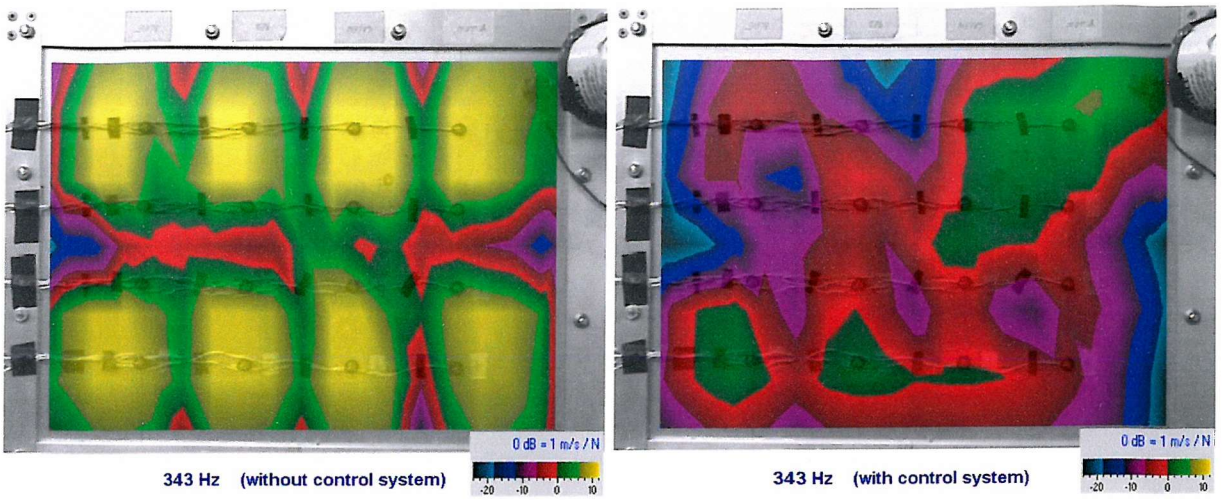

Figure 8.19: *Vibration level of the panel per unit excitation of the shaker measured with the laser vibrometer at 343 Hz without control (left pictures) and with sixteen decentralised feedback control systems (right pictures).*

9. CONCLUSION

9.1 Conclusions from individual sections

This dissertation describes a theoretical and experimental application of Active Structural Acoustic Control (ASAC) of a smart panel. The main objective was the design and the implementation of a decentralised velocity feedback control system for the reduction of the vibration and of the sound transmission of a smart panel. The system considered for this study was an aluminium panel, equipped with an embedded 4×4 array of small piezoceramic actuators and a closely located array of miniature accelerometers, which has been mounted on the top of a rectangular cavity with rigid walls. Two different types of primary disturbances have been considered either in the numerical or experimental study: a primary acoustic source (a loudspeaker) within the cavity and a primary structural source (a shaker) acting directly on the panel.

A theoretical model has been formulated with which the total kinetic energy and sound radiation ratio can be derived as a function of the feedback gain implemented in the sixteen decentralised control units. The stiffness and mass effects of the piezoelectric actuators and the mass effects together with the local dynamics of the accelerometers sensors have been taken into account in the theoretical model. Simulations results have been produced for a range of feedback control gains.

The numerical simulations have highlighted the following points.

1. The low frequency response of the panel before control is characterised by a selected number of resonances that, in the case of the cavity primary source, correspond to either panel or cavity natural frequencies of well coupled panel-cavity modes and in the case of the force primary source, includes most, if not all, the modes of the panel.
2. At low frequencies, only the modes whose modal integers are odd radiate sound significantly and also anti-resonances appear, due to destructive interference between the sound pressures radiated by adjacent odd modes.
3. When the control system is turned on, it can be noticed that as the gains of the feedback loops are increased, as the resonances that are controlled mainly by the panel natural modes become more heavily damped. In contrast, the resonances controlled by the cavity natural modes are not damped.

4. Larger control gains are required to control the panel modes with natural frequencies below the first natural frequency of the cavity since the control unit have to contrast the volumetric loading of the acoustic cavity on the panel.
5. When the system is excited by the monopole acoustic primary source in the cavity, it has been found that the kinetic energy or sound radiation integrated between 0 and 2 kHz are reduced respectively by 7.4 dB and 3.7 dB in correspondence of the optimal gain of 100. For higher gains the control effectiveness degrades up to a point where the overall kinetic energy or sound radiation are enhanced by 2.8 dB and 1.2 dB respectively.
6. Similar behaviour has been found when the system is excited by the primary force acting on the panel. For the optimal control gain of 100, the overall kinetic energy or sound radiation in the frequency range 0 to 2 kHz are reduced respectively by 8.1 dB and 5.5 dB while for higher gains there is an enhancement of 1.2 dB and 3.2 dB respectively.
7. The degrading performance of the control systems when higher gains are used are due to the fact that, for very high control gains, each control unit pins the vibration at the control point so that the response of the panel is transformed to that of a lightly damped structure with a new set of natural modes having higher natural frequencies because of the new pinning boundary conditions in correspondence of the sixteen control systems.

The work concerned with the design and the implementation of sixteen decentralised velocity feedback control systems embedded on smart panel has been structured into three stages: first the analysis of the sensor–actuator response function; second, the design of the single channel velocity feedback controller when only one control unit is working and third, the implementation of the designed controller on the sixteen control units of the smart panel. The analysis of the measured and simulated sensor–actuator response function has provided the following information.

1. At very low frequencies, below about 283 Hz, the response function is characterised by well separated resonant frequencies due to the panel natural modes while at higher frequencies the dynamic effects of the sensor and actuator transducers become more and more important and tend to flatten down the response function because of their mass effect.
2. At relatively higher frequencies the sensor-actuator frequency response function is

characterised by a relatively wide frequency band trough between 30 kHz and 40 kHz and a crest between 43 kHz and 46 kHz. This is due to the fact that the sixteen accelerometers are a sort of a single degree of freedom neutralizer that reduces the vibration level at the measurement point in correspondence to its natural frequency. Since their resonance frequencies are uniformly spread between 35 kHz and 42 kHz, then the wide-frequency through and crest are found.

3. The sensor–actuator frequency response function is affected by a large phase shift above 10 kHz which is due to the fact that the accelerometer and the piezoceramic patch are not a truly collocated and dual sensor–actuator pair. It has been demonstrated that the cut off frequency for a non collocated behaviour can be raised by reducing the size of the actuator.

The design of the single channel velocity feedback control system when only one control unit is active has shown the following features.

1. When direct velocity feedback control is implemented the Nyquist plot has shown that the above mentioned through of the frequency response function occupies the negative real side and therefore, it allows relatively large gain margin to implement a stable controller with low spillover phenomena.
2. The gain can be further increased by fifteen times when a phase lag compensator is used.

Finally the implementation of the sixteen decentralised control units has produced the following results.

1. Good low frequency control can be achieved that can reach reductions of the measured velocity at the error sensor up to 15 or 20 dB at relatively low frequencies and still are of the order of 3 to 6 dB at higher frequencies up to 2 kHz.
2. However, the control system find difficult to damp down some resonance frequencies for three possible factors: first, the loading effect on the panel generated by the low frequency volumetric acoustic response of the cavity; second, the low spatial control authority of the actuator transducers for some of the resonant structural modes and third, the low control strength of the actuator transducers for well coupled panel and cavity modes.

The final experimental tests carried out to assess the control effectiveness of the prototype smart panel with sixteen decentralised control units consist of two types of measurements: first, the total sound power radiation measured in an anechoic chamber without and with the

sixteen control units turned on and second, the vibratory field over the panel surface measured with a laser vibrometer. Both types of measurements have been taken with reference to the acoustic excitation produced by the loudspeaker placed in the cavity underneath the panel and the point force generated by a shaker mounted on the panel. The first types of tests have highlighted the following conclusions.

1. When the smart panel is excited by the acoustic field generated by the loudspeaker placed in the cavity underneath it, the control system is able to damp down the sound radiation in correspondence to the first three resonance frequencies by about 8 to 13 dB. Between 350 and 1200 Hz there is little control effect; in particular, the resonance frequency controlled by the first few cavity modes can not be controlled. However, between 1200 and 1400 Hz reductions of about 10 dB of the measured sound level are registered. The measurements in third octave bands between 0 and 5 kHz have shown frequency averaged reductions of about 6 dB in correspondence to the third octave bands at 63, 80 and 1250 Hz. Smaller reductions are measured for the other third octave bands.
2. When the panel is excited by the point force generated by a shaker, the control system is able to damp down the sound radiation in correspondence to the first five resonance frequencies by about 12 to 18 dB. Between 350 and 1300 Hz and between 1600 and 1800 Hz there are significant control effects that go from a minimum of 3 to a maximum of 8 dB. Reductions of the sound radiation are measured in correspondence of all third octave bands between 0 and 5 kHz and there are at least seven bands with reductions of about 5 to 8 dB.
3. Very little control spillover effects have been found in these tests and in most cases they correspond to antiresonance frequencies as one would expect with active damping.
4. When the panel is excited by the point force generated by a shaker the low frequency sound power radiation is characterised by a larger number of resonance frequencies while at higher frequencies there are less resonance frequencies than in the case of the acoustic primary excitation. Considering the loudspeaker primary excitation, then the smart panel is excited by the volumetric acoustic field in the cavity which is well coupled only with the panel modes with a net volumetric displacement, i.e. with either one or both odd modal order. However, at higher frequencies the sound radiation is characterised not only by the resonance frequencies associated to the natural modes of the panel but also those associated to the natural modes of the acoustic cavity.

The measurements of the vibratory field over the panel surface with the laser vibrometer have highlighted the following features of the control system with sixteen decentralised feedback units.

1. When the smart panel is excited by the acoustic field generated by the loudspeaker placed in the cavity underneath it, it has been found that the sixteen decentralised control units uniformly damp down the overall vibration associated to the low frequency (1,1) and (1,3) modes of the panel. In contrast the sixteen control units can not produce any control effect on the (1,4) mode of the panel because they are exactly arranged along the nodal lines of this mode.
2. Finally, it has been highlighted that the point force excitation produced by the shaker can excite even mode number as well as odd mode number. Also, this excitation is characterised by a local vibratory field that could not be contrasted by the decentralised control unit close to it.

It is important to emphasize that the testing configuration with the panel mounted on the top of the Perspex box has not given a complete picture of the effective control performance of the smart panel since the sixteen control units are not able to reduce the vibration of the panel in correspondence of well coupled cavity and panel resonating modes. Also, at some frequencies, the sound radiated by the panel is equivalent to the flanking sound radiation through the side walls of the Perspex box and therefore it was not possible to assess the true control effects. The control effectiveness of the smart panel is therefore expected to be relatively higher when tested on a proper sound transmission suite where the panel can be excited by a diffuse acoustic field without any low frequency volumetric effect or higher frequency modal pattern of the incident acoustic disturbance.

9.2 Overall conclusions

The overall conclusions of this dissertation are summarised below.

1. The analysis of the response of the smart panel with embedded piezoelectric actuators and acceleration sensors, has shown that the low frequency response of the panel before control is characterised by a selected number of resonances that, in the case of the cavity primary source, correspond to either panel or cavity natural frequencies of well coupled panel-cavity modes and in the case of the force primary source, includes most, if not all, the modes of the panel. When the control system is turned on, it can be noticed that as the gains of the feedback loops are increased, as the resonances that are controlled mainly by the panel natural modes become more heavily damped. In contrast, the resonances controlled by the cavity natural modes are not damped. For higher gains the control effectiveness degrades up to a point where the overall kinetic energy or sound radiation are enhanced (pinning effect). It has been found that, in correspondence of the optimal gain of 100, the kinetic energy or sound radiation integrated between 0 and 2 kHz are reduced respectively by 7.4 dB and 3.7 dB for the monopole acoustic excitation and respectively by 8.1 dB and 5.5 dB for the structural excitation.

3. The sensor–actuator frequency response function is affected by a large phase shift above 10 kHz which is due to the fact that the accelerometer and the piezoceramic patch are not a truly collocated and dual sensor–actuator pair. It has been demonstrated that the cut off frequency for a non collocated behaviour can be raised by reducing the size of the actuator. When direct velocity feedback control is implemented, the Nyquist plot has shown that the above mentioned through of the frequency response function occupies the negative real side and therefore, it allows relatively large gain margin to implement a stable controller with low spillover phenomena. The gain can be further increased by fifteen times when a phase lag compensator is used.
4. The implementation of the sixteen decentralised control units has achieved reductions of the measured velocity at the error sensor from 15 to 20 dB at relatively low frequencies and reductions of the order of 3 to 6 dB at higher frequencies up to 2 kHz. The control system, however, finds difficult to damp down some resonance frequencies for three possible factors: first, the loading effect on the panel generated by the low frequency volumetric acoustic response of the cavity; second, the low spatial

control authority of the actuator transducers for some of the resonant structural modes and third, the low control strength of the actuator transducers for well coupled panel and cavity modes.

5. The stability of the multi-channel decentralised velocity feedback has been analysed according to the Generalised Nyquist criterion: the eigenvalues of the measured matrix $\mathbf{G}(j\omega)\mathbf{H}(j\omega)$ have been calculated and represented as series of polar plots. The system is stable for the set of gain implemented in the decentralised feedback, since none of the eigenvalues loci of $\mathbf{G}(j\omega)\mathbf{H}(j\omega)$ encircle the (-1,0) point. However, all the eigenvalues cross the negative real axis and therefore the system is not unconditionally stable.
6. A third octave analysis of the sound power radiation from the smart panel with and without the decentralised feedback control has been carried out for a frequency range of 0 – 5 kHz. The sound power level has been measured in the anechoic chamber for both types of excitations (loudspeaker in the cavity and shaker on the panel), achieving overall reduction of the sound power respectively of 2.5 dB and 4.4 dB.

9.3 Suggestions for future work

1. The testing configuration considered in this thesis could be used to assess the feasibility of a "smart enclosure" for the control of sound radiation by machines. The results presented in this thesis have highlighted that the smart panel can not reduce the sound radiation at frequencies close to the cavity resonances. Therefore it would be interesting to analyse the feasibility of an enclosure with a smart wall of the type studied in this thesis and a set of decentralised acoustic control units placed within the cavity. Similarly to the structural case, the acoustic control units could consist of a microphone sensor closely located to a loudspeaker actuator connected by a feedback controller.
2. The testing configuration considered in this thesis could also be used to assess the control effectiveness to reduce the sound transmission through the smart panel inside the cavity in presence of an external acoustic source positioned above the panel.
3. The performance of the decentralised feedback control should be evaluated for different configurations of the sensor-actuator arrays, e.g. using only the four central control units or arranging the sixteen control units with a different geometry over the

panel surface. Probably a less regular arrangement of the sixteen control units would allow the control of a larger number of modes provided larger control gains could be generated by each control unit in order to make up for the lower number of effective control units for each mode of the panel.

4. The miniaturization of the control unit (velocity sensor – feedback controller – piezo actuator) should be investigated in such a way as to integrate micro-electro-mechanical systems (MEMS) transducers (sensors and actuators) and MEMS controllers.

APPENDIX A

Table A.1: *Technical specifications of the accelerometer PCB 352C67*

Parameter	Value
Product Type	Ceramic shear ICP Accelerometer
Model	PCB Piezotronics 352C67
Mass	2 gm
Sensitivity	10.2 mV/(m/s^2)
Frequency Range (±5%)	0.5 to 10000 Hz
Resonant Frequency	≥35 kHz

Table A.2: *Technical specifications of the force transducer B&K Type 8200*

Parameter	Value
Product Type	B&K Force Transducer
Model	Type 8200
Mass	21 gm
Sensitivity	3.82 pC/N
Polarity	Positive for compression
Capacitance	25 pF

Table A.3: *Technical specifications of the microphone B&K Type 4165*

Parameter	Value
Product Type	B&K Condenser Microphone Cartridge
Model	Type 4165
Sensitivity	48.4 mV/Pa
Cartridge Capacitance	20.2 pF
Frequency Response Characteristic	20 kHz
Dynamic Range	146 dB

APPENDIX B

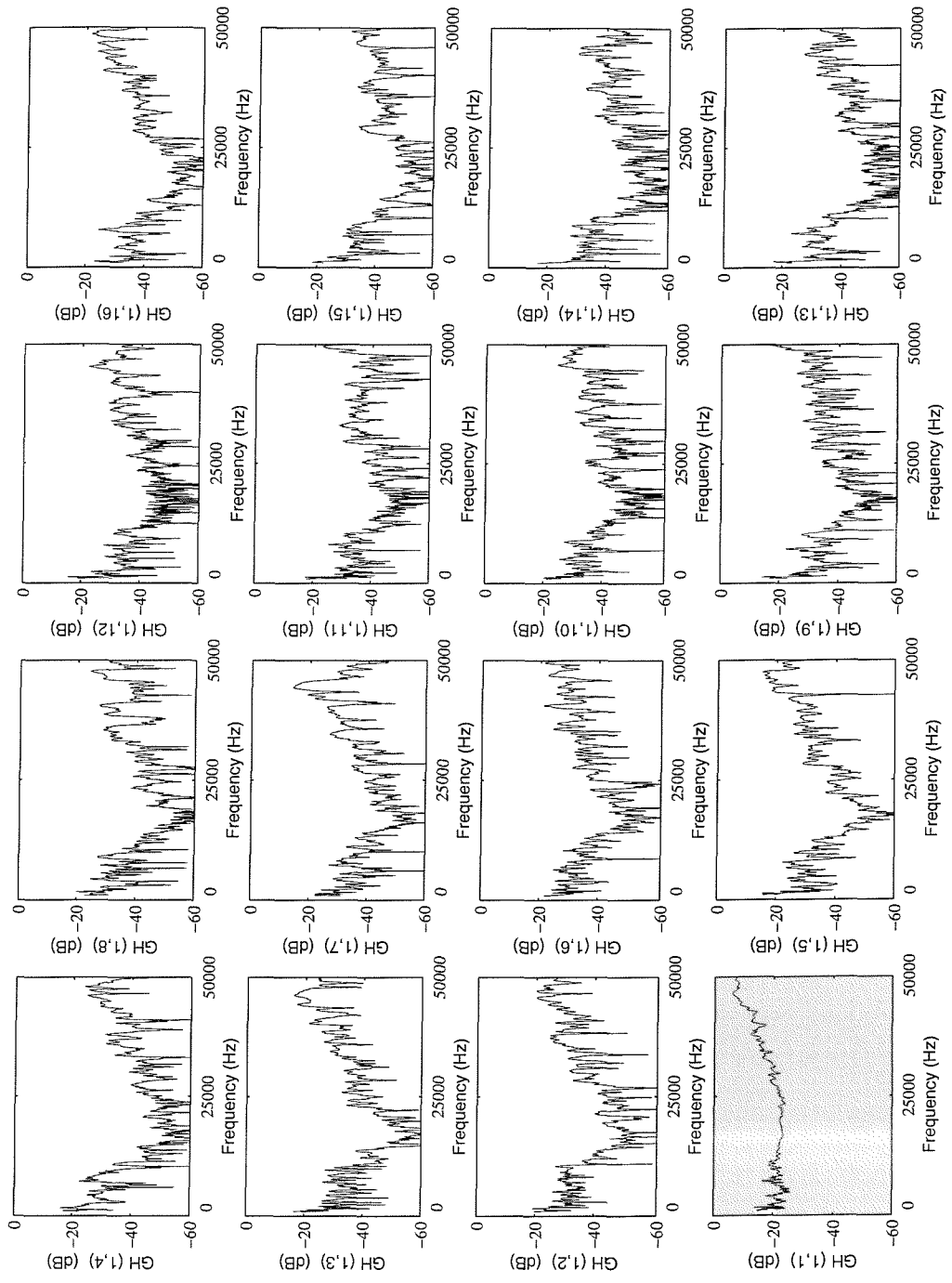

Figure B.1: *The sixteen measured frequency response functions between the sixteen control outputs and the piezo actuator n. 1, exciting the plate in a frequency range of 50 kHz*

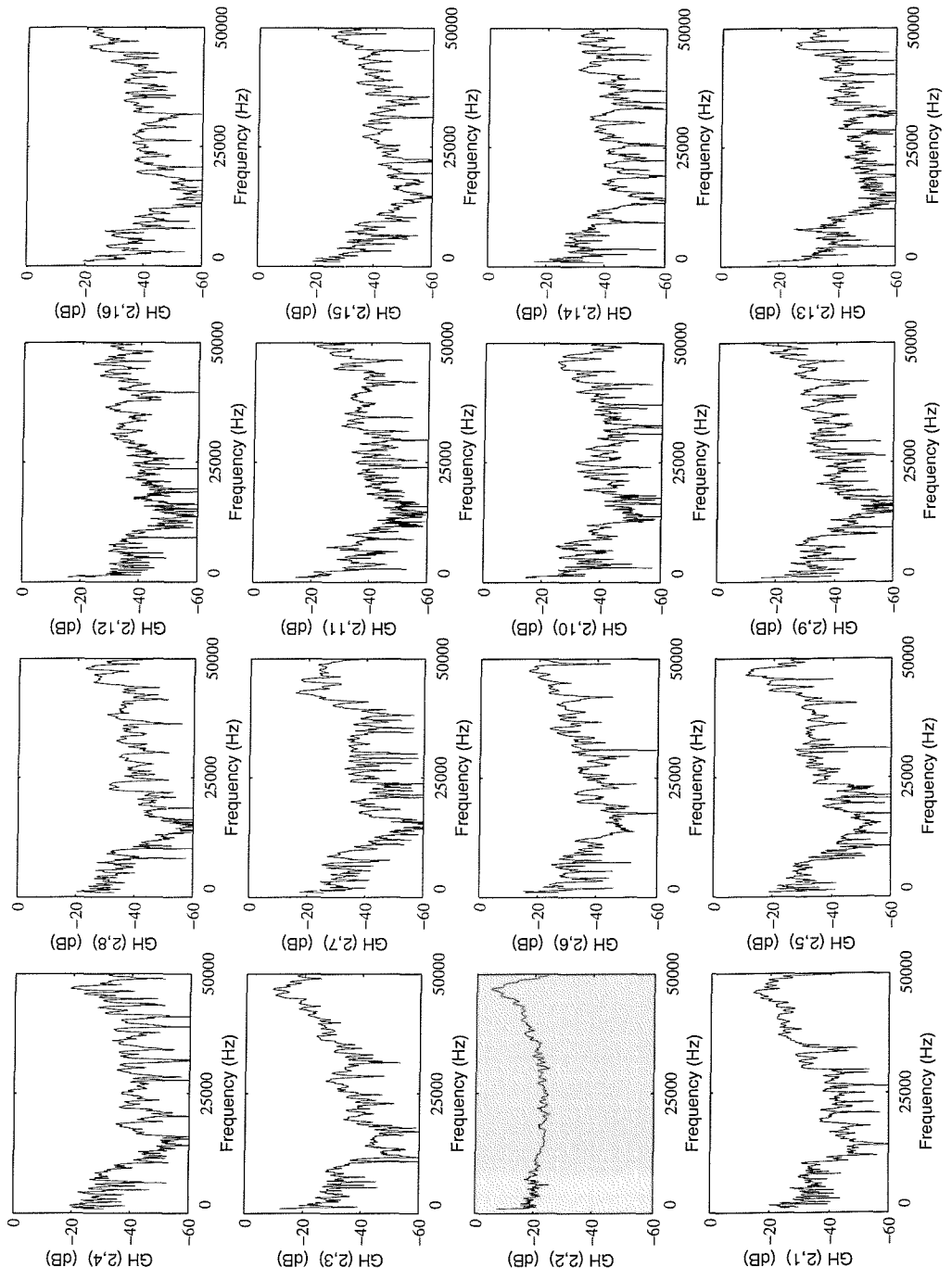

Figure B.2: *The sixteen measured frequency response functions between the sixteen control outputs and the piezo actuator n. 2, exciting the plate in a frequency range of 50 kHz*

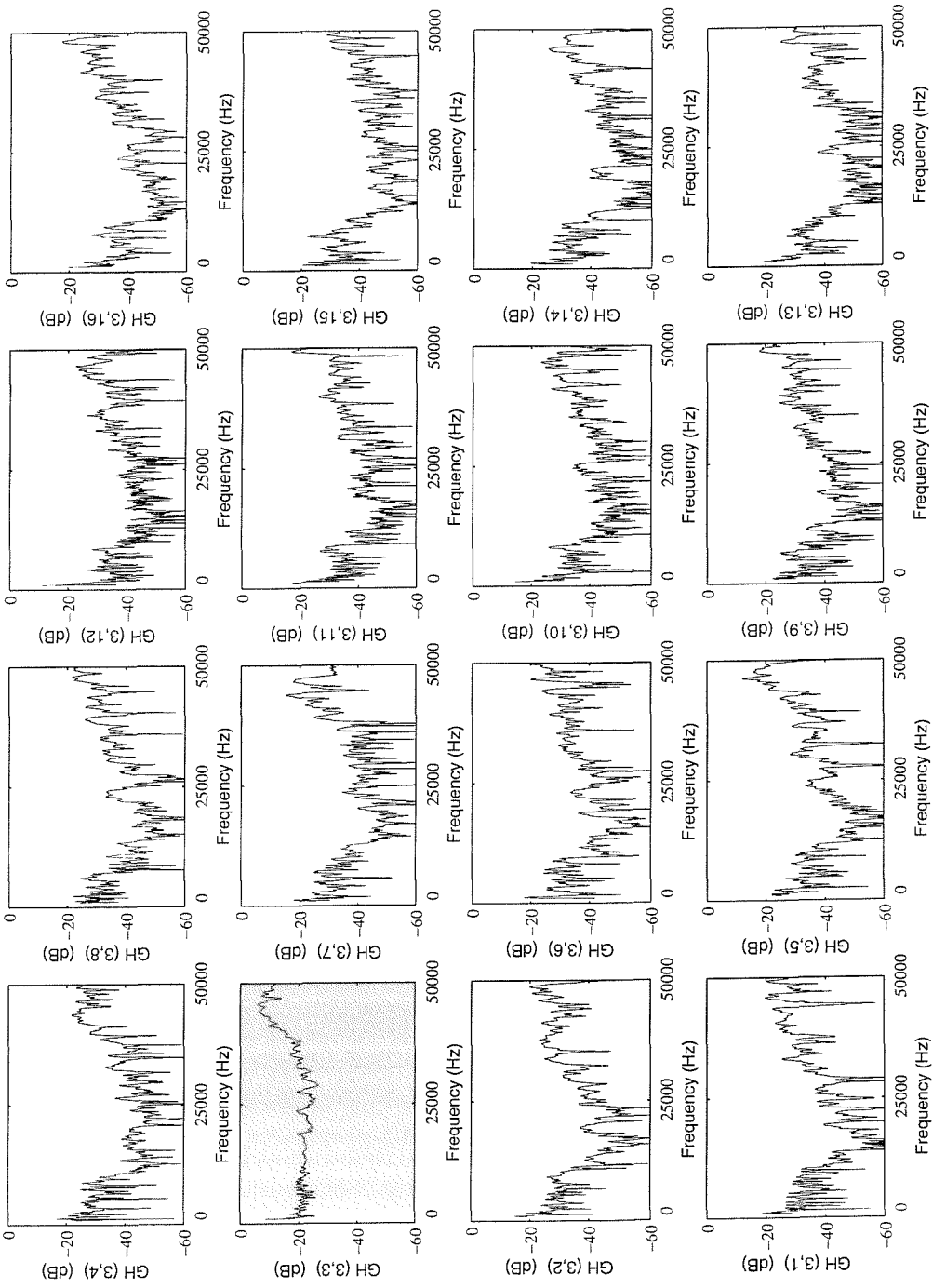

Figure B.3: *The sixteen measured frequency response functions between the sixteen control outputs and the piezo actuator n. 3, exciting the plate in a frequency range of 50 kHz*

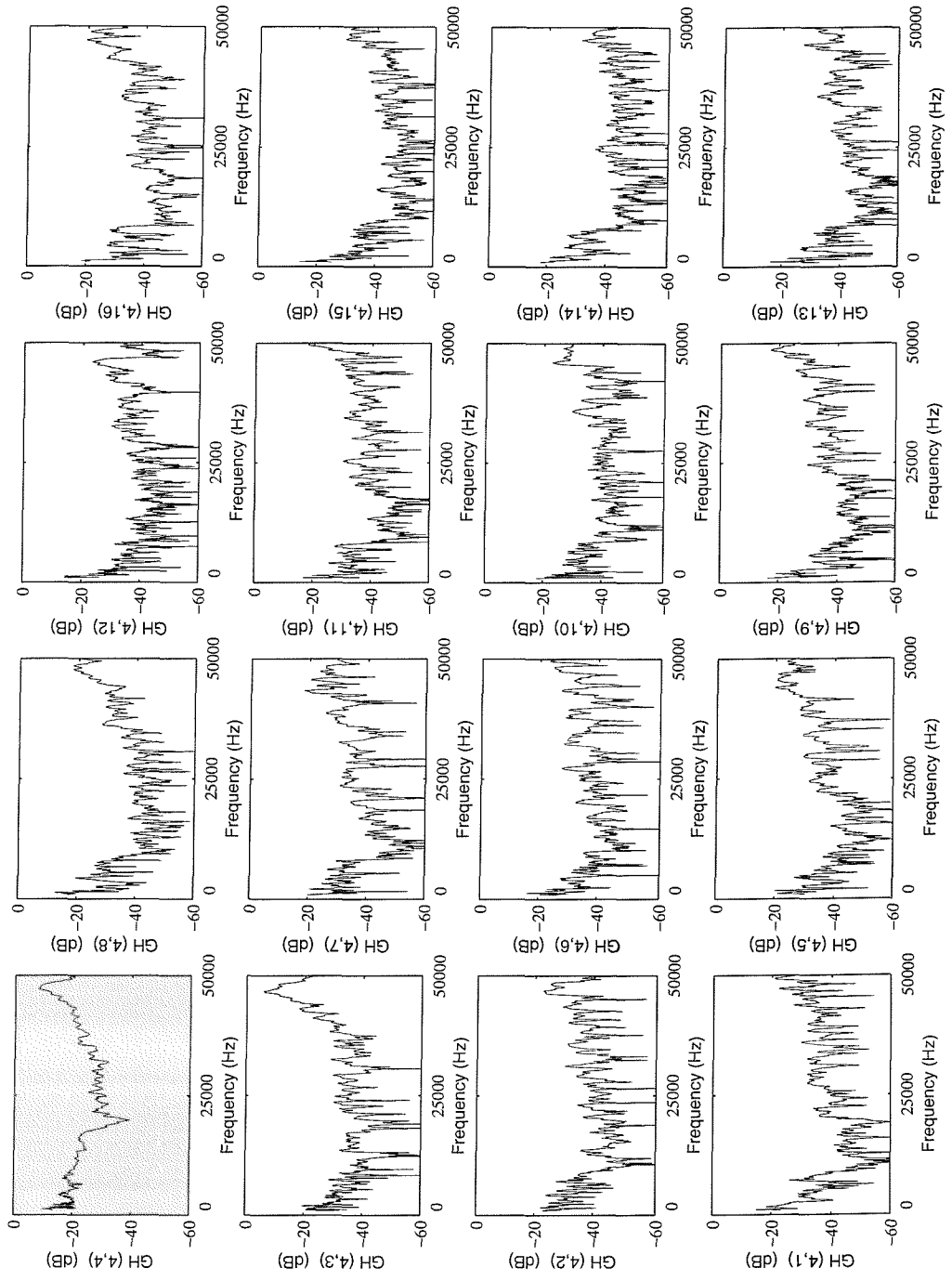

Figure B.4: *The sixteen measured frequency response functions between the sixteen control outputs and the piezo actuator n. 4, exciting the plate in a frequency range of 50 kHz*

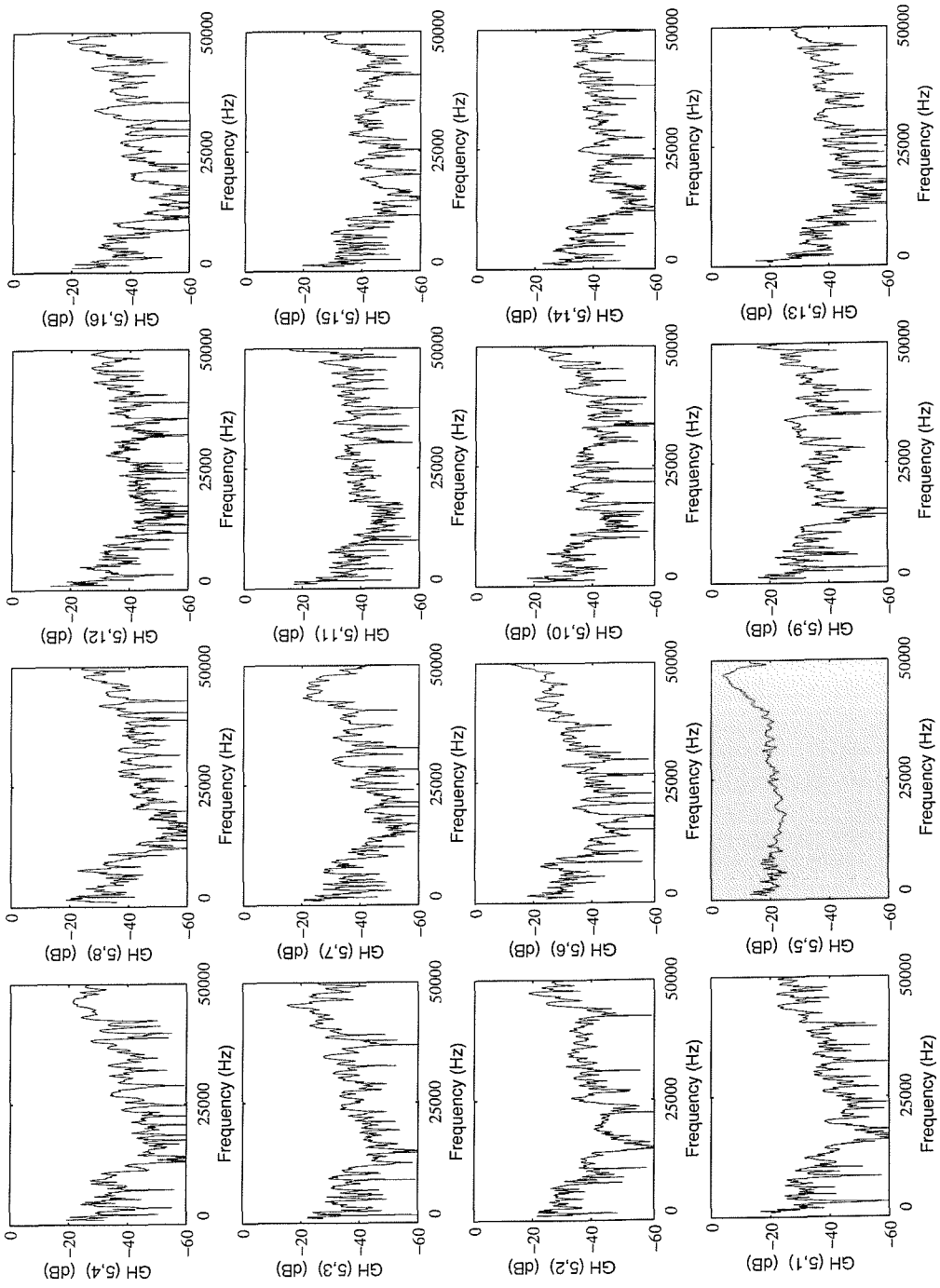

Figure B.5: *The sixteen measured frequency response functions between the sixteen control outputs and the piezo actuator n. 5, exciting the plate in a frequency range of 50 kHz*

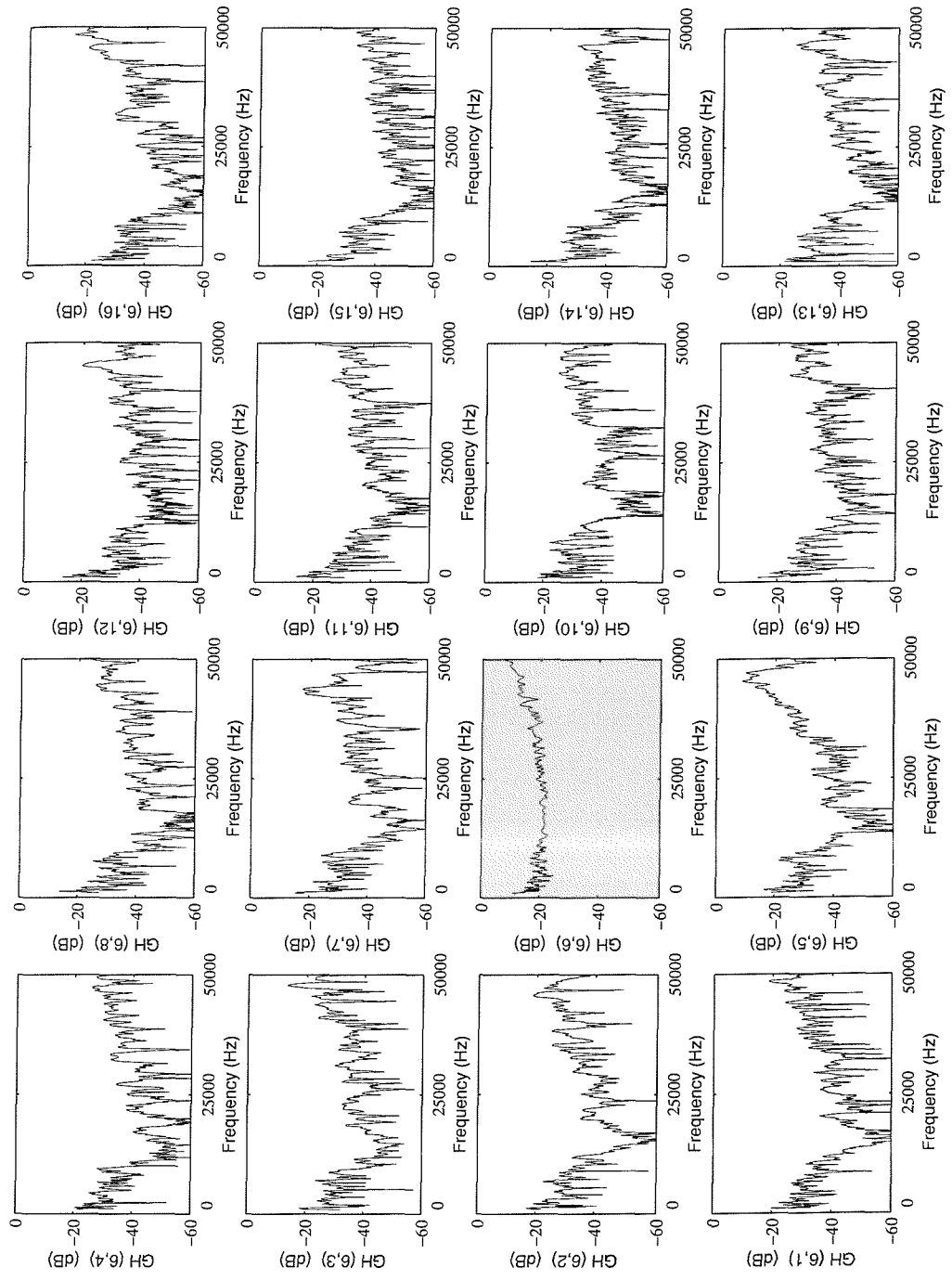

Figure B.6: *The sixteen measured frequency response functions between the sixteen control outputs and the piezo actuator n. 6, exciting the plate in a frequency range of 50 kHz*

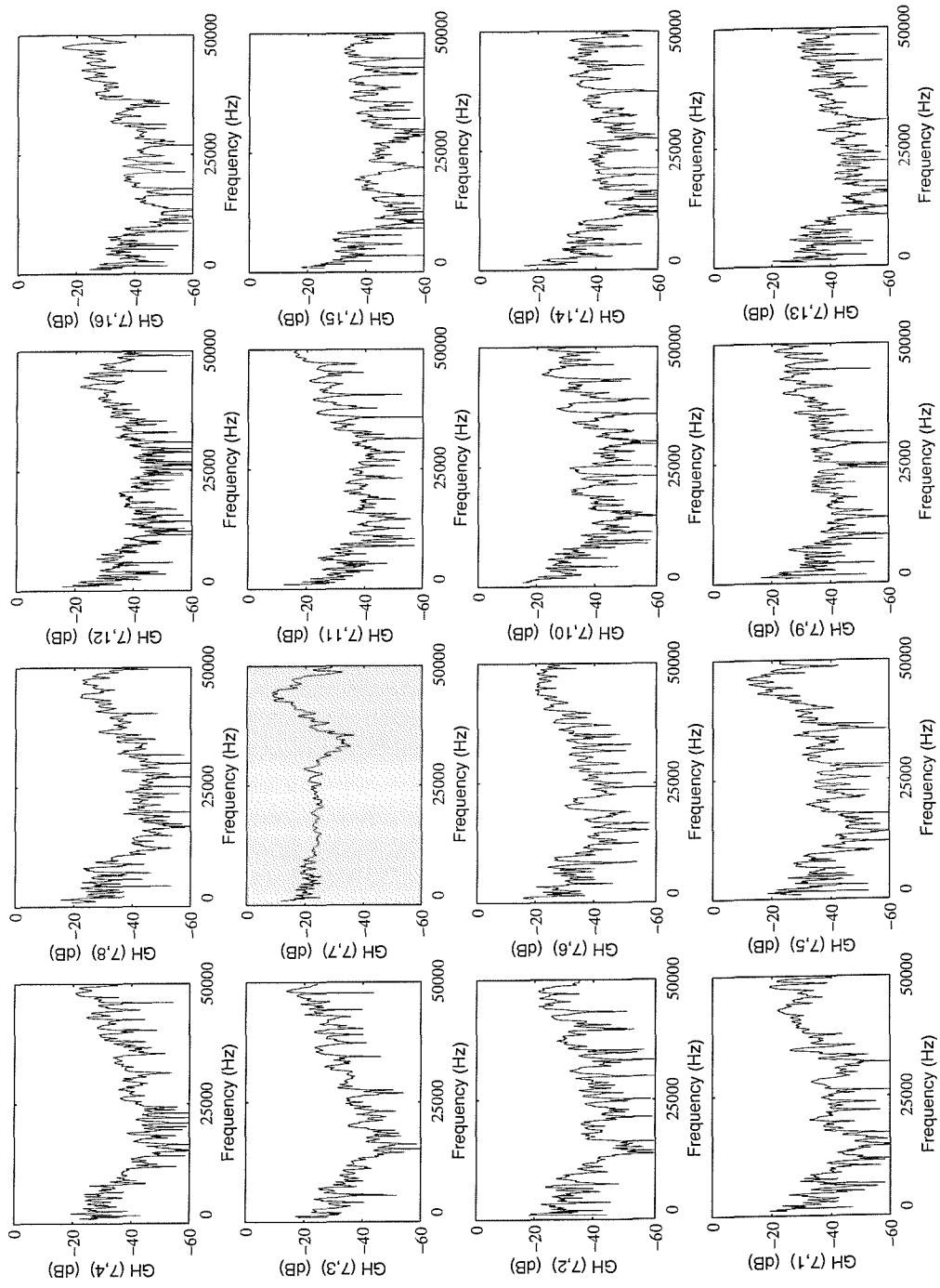

Figure B.7: *The sixteen measured frequency response functions between the sixteen control outputs and the piezo actuator n. 7, exciting the plate in a frequency range of 50 kHz*

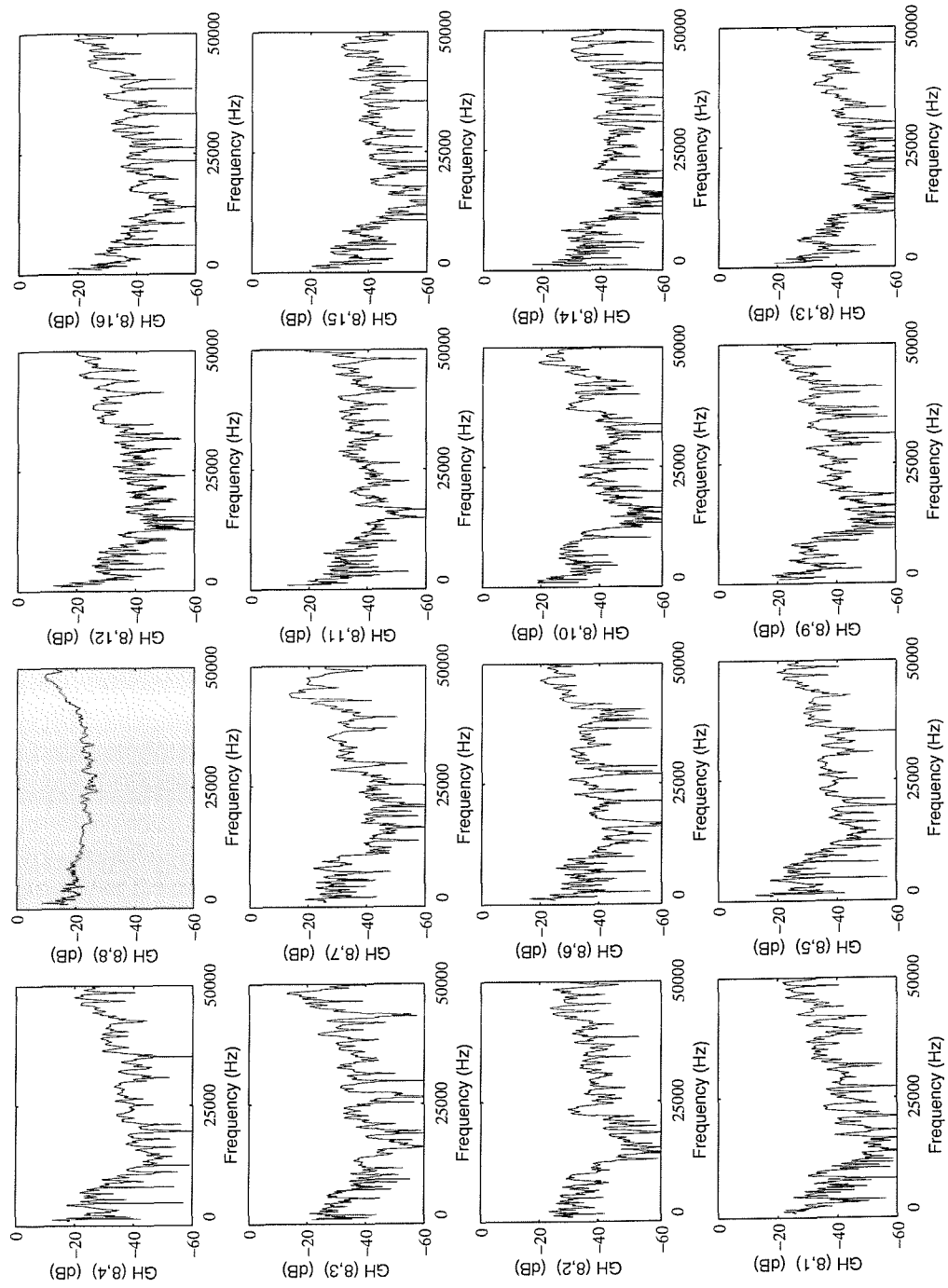

Figure B.8: *The sixteen measured frequency response functions between the sixteen control outputs and the piezo actuator n. 8, exciting the plate in a frequency range of 50 kHz*

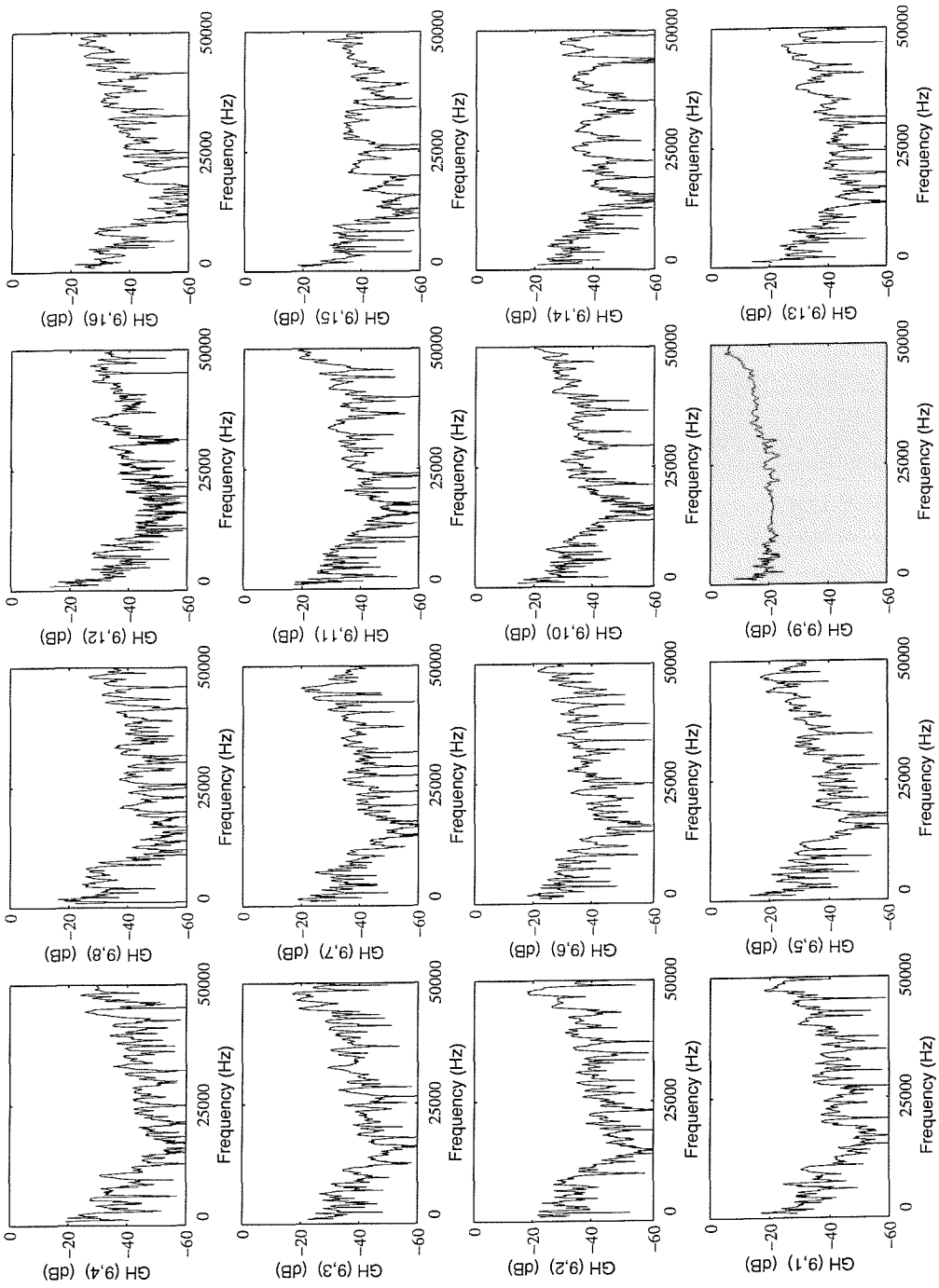

Figure B.9: *The sixteen measured frequency response functions between the sixteen control outputs and the piezo actuator n. 9, exciting the plate in a frequency range of 50 kHz*

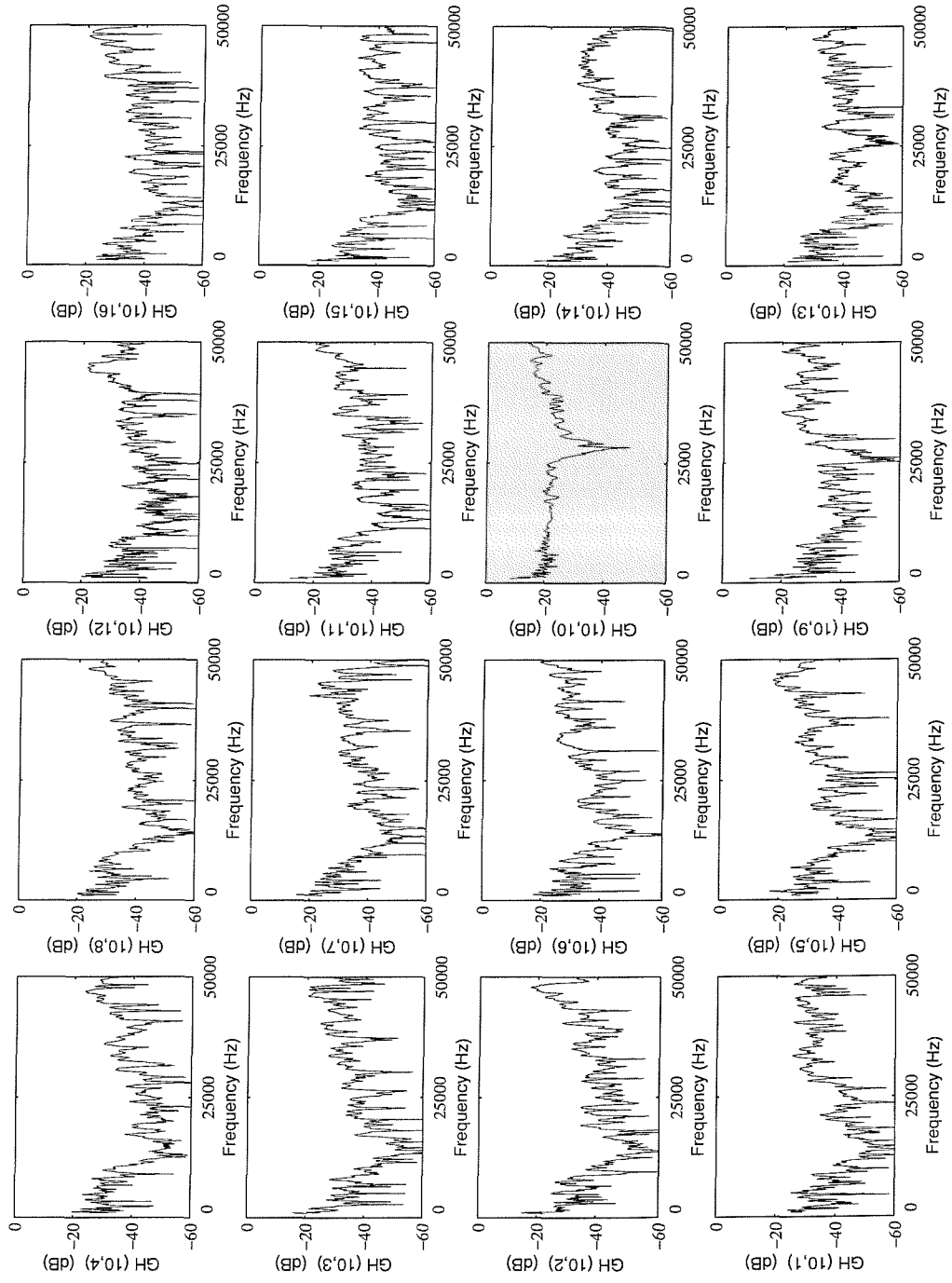

Figure B.10: *The sixteen measured frequency response functions between the sixteen control outputs and the piezo actuator n. 10, exciting the plate in a frequency range of 50 kHz*

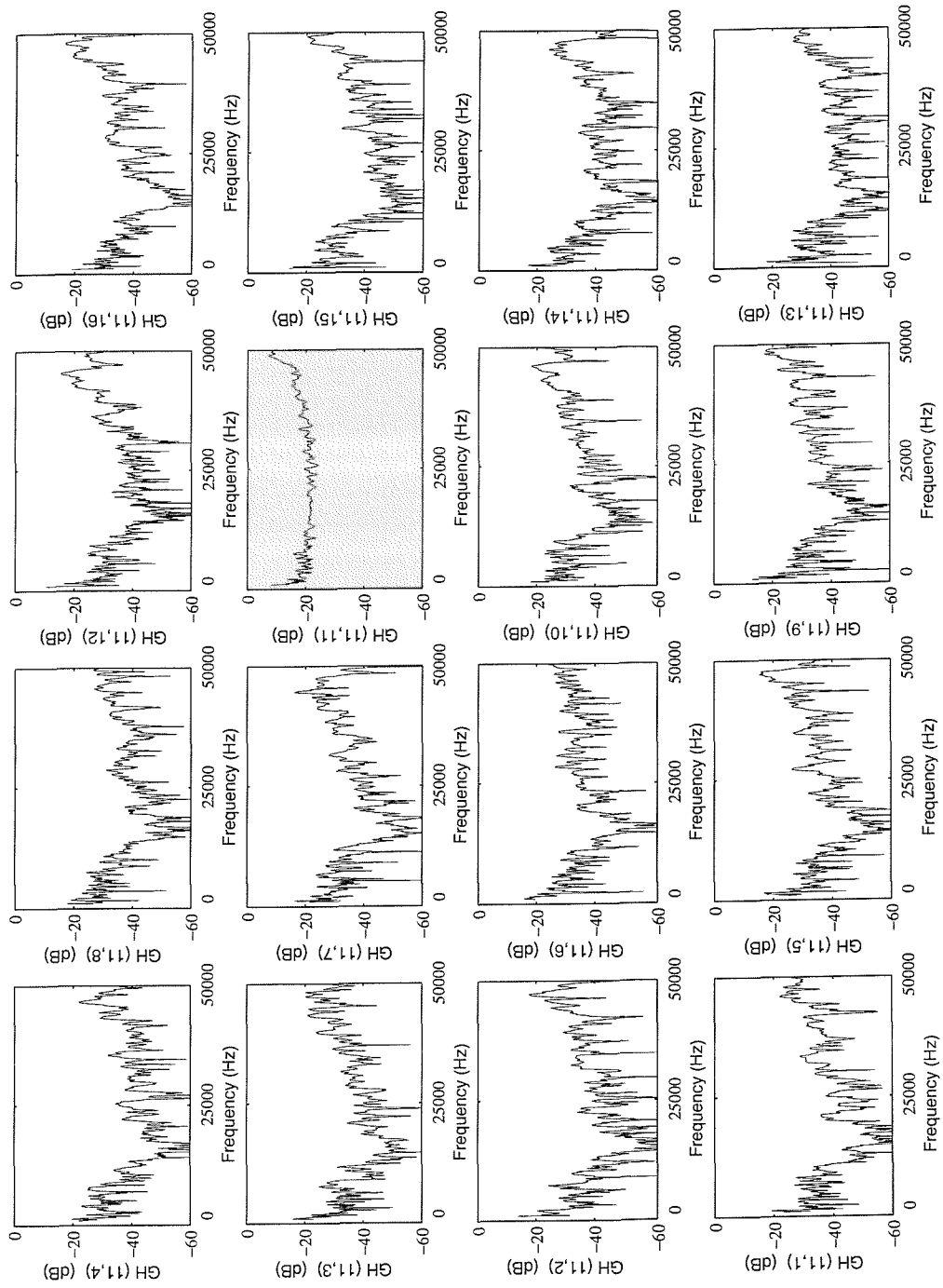

Figure B.11: *The sixteen measured frequency response functions between the sixteen control outputs and the piezo actuator n. 11, exciting the plate in a frequency range of 50 kHz*

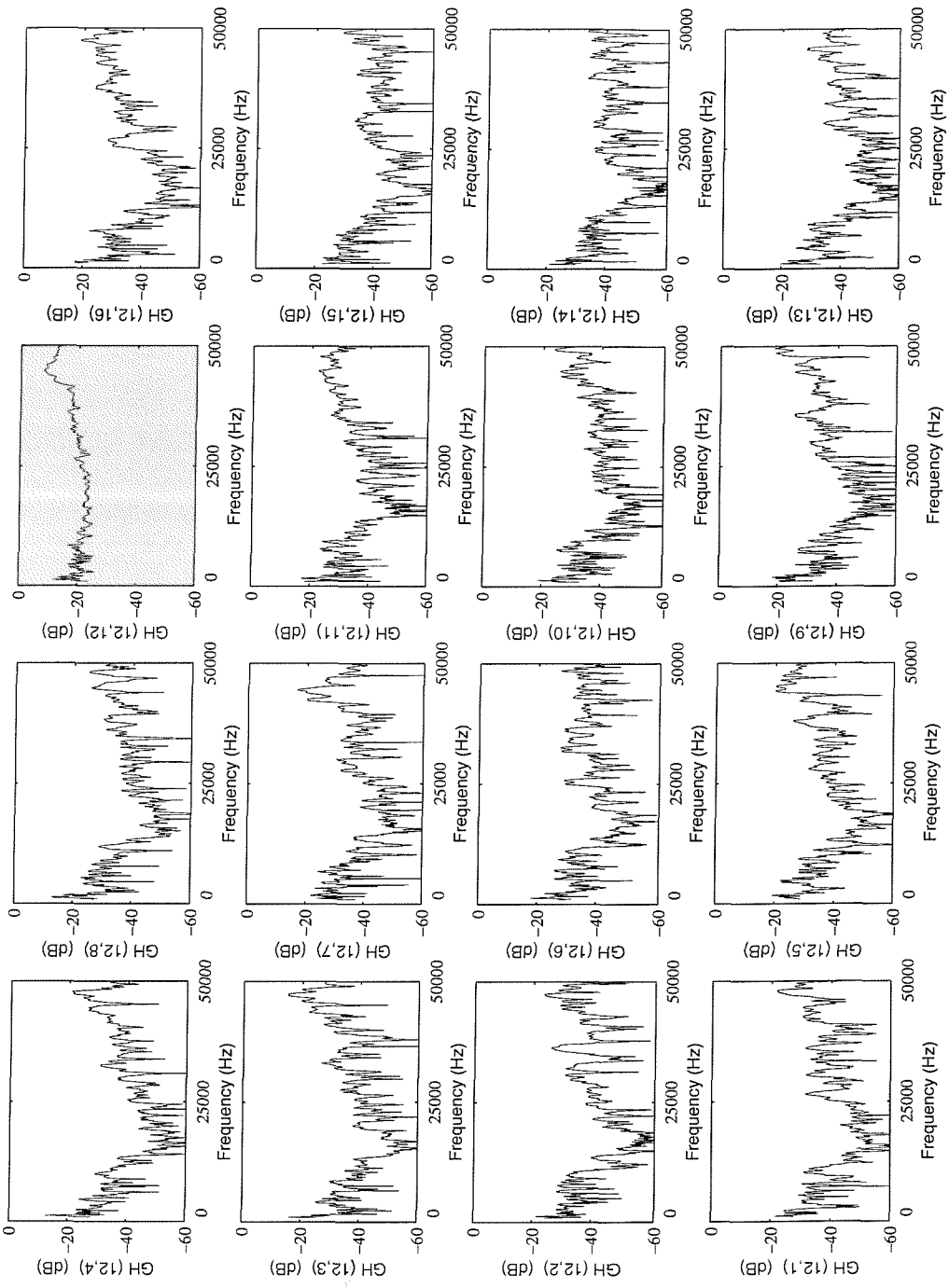

Figure B.12: *The sixteen measured frequency response functions between the sixteen control outputs and the piezo actuator n. 12, exciting the plate in a frequency range of 50 kHz*

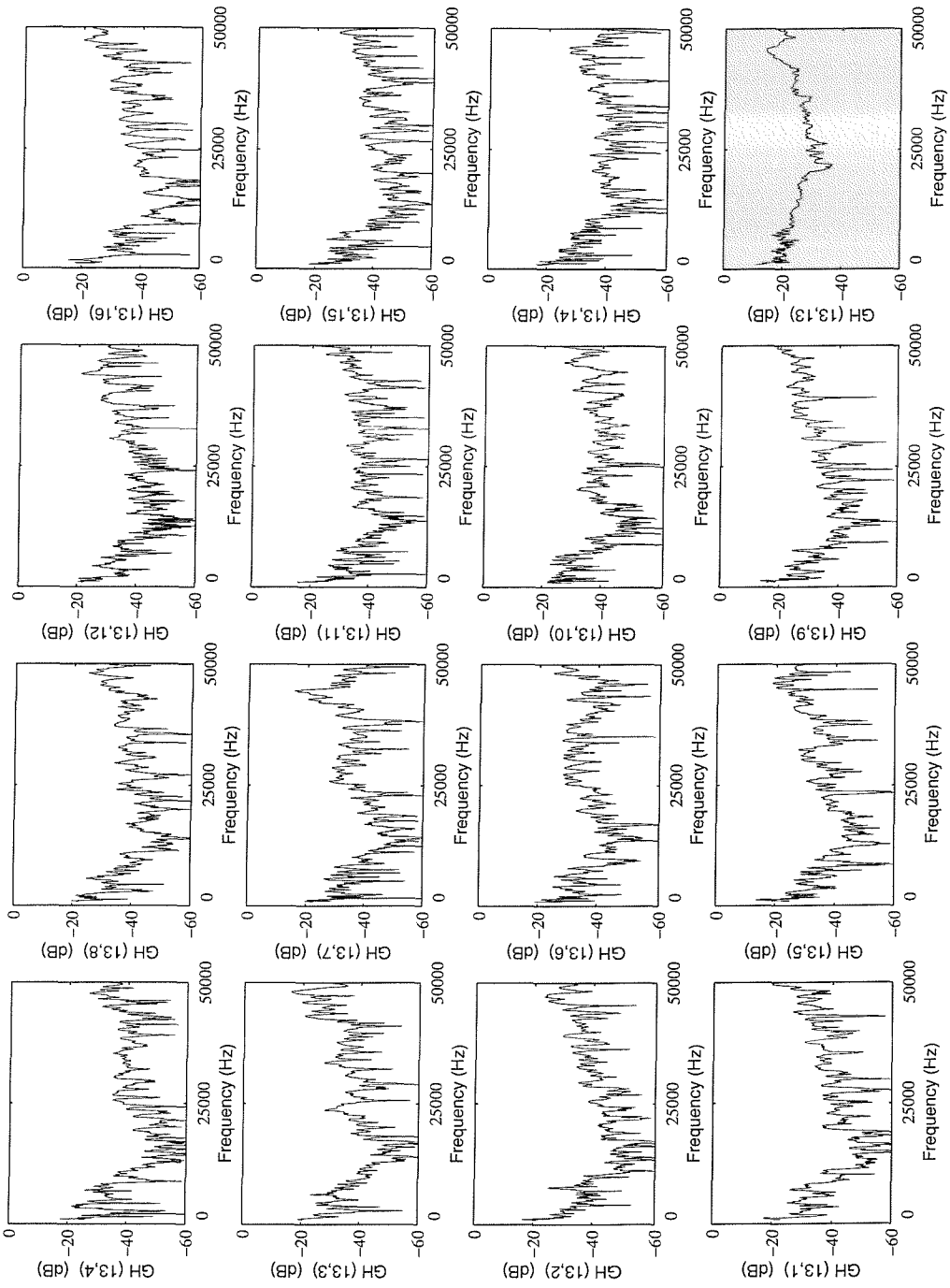

Figure B.13: *The sixteen measured frequency response functions between the sixteen control outputs and the piezo actuator n. 13, exciting the plate in a frequency range of 50 kHz*

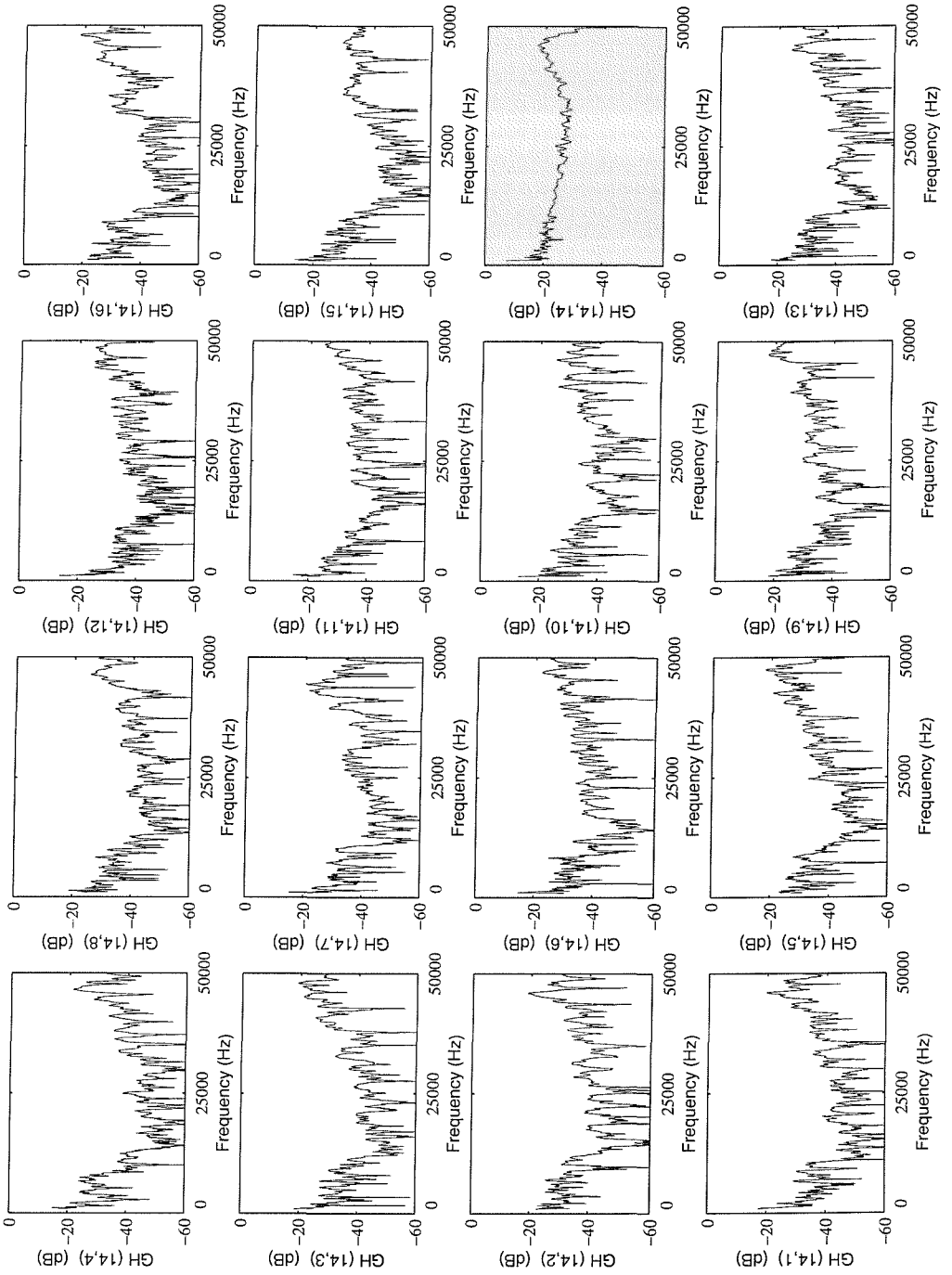

Figure B.14: *The sixteen measured frequency response functions between the sixteen control outputs and the piezo actuator n. 14, exciting the plate in a frequency range of 50 kHz*

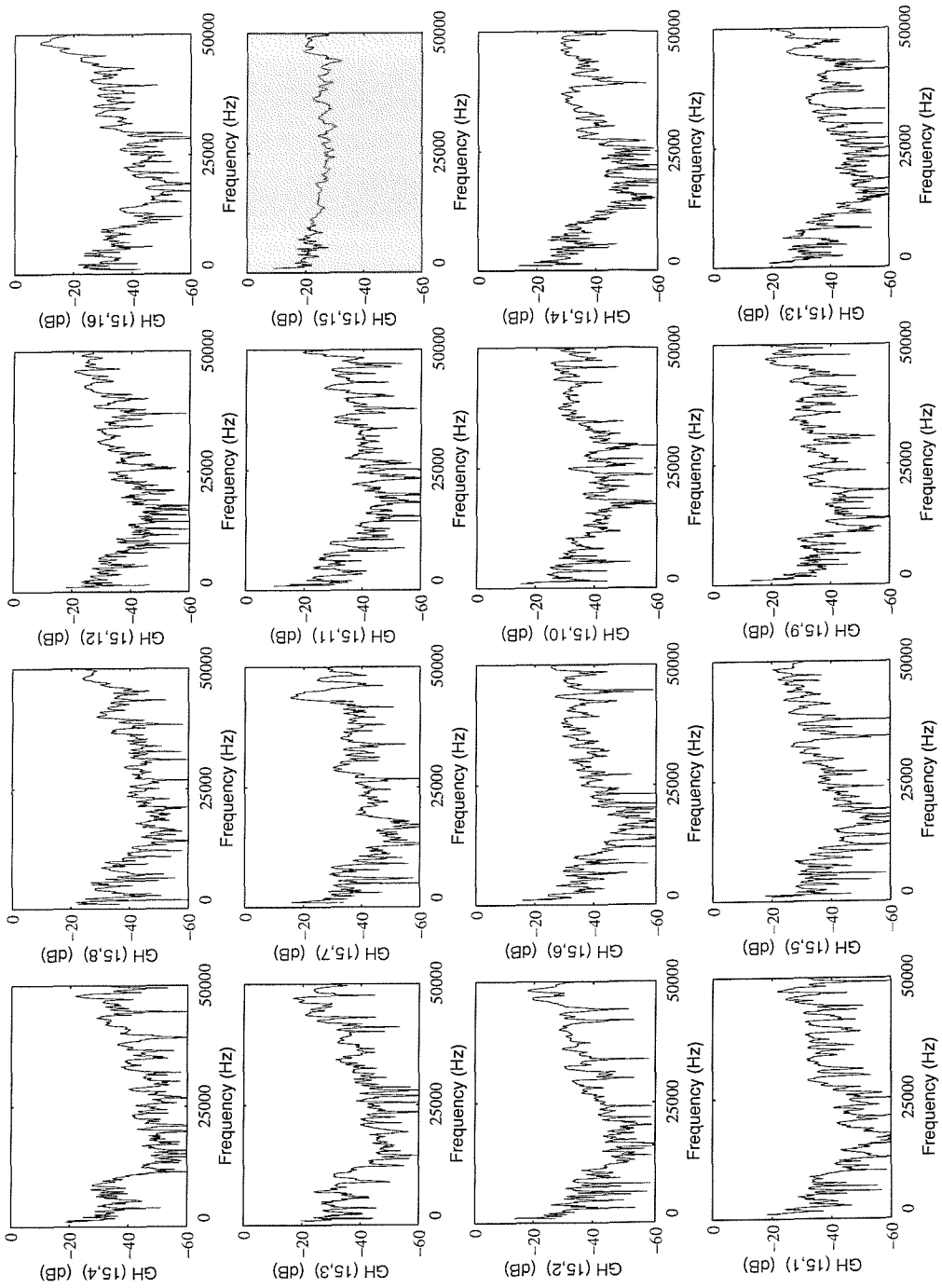

Figure B.15: *The sixteen measured frequency response functions between the sixteen control outputs and the piezo actuator n. 15, exciting the plate in a frequency range of 50 kHz*

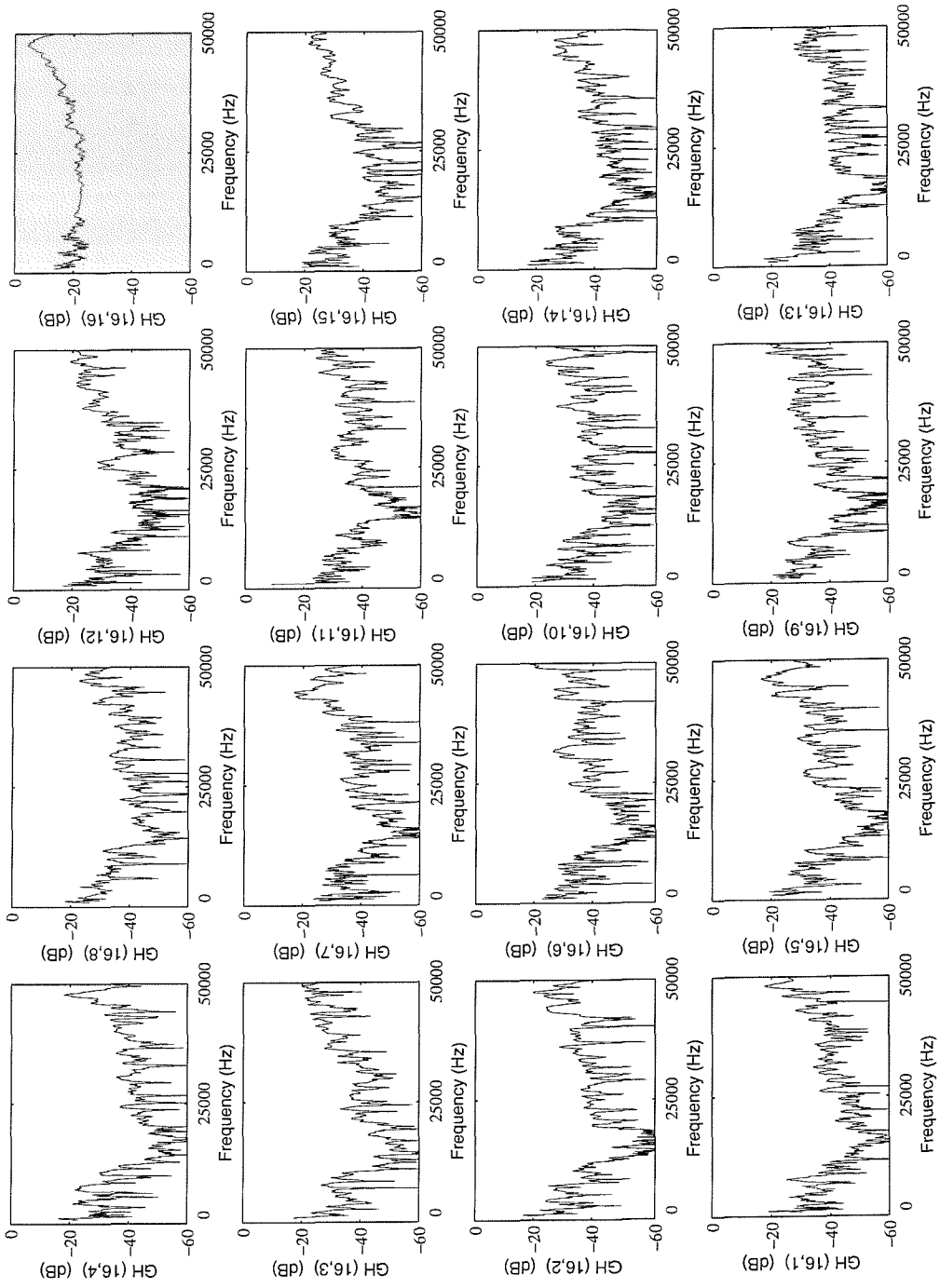

Figure B.16: *The sixteen measured frequency response functions between the sixteen control outputs and the piezo actuator n. 16, exciting the plate in a frequency range of 50 kHz*

APPENDIX C

A Laser Doppler Vibrometer (LDV) is based on the principle of the detection of the Doppler shift of coherent laser light that is scattered from a small area of the test object. The object scatters or reflects light from the laser beam and the Doppler frequency shift is used to measure the component of velocity, which lies along the axis of the laser beam.

For this particular application a Polytec PSV-300 Laser Vibrometer has been used. This device consists of two main components: the *scan head* and the *processing system*. The scan head contains XY deflection mirrors, live colour video camera and LDV sensors. The deflection mirrors automatically steer the laser beam to the desired position on the target within a 40^{o}x40^{o} field of view. The mirrors move very fast (typical settling time is <10ms), so an area can be measured very quickly. The live video camera displays the laser beam on the target and allows the user to draw a grid of desired measurement points right over a video image. With live video, the scan head can be operated remotely, from a control room. After every measurement, the area data are conveniently overlaid directly upon the video image. The OFV-303 LDV sensor comes already mounted into the OFV-056 scan unit.

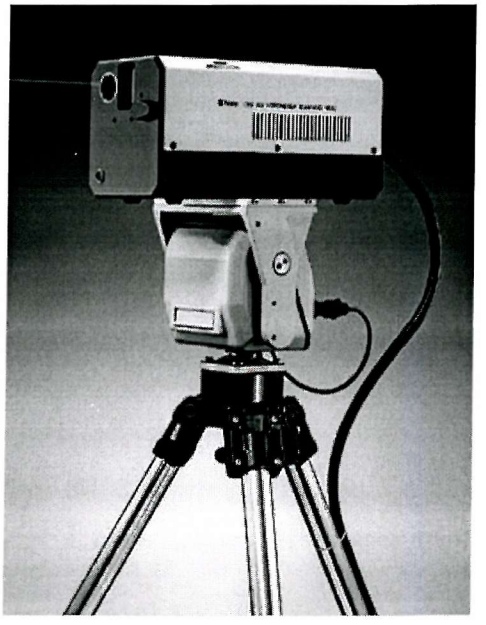

Figure C.1: *Scan Head of the Laser Vibrometer PSV-300*

The control/processing system consists of the LDV controller, the junction box and the Data Management System (DMS). The LDV controller produces an analogue voltage output

proportional to surface vibration, while the junction box is a central interface between the scan head, LDV controller and DMS. Finally, the Data Management System (DMS) is the "central brain" of the device, and controls every aspect of set-up, data acquisition, analysis, storage and transfer.

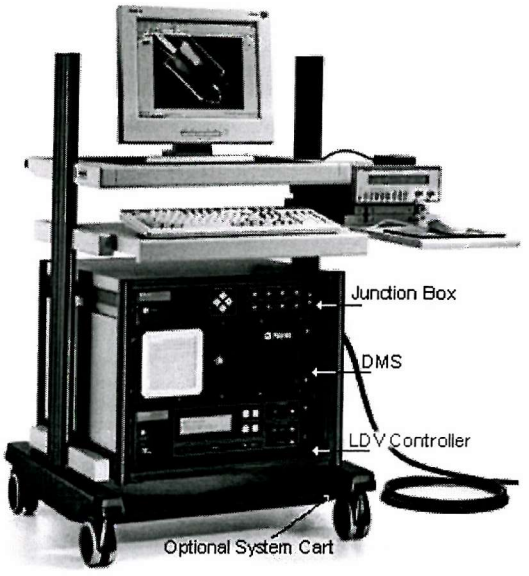

Figure C.2: *Control/processing system of the Laser Vibrometer PSV-300*

LIST OF REFERENCES

[1] Gardonio P., Bianchi E. and Elliott S.J. (2002) Smart panel with multiple decentralised units for the control of sound transmission. Part I: theoretical prediction. Part II: design of the decentralised control units. Part III: control system Implementation. *Proceedings of ACTIVE 2002, Southampton, United Kingdom,* 471-510.

[2] Gardonio P., Bianchi E. and Elliott S.J. (2002) Smart panel with multiple decentralised units for the control of sound transmission. Part I: theoretical prediction. Part II: design of the decentralised control units. Part III: control system Implementation. *Submitted to Journal of Sound and Vibration.*

[3] Elliott S.J., Gardonio P., Sors T.J. and Brennan M.J. (2002) Active vibroacoustic control with multiple local feedback loops. *Journal of the Acoustical Society of America* **111**(2), 908-915.

[4] Nelson P.A. and Elliott S.J. (1992) *Active Control of Sound.* London, Academic Press, 1st Edition.

[5] Ross C.F. and Purver M.R. (1997) Active cabin noise control. *Proceedings of ACTIVE 97, Budapest, Hungary,* XXXIX-XLVI.

[6] Emborg U., Leth S., Samuelson F. and Holmgren J. (1998) Active and passive noise control in practice on the SAAB 2000 high speed turboprop. *AIAA/CEAS Paper 98-2231, 4th AIAA/CEAS Aeroacoustic Conference (19th AIAA Aeroacoustics Conference), Tolouse, France.*

[7] Scott I., Purver M. and Stothers I. (2002) Tonal Active Control in Production on a Large Turbo-Prop Aircraft. *Proceedings of ACTIVE 2002, Southampton, United Kingdom,* 369-376.

[8] Gardonio P. (2002) Review of Active Techniques for Aerospace Vibro-Acoustic Control. *AIAA Journal of Aircraft 2002,* 206-214.

[9] Oswald L.J. (1999) Reduction of diesel engine noise inside passenger compartments using active adaptive noise control. *Proceedings of InterNoise 84,* 483-488.

[10] Elliott S.J., Stothers M., Nelson P.A., McDonald A.M., Quinn D.C. and Saunders T. (1998) The active control of engine noise inside cars. *Proceedings of InterNoise 88,* 987-990.

[11] Mathur G.P., Tran B.N. and Simpson M.A. (1997) Broadband active structural acoustic control of aircraft cabin noise – laboratory tests. *AIAA-97-1636-CP.*

[12] Guigou C. and Fuller C.R. (1999) Control of aircraft interior broadband noise with foam-PVDF smart skin. *Journal of Sound and Vibration* **220**(3), 541-557.

[13] Sutton T.J., Elliott S.J. and McDonald A.M. (1994) Active control of road noise inside vehicles. *Noise Control Engineering Journal* **42**, 137-147.

[14] Park C., Fuller C.R. and Kidner M. (2002) Evaluation and demonstration of advanced active noise control in a passenger automobile. *Proceedings of Active 2002, Southampton, United Kingdom,* 275-284.

[15] Roure A. (1985) Self-adaptive broadband active sound control system. *Journal of Sound and Vibration* **101**(3), 429-441.

[16] Fuller C.R., Elliott S.J. and Nelson P.A. (1996) *Active Control of Vibration.* London, Academic Press, 1st Edition.

[17] Clark R.L. and Fuller C.R. (1992) Experiments on active control of structurally radiated sound using multiple piezoceramic actuators. *Journal of the Acoustical Society of America* **91**(6), 3313-3320.

[18] Fuller C.R. (1990) Active control of sound transmission/radiation from elastic plates by

vibration inputs: I analysis. *Journal of Sound and Vibration* **136**(1), 1-15.

[19] Fuller C.R., Hansen C.H. and Snyder S.D. (1991) Active control of sound radiation from a vibrating rectangular panel by sound sources and vibration inputs: an experimental comparison. *Journal of Sound and Vibration* **145**(2), 195-215.

[20] Wang B.-T., Fuller C.R. and Dimitriadis E.K. (1991) Active control of noise transmission through rectangular plates using multiple piezoelectric or point force actuators. *Journal of the Acoustical Society of America* **90**(5), 2820-2830.

[21] Fahy F.J. (1994) *Sound and Structural Vibration.* London, Academic Press, 1st Edition.

[22] Li W.L. and Gibeling H.J. (2000) Determination of the mutual radiation resistances of a rectangular plate and their impact on the radiated sound power. *Journal of Sound and Vibration* **229**(5), 1213-1233.

[23] Li W.L. (2001) An analytical solution for the self- and mutual radiation resistances of a rectangular plate. *Journal of Sound and Vibration* **245**(1), 1-16.

[24] Skudrzyk E.J. (1958). Vibrations of a system with a finite or an infinite number of resonances. *Journal of the Acoustical Society of America* **30**(12), 1140-1152.

[25] Burdisso R.A. and Fuller C.R. (1992). Dynamic behaviour of structures in feedforward control of sound radiation. *Journal of the Acoustical Society of America* **92**(1), 277-286.

[26] Baumann W.T., Saunders W.R. and Robertshaw H.H. (1991) Active suppression of acoustic radiation from impulsively excited structures. *Journal of the Acoustical Society of America* **88**, 3202-3208.

[27] Baumann W.T., Ho F.-S. and Robertshaw H.H. (1992) Active structural acoustic control of broadband disturbances. *Journal of the Acoustical Society of America* **92**(4), 1998-2005.

[28] Clark R.L. and Fuller C.R. (1992) A model reference approach for implementing active structural acoustic control. *Journal of the Acoustical Society of America* **92**(3), 1534-1544.

[29] Fuller C.R., Rogers C.A. and Robertshaw H.H. (1992) Control of sound radiation with active/adaptive structures. *Journal of the Sound and Vibration* **145**(2), 19-39.

[30] Fuller C.R. and Burdisso R.A. (1992) A wavenumber domain approach to the active control of structure-borne sound. *Journal of the Sound and Vibration* **148**(2), 355-360.

[31] Clark R.L. and Fuller C.R. (1992) Active Structural Acoustic Control with adaptive structures including wavenumber considerations. *Journal of Intelligent Material Systems and Structures* **3**(2), 296-315.

[32] Elliott S.J. and Johnson M.E. (1993) Radiation modes and the active control of sound power. *Journal of the Acoustical Society of America* **94**(4), 2194-2204.

[33] Snyder S.D., Tanaka N. and Kikushima Y. (1996) The use of optimally shaped piezo-electric film sensors in the active control of free field structural radiation. Part 1: feedforward control. *ASME Journal of Vibration and Acoustics* **117**, 311-322.

[34] Fuller C.R. and Silcox R.J. (1992) Active Structural Acoustic Control. *Journal of the Acoustical Society of America* **91**(1), 519.

[35] Johnson M.E. and Elliott S.J. (1995) Active control of sound radiation using volume velocity cancellation. *Journal of the Acoustical Society of America* **98**(4), 2174-2186.

[36] Lee C.K. (1990) Theory of laminated piezoelectric plates for the design of distributed sensor/actuators. Part I: Governing equations and reciprocal relationships. *Journal of the Acoustical Society of America* **87**(3), 1144-1158.

[37] Rex J. and Elliott S.J. (1992) The QWSIS – a new sensor for structural radiation control. *Proceedings of the International Conference on Motion and Vibration Control (MOVIC), Yokohama,* 339-343.

[38] Clark R.L., Fuller C.R. and Burdisso R.A. (1992) Design approaches for shaping

Polyvinylidene Fluoride sensors in active structural acoustic control (ASAC). *Proceedings of the Conference on Recent Advances in Adaptive and Sensory Materials and Their Application , Blacksburg, Virginia,* 702-726.

[39] Clark R.L. and Fuller C.R. (1992) Optimal placement of piezoelectric actuators and polyvinylidene fluoride error sensors in active structural acoustic control approaches. *Journal of the Acoustical Society of America* **92**(3), 1521-1533.

[40] Clark R.L. and Fuller C.R. (1992) Modal sensing of efficient acoustic radiators with polyvinylidene fluoride distributed sensors in active structural acoustic control approaches. *Journal of the Acoustical Society of America* **91**(6), 3321-3329.

[41] Burdisso R.A. and Fuller C.R. (1993) Optimum actuator and sensor design for active structural acoustic control. *Proceedings of the American Society of Mechanical Engineers Winter Annual Meeting, New Orleans, Louisiana, ASME AD-35 363-370.*

[42] Johnson M.E. and Elliott S.J. (1993) Volume velocity sensors for active control. *Proceedings of the Institute of Acoustics,* **15**(3), 411-420.

[43] Clark R.L., Burdisso R.A. and Fuller C.R. (1993) Design approaches for shaping PVDF sensors in active structural acoustic control. *Journal of Intelligent Material Systems and Structures* **4**, 354-365.

[44] Carey D.M. and Stulen F.B. (1993) Experiments with a two-dimensional multi-modal sensor. *Proceedings of Recent Advances in Active Control of Sound and Vibration, supplement,* 41-52.

[45] Collins S.A., Miller D.W. and von Flotow A.H. (1994) Distributed sensors as spatial filters in active structural control. *Journal of Sound and Vibration* **173**(4), 471-501.

[46] Gu Y., Clark R.L., Fuller C.R. and Zander A.C. (1994) Experiments on active control of plate vibration using piezoelectric actuators and polyvinylidene floride (PVDF) modal sensors. *ASME Journal of Vibration and Acoustics* **116**, 303-308.

[47] Johnson M.E. (1996) Active control of sound transmission. *University of Southampton, PhD thesis.*

[48] Charette F., Berry A. and Guigou C. (1998) Active control of sound radiation from a plate using a polyvinylidene fluoride volume displacement sensor. *Journal of the Acoustical Society of America* **103**(3), 1493-1503.

[49] Henrioulle K. (2001) Distributed actuators and sensors for active noise control. *Katholieke Universiteit Leuven, PhD thesis*

[50] Clark R.L., Saunders W.R. and Gibbs G.P. (1998) *Adaptive Structures.* New York, John Wiley & Sons, Inc., 1st Edition.

[51] Preumont A. (2002) *Vibration control of active structures.* Kluwer Academic Publishers, 2nd Edition.

[52] Gardonio P. and Elliott S.J. (2002) Smart panels for active structural acoustic control. *Proceedings of ISMA 2002, Katholieke Universiteit Leuven, Belgium.*

[53] Burke S.E. and Hubbard Jr. J.E. (1991) Distributed transducer vibration control of thin plates. *Journal of the Acoustical Society of America* **90**(2), 937-944.

[54] Maillard J.P. and Fuller C.R. (1994) Advanced time domain wave-number sensing for structural acoustic systems. I. Theory and design. *Journal of the Acoustical Society of America* **95**(6), 3252-3261.

[55] Masson P., Berry A. and Nicolas J. (1997) Active structural acoustic control using strain sensing. *Journal of the Acoustical Society of America* **102**(3), 1588-1599.

[56] Maillard J.P. and Fuller C.R. (1998) Comparison of two structural sensing approaches for active structural acoustic control. *Journal of the Acoustical Society of America* **103**(1), 396-400.

[57] Gibbs G.P., Clark R.L., Cox D.E. and Vipperman J.S. (2000) Radiation modal expansion: application to active structural acoustic control. *Journal of the Acoustical Society of America* **107**(1), 332-339.

[58] Preumont A., Francois A. and Durbru S. (1999) Piezoelectric array sensing for real-time, broad-band sound radiation measurement. *ASME Journal of Vibration and Acoustics* **121**, 446-452.

[59] Francois A., De Man P. and Preumont A. (2001) Piezoelectic array sensing of volume displacement: a hardware demonstration. *Journal of Sound and Vibration* **244**(3), 395-405.

[60] Lee Y.-S., Gardonio P. and Elliott S.J. (2002) Experimental study of volume velocity vibration control of a smart panel using a quadratically shaped PVDF actuator and a multiple accelerometers arrangement. *The Journal of Smart Materials and Structures (in press)*

[61] Dimitriadis E.K., Fuller C.R. and Rogers C.A. (1991) Piezoelectric actuators for distributed vibration excitation of thin plates. *ASME Journal of Vibration and Acoustics* **113**, 100-107.

[62] Rogers C.A., Liang C., and Fuller C.R. (1991) Modelling of shape memory alloy hybrid composites for structural acoustic control. *Journal of the Acoustical Society of America* **89**(1), 210-220.

[63] Clark R.L., Fuller C.R. and Wicks A.L. (1991) Characterization of multiple piezoelectric actuators for structural excitation. *Journal of the Acoustical Society of America* **90**(1), 346-357.

[64] Clark R.L., Fleming M.R. and Fuller C.R. (1993) Piezoelectric actuators for distributed vibration excitation of thin plates. *ASME Journal of vibration and acoustics* **115**, 332-339.

[65] Zhou S.-W., Liang C., and Rogers C.A. (1994) Modelling of distributed piezoelectric actuators integrated with thin cylindrical shells. *Journal of the Acoustical Society of America* **96**(3), 1605-1612.

[66] Sullivan J.M., Hubbard Jr J.E. and Burke S.E. (1996) Modelling approach for two-dimensional distributed transducers of arbitrary spatial distribution. *Journal of the Acoustical Society of America* **99**(5), 2965-2974.

[67] Sullivan J.M., Hubbard Jr J.E. and Burke S.E. (1997) Distributed sensor/actuator design for plates: spatial shape and shading as design parameters. *Journal of Sound and Vibration* **203**(3), 473-493.

[68] Sutton T.J., Johnson M.E. and Elliott S.J. (1997) A distributed actuator for the active control of sound transmission through a partition. *Proceedings of the 6th International Conference on Structural Dynamics Recent Advances, University of Southampton, United Kingdom,* 1247-1255.

[69] Gardonio P., Lee Y.-S., Elliott S.J. and Debost S. (2001) A panel with matched polyvinylidene fluoride volume velocity sensor and uniform force actuator for the active control of sound transmission. *Proceedings of the Institution of Mechanical Engineers Vol. 215, Part G,* 187-206.

[70] Gardonio P., Lee Y.-S., Elliott S.J. and Debost S. (2001) Analysis and measurement of a matched volume velocity sensor and uniform force actuator for active structural acoustic control. *Journal of the Acoustical Society of America* **110**(6), 3025-3031.

[71] Burke S.E., Hubbard Jr J.E., and Meyer J.E. (1993) Distributed transducers and collocation. *Mechanical Systems and Signal Processing* **7**(4), 765-770.

[72] Sun J.Q. (1996) Some observations on physical duality and collocation of structural control sensors and actuators. *Journal of Sound and Vibration* **194**(5), 765-770.

[73] Jayachadran V. and Sun J.Q. (1997) Unconditional stability domains of structural control systems using dual actuator-sensor pairs. *Journal of Sound and Vibration* **208**(1), 159-166.

[74] Balas M.J. (1979) Direct velocity feedback of large space structures. *Journal of Guidance and Control* **2**, 252-253.

[75] Smith J.P., Fuller C.R., and Burdisso R.A. (1992) Active structural acoustic control of radiation due to broadband disturbances. *Journal of the Acoustical Society of America* **92**(4), 2409-2410.

[76] Burdisso R.A., Vipperman J.S., and Fuller C.R. (1993) Causality analysis of feedforward-controller systems with broadband inputs. *Journal of the Acoustical Society of America* **94**(1), 234-242.

[77] Carneal J.P. and Fuller C.R. (1993) Active structural acoustic control of noise transmission through double panel systems. *AIAA Paper 93-4421 Presented at 15th American Institute of Aeronautics and Astronautics Aeroacoustics Conference, Long Beach, California.*

[78] Thomas D.R. and Nelson P.A. (1995) Feedback control of sound radiation from a plate excited by a turbulent boundary layer. *Journal of the Acoustical Society of America* **98**(5), 2651-2662.

[79] Clark R.L. and Cox D.E. (1996) Multi-variable structural acoustic control with static compensation. *Journal of the Acoustical Society of America* **102**(5), 2747-2756.

[80] Dehandschutter W., Henrioulle K., Swevers J. and Sas P. (1997) Feedback control of broadband sound radiation using a volume velocity sensor. *Proceedings of ACTIVE 97, Budapest, Hungary, 979-992.*

[81] Cox D.E., Gibbs G.P., Clark R.L. and Vipperman J.S. (1999) Experimental robust control of structural acoustic radiation. *ASME Journal of Vibration and Acoustics* **121**, 433-439.

[82] Vipperman J.S. and Clark R.L. (1999) Acoustic power suppression of a panel structure using H∞ output feedback control. *Journal of the Acoustical Society of America* **105**(1), 219-225.

[83] Seto K., Ren M. and Doi F. (2001) Modelling and feedback structural acoustic control of a flexible plate. *ASME Journal of Vibration and Acoustics* **123**, 18-23.

[84] Smith G.C. and Clark R.L. (2001) A crude method of loop-shaping adaptive structures through optimum spatial compensator design. *Journal of Sound and Vibration* **247**(3), 489-508.

[85] Henry J.K. and Clark R.L. (2002) Active control of sound transmission through a curved panel into a cylindrical enclosure. *Journal of Sound and Vibration* **249**(2), 325-349.

[86] Chang W., Varadan S.V. and Varadan V.K. (2002) Design of robust vibration controller for a smart panel using finite element model. *ASME Journal of Vibration and Acoustics* **124**, 265-276.

[87] Doyle J.C., Glover K., Khargonekar P.P. and Francis B.A. (1989) State-space solutions to standard H2 and H∞ control problems. *IEEE Transactions on Automatic Control* **34**(8), 831-847.

[88] Boyd S. and Barratt C. (1991) *Linear Controller Design: Limits of Performance.* Prentice-Hall, Englewood Cliffs, NJ.

[89] Snyder S.D., Tanaka N. and Kikushima Y. (1996) The use of optimally shaped piezo-electric film sensors in the active control of free field structural radiation. Part 2: feedback control. *ASME Journal of Vibration and Acoustics* **118**, 112-121.

[90] De Man P., Francois A. and Preumont A. (2002) Robust feedback control of a baffled plate via open-loop optimisation. *ASME Journal of Vibration and Acoustics* **124**, 154-157.

[91] Bingham B., Atalla M.J. and Hagood N.W. (2001) Comparison of structural-acoustic control designs on an active composite panel. *Journal of Sound and Vibration* **244**(5), 761-778.

[92] Heatwole C.H., Franchek M.A. and Bernhard R.J. (1997) Robust feedback control of flow-induced structural radiation of sound. *Journal of the Acoustical Society of America* **102**(2), 989-997.

[93] Lee Y.-S., Gardonio P. and Elliott S.J. (2002) Coupling analysis of a matched piezoelectric sensor and actuator pair for vibration control of a smart beam. *The Journal of the Acoustical Society of America* **111**(6), 2715-2726.

[94] Cole D.G. and Clark R.L. (1994) Adaptive compensation of Piezoelectric sensors-actuators.

Journal of Intelligent Material Systems and Structures **5**, 665-672.

[95] Gardonio P., Lee Y.S., Elliott S.J. and Debost S. (1999) Active control of sound transmission through a panel with matched PVDF sensor and actuator pair. *Proceedings of Active 99, the 1999 International Symposium on Active Control of Sound and Vibration, Fort Lauderdale Florida, USA,* 341-354.

[96] Morari M. and Zafiriou E. (1989) *Robust process control.*, NJ, Prentice-Hall.

[97] Johnson M.E., Sors T., Elliott S.J. and Rafaely B. (1997) Feedback control of broadband sound radiation using a volume velocity sensor. *Proceedings of ACTIVE 97, Budapest, Hungary,* 1007-1020.

[98] Sors T.C. and Elliott S.J. (1999) Modelling and feedback control of sound radiation from a vibrating panel. *Smart Material Structures* **8**, 301-314.

[99] Guigou C. and Fuller C.R. (1998) Adaptive feedforward and feedback methods for active/passive sound radiation control using smart foam. *Journal of the Acoustical Society of America* **104**(1), 226-231.

[100] Petitjean B. and Legrain I. (1996) Feedback controllers for active vibration suppression. *Journal of Structural Control* **3**(1-2), 111-127.

[101] Petitjean B., Legrain I., Simon F. and Pauzin S. (2002) Active control experiments for acoustic radiation reduction of a sandwich panel: feedback and feedforward investigations. *Journal of Sound and Vibration* **252**(1), 19-36.

[102] Gardonio P. and Elliott S.J. (1999) Driving point and transfer mobility matrices for thin plates excited in flexure. *ISVR Technical Report No. 277.*

[103] Warburton G.B. (1976) *The dynamical behaviour of Structures*, Pergamon Press.

[104] Bianchi E., Gardonio P., and Elliott S.J. (2002) Smart panel with an array of decentralized control systems for active structural acoustic control. *ISVR Technical Memorandum No. 886.*

[105] Rao S.S. (1995) *Vibration measurement and applications*, Chap. 10 in Mechanical Vibration, Addison-Wesley, USA.

[106] Nefske D. J. and Sung S. H. (1992) *Sound in Small Enclosures*, Chap. 6 in Noise and Vibration control Engineering, edited by L. L. Beranek and I. L. Ver, John Wiley & Sons, USA.

[107] Elliott S.J. (2001) *Signal Processing for Active Control.* London, Academic Press, 1st Edition.

[108] Skogestad S. and Postlethwaite I. (1996) *Multivariable Feedback Control – Analysis and Design..* Chichester, John Wiley & Sons, Inc. 1st Edition.

[109] Postlethwaite I. (1998) *Adaptive Structure.* New York, John Wiley & Sons, Inc. 1st Edition.